coatings

Tribological Behavior of Functional Surface

Models and Methods

Edited by
Pawel Pawlus and Andrzej Dzierwa

Printed Edition of the Special Issue Published in *Coatings*

www.mdpi.com/journal/coatings

MDPI

Tribological Behavior of Functional Surface: Models and Methods

Tribological Behavior of Functional Surface: Models and Methods

Editors

Pawel Pawlus
Andrzej Dzierwa

MDPI • Basel • Beijing • Wuhan • Barcelona • Belgrade • Manchester • Tokyo • Cluj • Tianjin

Editors
Pawel Pawlus
Rzeszow University of Technology
Poland

Andrzej Dzierwa
Rzeszow University of Technology
Poland

Editorial Office
MDPI
St. Alban-Anlage 66
4052 Basel, Switzerland

This is a reprint of articles from the Special Issue published online in the open access journal *Coatings* (ISSN 2079-6412) (available at: https://www.mdpi.com/journal/coatings/special_issues/Tribology_Surface).

For citation purposes, cite each article independently as indicated on the article page online and as indicated below:

LastName, A.A.; LastName, B.B.; LastName, C.C. Article Title. *Journal Name* **Year**, *Volume Number*, Page Range.

ISBN 978-3-0365-1036-1 (Hbk)
ISBN 978-3-0365-1037-8 (PDF)

Contents

About the Editors

Pawel Pawlus Professor at the Department of Manufacturing Processes and Production Engineering, Rzeszow University of Technology, Poland. His scientific interests are tribology and surface metrology. He is then author or co-author of more than 300 papers and publications (over 100 from JCR base), including four books. He is also a British Council scholar at Warwick University (United Kingdom) and a supervisor of 10 PhD theses.

Andrzej Dzierwa Associate Professor at the Department of Manufacturing Processes and Production Engineering, Rzeszow University of Technology, Poland. His scientific interests include tribology, surface engineering, surface texturing, and surface topography measurements. He is the author or co-author of more than 70 papers and publications (over 30 from JCR base). He actively participates in national and international research projects conducted with the aid of funds from European Union and national centers.

coatings

MDPI

Editorial

Tribological Behavior of Functional Surface: Models and Methods

Pawel Pawlus * and Andrzej Dzierwa

Faculty of Mechanical Engineering and Aeronautics, Rzeszow University of Technology, Powstancow Warszawy 8 Street, 35-959 Rzeszow, Poland; adzierwa@prz.edu.pl
* Correspondence: ppawlus@prz.edu.pl; Tel.: +48-17-865-1183

Surfaces of solid bodies contain characteristic features, affecting the functional properties of machine elements. Surface topography restricts the contact area to a very small ratio of the nominal area [1]. It is a link between manufacturing and function. In some cases, the effect of surface topography on functional properties can be large. The effect of surface topography on contact (stiffness, conductivity, adhesive properties) is very high, followed by friction, lubrication, wear and fatigue. Loss due to wear and corrosion generates high costs. They can be reduced by surface engineering. The proper creation of surface topography may cause a decrease in friction and wear [2,3]. The frictional properties of machined elements can be improved by surface texturing [4–6]. Coatings make the surface life robust from wear [3,5–11] and corrosion [7–9]. The resistance to motion can be improved by change of the oil [12].

The aim of this Special Issue was to collect high-quality research papers, short communications, and review articles that focus on the tribological behavior of functional surfaces.

In [1], the methodology of prediction of the statistics of contact pressure from roughness analysis was proposed. It was applied to modeled fractal surfaces but could be also used to measure textures.

The effect of the disc surface topography after vapor blasting on tribological properties of a disc–ball assembly under dry friction conditions was studied experimentally [2]. This effect was shown to be substantial. Especially the shape of the ordinate distribution affected volumetric wear.

The Ti-6Al-4V alloy is widely applied for orthopedic implants. Its tribological properties can be improved by various engineering techniques, with PEO (plasma electrolytic oxidation) being one of them. The authors of [3] studied the effect of process parameters and surface finishing of the PEO-treated Ti-6Al-4V alloy using different process parameters on dry sliding behavior. Surface finishing by abrasive blasting with spheroidal glass beads led to a reduction in surface roughness height and to higher wear resistance and less friction.

The aim of [4] was to find the effect of the groove bottom profiles on the reduction of the friction force in lubricated sliding. Surface texturing led to a reduction in the friction force up to 55% compared to the untextured sample.

Surface texturing can be combined with coating. The authors of [5] found that the laser-textured surface combined with carbon coating (textured + coating) led to low wear and friction under lubricated conditions, in comparison to untextured, textured, and carbon-coated surfaces.

The authors of [6] studied experimentally and numerically the effects of DLC coating and surface texturing on friction reduction in the TEHL cam/tappet-contact. It was found that DLC coating led to a reduction in the solid and fluid friction force in a wide range of lubrication regimes. Texturing could reduce solid friction, increasing the fraction of fluid friction.

Epoxy–PTFE composite coatings are characterized by good functional properties such as a low friction coefficient and anticorrosion ability. However, due to small hardness

Citation: Pawlus, P.; Dzierwa, A. Tribological Behavior of Functional Surface: Models and Methods. *Coatings* **2021**, *11* , 333 . https://doi.org/10.3390/coatings11030333

Received: 9 March 2021
Accepted: 10 March 2021
Published: 15 March 2021

they have a low wear resistance. The tribological properties and corrosion resistance of epoxy–PTFE composite coating were improved by nanoparticle modification [7].

There is a risk of tribocorrosion for sliding pairs operating in a seawater environment. In order to overcome this problem, elements with high hardness can be used. It was found that the Cr/CrN PVD coating on AISI 1045 steel led to better tribocorrosion resistance than the gas nitrided with subsequent oxidation and impregnation coating [8].

Fe-based amorphous coatings obtained by supersonic plasma spraying and laser cladding exhibit excellent functional properties due to high hardness as well as high wear and corrosion resistance. The tribological and anti-corrosion behavior of these coatings on 45 steels were compared. Fe-based amorphous coating prepared by laser cladding led to better properties than plasma-sprayed coatings [9].

Manufacturers of turbomachines try to improve the engine performance. This can be achieved through the reduction of clearances between the rotor and the stator. However, due to it, a contact between these elements is possible. To reduce the severity of this contact, an abradable coating can be deposited along the stator circumference. The analysis of rotor/stator interactions considering the rotor angular speed and the initial clearances was performed in [10].

Among the coating methods, detonation spraying has a merit over other spraying methods due to lower operating temperatures and the high speed of particle flight. It was found that the properties of detonation coatings depended on the technological parameters of the spraying process. The best detonation coatings were characterized by small wear and high adhesive strength [11].

Ionic liquids can be used as new base oils or additives. Especially, cyano-based ionic liquids led to low friction. In [12], the lubricating properties of cyano-based ionic liquids against a tetrahedral amorphous carbon film were studied in reciprocating conditions. They were affected by the anion structure and ambient temperature. Low friction was achieved at 170 °C.

The guest editors of this Special Issue would like to thank the authors for their valuable high-quality work submitted, the reviewers for their efforts and time spent in order to improve the submissions, and the publisher for their excellent work and cooperation. The contact between rough surfaces was also taken into consideration.

Author Contributions: Conceptualization, P.P. and A.D.; methodology, P.P. and A.D.; formal analysis, P.P. and A.D.; writing—original draft preparation, P.P.; writing—review and editing, P.P. and A.D.; All authors have read and agreed to the published version of the manuscript.

Funding: This research received no external funding.

Institutional Review Board Statement: Not applicable.

Informed Consent Statement: Not applicable.

Data Availability Statement: The data are available from the corresponding author upon request.

Conflicts of Interest: The authors declare no conflict of interest.

References

1. Bigerelle, M.; Plouraboue, F.; Robache, F.; Jourani, A.; Fabre, A. Mechanical Integrity of 3D Rough Surfaces during Contact. *Coatings* **2020**, *10*, 15. [CrossRef]
2. Dzierwa, A.; Pawlus, P.; Zelasko, W. The Influence of Disc Surface Topography after Vapor Blasting on Wear of Sliding Pairs under Dry Sliding Conditions. *Coatings* **2020**, *10*, 102. [CrossRef]
3. Bertuccioli, C.; Garzoni, A.; Martini, C.; Morri, A.; Rondelli, G. Plasma Electrolytic Oxidation (PEO) Layers from Silicate/Phosphate Baths on Ti-6Al-4V for Biomedical Components: Influence of Deposition Conditions and Surface Finishing on Dry Sliding Behaviour. *Coatings* **2019**, *9*, 614. [CrossRef]
4. Wos, S.; Koszela, W.; Dzierwa, A.; Pawlus, P. Friction Reduction in Unidirectional Lubricated Sliding Due to Disc Surface Texturing. *Coatings* **2020**, *10*, 221. [CrossRef]
5. Zhang, Y.; Fu, H.; Wang, X.; Liang, H.; Puoza, J.C.; Ji, J.; Hua, X.; Xu, X.; Fu, Y. Additional Tribological Effect of Laser Surface Texturing and Diamond-Like Carbon Coating for Medium Carbon Steel at Near Room Temperature. *Coatings* **2020**, *10*, 929. [CrossRef]

6. Marian, M.; Weikert, T.; Tremmel, S. On Friction Reduction by Surface Modifications in the TEHL Cam/Tappet-Contact-Experimental and Numerical Studies. *Coatings* **2019**, *9*, 843. [CrossRef]
7. Ying, L.; Wu, Y.; Nie, C.; Wu, C.; Wang, G. Improvement of the Tribological Properties and Corrosion Resistance of Epoxy–PTFE Composite Coating by Nanoparticle Modification. *Coatings* **2021**, *11*, 10. [CrossRef]
8. Kowalski, M.; Stachowiak, A. Tribocorrosion Performance of Cr/CrN Hybrid Layer as a Coating for Machine Components Used in a Chloride Ions Environment. *Coatings* **2021**, *11*, 242. [CrossRef]
9. Li, G.; Gan, Y.; Liu, C.; Shi, Y.; Zhao, Y.; Kou, S. Corrosion and Wear Resistance of Fe-Based Amorphous Coatings. *Coatings* **2020**, *10*, 73. [CrossRef]
10. Nyssen, F.; Batailly, A. Sensitivity Analysis of Rotor/Stator Interactions Accounting for Wear and Thermal Effects within Low- and High-Pressure Compressor Stages. *Coatings* **2020**, *10*, 74. [CrossRef]
11. Rakhadilov, B.; Buitkenov, D.; Sagdoldina, Z.; Seitov, B.; Kurbanbekov, S.; Adilkanova, M. Structural Features and Tribological Properties of Detonation Gun Sprayed Ti–Si–C Coating. *Coatings* **2021**, *11*, 141. [CrossRef]
12. Kawada, S.; Okubo, H.; Watanabe, S.; Tadokoro, C.; Tsuboi, R.; Sasaki, S.; Miyatake, M. Lubricating Properties of Cyano-Based Ionic Liquids against Tetrahedral Amorphous Carbon Film. *Coatings* **2020**, *10*, 153. [CrossRef]

coatings

MDPI

Article

Plasma Electrolytic Oxidation (PEO) Layers from Silicate/Phosphate Baths on Ti-6Al-4V for Biomedical Components: Influence of Deposition Conditions and Surface Finishing on Dry Sliding Behaviour

Chiara Bertuccioli [1,3], Andrea Garzoni [2], Carla Martini [2,3,*], Alessandro Morri [2,3] and Gianni Rondelli [4]

[1] Imperial College, Tribology Group, SKF University Technology Centre (UTC), 456 City and Guilds Building, South Kensington Campus, London SW7 2AZ, UK; c.bertuccioli18@imperial.ac.uk
[2] Industrial Research Centre for Advanced Mechanics and Materials (CIRI-MAM), Alma Mater Studiorum—University of Bologna, Viale Risorgimento 4, 40136 Bologna, Italy; andrea.garzoni2@unibo.it (A.G.); alessandro.morri4@unibo.it (A.M.)
[3] Department of Industrial Engineering (DIN), Alma Mater Studiorum—University of Bologna, Viale Risorgimento 4, 40136 Bologna, Italy
[4] NanoSurfaces Industries srl, Via Bruno Buozzi 13, 40057 Cadriano di Granarolo nell'Emilia (BO), Italy; rondgia@yahoo.it
* Correspondence: carla.martini@unibo.it

Received: 26 August 2019; Accepted: 23 September 2019; Published: 26 September 2019

Abstract: Plasma Electrolytic Oxidation (PEO) layers were produced on Ti-6Al-4V in different conditions, so as to assess the influence of layer structure, current mode, duty cycle and surface finishing on microstructural features and tribological behaviour. In DC regime, the double-layer structure (silicate bath followed by phosphate bath) beneficially affected wear resistance. In unipolar pulsed DC (phosphate bath), the wear resistance of single layers improved with increasing duty cycle, due to improved microstructure and adhesion: high duty cycle single layers can be considered an alternative to double-layer deposition. Surface finishing by abrasive blasting with spheroidal glass beads leads to surface roughness decrease and hence to decreased friction and improved wear resistance. The best-performing PEO layers showed promising results in the comparison with reference materials such as CoCrMo (both uncoated and (Ti,Nb)N PVD-coated) and PVD-coated Ti-6Al-4V up to 30 N normal load.

Keywords: Plasma Electrolytic Oxidation (PEO); Ti-6Al-4V; friction; wear

1. Introduction

The Ti-6Al-4V alloy is widely used for orthopaedic implants due to its lower elasticity modulus, superior specific strength (strength/density), biocompatibility and enhanced corrosion resistance compared to stainless steels and Co-based alloys. In fact, Chen et al. [1] stated that, among all metallic biomaterials, Ti alloys are the only system which can bond with bone, demonstrating intimate integration with host bone tissue. Conversely, Jarcho et al. [2] observed that bioinert devices such as Co-based implants may induce foreign body responses which contribute to the loosening of permanent implants. Therefore, even though Ti-6Al-4V shows low abrasion resistance and undergoes severe adhesive wear, it provides an important alternative to Co-based alloys: Chen and Thouas [1] demonstrated that Co-based alloys are affected by other limitations due to adverse stress shielding effects as well as to toxic metal ions release. From a metal toxicity point of view, also alloying elements such as Al and V in Ti-6Al-4V may be associated to long term health problems and newly developed,

Al- and V-free alloys were proposed for the biomedical field (e.g., Ti-13Nb-13Zr) [3], however Ti-6Al-4V still covers a large number of applications, considering also non-permanent components such as intramedullary nails and screws.

In order to compensate for possible metal release and, most of all, for the unsatisfactory tribological behaviour of Ti-6Al-4V in implantable biomedical devices, Huang et al. [3] proposed several surface engineering techniques: oxidation produced by either heat treatment or electrolytic anodizing is one of the most popular but also the vapour-phase deposition of carbon-based films (DLC-type) and thermal spraying of hydroxyapatite have been widely investigated. Among oxidation techniques, Plasma Electrolytic Oxidation (PEO), sometimes also named Anodic Spark Deposition (ASD) or Micro-Arc oxidation (MAO), is attracting a significant research and development interest, due to its ability to enhance tribological substrate properties of light alloy and valve metals, forming an effective ion release barrier. Moreover, PEO allows to integrate bioactive components in the growing layer: Durdu et al. [4] demonstrated that it is possible to form hydroxyapatite, calcium apatite-based coatings and to incorporate beneficial ions, such as Ca and P, that enhance the biocompatibility and bioactivity of the surface. Studies by Li et al. [5] on the biological response of Ti implants showed that the PEO process constitutes one of the most successful methods to modify implant surface.

Specifically, Plasma Electrolytic Oxidation (PEO) is based on the modification of the growing anodic layer by spark arc micro-discharges initiated at potentials above its breakdown voltage. This allows the production of thick and adherent coatings mostly consisting of oxides, containing elements from both the metal substrate and the electrolyte solution [6]. The microstructure of PEO coatings is influenced by several factors: (i) type and concentration of electrolyte, (ii) substrate composition and microstructure, (iii) electrical parameters used during the oxidation treatment. PEO electrolytes are commonly alkaline, containing species with pH values typically up to about 13 such as aluminates, phosphates and silicates. PEO layer characteristics are also strongly influenced by polarization conditions such as DC, DC-pulsed (unipolar or bipolar) and AC sources, with control of the current, voltage or power supplied to the cell. The flexibility of electrical regimes allows discharges of intensity suitable to obtain specific microstructures and morphologies. By adjustment of the duty cycle parameters such as pulse duration, frequency and the applied current density, pulsed DC regime allows a better control over the plasma discharge. The pulsed process, reducing the more intense and hence destructive discharge regime, enables the creation of shorter and more energetic micro discharges, leading to more dense coatings. Jiang and Wang [6] found that the use of pulsed DC mode improves homogeneity and reduces the thickness of the porous outer layer (the so-called "technological layer"), resulting in a higher microhardness and a lower coefficient of friction compared to DC regime.

The aim of this work, carried out in a semi-industrial environment, was to optimize the PEO processing conditions for Ti-6Al-4V orthopaedic implants. In particular, PEO layers were produced in different conditions, so as to assess the influence of (i) layer structure (single layer, obtained in phosphate bath or double layer, obtained in silicate bath followed by phosphate bath), (ii) current mode (DC or pulsed DC), (iii) duty cycle (in case of pulsed DC deposition) and (iv) surface finishing (i.e., post-treatment by abrasive blasting) on the tribological behaviour. In fact, Shrestha and Dunn [7] reported that a reduction of PEO surface roughness, in order to remove the typical brittle and porous "technological layer" and to decrease the abrasive contribution to friction in sliding tests, is frequently carried out by conventional laboratory polishing methods. Also, Chen et al. [8] showed that polishing allowed a noticeable decrease of friction coefficient. Fei et al. [9] reported that, for PEO-treated Ti-6Al-4V (silicate-based bath), the coefficient of friction of the polished PEO layer, dry sliding versus SAE52100 steel, was about 50% lower than that of the unpolished one. Wang et al. [10] brought further evidence on the beneficial role of polishing in decreasing friction, both in dry and in solid-lubricated sliding (with graphite top layer). Therefore, in this work, we included an industrial abrasive blasting procedure in the process sequence (after PEO treatment), carried out in typical conditions for implantable metallic components and investigated how abrasive blasting affects the main microstructural features of the PEO layer, beyond the obvious surface roughness reduction. Hence this paper aims to bring further

knowledge also regarding the influence of surface finishing, which plays a very important role in biomedical applications but is seldom the subject of specific investigations.

Hence, this work reports on microstructural and tribological characterization (by dry sliding tests against 100Cr6 (AISI 52100) bearing steel with a block-on-ring contact geometry), aimed to evaluate the influence of the above described process conditions on PEO layer performance. As external references for tribological tests, the following materials were considered: (i) uncoated Co-28Cr-6Mo; (ii) (Ti,Nb)N coated Co-28Cr-6Mo; (iii) (Ti,Nb)N coated Ti-6Al-4V. These references were selected by considering current alternatives for the PEO treatments, based either on the deposition of PVD layers such as (Ti,Nb)N or on the use of a Co-based substrate (uncoated or PVD coated so as to hinder Ni leaching). Thanks to the inclusion of these reference materials in the tribological testing campaign, it was possible to rank the investigated PEO layers among other commercially available solutions: to our knowledge, these data are not available in other papers on this subject.

2. Materials and Methods

2.1. Materials

The substrate for all PEO treatments carried out in this work was the Ti-6Al-4V alloy, supplied by Titanium International Group SrL (Sala Bolognese (BO), Italy) in the form of heat treated extruded bars (solution at 950 °C for 0.5 h, water-quenching, final aging at 515 °C for 8.5 h) with a microhardness of 389 ± 58 $HK_{0.025}$ The surface roughness prior to PEO treatment was 0.20 ± 0.05 μm. The composition of the bars (indicated in the supplier's certificate) was—Al: 5.50–6.75; V: 3.5–4.5; Fe: 0–0.3; H: 0–0.15; N: 0–0.05; O: 0–0.20; C: 0–0.08 (wt.%); Ti to balance.

2.2. PEO Treatment

The main treatment parameters used for the production of the investigated PEO layers are summarised in Table 1.

Table 1. Treatment conditions for the production of PEO layers.

	Layer(s)	Current Mode	Current Density (mA cm^{-2})	Deposition Time (s)	Duty Cycle (%)	Post-Treatment
P	phosphate	DC	30	600	-	abrasive blasting
S	silicate	DC	70	600	-	abrasive blasting
PP	phosphate	Pulsed DC	30	600	60	abrasive blasting
PM	phosphate	Pulsed DC	30	600	72	abrasive blasting
PN	phosphate	Pulsed DC	30	600	80	abrasive blasting
D5	internal: silicate	DC	70	300	-	abrasive blasting
	external: phosphate		70	300	-	
DA	internal: silicate	Pulsed DC	30	600	25	abrasive blasting
	external: phosphate		30	600	68	
DB	internal: silicate	Pulsed DC	30	600	25	none
	external: phosphate		30	600	68	

All the PEO treatments were carried out in galvanostatic regime inside a water-cooled cell (where electrolytes were kept at 5 °C), with Ti-6Al-4V samples as the anode and a grade 1 Ti mesh as the cathode. Both phosphate-based and silicate-based aqueous solutions were used as electrolytic

baths. The silicate-based solution (SiO_2-related compounds 0.015–0.035 mol L^{-1}, pH 11.8) displayed a conductivity of 8.8 mS cm^{-1} at room temperature, whilst the phosphate-based solution (Na_3PO_4 0.05–0.20 mol L^{-1}, pH 12.1) displayed a conductivity of 6.4 mS cm^{-1} at room temperature. For both solutions, KOH was used for achieving the reported pH values.

Three main sets of PEO layers were produced: (i) single layers, DC mode (samples P and S, obtained in phosphate and silicate baths respectively, for preliminary assessment of the influence of abrasive blasting as well as of tribological behaviour); (ii) single layers, unipolar pulsed DC mode, phosphate bath (samples PP, PM, PN, for the evaluation of the influence of duty cycle on coating properties); (iii) double layers (obtained by firstly depositing the internal layer in a silicate bath, then depositing the external layer in a phosphate bath, samples D5, DA and DB).

The layer sequence in double layers was defined on the basis of preliminary tribological testing on PEO single layers obtained in DC mode (samples P and S). A comparison of tribological results from samples P and S (loads to failure in dry sliding, Table 2) indicated that PEO single layers from silicate baths behaved slightly better than those from phosphate baths (in agreement with data summarised by Jiang and Wang [6]).

Table 2. Main features of the investigated PEO layers.

Title	Layer (s)	Phase Composition, XRD			Surface Roughness Ra (μm)	Thickness (μm)	Hardness ($HK_{0.025}$)	Lc3 (N)	Load to Failure in Dry Sliding (N)
		Anatase (TiO_2)	Rutile (TiO_2)	Aluminium Phosphate ($AlPO_4$)					
P	single	++	+	-	0.28 ± 0.06	12.8 ± 1.6	380 ± 26	12 ± 3	20
S	single	++	+	-	0.55 ± 0.04	15.2 ± 0.4	410 ± 35	14 ± 2	30
PP	single	++	-	+	0.34 ± 0.06	7.2 ± 0.8	400 ± 169	10 ± 6	30
PM	single	++	-	+	0.48 ± 0.02	6.5 ± 0.9	356 ± 170	15 ± 1	10
PN	single	++	+	+	0.48 ± 0.10	5.1 ± 1.1	390 ± 135	25 ± 1	40
D5	double	++	+	++	0.68 ± 0.04	6.7 ± 1.0	467 ± 71	16 ± 2	40
DA	double	++	+	+	0.65 ± 0.02	5.4 ± 1.9	352 ± 126	21 ± 5	40
DB	double	+	-	+	0.98 ± 0.06	10.9 ± 7.2	290 ± 108	13 ± 1	10

-: not detectable; +: detected; ++: main phase.

Hence, silicate baths were deemed more appropriate for producing the internal layer in double-layered structures. Moreover, the higher surface roughness imparted by the silicate bath (before abrasive blasting, Ra was 3.2 μm for S versus 0.62 μm for P, as shown in Figure 1) was considered advantageous for mechanical interlocking (and hence higher adhesion) of the external layer.

Conversely, samples PP, PM and PN (Table 1) have a single layer structure (obtained by treatment in the same phosphate bath as for P and for the previously mentioned double layers) but for these single layers the PEO treatment was always carried in pulsed DC mode. Phosphate baths were used for single layers due to their ability to produce compact and smooth layers (particularly appreciated for biomedical applications), as well as for their intrinsically higher corrosion resistance and bioactivity, as reported by Jiang and Wang [6]. In the case of single layers from phosphate baths in pulsed DC, the investigations aimed at improving their slightly less advantageous wear resistance by optimising the treatment conditions (namely the duty cycle conditions for the pulsed DC bi-polar square waveform, Table 1).

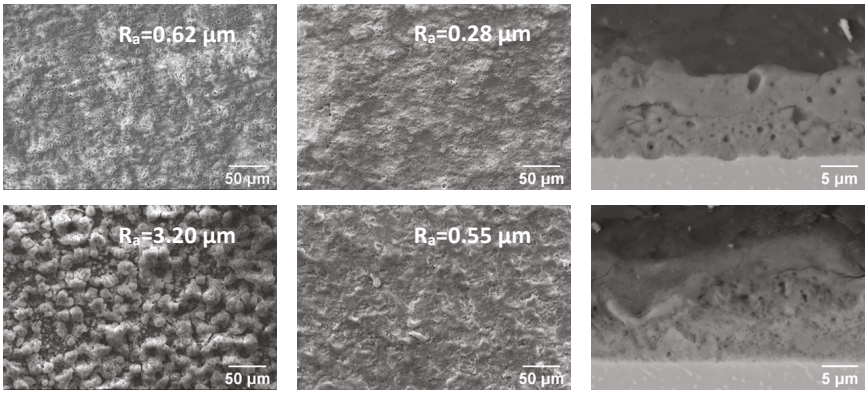

Figure 1. Free surface morphology of PEO single layers obtained in phosphate (P) or silicate (S) bath (DC mode), before (left) and after (centre) abrasive blasting (SE images). Cross-sections of the same layers after abrasive blasting (right, BSE images).

The abrasive blasting post-treatment mentioned in Table 1 was carried out by using spheroidal glass beads (100 ± 10 µm average diameter, average elemental composition measured by EDS, wt.%: Si 30, O 52, Na 9, Ca 6, Mg 2, Al 1) as abrasive medium in an industrial blasting device used for implantable metallic components. In fact, a low surface roughness is required in tribological contacts, so as to limit the production of hard wear debris which also adversely affect the biological response [3]. Therefore, all the PEO-treated specimens were abrasive-blasted, with the exception of sample B, used only as a reference: by comparing it to sample A, obtained in the same treatment conditions, it is possible to assess the influence of the abrasive blasting process on microstructure and tribological behaviour of PEO layers.

2.3. Microstructural and Micro-Mechanical Characterization

Surface and cross-sectional analyses of the microstructure of the PEO-treated specimens were performed by means of a scanning electron microscope (SEM, Zeiss EVO 50, Oberkochen, Germany) in low vacuum mode.

X-ray diffraction (XRD, Panalitycal, Eindhoven, Netherlands was used for assessing the phase composition of PEO layers. Analyses were carried out by performing θ–2θ scans from 20° to 90° with a 0.05 step size and a 5 s dwell time, by a Philips PW1729 X-ray diffractometer with a Cu-Kα radiation source (λ = 0.15406 nm, Ni-filter), at 40 kV and 30 mA. XRD patterns were collected from the free surface of PEO layers.

A Renishaw InVia micro-spectrometer (Renishaw plc, New Mils, UK), coupled with a Leica DMLM microscope, using the 50 mW Ar^+ laser (wavelength: 514.5 nm) as excitation source, was used to acquire Raman spectra. The analyses were performed by focusing the laser on spots of about 2 µm diameter and, in order to avoid sample degradation, different filters were used to reduce laser power.

Glow Discharge-Optical Emission Spectroscopy (GD-OES, Spectruma Analitik GDA 650, Hof, Germany) concentration versus depth profiles were carried out on PEO-treated specimens. Before each analysis surface contamination was removed by ethanol rinsing. The profiles were obtained with a Grimm-style glow discharge lamp in RF mode. The analysed area in each measurement was about 5 mm^2, corresponding to the internal area of the tubular anode (2.5 mm diameter). A rotary pump was used to evacuate the Grimm-type atomisation/excitation source down to a pressure of 0.05 hPa.

Argon was used as working gas (99.995% purity) and after evacuation it was injected to a constant pressure of 3 hPa.

Surface roughness measurements were carried out on coating free surfaces by stylus profilometry (Hommelwerke T2000, stylus tip: 5 μm curvature radius, Villingen- Schwenningen, Germany). Microhardness was evaluated on the free surface of PEO-treated samples by means of Knoop ($HK_{0.025}$) indentation testing.

The practical adhesion of the anodic oxides was assessed by means of scratch tests, according to the International Standard ISO 20502 [11], using a Revetest XPress device (Anton Paar GmbH, Graz, Austria) with a Rockwell diamond indenter (200 μm spherical tip radius). Scratch tests were carried out by applying a linearly increasing load (from 1 to 30 N), with a 10 mm scratch length and a 10 mm/min speed rate.

2.4. Dry Sliding Tests

A flat-on-cylinder tribometer (block-on-ring contact geometry, ASTM Standard G77 [12], described in further detail elsewhere by Ceschini et al. [13], was used to carry out dry sliding test on both untreated Ti-6Al-4V and PEO-treated samples. Stationary blocks consisted of the PEO treated specimens (as well as of the untreated alloy and of the reference materials for comparison described in Section 2.5), whilst the counter material was a 100Cr6 (AISI 52100) bearing steel cylinder (60 HRC, Ra = 0.2 μm). Sliding tests were performed at room temperature (between 20 and 23 °C) with a relative humidity ranging from 50% to 60%. The sliding speed was fixed at 0.3 m s^{-1}, while the sliding distance was set at 1000 m. The normal load was maintained constant in each test, ranging from 5 to 40 N. This led to initial maximum Hertzian contact pressures from 40 to 100 MPa on PEO layers (considering anatase as prevalent phase for the treated specimens, as indicated by phase identification results obtained in this work and deriving anatase mechanical properties from literature values of Borgese et al. [14] and Soares et al. [15]. A bending load cell was employed for continuously recording friction force as a function of sliding distance. The coefficient of friction (COF) was evaluated for each test by averaging steady-state data. The COF value for each condition and each sample was then calculated by averaging the COF of at least 3 test repetitions. The same stylus profilometer described in Section 2.3 was used to evaluate both wear scar depths and widths on both flat blocks and rotating cylinders. Wear depth values were determined by averaging at least 3 profiles on each wear scar and then averaging again the mean values over the repetitions. The dominant wear mechanisms were identified by carrying out analyses of the worn surfaces and wear debris by means of a Hirox KH 7700 3D-digital microscope (Hirox Co Ltd., Tokyo, Japan) as well as by SEM-EDS (SEM, Zeiss EVO 50, Oberkochen, Germany).

2.5. References for the Comparison of Tribological Behaviour

The tribological behaviour of PEO-treated Ti-6Al-4V was compared with the following references: (i) uncoated Co-28Cr-6Mo; (ii) (Ti,Nb)N coated Co-28Cr-6Mo; (iii) (Ti,Nb)N coated Ti-6Al-4V.

The PVD (Ti,Nb)N coating was considered as reference for comparison because Galetz et al. [16] and Malchesky [17] showed that it produced a low friction coefficient against polyethylene. Moreover, Paschoal et al. [18] proved that (Ti,Nb)N is an effective barrier against ion release from the substrate. The PVD (Ti,Nb)N coating was deposited on both substrates by an industrial Arc Evaporation process. The main features of the PVD coating were—thickness 5.0 μm, hardness 2300 $HV_{0.01}$, surface roughness 0.26 ± 0.05 μm.

The Co-28Cr-6Mo alloy (ASTM F1537 [19], Low-Carbon type) was in the wrought, un-annealed state (42 HRC, grain size 10 according to ASTM E112 [20], surface roughness 0.20 ± 0.11 μm).

3. Results and Discussion

3.1. Phase Composition (General Remarks)

The main features of the PEO layers are summarized in Table 2. In several layers, the main phases detected by XRD (which analyses the coating full-thickness composition, as demonstrated by the presence of peaks from the substrate) are the two crystalline forms of TiO_2: anatase and rutile (Table 2). Representative XRD spectra, recorded on single layers from silicate- or phosphate-rich baths (samples S and P, respectively) are reported in Figure 2.

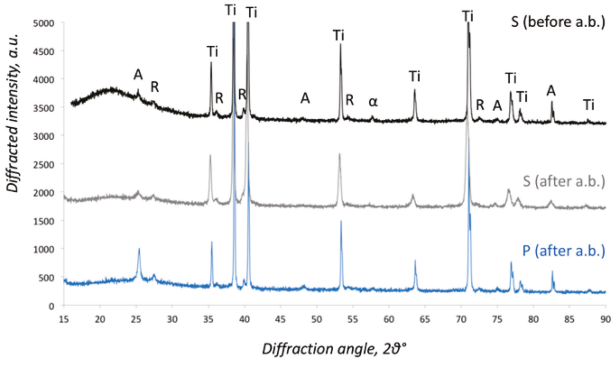

Figure 2. Indexed XRD patterns (Cu Kα radiation) characteristic of the through-thickness composition of PEO single layers obtained in DC mode from silicate- or phosphate-based baths (a.b.: abrasive blasting). Ti: Ti-6Al-4V; A: anatase (TiO_2); R: rutile; α: α-Al_2O_3

XRD patterns for sample S in Figure 2 also show the influence of abrasive blasting on phase composition but this point will be discussed subsequently (Section 3.2).

Anatase was the dominating phase in XRD patterns of all samples (Table 2) and it was the only phase detected by micro-Raman (Figure 3), using spectra reported in Bouchard and Smith [21] as references for Raman peaks indexing. Further reference spectra were found in Friedemann et al. [22].

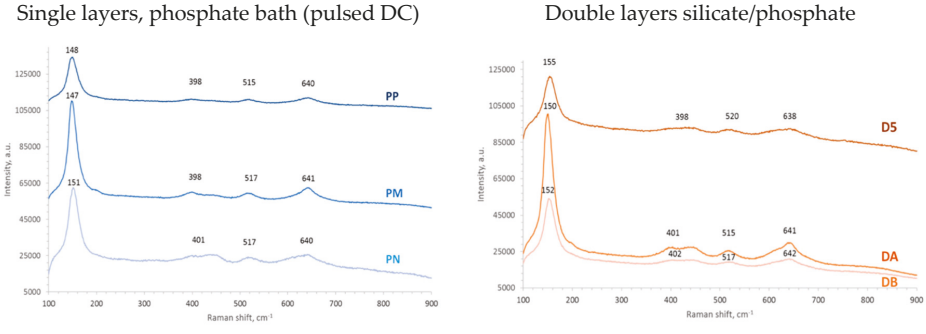

Figure 3. Raman spectra (λ = 514.5 nm) on free surfaces of PEO single (**a**) and double layers (**b**). All indexed peaks are assigned to anatase.

The inability of Raman (characterized by a shallower penetration through the PEO layer than XRD) to detect rutile may be due to the higher concentration of the anatase in the outermost portion of

the PEO layers. In fact, prevalence of the metastable oxide in the outer portion of PEO layer, where a high cooling rate and hence rapid quenching is likely to predominate on annealing effects, has been observed also in the case of aluminium alloys by Xue et al. [23].

The prevalence of anatase over rutile both in single layers (P, PN) and in double layers (DA) obtained in pulsed DC is most likely due to the use of phosphate-based baths (either for the single layer or for the external layer in double-layered architectures). In fact Khan [24] showed that phosphate baths in DC mode are known to produce anatase-rich PEO layers, where phosphorus, incorporated during the growth, tends to limit the anatase to rutile transformation (which is the final transformation in the sequence from amorphous titania to metastable anatase (T > 550 °C) and then to thermodynamically stable rutile (T > 850 °C) under the action of micro-arc discharges.

By comparing samples DA and DB (treated in the same conditions and differing only in the abrasive blasting post-treatment carried out on DA, Table 1), it is possible to notice that a minor contribution of rutile was detectable by XRD only in the abrasive-blasted sample DA, probably due to the smoother surface that improves the signal-to-noise ratio.

In all the layers produced by phosphate-based electrolyte (with the exception of the DC mode single layer P), also some orthorhombic aluminium phosphate ($AlPO_4$) was detected (Table 2), as observed by Martini et al. [25] in a previous work on PEO treatment of Ti-6Al-4V. According to Wang et al. [26], crystalline $AlPO_4$ is supposed to form as a consequence of high-temperature thermolysis of hydrated aluminium polyphosphates inside discharge channels. In single layers S and P (DC mode), also traces of α-Al_2O_3 were detected by XRD (Figure 2), as previously observed by Yerokhin [27] for PEO treatment of Ti-6Al-4V. In this work, silicate-based electrolyte in DC (sample S) did not produce a rutile-dominated layer, as the one observed by Yerokhin as well as by Wang [27,28] in AC-treated Ti-6Al-4V (phosphate-based bath). In our case, the prevalence of anatase may be due to less intensive arcing and lower temperatures inside discharge channels.

As regards the influence of the incorporation of P-based compounds in the PEO layers on biological response (which has not been investigated yet for these layers), literature data indicate that P-containing PEO coatings on Ti-6Al-4V induce a homogeneous distribution of growing MG-63s cells as well as a higher collagen deposition per cell than plasma-sprayed hydroxyapatite [29]. Also, the incorporation of Si (as amorphous silicate) is not expected to have a negative impact on biological response (SiO_2-based bioactive materials are known for their excellent bioactivity [30]). However, the actual biological response to these PEO layer will require specific investigations in a further step of the work.

The influence of treatment conditions and surface finishing on microstructure, phase composition and micro-mechanical properties will be discussed in the following Sections 3.2–3.4). Subsequently, the tribological behaviour of all the PEO layers will be discussed and compared to selected reference materials in the final Section 3.5.

3.2. Influence of Abrasive Blasting

The influence of abrasive blasting on surface morphology and roughness is shown in Figure 1 for PEO single layers obtained in DC mode (P and S in Table 1).

The comparison of images and Ra values in Figure 1, before and after abrasive blasting, shows that this mechanical surface finishing treatment effectively removes the brittle and porous external layer of the anodic oxides, most notably in the case of samples from silicate-based baths (S). For the S samples, the free surface displays a rough appearance, with nodular features (ranging from about 5 to 20 μm) and large pores between the nodules, typical of PEO layers grown in silicate-rich electrolyte as shown by Aliasghari et al. [31]. In the case of samples treated in the phosphate-based solution (P), which already showed a rather smooth surface morphology in the as-treated condition, the decrease of surface roughness as well as the morphological modification is less remarkable. In fact, also after abrasive blasting, typical PEO defects due to stochastic discharge events and gas evolution, such as cavities and volcano-like features, are still visible in P samples.

For samples obtained in silicate baths (S), the influence of abrasive blasting on phase composition is shown in Figure 2, where XRD patterns recorded before and after mechanical surface finishing are compared. In this case, the most evident effect of abrasive blasting is the removal of the amorphous contribution (wide band at low diffraction angle), likely due to amorphous silica as suggested by Wang et al. [28]. Also, Yerokhin et al. [27] detected amorphous silica in PEO layers produced on Ti-6Al-4V in silicate-based baths. In fact, also large-area EDS analysis (Table 3) displays a remarkable decrease in Si concentration after blasting (from about 28 to 15 wt.%).

Table 3. Surface composition of the PEO layers (EDS, wt.%; average data, recorded on several areas imaged at 500× on each sample) before and after abrasive blasting (a.b.).

Title	Title	O	Ti	Al	V	Na	K	Si	P
P	Before a.b.	48.3 ± 0.9	40.1 ± 0.1	2.4 ± 0.1	0.8 ± 0.2	0.4 ± 0.1	-	0.2 ± 0.1	7.8 ± 0.1
	After a.b.	47.8 ± 0.8	39.5 ± 0.5	2.5 ± 0.1	1.3 ± 0.1	0.5 ± 0.1	-	0.4 ± 0.1	8.0 ± 0.1
S	Before a.b.	58.3 ± 0.4	8.4 ± 0.3	0.3 ± 0.1	0.4 ± 0.1	0.7 ± 0.1	0.6 ± 0.1	27.9 ± 0.7	3.4 ± 0.1
	After a.b.	56.6 ± 0.6	22.9 ± 0.4	1.4 ± 0.1	0.9 ± 0.1	0.5 ± 0.1	0.3 ± 0.1	15.0 ± 0.1	2.4 ± 0.1

The influence of abrasive blasting on surface composition was also evaluated for single layers deposited from phosphate baths in pulsed DC mode (PP, PM, PN, Table 1), in order to check for accumulation of Si from the blasting medium also in this set of samples. Results of large-area EDS analysis on the free surface demonstrated that sample PP (obtained at lowest duty cycle, that is, at lowest pulse-on times) shows a significantly higher Si concentration (visible also in cross-section X-ray maps discussed in Figure 4) than the others.

The shorter pulse-on times for the treatment of sample PP may be responsible for a lower density of the layer, as shown by cross-sections in Figure 4, hence for the increased tendency to abrasive incorporation by comparison to other PEO layers obtained in pulsed DC. In this current regime, also Dehnavi et al. [32] observed that layer density and microstructure improved with increasing pulse-on time. This Si enrichment is likely to be responsible for the relatively high microhardness of sample PP (Table 2), thus beneficially influencing its tribological behaviour.

These results show that, also for the S single layers discussed above (Table 3), surface contamination due to Si from the blasting medium cannot be ruled out, because it can be masked by the decrease of Si% as a consequence of the removal of the outermost amorphous silica layer. Therefore, in the case of silicate-phosphate double layers (DA and DB, Table 1), the possible surface enrichment of Si due to abrasive blasting was assessed by measuring GD-OES depth profiles (Figure 5), in order to take into appropriate consideration also the layered structure of the coatings.

Glow Discharge-Optical Emission Spectroscopy (GD-OES) depth profiles in Figure 5 show the trend of Ti, Si and P signal intensity as a function of depth for the same double layer coating, both before (as-treated) and after abrasive-blasting. Oxygen was not included in this graph because its profile typically has a lower S/N ratio than the others and it would affect readability without yielding further useful information. Also, Al and V, which showed similar trends as Ti but with proportionally lower intensity due to their lower alloy concentration, were not added in the graph so as to preserve its readability. Based on the comparison of Si profiles, abrasive blasting decreases the total layer thickness of about 10 μm (from 15 to 5 μm). Such an estimate is probably more accurate than the one obtainable by polished cross-sections (Table 2), because GD-OES data are averaged over a relatively large analysed area whilst the intrinsic brittleness of as-treated PEO layers makes them prone to damage during metallographic preparation.

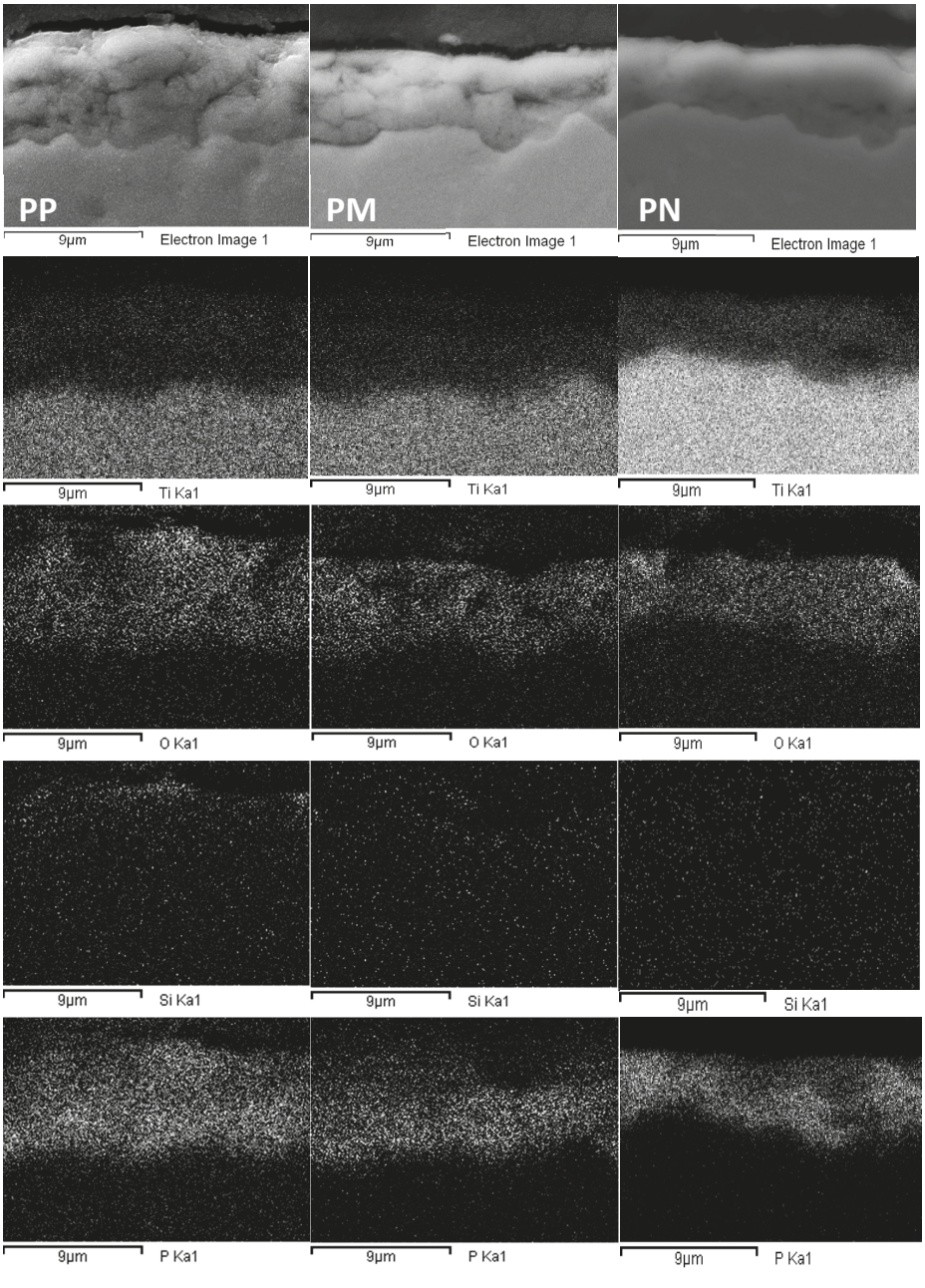

Figure 4. Polished cross sections and EDS X-ray maps of single layer PEO coatings obtained in pulsed DC (phosphate bath): PP (left column), PM (centre column) and PN (right column). The duty cycle increases on going from left to right (Table 1). The X-ray maps were recorded for each coating in the same area of the electron image in the top row.

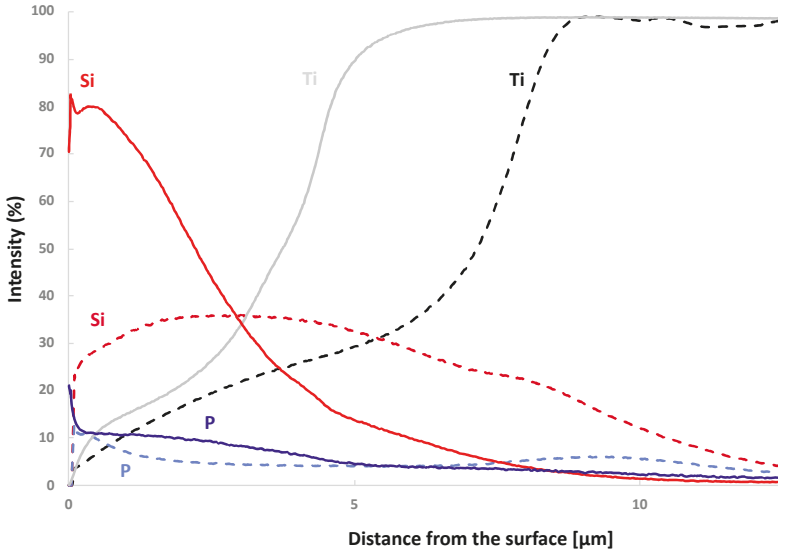

Figure 5. GD-OES depth profiles of Si, Ti and P measured from the free surface of PEO double layers DA (abrasive-blasted, solid lines) and DB (as-treated, dashed lines) obtained by treatment in silicate bath followed by phosphate bath.

In the as-treated double layer (DB), P can be detected through the whole thickness of the PEO layer and its signal shows a slight intensity increase at around 10 µm from the surface. In the abrasive-blasted layer (DA), thinned and compacted by the finishing procedure, the P signal is more intense than in the previous case and rather constant throughout the layer thickness, indicating in both cases that the electrolyte was able to penetrate the inner regions of the coating, probably through breakdown channels, as observed also by Galvis et al. [33] for single layers obtained in DC mode from phosphate baths. Even though the immersion in the phosphate solution was the second step of the treatment, after the first step in silicate bath, it induced P enrichment of the whole layer (as shown also by EDS X-ray maps in Figure 4). GD-OES depth profiles also show a remarkable increase of Si in the outermost portion of the abrasive-blasted layer (DA), by comparison to the same coating in the as-treated condition (DB). The different trend and the higher concentration of Si in the abrasive-blasted layer (DA) is most likely due to embedding of silicate glass fragments during abrasive blasting.

3.3. Influence of Current Mode (DC Versus Pulsed DC)

In the case of phosphate-based single layers, the influence of current mode can be estimated by comparing sample P (DC mode) with PP, PM, PN (pulsed DC). Cross-section images in Figure 1 (sample P) and 4 (PP, PM, PN), as well as average thickness values in Table 2, show that the use of pulsed DC current induces a slight densification of the PEO layer, accompanied by a thickness decrease. This is probably due to the beneficial influence of pulse-off time which, in the pulsed DC mode, contribute to interrupt spark discharges, decreasing the growth rate but also limiting disruptive discharge events. In terms of phase composition, the use of pulsed DC slightly reduced the tendency towards the formation of stable rutile (Table 2), probably due to the attainment of lower temperatures than in DC mode. In terms of micromechanical properties (Table 2), there is no remarkable difference between microhardness and critical loads for full delamination (Lc3) among samples obtained in DC or pulsed DC mode. However, the PN layer, obtained in pulsed DC at the highest duty cycle

(Table 1), makes an exception, with its highest Lc3 value due to improved microstructure (discussed in Section 3.4).

In the case of double layers, the influence of current mode on microstructure can be assessed by comparing sample D5 (DC mode) with DA (pulsed DC). The cross-section images in Figure 6 show that both samples do not display significant porosity.

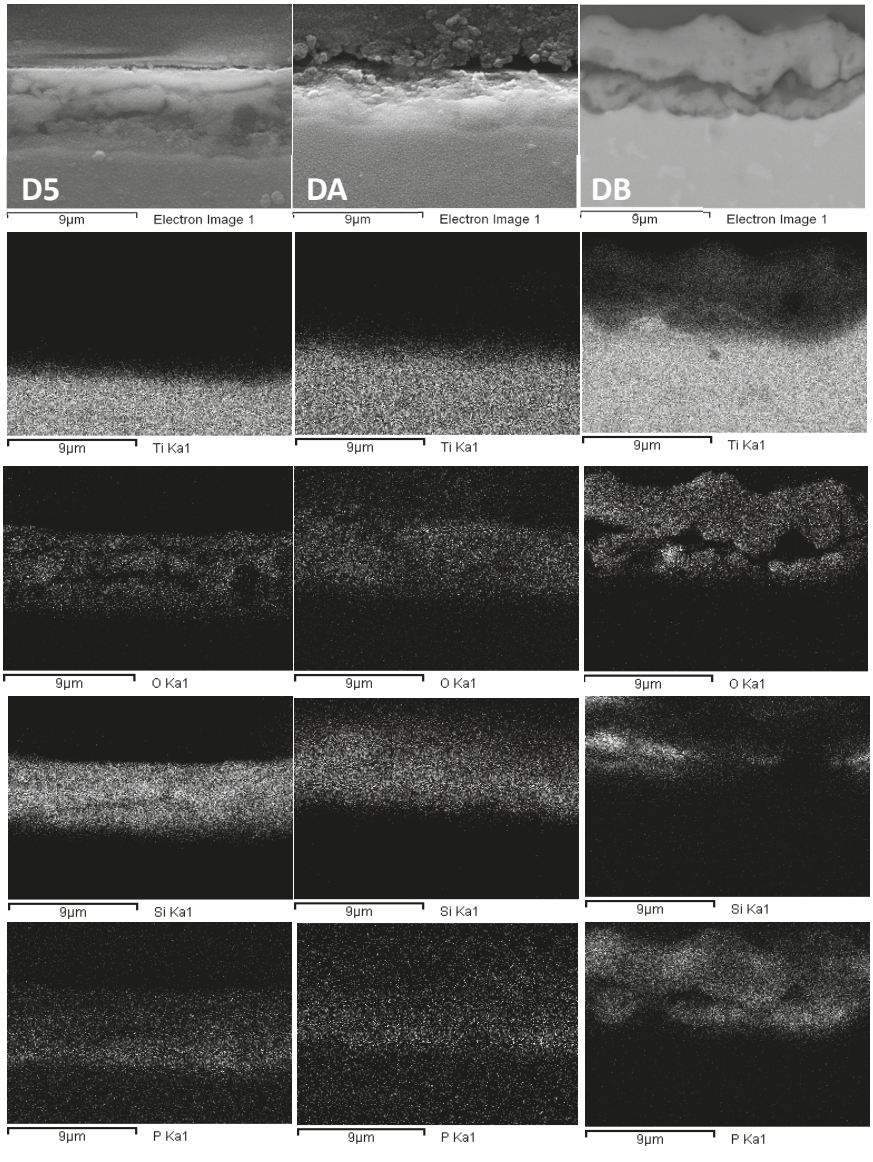

Figure 6. Polished cross sections and EDS X-ray maps of double layer PEO coatings (silicate bath followed by phosphate bath): D5 (top column), DA (centre column) and DB (right column). More information on deposition conditions of double layers can be found in Table 1. The X-ray maps were recorded for each coating in the same area of the electron image in the top row.

Double-layered sample DA is slightly thinner and less compact that D5, mostly in the outer zone. The only difference in terms of phase composition between these samples was a higher amount of crystalline $AlPO_4$ in the layer obtained in DC mode (D5), where high-temperature thermolysis of hydrated aluminium polyphosphates inside discharge channels was probably more likely than in pulsed DC (where pulse-off time may allow cooling during coating growth in a more effective way). In pulsed DC mode (sample DA), a lower current density was employed (Table 1), further contributing to the achievement of lower temperatures during discharge events. The use of pulsed DC lead to lower thickness and microhardness in sample DA but it induced a higher practical adhesion (Lc3) by comparison to D5 (Table 2).

3.4. Influence of Duty Cycle (Pulsed DC)

For phosphate-based single layers in pulsed DC (PP, PM and PN, Table 1), thickness decreased whilst compactness increased with increasing duty cycle (Figure 4), due to the beneficial microstructural effect of increasing pulse-on time, as previously discussed in Section 3.2. Accordingly, in terms of phase composition, rutile was detected only at the highest duty cycle values, in sample PN (Table 2). Correspondingly, a relatively high microhardness was detected in the same sample. The highest microhardness recorded for phosphate-based single layers was recorded in sample PP, obtained at the lowest duty cycle value: however, in this case the measured value in probably affected by the abrasive residues embedded in the surface layer, as previously discussed in Section 3.2.

In general, the low hardness of these PEO layers, which are only slightly higher than the substrate, may be due to the predominance of soft anatase (Table 2), as well as to residual non-oxidised titanium, as suggested also by Yerokhin et al. [27]. Also, Diamanti et al. [34] obtained a similar result, that is, thin anatase-based PEO layers on Ti-6Al-4V, produced in calcium glycerophosphate bath, displayed a hardness lower than the untreated substrate.

The microstructural modifications induced by the increase of duty cycle also showed a beneficial influence on practical adhesion (Lc3, Table 2), which can be ascribed to the denser microstructure [35,36].

3.5. Dry Sliding Tests

Average values of coefficient of friction (COF) as well as of maximum wear depth are plotted as a function of normal load in Figure 7.

Each PEO layer is characterised by a critical normal load (Table 2) at which failure of the coating occurs during the test, hence the load range for COF values in Figure 7a is wider for the best-performing coatings than for the worst ones.

Figure 8 shows the typical graph recorded during the tests which induced coating failure: when the substrate starts to be involved in the contact (after about 100 m in this case), COF decreases whilst system wear (i.e., material removal from both the block and the ring) increases with increasing sliding distance. The friction transition after coating failure lead to COF values comparable to that of the untreated substrate.

The observation of wear scar morphology after the above described friction and wear transitions (Figure 9) shows that, after coating failure, the underlying substrate is deeply ploughed (Figure 9b) due to abrasion.

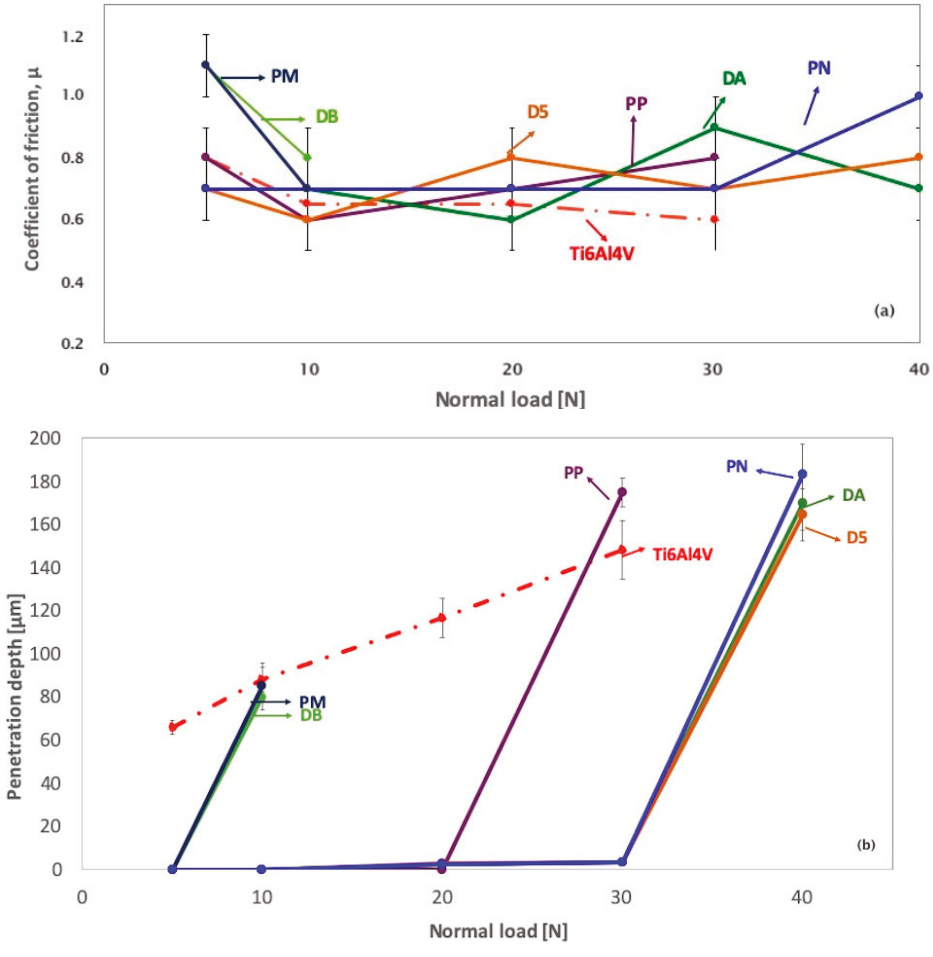

Figure 7. Average values of coefficient of friction (**a**) and maximum wear depth on blocks (**b**) as a function of normal load. In (**a**), the trend line for PM overlaps the one for DA between 5 and 10 N.

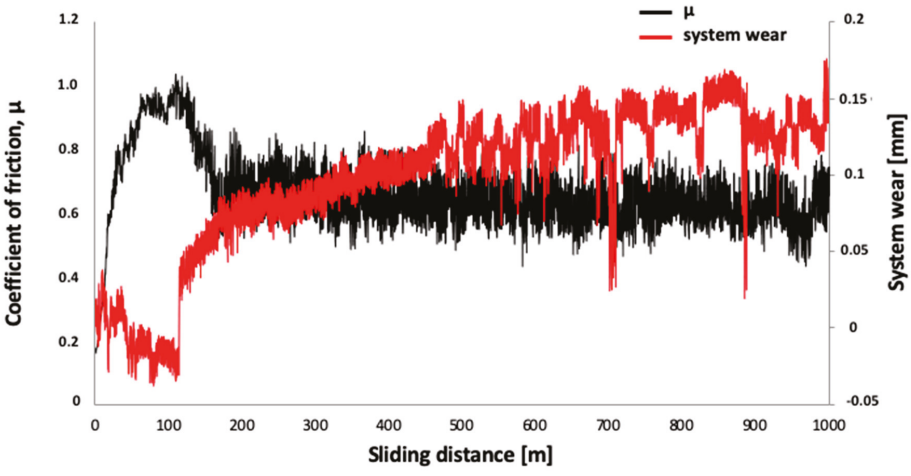

Figure 8. Friction and wear transitions for PEO layers at the critical load for coating failure: coefficient of friction (black line) and system wear (red line) as a function of sliding distance (sample DA, under a normal load of 40 N).

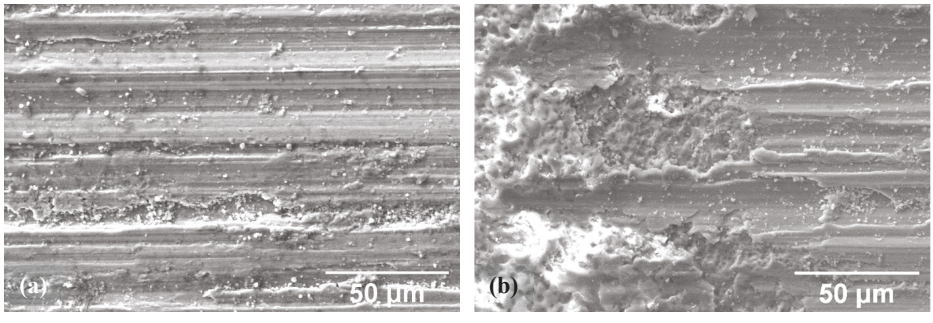

Figure 9. SEM images of wear scars on (**a**) untreated and (**b**) PEO-treated Ti-6Al-4V after the friction and wear transition that corresponds to the involvement of the substrate in the contact (i.e., coating failure).

Adhesion damage is also noticeable between the grooves, showing the same typical morphologies observed also for the untreated substrate (Figure 9a). The occurrence of these friction/wear transitions and the morphology of worn surfaces is completely comparable to the case of other PEO-treated Ti-6Al-4V samples tested in dry sliding conditions against bearing steel, discussed in a previous work by Martini et al. [25].

For this specific set of samples, the highest COF values were recorded for the as-treated (not abrasive-blasted) double layer DB (Figure 7) at 5 N. The COF of all abrasive-blasted PEO layers (with the exception of PM, discussed here below) is lower than for DB, demonstrating that the surface finishing procedure improved the frictional behaviour. Fei et al. [9] reported similar results on this phenomenon, which is due to the decrease of the abrasive component of friction, brought about by the decrease of surface roughness induced by abrasive blasting. Also, the single layer PM coating, with high roughness (Table 2) and low compactness (Figure 4), showed high COF values at 5 N. Similar to DB, also this coating failed already at 10 N, due to its detrimental combination of high roughness,

low compactness and low hardness (the latter two parameters being related, since pores and cracks negatively affect the hardness of PEO layers as shown by Curran and Clyne [37]).

For PEO layers that survived in a wider load range (namely D5 and PN), COF slightly increases on going from 30 to 40 N, due to destabilization of the iron oxide transfer layer that covers all the treated surfaces as a consequence of mild tribo-oxidation of the steel counterface. The presence of these iron oxide transfer layers, which is typically observed in the PEO-steel contact [25], is documented by the images of wear scars taken at 5 N in Figures 10 and 11 (the latter also reporting EDS and micro-Raman data).

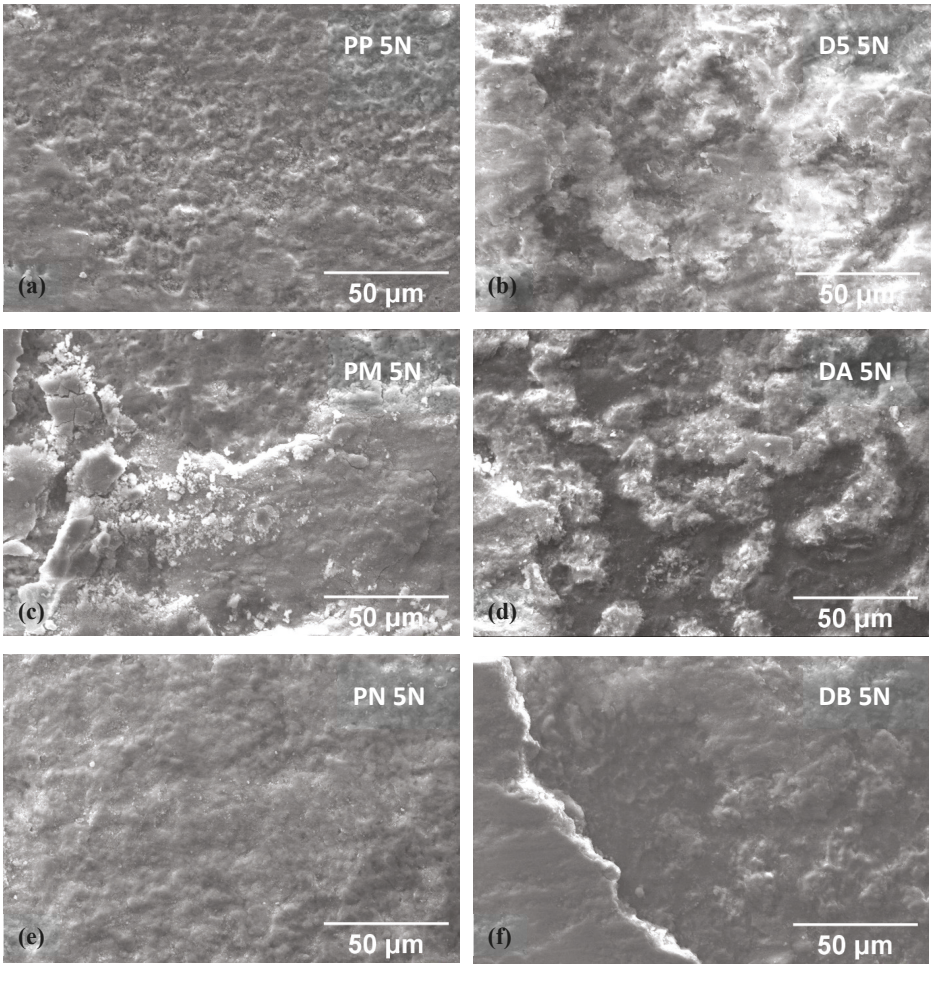

Figure 10. SEM images of wear scars at 5 N on single layers (PP: **a**, PM: **c**, PN: **e**) and double layers (D5: **b**, DA: **d**, DB: **f**) showing the presence of iron oxide based transfer layers with variable degrees of coverage and stability. Under 5 N, layers PM and DB are already at the load before coating failure and the transfer layer starts to detach.

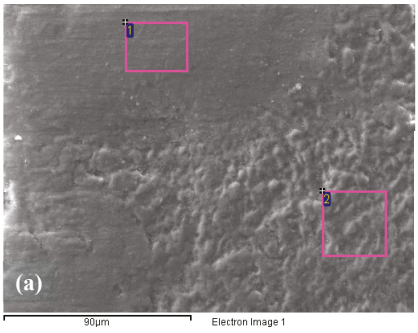

	C	O	Na	Al	Si	P	Ca	Ti	V	Fe
1	5.1	38.0						1.4		55.4
2	4.6	50.4	0.4	0.9	1.0	5.4	0.4	20.1	0.6	16.2

(b)

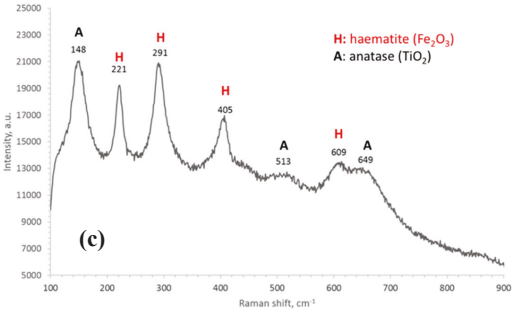

Figure 11. (**a**) representative SEM image of transfer layers on the surface of wear scars (single layer PN, 5 N) with (**b**) EDS data (wt.%) and (**c**) micro-Raman spectrum taken in area 1 of (**a**), showing that the thicker areas of the transfer layer mostly consist of haematite (Fe_2O_3).

These transfer layers, when formed during dry sliding against AISI 52100 at room temperature and at relatively low sliding speed (0.3 m s^{-1}), consist of haematite (Fe_2O_3) according to micro-Raman analyses (Figure 11c). Tonelli et al. [38] observed the same type of haematite-based transfer layers also for other PEO coatings in similar contact conditions.

The destabilization of the transfer layers starts to be appreciable at the load before friction and wear transition (e.g., in Figure 10c,f for layers PM and DB respectively, already being at the load before failure at 5 N and in Figure 12 for the other layers). Also, the detachment of micro-fragments from the PEO layer, which mostly occurs before complete coating failure, may contribute to increase the abrasive component of friction at high load.

As for COF, also the trend of maximum wear depth (measured on PEO-treated and untreated stationary blocks at the end of the tests) versus normal load (Figure 7b) shows the above described transitions, related to coating failure. After coating failure, in fact, wear depth of PEO-treated blocks noticeably increases with increasing normal load, achieving values comparable to the untreated substrate. However, before coating failure, all the PEO layers investigated in the present work performed better than the bare Ti-6Al-4V substrate, in terms of wear resistance.

As previously discussed for COF, the abrasive blasting process has a beneficial influence also on wear depth. By comparing the curves of samples DA and DB in Figure 7b, it is possible to notice that the removal of the porous and brittle external layer increased the critical load to failure from 10 N (DB) to 40 N (DA), probably due to a decreased tendency towards micro-crack driven damage accumulation, in the case of the smoother coating (DA).

It is worth noting that the PEO treatment in phosphate-based bath after the production of the inner layer in silicate bath (i.e., comparing S (single layer) to D5 (double layer)) was beneficial, leading to an increased critical load to failure (from 30 to 40 N). This effect can be probably ascribed to the higher compactness of D5 and hence to its increased hardness.

The critical load to failure for single layers obtained in phosphate bath increased in the following order: PM < P < PP < PN. This indicates that most layers obtained in pulsed DC perform better than the one obtained in DC (sample P) and the best tribological behaviour can be achieved for pulsed DC treatment at highest duty cycle (PN), due to combination of dense microstructure, relatively high hardness and high adhesion. In the case of PP, the unexpected good wear resistance (despite its low

adhesion and non-dense microstructure) may be due to the Si-rich top layer, formed as consequence of glass embedding during abrasive blasting (discussed in Section 3.2), which may also contribute to local enhancement of surface hardness.

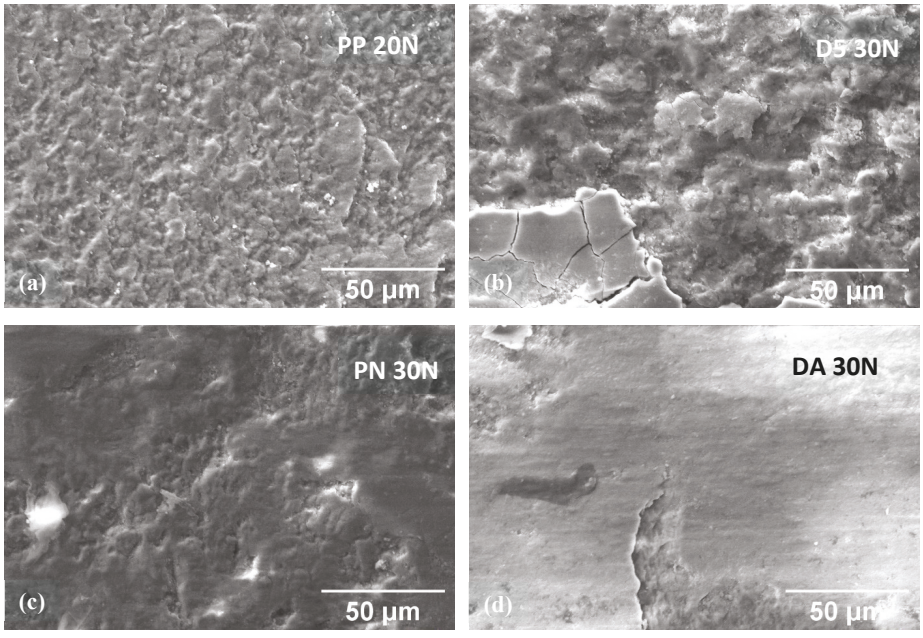

Figure 12. SEM images of wear scars at the load before coating failure for PEO coatings which survived at loads higher than 10 N: single layers (PP: **a**, PN: **c**) and double layers (D5: **b**, DA: **d**).

It is also worth noting that pulsed DC treatment at highest duty cycle (PN) attains the same critical load to failure in dry sliding as the best double layers. This is probably related to its dense microstructure and relatively high hardness. Moreover, the low roughness of PN by comparison to D5 and DA, induced by the absence of the intermediate silicate layer, is also likely to limit stress concentration at asperities, thereby limiting micro-crack driven damage, which is a typical wear mechanism associated with PEO layers as reported by Diamanti et al. [34]. The promising behaviour of PN therefore suggests that single-layer high duty cycle pulsed DC can be considered as an alternative and simpler processing route than double-layer deposition.

As regards abrasive-blasted double layers, both D5 and DA achieved the highest values of critical load to failure (40 N, Figure 7b). Their comparable performance indicates that microhardness alone is not the key parameter in influencing wear behaviour: both layers display a rather dense microstructure, hence practical adhesion plays a key role in determining the high critical load of DA, notwithstanding its lower hardness. It is also worth noting that embedding of glass residues was observed in the DA layer (as discussed in Section 3.2). As previously discussed for PP, this Si-rich surface layer may have a non-negligible beneficial influence, also predominating over other features such as microstructure, adhesion and hardness.

As for the comparison carried out under the highest normal loads (30 and 40 N) between the best-performing PEO layers (PN, D5 and DA) and reference materials (i.e., uncoated or PVD (Ti,Nb)N coated Ti-6Al-4V and CoCrMo), the average maximum wear scar depth values are reported in Figure 13.

As previously discussed, all PEO layers outperform the uncoated Ti-6Al-4V. At 30 N, all the selected PEO layers display wear depths comparable to CoCrMo (both uncoated and PVD-coated). The wear depth of PEO layers is also slightly lower than for PVD-coated Ti-6Al-4V, which is a promising

result considering that in this case the thickness of PEO layers is only slightly higher than that of the PVD coating, which is 5 μm thick). At 40 N, both the PEO the PVD layers on Ti-6Al-4V are worn out and their substrate is markedly involved in the contact. Only the PVD-coated CoCrMo still shows a very low wear depth (lower than that of the uncoated CoCrMo), due to the high load-bearing capacity of this substrate.

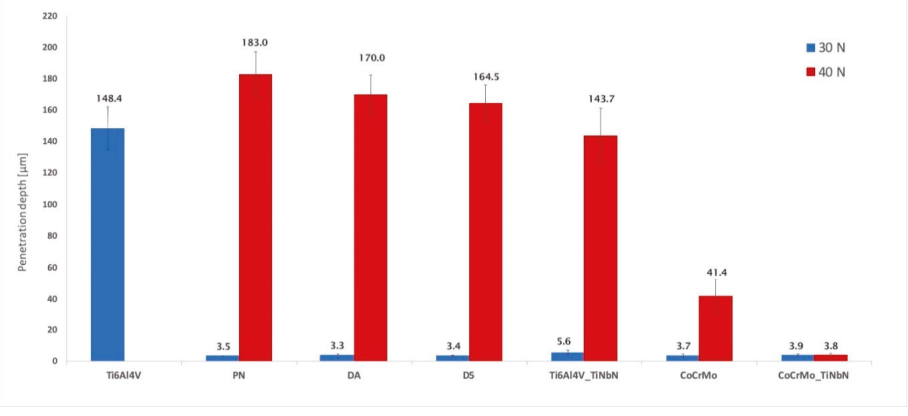

Figure 13. Wear depth values measured under normal loads of 30 and 40 N on the best-performing PEO layers and on the reference materials (uncoated or PVD (Ti,Nb)N coated Ti-6Al-4V and CoCrMo).

4. Conclusions

The dry sliding behaviour of the Ti-6Al-4V alloy, PEO-treated by using different process parameters, was assessed and correlated both to microstructure and micro-mechanical characteristics (hardness, practical adhesion). In particular, we investigated the influence on tribological behaviour of (i) layer structure (single layer, obtained in phosphate bath or double layer, obtained in silicate bath followed by phosphate bath), (ii) current mode (DC or pulsed DC), (iii) duty cycle (in case of pulsed DC deposition) and (iv) surface finishing (i.e., industrial post-treatment by abrasive blasting).

The results allowed to draw the following conclusions:

- Surface finishing by abrasive blasting with spheroidal glass beads leads to surface roughness decrease and hence to decreased friction and improved wear resistance. However, this procedure may also induce embedding of glass residues in the cortical zone of PEO layers, with an additional beneficial influence on tribological behaviour.
- The tribological behaviour of PEO layers obtained in pulsed DC tends to improve with increasing duty cycle values, due to improved microstructure and adhesion of PEO layers.
- Single-layer, high duty cycle, pulsed DC can be considered as an alternative, simpler processing route than double-layer deposition, leading to comparable wear performance.
- In the case of PEO layers obtained in the conventional DC regime, the double-layer structure (treatment in silicate bath followed by phosphate bath) beneficially affected wear behaviour.
- The best PEO layers among those developed in this study showed promising results in the comparison with reference materials. In particular, at 30 N normal load, PEO layers displayed wear depths comparable to CoCrMo (both uncoated and (Ti,Nb)N PVD-coated) and slightly lower than PVD-coated Ti-6Al-4V. At 40 N, however, both PEO layers and PVD coatings on Ti-6Al-4V underwent failure and only PVD-coated CoCrMo showed low wear depths.

Author Contributions: Conceptualization, C.M., G.R. and A.M.; methodology, C.M., G.R. and A.M.; investigation, A.G. and C.B.; data curation, C.M., A.G. and C.B.; writing—original draft preparation, A.G.; writing—review and editing, C.M., C.B., A.M. and G.R.

Funding: This research received no external funding.

Acknowledgments: This research did not receive any specific grant from funding agencies in the public, commercial or not-for-profit sectors. We wish to thank Iuri Boromei at Dept. of Industrial Engineering for SEM observations XRD and Raman analyses of PEO-treated samples, as well as Giovanni Barraco for his support to experimental work. We also wish to thank NanoSurfaces Industries srl for providing reference materials (CoCrMo alloy with/without PVD coating and PVD-coated Ti-6Al-4V).

Conflicts of Interest: The authors declare no conflict of interest.

References

1. Chen, Q.; Thouas, G.A. Metallic implant biomaterials. *Mater. Sci. Eng. R Rep.* **2015**, *87*, 1–57. [CrossRef]
2. Jarcho, M.; Kay, J.F.; Gumaer, K.I.; Doremus, R.H.; Drobeck, H.P. Tissue, cellular and subcellular events at a bone-ceramic hydroxylapatite interface. *J. Bioeng.* **1977**, *1*, 79–92. [PubMed]
3. Huang, N.; Leng, Y.X.; Ding, P.D. Surface engineered titanium alloys for biomedical devices. In *Surface Engineering of Light Alloys*; Woodhead Publishing: Cambridge, UK, 2010; pp. 568–602.
4. Durdu, S.; Deniz, Ö.F.; Kutbay, I.; Usta, M. Characterization and formation of hydroxyapatite on Ti6Al4V coated by plasma electrolytic oxidation. *J. Alloys Compd.* **2013**, *551*, 422–429. [CrossRef]
5. Li, L.H.; Kong, Y.M.; Kim, H.W.; Kim, Y.W.; Kim, H.E.; Heo, S.J.; Koak, J.Y. Improved biological performance of Ti implants due to surface modification by micro-arc oxidation. *Biomaterials* **2004**, *25*, 2867–2875. [CrossRef] [PubMed]
6. Jiang, B.L.; Wang, Y.M. 5-Plasma electrolytic oxidation treatment of aluminium and titanium alloys. In *Surface Engineering of Light Alloys: Aluminium, Magnesium and Titanium Alloys*; Dong, H., Ed.; Woodhead publishing Limited: Cambridge, UK, 2010; pp. 110–146. ISBN 1845699459.
7. Shrestha, S.; Dunn, B.D. Plasma electrolytic oxidation and anodising of aluminium alloys for spacecraft applications. In *Surface Engineering of Light Alloys*; Woodhead Publishing: Cambridge, UK, 2010; pp. 603–641.
8. Chen, Y.; Cheng, T.; Nie, X. Wear failure behaviour of titanium-based oxide coatings on a titanium alloy under impact and sliding forces. *J. Alloys Compd.* **2013**, *578*, 336–344. [CrossRef]
9. Chen, F.; Zhou, H.; Chen, C.; Xia, Y.J. Study on the tribological performance of ceramic coatings on titanium alloy surfaces obtained through microarc oxidation. *Prog. Org. Coat.* **2009**, *64*, 264–267.
10. Wang, Y.M.; Jiang, B.L.; Guo, L.X.; Lei, T.Q. Tribological behavior of microarc oxidation coatings formed on titanium alloys against steel in dry and solid lubrication sliding. *Appl. Surf. Sci.* **2006**, *252*, 2989–2998. [CrossRef]
11. International Standard ISO 20502. *Fine Ceramics (Advanced Ceramics, Advanced Technical Ceramics)—Determination of Adhesion of Ceramic Coatings by Scratch Testing*, 1st ed.; Korean Agency for Technology and Standards: Chungcheongbuk-do, Korea, 2002; Volume 6, pp. 1–16.
12. ASTM Standard G77. *Standard Test Method for Ranking Resistance of Materials to Sliding Wear Using Block-on-Ring Test*; ASTM International: West Conshohocken, PA, USA, 2017.
13. Ceschini, L.; Chiavari, C.; Marconi, A.; Martini, C. Influence of the countermaterial on the dry sliding friction and wear behaviour of low temperature carburized AISI316L steel. *Tribol. Int.* **2013**, *67*, 36–43. [CrossRef]
14. Borgese, L.; Gelfi, M.; Bontempi, E.; Goudeau, P.; Geandier, G.; Thiaudière, D.; Depero, L.E. Young modulus and Poisson ratio measurements of TiO_2 thin films deposited with Atomic Layer Deposition. *Surf. Coat. Technol.* **2012**, *206*, 2459–2463. [CrossRef]
15. Soares, P.; Mikowski, A.; Lepienski, C.M.; Santos, E.; Soares, G.A.; Filho, V.S.; Kuromoto, N.K. Hardness and elastic modulus of TiO_2 anodic films measured by instrumented indentation. *J. Biomed. Mater. Res. Part B Appl. Biomater.* **2008**, *84*, 524–530. [CrossRef]
16. Galetz, M.C.; Seiferth, S.H.; Theile, B.; Glatzel, U. Potential for adhesive wear in friction couples of UHMWPE running against oxidized zirconium, titanium nitride coatings, and cobalt-chromium alloys. *J. Biomed. Mater. Res. Part B Appl. Biomater.* **2010**, *93*, 468–475. [CrossRef]
17. Malchesky, P.S. Artificial Organs 2003: A Year in Review. *Artif. Organs* **2004**, *28*, 410–424. [CrossRef]
18. Paschoal, A.L.; Vanâncio, E.C.; Canale, L.C.F.; Silva, O.L.; Huerta-Vilca, D.; Motheo, A.J. Metallic Biomaterials TiN-Coated: Corrosion Analysis and Biocompatibility. *Artif. Organs* **2003**, *27*, 461–464. [CrossRef]
19. *Standard Specification for Wrought Cobalt-28Chronium-6Molybdenum Alloys for Surgical Implants (UNS R31537, UNS R31538, and UNS R31539)*; ASTM F1537; ASTM International: West Conshohocken, PA, USA, 2011.

20. *Standard Test Methods for Determining Average Grain Size*; ASTM E112; ASTM International: West Conshohocken, PA, USA, 2012.
21. Bouchard, M.; Smith, D.C. *Raman Spectroscopy in Archaeology and Art History*; Edwards, H.G.M., Chalmers, J.M., Eds.; Royal Society of Chemistry: London, UK, 2005; pp. 429–464. ISBN 9780854045228.
22. Friedemann, A.E.R.; Thiel, K.; Haßlinger, U.; Ritter, M.; Gesing, T.M.; Plagemann, P. Investigations into the structure of PEO-layers for understanding of layer formation. *Appl. Surf. Sci.* **2018**, *443*, 467–474. [CrossRef]
23. Xue, W.; Deng, Z.; Lai, Y.; Chen, R. Analysis of Phase Distribution for Ceramic Coatings Formed by Microarc Oxidation on Aluminum Alloy. *J. Am. Ceram. Soc.* **1998**, *81*, 1365–1368. [CrossRef]
24. Khan, R.H.U.; Yerokhin, A.L.; Li, X.; Dong, H.; Matthews, A. Influence of current density and electrolyte concentration on DC PEO titania coatings. *Surf. Eng.* **2014**, *30*, 102–108. [CrossRef]
25. Martini, C.; Ceschini, L.; Tarterini, F.; Paillard, J.M.; Curran, J.A. PEO layers obtained from mixed aluminate–phosphate baths on Ti–6Al–4V: Dry sliding behaviour and influence of a PTFE topcoat. *Wear* **2010**, *269*, 747–756. [CrossRef]
26. Wang, Y.; Lei, T.; Jiang, B.; Guo, L. Growth, microstructure and mechanical properties of microarc oxidation coatings on titanium alloy in phosphate-containing solution. *Appl. Surf. Sci.* **2004**, *233*, 258–267. [CrossRef]
27. Yerokhin, A.L.; Nie, X.; Leyland, A.; Matthews, A. Characterisation of oxide films produced by plasma electrolytic oxidation of a Ti–6Al–4V alloy. *Surf. Coat. Technol.* **2000**, *130*, 195–206. [CrossRef]
28. Wang, Y.M.; Jiang, B.L.; Lei, T.Q.; Guo, L.X. Microarc oxidation coatings formed on Ti6Al4V in Na2SiO3 system solution: Microstructure, mechanical and tribological properties. *Surf. Coat. Technol.* **2006**, *201*, 82–89. [CrossRef]
29. Yeung, W.K.; Reilly, G.C.; Matthews, A.; Yerokhin, A. In vitro biological response of plasma electrolytically oxidized and plasma-sprayed hydroxyapatite coatings on Ti–6Al–4V alloy. *J. Biomed. Mater. Res. B Appl. Biomater.* **2013**, *101*, 939–949. [CrossRef]
30. Mohammadi, H.; Hafezi, M.; Nezafati, N.; Heasarki, S.; Nadernezhad, A.; Ghazanfari, S.M.H.; Sepantafar, M. Bioinorganics in Bioactive Calcium Silicate Ceramics for Bone Tissue Repair: Bioactivity and Biological Properties. *J. Ceram. Sci. Technol.* **2014**, *5*, 1–12.
31. Aliasghari, S.; Němcová, A.; Skeldon, P.; Thompson, G.E. Influence of coating morphology on adhesive bonding of titanium pre-treated by plasma electrolytic oxidation. *Surf. Coat. Technol.* **2016**, *289*, 101–109. [CrossRef]
32. Dehnavi, V.; Luan, B.L.; Liu, X.Y.; Shoesmith, D.W.; Rohani, S. Correlation between plasma electrolytic oxidation treatment stages and coating microstructure on aluminum under unipolar pulsed DC mode. *Surf. Coat. Technol.* **2015**, *269*, 91–99. [CrossRef]
33. Galvis, O.A.; Quintero, D.; Castaño, J.G.; Liu, H.; Thompson, G.E.; Skeldon, P.; Echeverría, F. Formation of grooved and porous coatings on titanium by plasma electrolytic oxidation in H2SO4/H3PO4 electrolytes and effects of coating morphology on adhesive bonding. *Surf. Coat. Technol.* **2015**, *269*, 238–249. [CrossRef]
34. Diamanti, M.V.; Sebastiani, M.; Mangione, V.; Del Curto, B.; Pedeferri, M.P.; Bemporad, E.; Cigada, A.; Carassiti, F. Multi-step anodizing on Ti6Al4V components to improve tribomechanical performances. *Surf. Coat. Technol.* **2013**, *227*, 19–27. [CrossRef]
35. Tekin, K.C.; Malayoglu, U.; Shrestha, S. Tribological behaviour of plasma electrolytic oxide coatings on Ti6Al4V and cp-Ti alloys. *Surf. Eng.* **2016**, *32*, 435–442. [CrossRef]
36. Durdu, S.; Usta, M. The tribological properties of bioceramic coatings produced on Ti6Al4V alloy by plasma electrolytic oxidation. *Ceram. Int.* **2014**, *40*, 3627–3635. [CrossRef]
37. Curran, J.A.; Clyne, T.W. Porosity in plasma electrolytic oxide coatings. *Acta Mater.* **2006**, *54*, 1985–1993. [CrossRef]
38. Tonelli, L.; Pezzato, L.; Dolcet, P.; Dabalà, M.; Martini, C. Effects of graphite nano-particle additions on dry sliding behaviour of plasma-electrolytic-oxidation-treated EV31A magnesium alloy against steel in air. *Wear* **2018**, *404*, 122–132. [CrossRef]

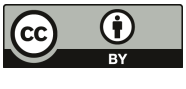

coatings

MDPI

Article

On Friction Reduction by Surface Modifications in the TEHL Cam/Tappet-Contact-Experimental and Numerical Studies

Max Marian *, Tim Weikert and Stephan Tremmel

Engineering Design, Friedrich-Alexander-Universität Erlangen-Nürnberg, Martensstr. 9, 91058 Erlangen, Germany; weikert@mfk.fau.de (T.W.); tremmel@mfk.fau.de (S.T.)
* Correspondence: marian@mfk.fau.de

Received: 14 November 2019; Accepted: 6 December 2019; Published: 9 December 2019

Abstract: The overall energy efficiency of machine elements and engine components could be improved by using new technologies such as surface modifications. In the literature, surface engineering approaches like micro-texturing and the application of diamond-like carbon (DLC) coatings were frequently studied separately, with focus on a specific model contact and lubrication conditions. The contribution of the current study is to elucidate and compare the underlying friction reduction mechanisms of the aforementioned surface modifications in an application-orientated manner. The study applied the operating conditions of the thermo-elastohydrodynamically lubricated (TEHL) cam/tappet-contact of the valve train. Therefore, tribological cam/bucket tappet component Stribeck tests were used to determine the friction behavior of ultrashort pulse laser fabricated microtextures and PVD/PECVD deposited silicon-doped amorphous carbon coatings. Moreover, advanced surface characterization methods, as well as numerical TEHL tribo-simulations, were utilized to explore the mechanisms responsible for the observed tribological effects. The results showed that the DLC-coating could reduce the solid and fluid friction force in a wide range of lubrication regimes. Conversely, micro-texturing may reduce solid friction while increasing the fraction of fluid friction.

Keywords: thermo-elastohydrodynamic lubrication; DLC-coating; microtexturing; surface modification; friction mechanisms; energy efficiency; internal combustion engine; cam/tappet-contact

1. Introduction

Approximately one-fifth of the fuel energy in passenger cars is used to overcome friction in engines, of which about 15% is consumed in the valve train (Holmberg et al. [1]). According to many experts, for example, Kalghatgi [2] and Serrano et al. [3], internal combustion engines (ICE) will not diminish in relevance worldwide even in times of increasing powertrain electrification. In addition, the obtained insights can also be transferred to other tribological rolling-sliding-contacts, for example, in the newly emerging field of electric vehicles (Farfan-Cabrera [4]). The total energy efficiency could be significantly increased by utilizing new technologies such as surface modifications (Holmberg and Erdemir [5]). This can be achieved, for instance, by applying amorphous carbon (DLC) coatings (Kalin et al. [6], Erdemir and Donnet [7]) or discrete microtextures (Gropper et al. [8], Gachot et al. [9–11]) onto the rubbing surfaces of lubricated tribological sliding contacts. Both approaches have been intensively investigated in the literature within various theoretical and experimental studies ranging from boundary (Pettersson and Jacobson [12]), to mixed (Löffler et al. [13], Borghi et al. [14]), as well as full-film hydrodynamic (Etsion [15], Pawlus et al. [16,17]) and elastohydrodynamic lubrication. With advancing experimental and numerical methods, the effects of surface modifications particularly

in non-conformal thermo-elastohydrodynamically lubricated (TEHL) contacts, have been the subject of numerous investigations.

Evans et al. [18] and Kalin et al. [19,20] identified the wall slip between dispersive lubricants and highly dispersive coated surfaces as being responsible for friction reductions of up to 20% using tetrahedral amorphous carbon (ta-C), hydrogenated amorphous carbon (a-C:H), and doped DLC (a-C:H:Si, a-C:H:N, a-C:H:F) coatings compared to uncoated references in ball-on-flat experiments. Björling et al. [21] investigated the frictional behavior of a-C:H coatings in a ball-on-disk tribometer, where friction decreased with increasing coating thickness, wherein a reduction of up to 41% was observed. From contact angles, surface energies, and spreading parameters, the authors concluded that the friction reduction was not only due to solid–liquid interactions but also due to a thermal insulation effect. The outcome was further observed by Björling et al. [22,23] using a combined experimental and numerical approach. In ball-on-disk tests, the authors observed a friction reduction of up to 16% if one contacting body was coated, and up to 25 % if both bodies were coated (a-C:H). Thermo-elastohydrodynamically lubricated (TEHL) simulation results indicated the highest contact temperatures when both bodies were coated, and the lowest temperatures for the uncoated reference case, which was attributed to the lower thermal inertia of the amorphous carbon coatings. Bobzin et al. [24] also attributed a friction reduction of up to 45% from a-C:H:ZrC and a-C:H:nc-ZrC coatings, observed in twin-disk tests to higher flash temperatures due to thermal insulation effects. The effects led to the lower shear resistance of the lubricant and lower mass temperatures of the disk, which resulted in a higher lubricant gap. Elsharkawy et al. [25] numerically studied the influence of mechanical coating properties and their thickness on the EHL pressure and fluid film thickness distribution. The authors found that coatings with a lower elastic modulus led to wider contact areas and lower maximum pressures. The influence of the mechanical coating properties increased with the coating thickness. Based on the finite element simulation approach, Habchi et al. [26] investigated the influence of both the thermal and mechanical effects of coatings on the TEHL contact. The results were in good agreement with the investigations mentioned above. Coatings with high thermal inertia showed temperature and friction coefficients that were similar to uncoated references, whereas low thermal inertia coatings featured a friction reduction of up to 50%. The result was enhanced by higher coating thickness and sliding speed. Using twin-disk tests and accompanying TEHL simulations with a 50% slip and a-C:H-coated specimens, Bobach et al. [27] showed a friction reduction of up to 40% compared to the uncoated references. Therefore, higher contact temperatures, as well as lower bulk temperatures, were observed due to the lower heat conductivity of the amorphous carbon coating, resulting in the observed fluid friction reduction. However, the authors noted that for pronounced mixed friction, the boundary friction between the surfaces could not be ignored. By comparing thin-film sensor measurements in a twin-disk test-rig using TEHL simulations, Ebner et al. [28] demonstrated higher contact temperatures due to ZrO_2 and Al_2O_3-coatings compared to the uncoated specimens.

Regarding texturing, various early investigations, e.g., by Choo et al. [29,30], Ehret et al. [31], and Venner and Lubrecht [32], on surfaces with regular features using optical interferometry or numerical simulations indicated the direct involvement of surface topography on elastohydrodynamic lubrication. Therefore, grooves and ridges orientated transversely to the direction of sliding tended to enhance the mean fluid film thickness, whereas longitudinal surface features instead induced adverse effects. Initial experimental and numerical studies on discrete surface features were carried out by Cusano and Wedeven [33] and Ai and Cheng [34], respectively. Using optical interferometry in an EHL tribometer under 50% slip conditions and accompanying numerical simulations, Mourier et al. [35] showed that deep cavities reduced the lubricant gap while shallow dimples fabricated by laser texturing enlarged the fluid film. The effect was related to the highly viscous lubricant that was drawn out of the texture due to shear effects and an additional elastic deformation. Complementary studies (Mourier et al. [36]) indicated the optimal depths and diameters of the dimples for lubricant gap enlargement below or above, wherein less positive or even detrimental effects occurred. The role of shallow textures, velocity differences, and high lubricant viscosity was further emphasized by Krupka and Hartl [37].

Moreover, Krupka et al. [38] studied shallow dimples under mixed EHL conditions using thin film colorimetric interferometry. They found that lubricant expelled from microtextures could effectively lift off real roughness features, providing an increase in the average film thicknesses. Investigations using a twin-disk test-rig by Bobzin et al. [24] showed a friction reduction induced by deterministic laser textures but only at higher contact stresses, low velocities, and high slips. Rosenkranz et al. [39] mapped the conditions under mixed and full film EHL from which friction reduction could be obtained using hot micro-coined samples in the ball-on-disk tests. Thus, shallow textures and lower area coverage between 10 and 20% resulted in pronounced friction reductions of up to a factor of 3 at low sliding velocities. Marian et al. [40] combined ball-on-disk experiments with EHL simulations, taking mixed lubrication into account, to study the influence of the structural parameters of single hemispherical microtextures on the resulting lubrication conditions, friction, and wear. The authors used meta-modeling and biological evolution-inspired optimization algorithms to derive beneficial and robust micro-texture designs. Textures with a shallow depth and a diameter close to the elastically deformed contact area were found to be favorable, with a friction reduction up to 60% due to an additional hydrodynamic pressure build-up, a local lubricant gap enlargement, as well as reduced asperity contact.

The studies above were limited to coating or microtexturing in model contacts or under constant lubrication conditions. Meanwhile, dynamic and different lubrication conditions are present in real applications. Since both surface modification approaches are particularly suitable for machine elements with high amounts of sliding, several investigations have dealt with gear wheel pairings. Bobzin et al. [24] studied the influence of a-C:H:ZrC and a-C:H:nc-ZrC coated and laser-textured spur gears using a gear efficiency test-rig. For the microtextured tooth flanks, a desirable friction behavior with an improvement of up to 7% compared to the polished references was observed under extreme mixed friction conditions. A significant friction reduction of up 39% was observed for the amorphous carbon-coated gear wheels. Although a reduction in frictional losses was observed at lower circumferential speeds, this reduction was more pronounced at higher gear wheel speeds. Again, this was attributed to the low thermal inertia of the amorphous carbon coatings. Beilicke et al. [41] performed transient TEHL simulations of an amorphous carbon-coated helical gear pair, taking mixed lubrication into account. The observed reduced friction up to 27% was explained by the thermal insulation of the coating, resulting in lower effective lubricant viscosity. Coating both the pinion and wheel resulted in higher temperatures, lower traction coefficients, and lower minimum lubricant gap compared to the single-sided coated gear pair. For the latter, the fluid temperature was shifted towards the coated surface. Using TEHL simulations of spur gears, Zieglтrum et al. [42] showed a similar trend in frictional behavior for different lubricants (mineral, polyalphaolefin, and polyglycol oil) due to the thermal insulation effects of the amorphous carbon coating. However, the degree of friction reduction varied between 14% and 28%, depending on the lubricant properties.

The TEHL cam/tappet-contact of the valve train represents another engine component with high frictional losses and a high amount of sliding. Kano et al. [43] reported that hydrogen-free amorphous carbon coatings (ta-C), while using additized (GMN) PAO base oïl, led to super-low friction coefficients (below 0.01) in a single cam and follower test-rig, as well as friction reductions up to 45% in motor-driven valve train tests. Dobrenizki et al. [44] studied the influence of engine oil, additives, temperature, and camshaft speed on efficiency improvement from a-C:H:ZrC and a-C:H:X coatings on single automobile bucket tappets in contact with a cam. Yu et al. [45] numerically investigated the effects of mechanical and thermal coating properties on the TEHL cam/tappet-contact under full-film conditions. They found that frictional losses were significantly affected by thermal effects and that soft coatings with low thermal inertia were most favorable. Coating both the tappet and cam resulted in higher TEHL temperatures and lower friction coefficients.

Furthermore, using transient full-film TEHL simulations, Meng et al. [46] concluded that amorphous carbon coating induced thermal insulation effects that are particularly beneficial in start-up processes of the cam/tappet-contact, leading to significantly reduced frictional losses. Gangopadhyay

and Watt [47] used a motored valve train test-rig to determine a friction reduction of up to 35% from shallow V-shaped grooves fabricated by a diamond cutting tool. Krupka et al. [48] studied the effect of an array of micro-dimples on lubrication conditions using optical interferometry in a ball-on-disk machine, mimicking the transient operating conditions of the cam/tappet-contact. They showed that lubricant drawn out from the micro-pockets helped to separate the rubbing surfaces especially under thin-film conditions where the counter-bodies featured opposing sliding speeds. Employing a component test-rig, Marian et al. [49] studied the tribological performance of shallow line-shaped microtextures applied on tappets in the cam-contact operating under mixed lubrication conditions. For pure mineral oil, a significant friction reduction of up to 14 % was determined, which correlated well with measurements from an electrical resistivity circuit. The results and accompanying EHL simulations indicated that reduced asperity contact was responsible for the outcome. From the same test-rig, Tremmel et al. [50] determined a strong dependency on the frictional behavior of microtextured tappets on the lubricant viscosity, with higher viscosities being favored. Based on TEHL simulations and subsequent meta-modeling and optimization, the same authors concluded that shallow line-shaped textures arranged perpendicular to the direction of motion and with a width close to the elastically deformed contact area were most beneficial.

In summary, amorphous carbon coating and surface micro-texturing offer great potential to improve the energy efficiency in EHL contacts with a high amount of sliding, operating under a mixed or full-film regime. However, many studies have only focused on model contacts and constant lubrication conditions. Moreover, despite the very similar basic idea of amorphous carbon coating and micro-texturing, i.e., to improve the energy efficiency of a tribological contact without influencing other components, e.g., through design changes, the two approaches were usually considered separately. For these reasons, this paper aims to elucidate and compare the underlying friction reduction mechanisms under application-orientated operating conditions in the cam/tappet-contact of the valve train. Therefore, component tests with amorphous carbon-coated and microtextured bucket tappets were carried out and supplemented by surface characterization, as well as numerical TEHL tribo-simulations, which offered the potential to explore the underlying mechanisms. The results of this study were partly presented orally at the 74th STLE Annual Meeting and Exhibition 2019 in Nashville, Tennessee [51].

2. Materials and Methods

2.1. Experimental Methods

2.1.1. Materials

For testing, mechanical bucket tappets with top adjusting shims made of 16MnCr5 (1.7131, AISI 5115), with a diameter of 28 mm and height of 2.5 mm, were used and either microtextured or coated with amorphous carbon. The specimens were case-hardened to 62 + 2 HRC, mirror-polished to $R_a \approx$ 0.005 µm, and ultrasonically cleaned in acetone and isopropyl alcohol.

2.1.2. Microtexturing

Texturing of the specimen surfaces, as depicted in Figure 1a, was carried out using an ultrashort pulse (USP) laser ablation process (Fuego, Time Bandwidth, Zurich, Swiss) and a 2D scanner system (Scanlab, Puchheim, Germany) with a scanning speed of 600 mm/s. Nd:YVO4 generated a beam with 1064 nm wavelength and an averaged power of 802 mW. The pulse rate of 200 kHz and the short pulse duration of 10 ps allowed a precise process with low ablation per pulse, a small heat-affected zone, and the high quality of fabricated microtextures. The beam was focused to a minimum spot diameter of 37 µm using an F-theta lens with a focal length of 160 mm. After texturing, the specimens were polished again to remove manufacturing induced material accumulation at the texture edges and to adjust the final roughness ($R_a \approx 0.005$ µm) and texture depth. Thus, we set a shallow depth of around 2 µm.

Lateral dimensions of each texture element were constant at 35 µm in, as well as 2 mm perpendicular to the direction of motion. Distances between the textures were 180 µm in and 1 mm perpendicular, respectively. This measure corresponded to area coverage of approximately 10%. The values were chosen as they were advantageous as described in the literature and previous studies [49,50].

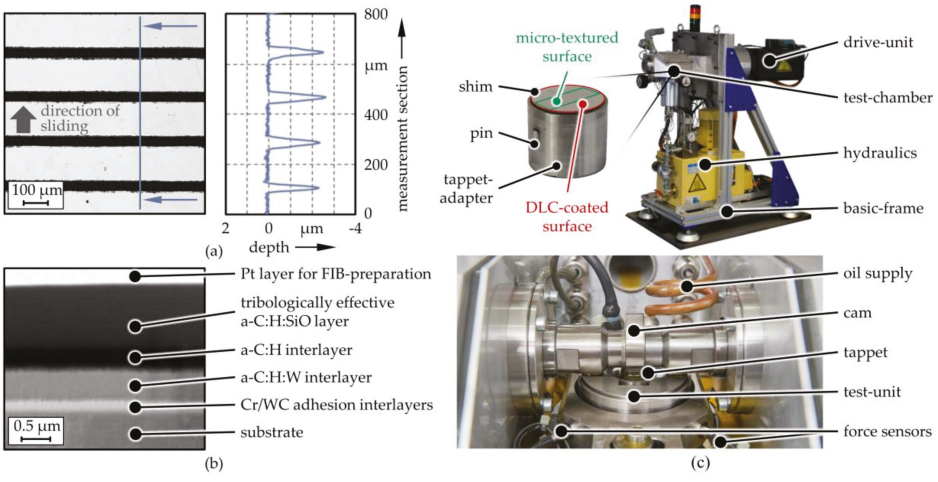

Figure 1. (**a**) Laser scanning microscopy image and a sectional view of a microtextured sample; (**b**) FIB-milled cross-section of a DLC-coated specimen; (**c**) Cam/bucket tappet component test-rig.

2.1.3. Coating

Among the group of DLC-coatings, a silicon-doped hydrogenated amorphous carbon coating (a-C:H:SiO), as illustrated in Figure 1b, was deposited using an industrial scale PVD/PECVD coating machine (TT 300, H-O-T, Nuremberg, Germany) with a two-fold rotating charging rack. Before deposition, the specimens were argon ion plasma-etched inside the deposition chamber, applying an argon flow of 500 sccm and a −500 V pulsed DC bias voltage at 300 °C for 40 min. Since carbon-based layers usually show poor adhesion when directly deposited on steel substrates, we applied a thin adhesion layer of chromium (Cr) and an interlayer of tungsten carbide (WC). Furthermore, interlayers of tungsten-doped hydrogenated amorphous carbon (a-C:H:W) and pure hydrogenated amorphous carbon (a-C:H) contributed to a gradual increase in hardness from the substrate towards the top layer and improved the coating's load-carrying capacity. Finally, a top layer of a-C:H:SiO served as a tribologically effective functional layer. Interfaces to the substrate and between layers were graded by continuous adjustment of the process parameters. The Cr adhesion layer and the WC interlayer were prepared by the steered arc evaporation of a Cr-target and unbalanced magnetron (UBM) sputtering of a binder-free WC-target, respectively. PECVD processes were employed to deposit a-C:H and a-C:H:SiO layers by evaporating HDMSO and applying argon and acetylene as process and reactive gas. The a-C:H:W layer was generated in a reactive PVD process by sputtering the WC-target under an argon-acetylene atmosphere. The WC-target was used with bipolar pulsed DC voltages applying set target voltages as the negative pulse amplitudes. The levels of the positive pulses represented 15% of the adjusted target voltages. During the deposition of the WC interlayer, the pulse frequency was kept constant at 40 kHz with the duration of a positive pulse of 5 µs. Preparing the a-C:H:W layer, the pulse parameters were set to 70 kHz and 4 µs, respectively, to prevent the WC-target from poisoning. The PECVD processes required bipolar (15% positive pulse voltage level) and unipolar pulsed bias voltages (pulse frequency of 40 kHz, positive pulse duration of 5 µs). Relevant deposition parameters for each coating layer are listed in Table 1. After deposition, the coated samples were polished to $R_a \approx 0.047$ µm.

Table 1. Deposition parameters of layers of the amorphous carbon coating according to the order of deposition.

Coating Layer	Duration in s	Arc Current of Cr-Target in A	Sputtering Power of WC-Target in W	Bias Voltage in V (Operating Mode)	Acetylene Gas Flow in sccm	Argon Gas Flow in sccm	HMDSO Gas Flow in sccm	Temperature in °C
Cr	280	70	–	−100 (DC)	–	70	–	140
WC	1080	–	1200	−50 (DC)	–	195	–	110
a-C:H:W	2267	–	1200	−130 (DC)	28	180	–	100
a-C:H	1155	–	–	−450 (bipolar pulsed)	250	100	–	100
a-C:H:SiO	2050	–	–	−575 (unipolar pulsed)	250	100	6	100

2.1.4. Characterization and Tribological Testing

The indentation hardness H_{IT} and indentation modulus E_{IT} were measured by nanoindentation using a Picodenter HM500 (HELMUT FISCHER, Sindelfingen, Germany). The H_{IT} and E_{IT} values of the coating were determined at a maximum load of 3 mN, ensuring indentation depths of the Vickers indenter of less than 10% of the coating thickness to minimize the influence of the substrate material [52]. A load of 500 mN was chosen for the indentation of the uncoated steel substrate. To compensate for the statistical scattering due to surface roughness and irregularities, we performed twenty indentations of which not more than four significant outliers were precluded from the evaluation.

The specimens were further characterized by laser scanning microscopy (LSM, VK-X200, Keyence, Neu-Isenburg, Germany) and focused ion beam preparation (FIB, Scientific Helios NanoLab 600i, Thermo Fisher, Waltham, Massachusetts, United States) to illustrate the textured surface and the coating architecture, as shown in Figure 1b,c.

Tribological testing was carried out on a single cam/single bucket tappet component test-rig (TSRP, KTmfk, Erlangen, Germany), as described by Dobrenizki et al. [44], Marian et al. [49], and Tremmel et al. [50]. This testing is illustrated in Figure 1c, utilizing standard valve train parts (cam, spring, valve) to ensure realistic conditions. The shims were fixed in the recess of a tappet adapter using a temperature and impact resistant adhesive (Loctite 480, HENKEL, Düsseldorf, Germany). A pin restricted the rotation of the tappets within their guidance during testing to maintain the same orientation of the line-shaped textures to the contact area. The 100Cr6 (1.3505, AISI 52100) cam ($R_a \approx$ 0.2 µm) without profiling, at a width of 10 mm, a base radius of 15 mm, and a tip radius of 2.3 mm was cut out of a series camshaft, provided with cone seats and held by two shafts. The same cam which had previously been run in for 24 h was used for all tests. The test-unit, in which the tappet and valve were moving linearly, was mounted elastically at the bottom and supported by four crosswise arranged, preloaded piezoelectric force sensors at the top. Thus, the friction force within the cam/tappet-contact could be determined. For lubrication, pure mineral oil FVA 3 (kinematic viscosity 95 mm/s^2 at 40 °C, viscosity index 195) was used and heated to 90 °C in the hydraulics-unit. Three samples of each, polished references, as well as the microtextured and DLC-coated specimens, were tested, and the sequence was randomized. After running in for one hour at 1000 min$^{-1,}$ the camshaft rotation speed was increased gradually from 200 to 2000 min$^{-1,}$ and each level was held for one minute. Measurement values were detected at the end of each speed level. For the evaluation, we compared the maximum friction force averaged over three samples per type and several rotations each.

To evaluate the solid friction of uncoated and coated specimens, we performed unlubricated ball-on-disk test (K-SST, KTmfk, Erlangen, Germany) under constant climatic conditions (relative humidity of 40 ± 5% at 23 ± 2 °C); noting that the specimens significantly affect the frictional behavior under mixed lubrication typical for cam/tappet-contacts [49]. Hardened 100Cr6 bearing balls with a diameter of 9.5 mm served as counter-bodies. The applied normal force of 10 N resulted in an initial Hertzian pressure of 1.1 GPa. We selected this force to obtain conditions similar to those in the cam/tappet component-tests after running in. Three uncoated and coated specimens each were tested at the same track radii with a constant rotational sliding velocity of 1.5 m/s and a sliding distance of 1000 m. The coefficient of friction averaged between 600 and 800 m for each test run.

2.2. Numerical Methods

For the numerical TEHL modeling of the cam/bucket tappet-contact, the full-system finite element modeling (FEM) approach, as first presented by Habchi et al. [53], was employed. The calculation model is part of the computation software TriboFEM, which in turn was implemented in Comsol Multiphysics. The main physical and numerical characteristics are briefly described below.

2.2.1. Hydrodynamics

To describe the hydrodynamics, we used a generalized Reynolds equation according to Yang and Wen [54] in a slightly modified form

$$\underbrace{\frac{\partial}{\partial x}\left[\left(\frac{\int_0^h \frac{\tilde{z}}{\eta}dz \cdot \int_0^h \rho \int_0^z \frac{1}{\eta}dz'dz}{\int_0^h \frac{1}{\eta}dz} - \int_0^h \rho \int_0^z \frac{z'}{\eta}dz'\mathrm{d}z\right)\frac{\partial p}{\partial x}\right]}_{\text{pressure / Poiseuille term}} - \underbrace{\frac{\partial}{\partial x}\left[\frac{\int_0^h \rho \int_0^z \frac{1}{\eta}dz'dz}{\int_0^h \frac{1}{\eta}dz} \cdot (u_1 - u_2) + \int_0^h \rho \mathrm{d}z \cdot u_2\right]}_{\text{velocity / Couette term}} - \underbrace{\frac{\partial}{\partial t}\left(\int_0^h \rho \mathrm{d}z\right)}_{\text{squeeze term}} = 0 \tag{1}$$

with zero pressure boundary conditions at in- and outlet was applied. Cavitation effects were addressed using a mass-conserving model as described by Marian et al. [55]. The Galerkin least squares (GLS) method and isotropic diffusion were used for the numerical stabilization.

2.2.2. Contact Mechanics

The elastic deformation of one body with the equivalent Young's modulus and Poisson's ratio was calculated by applying the linear elasticity equation while neglecting inertia effects or body forces:

$$\nabla \cdot \sigma = 0, \text{ with } \sigma = C \cdot \varepsilon(U), \ \delta_{\text{elastic}}(x,t) = \left|U_{\text{v}}(x,t)\right|. \tag{2}$$

Zero displacement at the bottom, as well as zero normal and tangential stress boundary conditions at the sides of the equivalent body, were applied. The effects of the coatings on the mechanical properties were considered by calculating the respective equivalent properties in accordance with Liu et al. [56].

The lubricant film thickness equation

$$h(x,t) = h_0 + \frac{x^2}{2R_{\text{x}}} + \delta_{\text{elastic}}(x,t) + a_{\text{texture}} \cdot e^{\frac{\ln\left(\frac{g}{a_{\text{texture}}}\right)\cdot\left[\left(\mathrm{mod}\left(x - x_{\text{start}} - \frac{t\cdot u_1}{u_m} + \frac{d_{\text{texture,x}}}{2},\ d_{\text{texture,x}}\right) - \frac{d_{\text{texture,x}}}{2}\right)\right)^2}}{w_{\text{texture,x}}^2}} \tag{3}$$

described the height of the separating fluid film in terms of the distance and shape of the undeformed geometry, the elastic deformation, as well as the geometrical microtexture description.

The load balance equation ensured the equilibrium of forces,

$$\frac{F}{l} = \int_\Omega p_{\text{total}}(x,t)\, d\Omega = \int_\Omega \left[p(x,t) + p_{\text{solid}}(x,t)\right] d\Omega\,, \tag{4}$$

which also allowed the consideration of simultaneously occurring asperity contact and hydrodynamic lubrication (mixed lubrication) by dividing the total pressure into hydrodynamic and solid contact pressure. Therefore, a statistical approach, as presented by Zhao et al. [57], was applied, while the implementation followed the example by Masjedi and Khonsari [58].

The dimensions of the computational domain were chosen to be large enough so that the results of the calculation corresponded to the results obtained from an infinite elastic half-space approach. Furthermore, a free triangular mesh with a refinement in the contact center of the upper surface was applied.

2.2.3. Thermodynamics

Following Habchi [59], the temperature distribution in the lubricant was described using the energy equation including heat sources due to lubricant compression and shearing

$$\underbrace{\rho \cdot c_p \cdot \left(\frac{\partial T}{\partial t} + u \cdot \frac{\partial T}{\partial x}\right)}_{\text{convection}} - \underbrace{\lambda \cdot \left(\frac{\partial^2 T}{\partial x^2} + \frac{\partial^2 T}{\partial z^2}\right)}_{\text{heat condution}} - \underbrace{\beta_p \cdot T \cdot \left(\frac{\partial p}{\partial t} + u \cdot \frac{\partial p}{\partial x}\right)}_{\text{compression or expansion}} - \underbrace{\eta \cdot \left[\left(\frac{\partial u}{\partial z}\right)^2\right]}_{\text{shearing}} = 0, \tag{5}$$

while the transient energy equation for the substrates and the coatings was considered as

$$\underbrace{\rho \cdot c_p \cdot \left(\frac{\partial T}{\partial t} + u_x \cdot \frac{\partial T}{\partial x}\right)}_{\text{convection}} - \underbrace{\lambda \cdot \left(\frac{\partial^2 T}{\partial x^2} + \frac{\partial^2 T}{\partial z^2}\right)}_{\text{heat condution}} = 0, \tag{6}$$

where $i = 1$ for the cam and $i = 2$ for the tappet. The transition between substrate, coating, and lubricant was implemented using temperature and conductive heat flux continuity equations. Solids and lubricant entering the calculation domain were set to bulk temperature while zero conductive heat flux was assumed for the respective properties leaving the domain. Dimensions of the computational domains were chosen so that the heat flux into the substrates became zero. Again, a free triangular mesh with refinement at the boundaries between substrate, coating, and lubricant was applied.

2.2.4. Numerical Procedure

All variables were normalized on initial or Hertzian parameters. The system of EHL equations was solved fully coupled and combined with the energy equations using an iterative procedure. A backward differentiation formula was used for adaptive time stepping. More fundamental aspects of the FEM of TEHL contacts are given by Habchi [59]. For further information about implementation in the software Comsol Multiphysics, the interested reader is referred to Tan et al. [60], Lohner et al. [61], and Weschta [62].

2.2.5. Load Cases, Material and Lubricant Properties

Relevant mechanical, thermal bulk and coating properties were chosen based on the measurement or literature values and they are summarized in Table 2. Pressure and temperature dependency of the lubricant was modeled according to Roelands (Sadeghi and Sui [63]), whereas a modified Carreau-Yasuda model described the shear dependency in accordance with Bair [64]. Density was modeled pressure and temperature-dependent according to Dowson and Higginson [65]. The relevant lubricant properties are summed up in Table 3.

Table 2. Material properties.

Parameter	Cam(100Cr6)	Tappet (16MnCr5)	Coating (a-C:H:SiO)
Young's/indentation modulus E in MPa	209,000 [1]	216,000 [2]	110,000 [2]
Poisson's ratio ν	0.3 [1]	0.3 [1]	0.3 [1]
density ρ in kg/m^3	7850 [1]	7760 [1]	4655 [1]
thermal conductivity λ in W/(m·K)	47 [1]	44 [1]	1.1 [1]
specific heat capacity c_p in J/(kg·K)	460 [1]	431 [1]	8263 [1]
dry coefficient of friction against 100Cr6 μ_{solid}	–	0.5 [2,3]	0.2 [2,3]

[1] based upon literature [41,42]. [2] based upon measurements, see Section 3.1. [3] conservative estimation compared to measurement results in Section 3.1.

Table 3. Lubricant properties [62].

Base Density at 90 °C ρ in kg/m^3	840
Base Viscosity at 90 °C η_0 in Pa·s	0.03
Pressure Viscosity Coefficient α_p in Pa$^{-1,}$	1.31·10^{-8}
Roelands Temperature Coefficient β_η	0.042
Critical Shear Stress G_c	0.2 η_0
Carreau Parameter a_c	2.2
Carreau Parameter n_c	0.8
Thermal Conductivity λ in W/(m·K)	0.14
Specific Heat Capacity c_p in J/(kg·K)	2000

Derived from multibody dynamics analysis (Weschta [62]), three different load cases corresponding to the contact between the cam tip and tappet at 500 min^{-1} (Moes parameters M = 9.3, L = 8.1, SRR = −2.6), 1000 min^{-1} (M = 6.3, L = 9,7, SRR = −2.6), and 2000 min^{-1} (M = 3.6, L = 11.5, SRR = −2.6), were studied within the scope of this manuscript.

For evaluation of the friction reduction mechanisms induced by microtexturing and amorphous carbon coating, we calculated the changes in the fluid friction force from integrating the shear stress in the middle of the lubricant film [59]

$$F_{\text{fluid}} = \int_{x_{\text{inlet}}}^{x_{\text{outlet}}} \tau_{zx}|_{z=h/2}\, dx \tag{7}$$

and changes to the solid friction force from integrating the product of solid contact pressure and the dry friction coefficient [27]

$$F_{\text{solid}} = \int_{x_{\text{inlet}}}^{x_{\text{outlet}}} \mu_{\text{solid}} \cdot p_{\text{solid}} dx. \tag{8}$$

3. Results and Discussion

3.1. Experimental Results

Representative LSM-measurements of a microtextured surface and a FIB-milled cross-section of the amorphous carbon coating are depicted in Figure 1a,b, respectively. It can be seen that the textures were fabricated with high shape accuracy and precision, showing well defined structural parameters such as depth, width, and lateral distance. For the coating, we determined a thickness of approximately 2 µm, an indentation hardness H_{IT} of 15.8 ± 0.5 GPa, and an indentation modulus E_{IT} of 110.9 ± 3.3 GPa. Therefore, compared to the substrate (H_{IT} = 8.3 ± 0.2 GPa, E_{IT} = 216.5 ± 2.5 GPa), the coating was harder, though elastically less stiff.

Since we found no significant wear after the performance of the short-term component-test, the following evaluations refer purely to the frictional behavior. Therefore, the maximum detected friction force was averaged for all revolutions within the respective measurement ramp of each specimen. Subsequently, we calculated the mean values of all three samples for the reference, microtextured, and DLC-coated tappet. Corresponding results in dependency of the cam rotation speed are summarized in Figure 2, normalized to the polished references at the first speed level (a), and to the polished references at each speed level (b). All specimens featured a continuous Stribeck-like decrease of friction with an increasing camshaft speed.

A reduction of friction up to 12% compared to the references was achieved by micro-texturing. It can be assumed that the solid–solid contact ratio was reduced during contact between the counter-body and the texture [49]. In addition, the build-up of an additional hydrodynamic pressure can be expected. However, friction reduction was pronounced more strongly for lower camshaft speeds, and the measured values almost reached the reference level at higher speeds. The result matched well with observations previously made in the literature [24]. However, since the considered cam/tappet pairing works under mixed lubrication conditions in the whole speed range tested [49,62], the complete

separation of rubbing surfaces, and thus, a loss of texture induced effects alone does not provide a sufficient explanation.

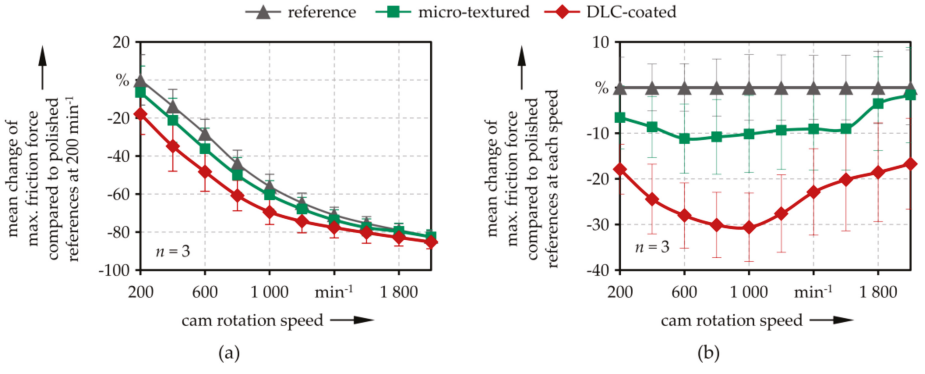

Figure 2. Mean change of friction force in the cam/tappet-contact for the microtextured and DLC-coated specimens at different cam rotation speeds compared to the polished references (**a**) at the first speed level and (**b**) at each speed level.

For the amorphous carbon coating, a friction reduction of up to 31% was observed. Contrary to the microtextured specimens, the coated specimens did not fully reach the reference level but featured a significant friction decrease of at least 17% for all cam rotation speeds. As far as solid friction was concerned, these observations could be attributed to a lower coefficient of friction as measured in the dry ball-on-disk experiments and depicted in Figure 3a,b. However, the highest reduction was recorded in the medium speed range. Therefore, besides surface energy and spreading parameters of the lubricant, the shear-thinning effects induced by thermal insulation could also influence the fluid friction behavior. However, the relative friction reduction decreased at higher speed levels.

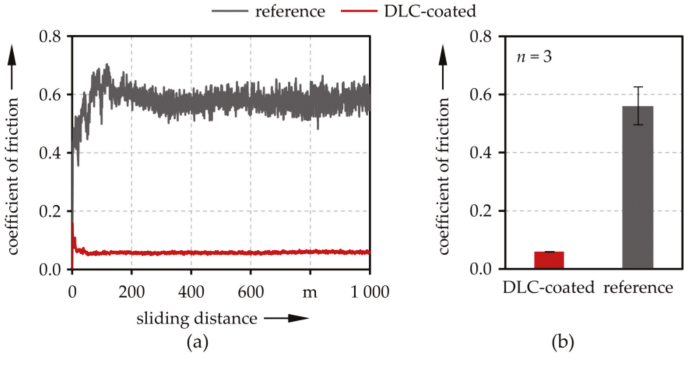

Figure 3. Coefficient of friction of the reference and DLC-coated specimens under dry conditions (**a**) over the sliding distance of one exemplary test-run and (**b**) as the averaged value.

3.2. Numerical Results

An overview of the computed friction force, which is normalized to the first speed level and divided into its fraction of solid and fluid friction, is shown in Figure 4a. Furthermore, the representative plots of the characteristic properties along the contact length at the medium speed level for the reference, the microtextured case, and the coated case, are provided in Figure 4b–d. Similar to the experiments, a

Stribeck-like decrease of total friction, as well as the declining fraction of solid friction and increasing fluid friction with cam rotation speed, was observed for all cases.

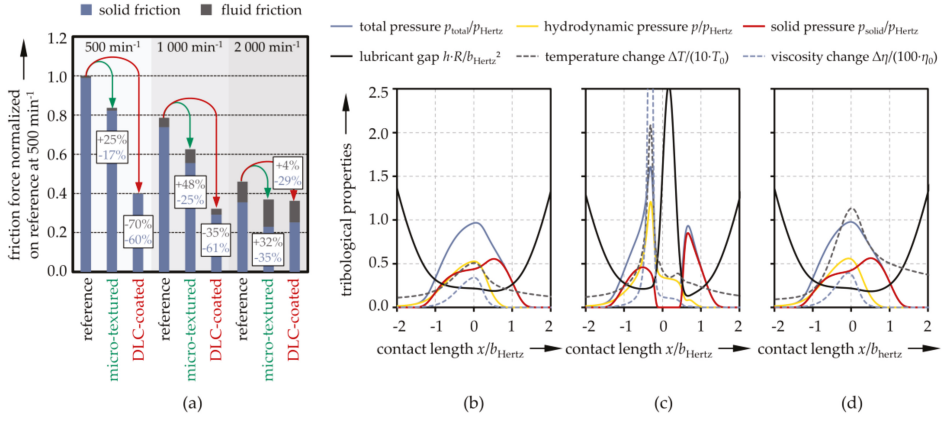

Figure 4. (**a**) Computed solid and fluid friction force for the reference, microtextured, and DLC-coated case, normalized total, hydrodynamic and solid contact pressure, lubricant gap, temperature, and viscosity change for the (**b**) reference, (**c**) microtextured, and (**d**) DLC-coated case.

The total friction reduction from microtexturing and amorphous carbon coating was pronounced more strongly at lower speed levels, as observed in the experiments. The first featured reduced solid friction and increased fluid friction. Besides a local constriction in the lubricant gap and an additional pressure increase, the trailing effects in the area behind the texture induced enlargement of the lubricant gap, thereby reducing the overall asperity contact and solid contact pressure. Similar to other studies reported in the literature, this could be explained by lubricant drawn out of the texture due to the elastic deformation and velocity differences of the rubbing surfaces [40], which increased the viscosity and built additional hydrodynamic pressure (Figure 4c). However, this also meant an increase in the fraction of fluid friction as the lubricant became more shear-resistant. At higher speed levels, despite the decreased solid friction, the reference and microtexturing converge due to the higher fluid friction of the latter. On the contrary, amorphous carbon coating could reduce both solid and fluid friction. The result was due to a lower solid friction coefficient of the coated surface and the thermal insulation effect. Therefore, the viscosity, and thus, the shear resistance of the lubricant was reduced due to a temperature increase (Figure 4d), which resulted from the lower thermal diffusivity of the coating. However, at higher speed levels, the amorphous carbon coating also approached the reference level due to the negative slide-to-roll-ratio. This outcome led to higher temperatures at the contact inlet, and thus, lower fluid film thickness. In turn, this might even lead to an increased fraction of fluid friction. Thus, the simulation results matched well with the literature and experimental observations. Slight quantitative discrepancies could be attributed, for example, to simplifications in modeling the TEHL cam/tappet-contact, such as the negligence of edge effects due to the 2D assumption, as well as deviations in the assumed material, coating, and fluid properties from the real ones.

4. Conclusions

Tribological cam/bucket tappet component tests were performed to determine the friction behavior of ultrashort pulse laser fabricated microtextures and PVD/PECVD deposited silicon-doped hydrogenated amorphous carbon coatings. Within the scope of this study, a significant friction reduction of over ten and up to thirty percent was achieved from microtexturing and amorphous carbon coating, respectively. Furthermore, TEHL tribo-simulations acted as a 'numerical zoom' into the contact area and contributed to the numerical explanation of the tribological behavior. It was shown

that microtexturing could reduce the fraction of solid friction while increasing fluid friction. The result was due to trailing effects with lubricant being emitted from the texture, locally increasing viscosity, enlarging the lubricant gap and reducing asperity contact. The effect resembled a counterclockwise tilt of the Stribeck curve. Contrarily, amorphous carbon coatings could reduce solid and fluid friction, which could be interpreted as a shift of the Stribeck curve to the lower left. This was due to lower dry friction and lower thermal inertia of the coating. It should be noted that the change in frictional behavior induced by the studied surface modifications was highly dependent on application conditions. For example, potentially positive effects could be consumed in the case of microtextured contacts with higher sliding speeds or in the case of amorphous carbon coatings in contacts with opposing moving surfaces at high velocities. Therefore, the TEHL simulations can be used as preliminary studies to estimate the effects of such surface modifications on the tribological behavior in each case. However, this study showed the potential of both microtexturing and the application of amorphous carbon coatings to improve the energy efficiency of the cam/tappet-contact in a wide range of rotational speeds. However, the results are certainly not limited to the investigated application in combustion engines, as the findings can also be considered for the optimization of other tribological contacts such as in electric vehicles.

Author Contributions: Conceptualization and methodology of experimental studies, M.M. and T.W.; Component tests and data analysis, M.M.; Specimen preparation and micro-texturing, M.M.; DLC-coating deposition, T.W.; Tribological and mechanical analysis, T.W.; Conceptualization and analysis of numerical studies, M.M.; Original draft preparation, M.M. and T.W.; Review and editing, S.T.; Supervision, project administration, and funding acquisition, S.T.

Funding: This research was funded partly by the German Federal Ministry for Economic Affairs and Energy (BMWi) under grant number 03ET1609H (PROMETHEUS), as well as partly by the German Research Foundation (DFG) under project SFB/TR 73 TP B4.

Acknowledgments: The authors greatly acknowledge the continuous support of the technical faculty and the mechanical engineering department of Friedrich-Alexander-Universität (FAU) Erlangen-Nürnberg, Germany. T. Häfner from Bayerisches Laserzentrum GmbH (BLZ) in Erlangen, Germany, is thanked for the microtexturing of the specimens. Furthermore, Ing U. Wolf from Engineering Design and Ing. B. Merle and S. Gabel, M.Sc. from the General Materials Properties Institute (all FAU Erlangen Nürnberg, Germany) are thanked for their assistance in the tribological characterization and FIB-preparation of the coating, respectively.

Conflicts of Interest: The authors declare no conflict of interest. The funders had no role in the design of the study; in the collection, analyses, or interpretation of data; in the writing of the manuscript, or in the decision to publish the results.

Nomenclature

a_c	Carreau parameter
a_{texture}	micro-texture amplitude
b_{Hertz}	Hertzian contact half-width
c_{P}	specific heat capacity
C	compliance matrix
d_{texture}	micro-texture distance
E	Young's modulus
E_{IT}	indentation modulus
F	normal force
F_{fluid}	fluid friction force
F_{solid}	solid friction force
g	zero level correction parameter
G_{c}	critical shear stress
h	lubricant gap
h_0	rigid body motion
H_{IT}	indentation hardness
l	cam width in y-direction

L	Moe's dimensionless material properties parameter
M	Moe's dimensionless load parameter
n_c	Carreau parameter
p	hydrodynamic pressure
p_{Hertz}	Hertzian contact pressure
p_{solid}	solid contact pressure
p_{total}	total contact pressure
R	equivalent radius
SRR	slide-to-roll ratio
u_1	sliding velocity of body 1
u_2	sliding velocity of body 2
u_m	mean hydrodynamic velocity
U_z	displacement in z-direction
t	time
T	temperature
$w_{texture}$	micro-texture width in x-direction
x, y, z	space coordinates
x_{start}	starting position of the micro-texture in x-direction
α_p	pressure viscosity coefficient
β_p	volume expansion coefficient
β_η	Roelands temperature viscosity coefficient
$\delta_{elastic}$	elastic deformation in z-direction
ε	strain tensor
η	lubricant viscosity
η_0	lubricant viscosity at reference state
λ	thermal conductivity
μ_{solid}	solid friction coefficient
ρ	density
σ	stress tensor of the equivalent body
τ_{zx}	shear stress
υ	Poisson's ratio
Ω	computational domain

References

1. Holmberg, K.; Andersson, P.; Erdemir, A. Global energy consumption due to friction in passenger cars. *Tribol. Int.* **2012**, *47*, 221–234. [CrossRef]
2. Kalghatgi, G. Is it really the end of internal combustion engines and petroleum in transport? *Appl. Energy* **2018**, *225*, 965–974. [CrossRef]
3. Serrano, J.R.; Novella, R.; Piqueras, P. Why the development of internal combustion engines is still necessary to fight against global climate change from the perspective of transportation. *Appl. Sci.* **2019**, *9*, 4597. [CrossRef]
4. Farfan-Cabrera, L.I. Tribology of electric vehicles: A review of critical components, current state and future improvement trends. *Tribol. Int.* **2019**, *138*, 473–486. [CrossRef]
5. Holmberg, K.; Erdemir, A. Influence of tribology on global energy consumption, costs and emissions. *Friction* **2017**, *5*, 263–284. [CrossRef]
6. Kalin, M.; Velkavrh, I.; Vižintin, J.; Ožbolt, L. Review of boundary lubrication mechanisms of DLC coatings used in mechanical applications. *Meccanica* **2008**, *43*, 623–637. [CrossRef]
7. Erdemir, A.; Donnet, C. Tribology of diamond-like carbon films: Recent progress and future prospects. *J. Phys. D Appl. Phys.* **2006**, *39*, R311–R327. [CrossRef]
8. Gropper, D.; Wang, L.; Harvey, T.J. Hydrodynamic lubrication of textured surfaces: A review of modeling techniques and key findings. *Tribol. Int.* **2016**, *94*, 509–529. [CrossRef]
9. Gachot, C.; Rosenkranz, A.; Hsu, S.M.; Costa, H.L. A critical assessment of surface texturing for friction and wear improvement. *Wear* **2017**, *372–373*, 21–41. [CrossRef]

10. Rosenkranz, A.; Grützmacher, P.G.; Gachot, C.; Costa, H.L. Surface texturing in machine elements—A critical discussion for rolling and sliding contacts. *Adv. Eng. Mater.* **2019**, *86*, 1900194. [CrossRef]
11. Grützmacher, P.G.; Profito, F.J.; Rosenkranz, A. Multi-scale surface texturing in tribology—Current knowledge and future perspectives. *Lubricants* **2019**, *7*, 95. [CrossRef]
12. Pettersson, U.; Jacobson, S. Textured surfaces in sliding boundary lubricated contacts—Mechanisms, possibilities and limitations. *Tribol. Mater. Surf. Interfaces* **2013**, *1*, 181–189. [CrossRef]
13. Löffler, M.; Andreas, K.; Engel, U.; Schulte, R.; Groebel, D.; Krebs, E.; Freiburg, D.; Biermann, D.; Stangier, D.; Tillmann, W.; et al. Tribological measures for controlling material flow in sheet-bulk metal forming. *Prod. Eng.* **2016**, *10*, 459–470. [CrossRef]
14. Borghi, A.; Gualtieri, E.; Marchetto, D.; Moretti, L.; Valeri, S. Tribological effects of surface texturing on nitriding steel for high-performance engine applications. *Wear* **2008**, *265*, 1046–1051. [CrossRef]
15. Etsion, I. Modeling of surface texturing in hydrodynamic lubrication. *Friction* **2013**, *1*, 195–209. [CrossRef]
16. Wos, S.; Koszela, W.; Pawlus, P. Tribological behaviours of textured surfaces under conformal and non-conformal starved lubricated contact conditions. *Proc. Inst. Mech. Eng. Part J J. Eng. Tribol.* **2015**, *229*, 398–409. [CrossRef]
17. Grabon, W.; Koszela, W.; Pawlus, P.; Ochwat, S. Improving tribological behaviour of piston ring–cylinder liner frictional pair by liner surface texturing. *Tribol. Int.* **2013**, *61*, 102–108. [CrossRef]
18. Evans, R.D.; Cogdell, J.D.; Richter, G.A.; Doll, G.L. Traction of lubricated rolling contacts between thin-film coatings and steel. *Tribol. Trans.* **2008**, *52*, 106–113. [CrossRef]
19. Kalin, M.; Polajnar, M. The wetting of steel, DLC coatings, ceramics and polymers with oils and water: The importance and correlations of surface energy, surface tension, contact angle and spreading. *Appl. Surf. Sci.* **2014**, *293*, 97–108. [CrossRef]
20. Kalin, M.; Polajnar, M. The effect of wetting and surface energy on the friction and slip in oil-lubricated contacts. *Tribol. Lett.* **2013**, *52*, 185–194. [CrossRef]
21. Björling, M.; Larsson, R.; Marklund, P. The Effect of DLC Coating Thickness on Elstohydrodynamic Friction. *Tribol. Lett.* **2014**, *55*, 353–362. [CrossRef]
22. Björling, M.; Habchi, W.; Bair, S.; Larsson, R.; Marklund, P. Friction Reduction in Elastohydrodynamic Contacts by Thin-Layer Thermal Insulation. *Tribol. Lett.* **2014**, *53*, 477–486. [CrossRef]
23. Björling, M.; Isaksson, P.; Marklund, P.; Larsson, R. The Influence of DLC Coating on EHL Friction Coefficient. *Tribol. Lett.* **2012**, *47*, 285–294. [CrossRef]
24. Bobzin, K.; Brögelmann, T.; Stahl, K.; Michaelis, K.; Mayer, J.; Hinterstoißer, M. Friction reduction of highly-loaded rolling-sliding contacts by surface modifications under elasto-hydrodynamic lubrication. *Wear* **2015**, *328–329*, 217–228. [CrossRef]
25. Elsharkawy, A.A.; Hamrock, B.J. EHL of Coated Surfaces: Part I—Newtonian Results. *J. Tribol.* **1994**, *116*, 29. [CrossRef]
26. Habchi, W. A numerical model for the solution of thermal elastohydrodynamic lubrication in coated circular contacts. *Tribol. Int.* **2014**, *73*, 57–68. [CrossRef]
27. Bobach, L.; Bartel, D.; Beilicke, R.; Mayer, J.; Michaelis, K.; Stahl, K.; Bachmann, S.; Schnagl, J.; Ziegele, H. Reduction in EHL Friction by a DLC Coating. *Tribol. Lett.* **2015**, *60*, 1270. [CrossRef]
28. Ebner, M.; Ziegltrum, A.; Lohner, T.; Michaelis, K.; Stahl, K. Measurement of EHL temperature by thin film sensors—Thermal insulation effects. *Tribol. Int.* **2018**, 105515. [CrossRef]
29. Choo, J.W.; Olver, A.V.; Spikes, H.A. The influence of transverse roughness in thin film, mixed elastohydrodynamic lubrication. *Tribol. Int.* **2007**, *40*, 220–232. [CrossRef]
30. Choo, J.W.; Olver, A.V.; Spikes, H.A.; Dumont, M.-L.; Ioannides, E. The Influence of Longitudinal Roughness in Thin-Film, Mixed Elastohydrodynamic Lubrication. *Tribol. Trans.* **2006**, *49*, 248–259. [CrossRef]
31. Ehret, P.; Dowson, D.; Taylor, C.M. Waviness Orientation in EHL Point Contact. In *The Third Body Concept Interpretation of Tribological Phenomena*; Elsevier: Amsterdam, The Netherlands, 1996; pp. 235–244. ISBN 9780444825025.
32. Venner, C.H.; Lubrecht, A.A. Numerical Simulation of a Transverse Ridge in a Circular EHL Contact Under Rolling/Sliding. *J. Tribol.* **1994**, *116*, 751. [CrossRef]
33. Cusano, C.; Wedeven, L.D. The Effects of Artificially-Produced Defects on the Film Thickness Distribution in Sliding EHD Point Contacts. *J. Lubr. Technol.* **1982**, *104*, 365. [CrossRef]

34. Ai, X.; Cheng, H.S. The Influence of Moving Dent on Point EHL Contacts. *Tribol. Trans.* **1994**, *37*, 323–335. [CrossRef]
35. Mourier, L.; Mazuyer, D.; Lubrecht, A.A.; Donnet, C. Transient increase of film thickness in micro-textured EHL contacts. *Tribol. Int.* **2006**, *39*, 1745–1756. [CrossRef]
36. Mourier, L.; Mazuyer, D.; Ninove, F.-P.; Lubrecht, A.A. Lubrication mechanisms with laser-surface-textured surfaces in elastohydrodynamic regime. *Proc. Inst. Mech. Eng. Part. J J. Eng. Tribol.* **2010**, *224*, 697–711. [CrossRef]
37. Krupka, I.; Hartl, M. The effect of surface texturing on thin EHD lubrication films. *Tribol. Int.* **2007**, *40*, 1100–1110. [CrossRef]
38. Krupka, I.; Vrbka, M.; Hartl, M. Effect of surface texturing on mixed lubricated non-conformal contacts. *Tribol. Int.* **2008**, *41*, 1063–1073. [CrossRef]
39. Rosenkranz, A.; Szurdak, A.; Gachot, C.; Hirt, G.; Mücklich, F. Friction reduction under mixed and full film EHL induced by hot micro-coined surface patterns. *Tribol. Int.* **2016**, *95*, 290–297. [CrossRef]
40. Marian, M.; Grützmacher, P.; Rosenkranz, A.; Tremmel, S.; Mücklich, F.; Wartzack, S. Designing surface textures for EHL point-contacts—Transient 3D simulations, meta-modeling and experimental validation. *Tribol. Int.* **2019**, *137*, 152–163. [CrossRef]
41. Beilicke, R.; Bobach, L.; Bartel, D. Transient thermal elastohydrodynamic simulation of a DLC coated helical gear pair considering limiting shear stress behavior of the lubricant. *Tribol. Int.* **2016**, *97*, 136–150. [CrossRef]
42. Ziegltrum, A.; Lohner, T.; Stahl, K. TEHL Simulation on the Influence of Lubricants on the Frictional Losses of DLC Coated Gears. *Lubricants* **2018**, *6*, 17. [CrossRef]
43. Kano, M. Super low friction of DLC applied to engine cam follower lubricated with ester-containing oil. *Tribol. Int.* **2006**, *39*, 1682–1685. [CrossRef]
44. Dobrenizki, L.; Tremmel, S.; Wartzack, S.; Hoffmann, D.C.; Brögelmann, T.; Bobzin, K.; Bagcivan, N.; Musayev, Y.; Hosenfeldt, T. Efficiency improvement in automobile bucket tappet/camshaft contacts by DLC coatings—Influence of engine oil, temperature and camshaft speed. *Surf. Coat. Technol.* **2016**, *308*, 360–373. [CrossRef]
45. Yu, C.; Meng, X.; Xie, Y. Numerical simulation of the effects of coating on thermal elastohydrodynamic lubrication in cam/tappet contact. *Proc. Inst. Mech. Eng. Part. J J. Eng. Tribol.* **2017**, *231*, 221–239. [CrossRef]
46. Meng, X.; Yu, C.; Xie, Y.; Mei, B. Thermal insulation effect on EHL of coated cam/tappet contact during start up. *Ind. Lubr. Tribol.* **2018**, *70*, 917–926. [CrossRef]
47. Gangopadhyay, A.; McWatt, D.G. The Effect of Novel Surface Textures on Tappet Shims on Valvetrain Friction and Wear. *Tribol. Trans.* **2008**, *51*, 221–230. [CrossRef]
48. Krupka, I.; Hartl, M.; Zimmerman, M.; Houska, P.; Jang, S. Effect of surface texturing on elastohydrodynamically lubricated contact under transient speed conditions. *Tribol. Int.* **2011**, *44*, 1144–1150. [CrossRef]
49. Marian, M.; Tremmel, S.; Wartzack, S. Microtextured surfaces in higher loaded rolling-sliding EHL line-contacts. *Tribol. Int.* **2018**, *127*, 420–432. [CrossRef]
50. Tremmel, S.; Marian, M.; Zahner, M.; Wartzack, S.; Merklein, M. Friction reduction in EHL contacts by surface microtexturing—Tribological performance, manufacturing and tailored design. *Ind. Lubr. Tribol.* **2018**, 0306. [CrossRef]
51. Marian, M.; Weikert, T.; Tremmel, S. Numerical and experimental studies on friction reduction by surface modification in TEHL contacts. In Proceedings of the STLE 2019—74th Annual Meeting and Exhibition of the Society of Tribologists and Lubrication Engineers, Nashville, TN, USA, 19–23 May 2019.
52. ISO 14577-1:2015. *Metallic Materials—Instrumented Indentation Test for Hardness and Materials Parameters—Part. 1: Test, Method*; International Organization for Standardization: Geneva, Switzerland, 2015.
53. Habchi, W.; Demirci, I.; Eyheramendy, D.; Morales-Espejel, G.; Vergne, P. A finite element approach of thin film lubrication in circular EHD contacts. *Tribol. Int.* **2007**, *40*, 1466–1473. [CrossRef]
54. Yang, P.; Wen, S. A Generalized Reynolds Equation for Non-Newtonian Thermal Elastohydrodynamic Lubrication. *J. Tribol.* **1990**, *112*, 631–636. [CrossRef]
55. Marian, M.; Weschta, M.; Tremmel, S.; Wartzack, S. Simulation of Microtextured Surfaces in Starved EHL Contacts Using Commercial FE Software. *Mater. Perform. Charact.* **2017**, *6*, 165–181. [CrossRef]
56. Liu, S.; Peyronnel, A.; Wang, Q.J.; Keer, L.M. An extension of the Hertz theory for 2D coated components. *Tribol. Lett.* **2005**, *18*, 505–511. [CrossRef]

57. Zhao, Y.; Maietta, D.M.; Chang, L. An Asperity Microcontact Model Incorporating the Transition from Elastic Deformation to Fully Plastic Flow. *J. Tribol.* **2000**, *122*, 86. [CrossRef]
58. Masjedi, M.; Khonsari, M.M. Film Thickness and Asperity Load Formulas for Line-Contact Elastohydrodynamic Lubrication With Provision for Surface Roughness. *J. Tribol.* **2012**, *134*, 11503. [CrossRef]
59. Habchi, W. *Finite Element Modeling of Elastohydrodynamic Lubrication Problems*; John Wiley & Sons Incorporated: Newark, NJ, USA, 2018; ISBN 978-1119225126.
60. Tan, X.; Goodyer, C.E.; Jimack, P.K.; Taylor, R.I.; Walkley, M.A. Computational approaches for modelling elastohydrodynamic lubrication using multiphysics software. *Proc. Inst. Mech. Eng. Part. J J. Eng. Tribol.* **2012**, *226*, 463–480. [CrossRef]
61. Lohner, T.; Ziegltrum, A.; Stemplinger, J.-P.; Stahl, K. Engineering Software Solution for Thermal Elastohydrodynamic Lubrication Using Multiphysics Software. *Adv. Tribol.* **2016**, *2016*, 1–13. [CrossRef]
62. Weschta, M. Untersuchungen zur Wirkungsweise von Mikrotexturen in elastohydrodynamischen Gleit/Wälz-Kontakten. Ph.D. Thesis, Friedrich-Alexander-Universität, Erlangen-Nürnberg, Germany, 2017. urn:nbn:de:bvb:29-opus4-91095.
63. Sadeghi, F.; Sui, P.C. Thermal Elastohydrodynamic Lubrication of Rolling/Sliding Contacts. *J. Tribol.* **1990**, *112*, 189–195. [CrossRef]
64. Bair, S. A Rough Shear-Thinning Correction for EHD Film Thickness. *Tribol. Trans.* **2004**, *47*, 361–365. [CrossRef]
65. Dowson, D.; Higginson, G.R. *Elasto-Hydrodynamic Lubrication*, SI ed.; Pergamon Press: Oxford, UK, 1977; ISBN 0080213022.

coatings

MDPI

Article

Mechanical Integrity of 3D Rough Surfaces during Contact

Maxence Bigerelle [1,*], Franck Plouraboue [2], Frederic Robache [1], Abdeljalil Jourani [3] and Agnes Fabre [4]

[1] Laboratory of Industrial and Human Automation Control, Mechanical engineering and Computer Science, LAMIH, UMR CNRS 8201, Université de Valenciennes, 59300 Valenciennes, France; frederic.robache@uphf.fr
[2] Institut de Mécanique des Fluides, UMR CNRS 5502, 31400 Toulouse, France; franck.plouraboue@toulouse-inp.fr
[3] Laboratoire Roberval, Université de Technologie de Compiègne, UMR 7337, 60200 Compiègne, France; abdeljalil.jourani@utc.fr
[4] Laboratoire MSMP, Arts et Métiers ParisTech, 13617 Aix-en-Provence, France; agnes.fabre@ensam.eu
* Correspondence: maxence.bigerelle@uphf.fr

Received: 30 October 2019; Accepted: 19 December 2019; Published: 25 December 2019

Abstract: Rough surfaces are in contact locally by the peaks of roughness. At this local scale, the pressure of contact can be sharply superior to the macroscopic pressure. If the roughness is assumed to be a random morphology, a well-established observation in many practical cases, mechanical indicators built from the contact zone are then also random variables. Consequently, the probability density function (PDF) of any mechanical random variable obviously depends upon the morphological structure of the surface. The contact pressure PDF, or the probability of damage of this surface can be determined for example when plastic deformation occurs. In this study, the contact pressure PDF is modeled using a particular probability density function, the generalized Lambda distributions (GLD). The GLD are generic and polymorphic. They approach a large number of known distributions (Weibull, Normal, and Lognormal). The later were successfully used to model damage in materials. A semi-analytical model of elastic contact which takes into account the morphology of real surfaces is used to compute the contact pressure. In a first step, surfaces are simulated by Weierstrass functions which have been previously used to model a wide range of surfaces met in tribology. The Lambda distributions adequacy is qualified to model contact pressure. Using these functions, a statistical analysis allows us to extract the probability density of the maximal pressure. It turns out that this density can be described by a GLD. It is then possible to determine the probability that the contact pressure generates plastic deformation.

Keywords: surface; roughness; failure analysis; contact modeling; statistic approach

1. Introduction

Surface integrities has been a growing field over the last 30 years. During contact, stress can induce fractures, scratches and micro-cracks influencing operational life, secular stability and coating quality [1–4]. Rough surfaces are locally and sparsely in contact, essentially at roughness peaks. At this specific scale, the contact pressure can be sharply superior to the apparent or macroscopic pressure. In numerous practical cases, the roughness is a random morphology. So it becomes obvious to integrate the surface morphology as a random process to compute the local pressures as a probability density function (PDF). Then, the probability of damage on the surface can also be computed from macroscopic material properties. Greenwood pioneered the first rough contact model in 1966 [5] on a pure elastic contact to explain that the real area of contact between asperities can be proportional to the load. One advantage of this model is that it becomes possible to measure macroscopic features

taking account some roughness parameters measurements. The rough surface is presented as a set of uncorrelated rough peaks with spherical tips of constant radius of curvature. Thus, for each asperity, Hertz's theories can be then applied. Greenwood assumed that the heights of the asperities varied randomly with known PDF without lack of generality but analyzed analytically and numerically the exponential and Gaussian PDFs. In his paper, roughness estimators used to compute these PDFs and PDF itself are considered as perfectly known i.e., adequation between the theoretical model fit perfectly with experimental data and estimator are supposedly known, meaning that there are calculated one an infinite surface. These two strong assumptions are intensively used in all modelling on rough surfaces (optics, mechanics, thermal, biology ...). However, four years after this pioneering work, Greenwood treated the problems of the first contact point of an asperity [6]. A sentence written marginally by Greenwood is of major interest: " ... *Some arguments arise from confusion between a sample and a population* ... " and points to the problems of sampling variations. For the first time (in Appendix A of Greenwood's publication) the extreme values theory is applied but restricted to the case when estimators of the parent distribution are perfectly known. Different distributions are discussed and the role of the spread of the distribution emphasised. It is pointed in this article that the first contact determination is experimentally a difficult task due to the lack of knowledge's of the reference point. About the remarks of T. R. Thomas, R. M. Baul and W. Scott, Greenwood recognized that more experimental evidence is needed on the tails of height distributions to settle the question of whether heights are truly Gaussian or not. In 1972, Tsakada et al. [7] introduce a method to determine the highest point of ground surfaces (the extreme value of surface roughness). As pointed by the authors, the probability density function of surface asperity has always been assumed to be a normal distribution. However, Tsakada showed the Weibull distribution gives a better approximation to characterize the extreme value of rough surfaces and estimate experimentally that the extreme value of surface asperity coincides with the value calculated by the Weibull distribution that represent one of the extreme statistics of PDF. Curiously, since Tsakada's article, it has become difficult over nearly four decades (1970–2010) to find in the bibliography an article presenting the relationships between extreme values of roughness and the problematic of contact mechanics. In 2009, Zwol et al. [8] showed that the point at which two random rough surfaces in a plate-plate contact takes place at the contact of the highest asperities and has a crucial importance for determination of dispersive forces. This uncertainty depends on the roughness of interacting bodies but authors no not used extreme values theory to model this effect. In 2012, Broer et al. [9] used explicity extreme values statistics to calculate the Casimir force at separations linked to the root-mean square of the height fluctuations of the two rough surfaces. Applied on gold samples, they showed the presence of peaks considerably higher than the root-mean-square roughness. These peaks redefine the minimum separation distance between the bodies and can be described by extreme value statistics. Ponthus et al. [10] show that the statistical properties of the normal motion's amplitude are well captured by a simple analytic model based on the extreme value theory framework, extending its applicability to sliding-contact-related topics. A complete analysis of extreme values applied on friction between rough surfaces is undertaken by Melekan and Rouhani [11]. They proposed a model based on extreme value statistics and combine it with different models for single-asperity contact, including adhesive and elasto-plastic contacts, to derive a relation between the applied load and the friction force on a rough interface. They show that extreme values probabilities of peak asperities can better fit the contact features of Greenwood models, closest to Amonton's law.

2. Materials and Methods

2.1. Simulation of Rough Surfaces

In a first step, surfaces are simulated using Weierstrass functions. A set of real surfaces are created presenting a wide range of surfaces met in tribology [12,13]. The three dimensional fractal Weierstrass surfaces are defined as [14]:

$$W(x,y) = A\sum_{n_1=0}^{\infty}\sum_{n_2=0}^{\infty} a_{n_1,n_2}\frac{\gamma^{\frac{n_1+n_2}{2}}}{\left(\gamma^{2n_1}+\gamma^{2n_2}\right)^{\frac{H+1}{2}}}cos(2\pi\gamma^{n_1}+\varphi_{n_1,n_2})cos(2\pi\gamma^{n_2}+\Psi_{n_1,n_2}) \quad (1)$$

where $\varphi_{n_1n_2}$ and $\Psi_{n_1n_2}$ are stochastic phases of uniform density defined in $[0, 2\pi]$.

A is a scale coefficient, a_{n_1,n_2} are normal random numbers, H is the Hölder exponent ($H \in [0, 1]$), γ is the frequency of the function with $\gamma > 1$.

The functions plotting for fractal dimension $\Delta = (2, 2.5, 3)$ i.e., $H = (1, 0.5, 0)$ are shown in Figure 1.

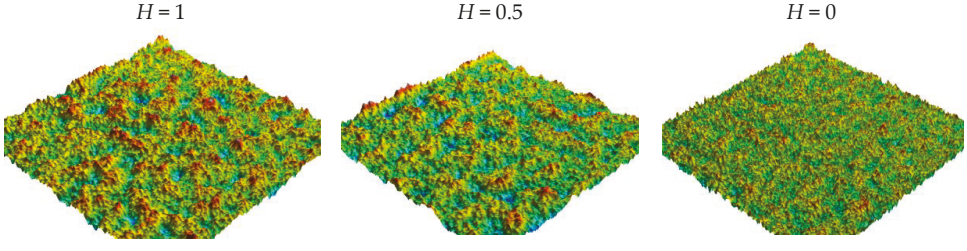

Figure 1. Simulated surfaces (1024 × 1024) following Weierstrass distribution with three different Hurst exponents (1, $\frac{1}{2}$, 0) from left to right.

2.2. Semi-Analytical Model

In this approach, a rough hard surface is in contact with a perfectly smooth rigid plane. In this case, local contacts are localized at the surface peaks. We consider the approximation of geometric contacts where elastic deformation between asperities is neglected.

2.2.1. Conical Model of Roughness

The roughness is modeled by a succession of indenters with a distribution of attack angles. Each asperity is described by a cone with a hemispherical end tip. The definition of the average deformation is introduced by taking into account the average attack angle of the roughness $\overline{\beta}$. The indentation by an axi-symmetrical indenter allows estimating the stresses and strains applied in the indented material. For conical tip geometry [15], the mean pressure is related to the attack angle β of the tip. Following the pressure supported by the summit, we can distinguish three regimes of deformation. In the case of an elastic contact, the mean pressure (mp) undergone by the asperity can be written [16]:

$$p_m = 0.2\, E^* tan\, \beta \quad (2)$$

where E^* stands for the combined Young's modulus of the two surfaces in contact given by $\frac{1}{E^*} = \frac{1-\nu_1^2}{E_1} + \frac{1-\nu_2^2}{E_2}$, E_j and ν_j are respectively the Young modulus and the Poisson' ratio relative to surface j.

2.2.2. Solution Procedure

The local behavior of each asperity is investigated numerically by the analysis of the local peak geometry. The local area of the contact A_j between an asperity j and the plane is assumed elliptic, having semi-axes a_j and b_j, A_j is given by:

$$A_j = \pi a_j b_j \quad (3)$$

For numerical purpose, the local area A_j is discretized into N elements c_{ji} ($i = 1, 2, \ldots N$). The local pressure distribution on each asperity j, is given by:

$$p_j = \left(x_i, y_j\right) = \frac{3}{2} p_{jm} \left[1 - \left(\frac{x_i}{a_j}\right)^2 - \left(\frac{y_i}{b_j}\right)^2\right]^{1/2} \tag{4}$$

where p_{jm} is the mean pressure associated with asperity j. The normal force F_j exerted on the asperity j is given by the following relation:

$$F_j = \sum_i c_{ji} p_i \tag{5}$$

The total load supported by summits is thus:

$$F = \sum_{j=1}^{m} F_j \tag{6}$$

where m is the total number of asperities in contact.

Figure 2 is a flowchart for the contact calculation program. The three-dimensional surface topography is directly sampled by the computer-generated surface topography.

The surface topography is characterised by N × M points. Each point of the coordinates (x,y) has a height z. Data are saved in binary format and are used as input for a three dimensional surface topology detection algorithm [17,18]. The latter is used to determine the position and the peak of each asperity. For each point i located at (x_i,y_i) of amplitude z_i (denoted by $z_i(x_i,y_i)$), the difference $\Delta z(x_i,y_i)$ = $z_i(x_i,y_i) - z(x_s,y_r)$ is calculated and compared to the heights of the eight neighboring points in the Cartesian grid where $s = i - 1, i, i + 1$ and $r = j - 1, j, j + 1$. If all $\Delta z(x_i,y_i) > 0$, $z(x_i,y_j)$ will be regarded as the asperity peak.

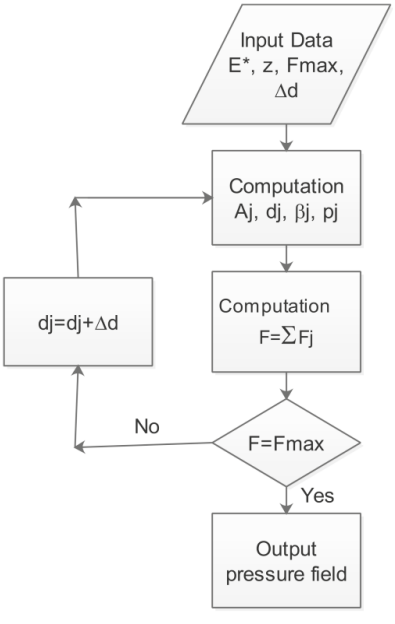

Figure 2. Flowchart for the numerical calculation of the pressure field.

For a given initial separation d, the local displacement d_j, the local contact area A_j, and the average attack angle β_j of each asperity can be determined. These parameters allow the distribution of the pressure and the real contact area undergone by the roughness to be determined. For a macroscopic displacement, the two surfaces are progressively brought to contact with several displacement

increments Δd of the smooth rigid plane. The displacement is interrupted when the resulting effort F reaches the imposed normal effort F_{MAX} (i.e., the convergence of the numerical software is reached).

2.2.3. Pressure Distribution

The model is applied on the three surfaces defined on Figure 1. The macroscopic pressure is equal to P_m = 20 MPa, using Young modulus E = 210 GPa. Surface are normalized such with their r.m.s. roughness R_q = 50 µm on a 1 mm^2 surfaces discretized over 1024 points in each direction. Figure 3 represents the pressure distribution for the three surfaces, respectively, described in the Figure 1.

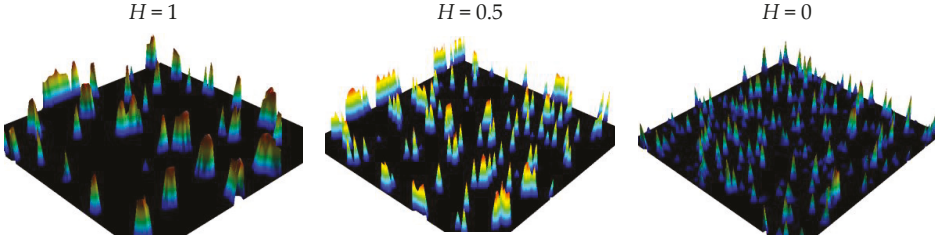

Figure 3. Results of the pressure distribution for the three surfaces described in Figure 1 with 3 Hurst exponents.

3. Results

3.1. Probability Density Functions (PDFs)

As described in the introduction, the pressure is stochastic. Its PDF depends on the roughness's PDF. In our case, we decide to directly model the pressure without taking account directly the roughness in the computation. Taking the pressure map, pressure distribution is supposed to be stationary in the spatial scale. This means that peaks morphology do not depends on space in average. Under these conditions, the probability density function do not depends on positions x and y and thus becomes one-dimensional. However this probability density function can be split into two parts. Let α be the probability to meet a zero pressure (no contact) then the probability of meeting a non-zero pressure is equals to $1 - \alpha$. The PDF can be written:

$$\mathrm{PR}(p) = \alpha\delta_{p=0} + (1-\alpha)G(p) \tag{7}$$

$\delta_{p=0}$ is the Dirac function localized on $p = 0$, and $G(p)$ is the PDF associated with continuous non zero pressure.

In practice, only $G(p)$ is required to compute the contact pressure. Moreover, primary hypotheses linked to spatial homogeneity of date are problematic to evaluate. Furthermore, the selection of PDF is frequently associated to the authors' modelling backgrounds or the suitability of the PDF to adjust adequately the data under study. Moreover, the retained distributions are poorly compared between others distributions and rarely checked by statistical tests of goodness of fit. In this paper, the maximum pressure PDF, a major interest in contact mechanics, will be modelled which is why the statistics of the extreme value theory will be applied. However, the application of classical extreme value analysis could have significant limits. As the most commonly used Gumbel and Generalized Extreme Value (GEV) methods [19] include inferred parental PDF constrained by mathematical assumptions, we suggest another way to circumvent the need for a priori hypothesis.

Our approach is a combination of the Generalized Lambda Distribution (GLD) and the Computer-Based Bootstrap Method (CBBM). Unlike the Gumbel and GEV models, which incorporate the statistical properties of the parent PDF, the GLD and the CBBM both have the common benefit of bypassing the preconceived choice of a well-known theoretical PDF that would approximate the physics of contact mechanisms.

It should be noted that GLD's are extremely flexible due to their capacity to adopt a wide spectrum of shapes, including common unimodal distributions. GLD's are defined by four parameters and can thus correspond to the first four moments of the experimental data (mean, variance, asymmetry, kurtosis) and also include asymptotic properties on the extreme values (tails extended to infinity or truncated, on either or both sides).

In the field of surface integrities, there are a multitude of known statistical distributions that model, using more or less well-founded simplifying assumptions, the damage mechanisms. For example, the normal law is often used to model static mechanical properties (stiffness, plasticity), Weibull's laws for cumulative damage mechanisms (fatigue, corrosion), lognormal laws the distribution of defects (porosity density), Gumbel's law the distribution of critical defects (pitting), Pareto's law the fracture values at interfaces (toughness) and all these distributions are well model by GLD [20,21]. The quality of fit obtained with the GLD's is especially notable in the region of the right tail of the empirical PDF, which is of interest to the extreme values of the pressure distribution described in this paper. For several years, one of the author of the present paper has been developing the use of this flexible family of PDF in the field of Materials Science [22–24] and also in Statistical Process Control [25,26].

The principle of statistical modelling of extreme contact pressures is a four-step process. In the first step, the distribution of contact pressures is modelled by the semi-analytical model for calculating local pressures corresponding to an experimental distribution of n pressure values. In a second step, a bootstrap (CBBM) is applied to generate a large number of k sets of n pressure data. In a third step, k GLD are modeled from the k^*n bootstrapped data. Finally (step 4), for each of the k GLD, the extreme values are estimated and the histogram of extreme values (probability density of extreme values) is constructed. From this empirical density, the mean of the maximum pressure and a 90% confidence interval can be estimated.

3.1.1. Basic Concept

The GLD family is specified in terms of its inverse distribution function with four parameters (λ_1, λ_2, λ_3 and λ_4):

$$Q_X(y) = \lambda_1 + \frac{y^{\lambda_3} - (1-y)^{\lambda_4}}{\lambda_2} \tag{8}$$

The parameters λ_1 and λ_2 are, respectively, the location and scale parameters, while λ_3 and λ_4 are related respectively to the skewness and the kurtosis of the GLD with $0 \le y \le 1$ (see [25,26] for details). The PDF $f_x(x)$ is obtained from the inverse distribution function of Equation (8):

$$f_x(x) = \frac{\lambda_2}{\lambda_3 y^{\lambda_3 - 1} + \lambda_4 (1-y)^{\lambda_4 - 1}} \tag{9}$$

where y is the solution of the equation $Q_X(y) = x$ which can be solved numerically.

Equation (9) defines a valid PDF if and only if Q_X meets the following conditions:

$$\begin{cases} f_x(x) \ge 0, \forall x \in D \\ \int_{-\infty}^{+\infty} f_X(x)dx = 1 \end{cases} \tag{10}$$

where D is the domain of definition of Q_X.

3.1.2. Numerical Estimation of Pressure PDF

An algorithm was developed using the Statistical Analyses System (SAS) language to compute the GLD parameters from an experimental dataset (in our study, *moment method* is used). Applied on the pressure described on Figure 3, the value of λ_1, λ_2, λ_3, λ_4 are computed from the four moment estimators $\hat{\alpha_1}$, $\hat{\alpha_2}$, $\hat{\alpha_3}$, $\hat{\alpha_4}$ (Table 1).

Table 1. Values of the fourth moments and the generalized Lambda distribution (GLD) parameters for the three pressure corresponding to the Hurst exponent of $H = 0$, 0.5 and 1 (Figure 3).

	Moments				GLD Parameters			
H	$\hat{\alpha_1}$	$\hat{\alpha_2}$	$\hat{\alpha_3}$	$\hat{\alpha_4}$	λ_1	λ_2	λ_3	λ_4
1	1108	213	0.687	3.03	1307	9.2×10^{-4}	0.276	0.032
0.5	1369	199	0.702	3.41	1509	8.1×10^{-4}	0.181	0.041
0	1724	193	0.874	5.62	1789	2.6×10^{-4}	−0.018	−0.034

Figure 4 presents the PDF of the GLD corresponding to the PDF of contact pressure computed from surface topography (Figure 3, Table 1). GLD fits very well contact pressure computed from experimental surface topography.

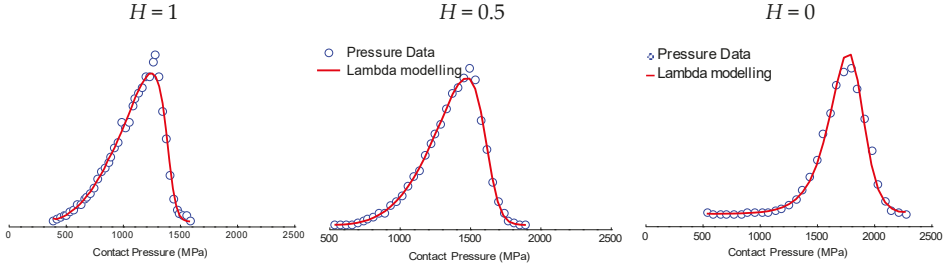

Figure 4. Plots of the GLD probability density functions and empirical histograms parameters for the three local pressures corresponding to the Hurst exponent of $H = 0$, 0.5 and 1.

3.1.3. Bootstrap Protocol

Efron [27,28] introduced first the Computer-Based Bootstrap Method (CBBM) to avoid the risk of asserting wrong conclusions when analysing experimental data that transgress inference assumptions of the traditional statistical theory. A main reason for making parametric assumptions is to facilitate the derivation from textbook formulae for standard errors. Based on the mathematical resampling technique, the main principle of the CBBM consists in generating a high number B of simulated bootstrap samples from the original data points. The original dataset consists of either experimental or simulated points. A bootstrap dataset of pressures of size n, noted (p^*_1, p^*_2, … , p^*_n), is a collection of n values simply obtained by randomly sampling with replacement from the original pressure data (p_1, p_2, … , p_n), each of them with a probability of $1/n$. The bootstrap dataset thus consists of elements of the original data points; some appearing zero times, some appearing once, some twice, etc.

Applied on the surface $H = 0.5$, probability density functions of Lambda coefficients can be plotted (Figure 5).

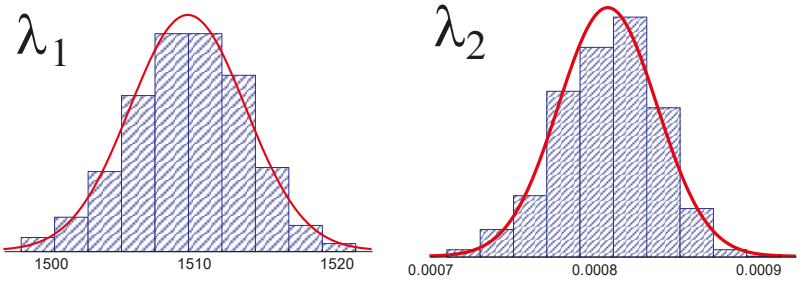

Figure 5. *Cont.*

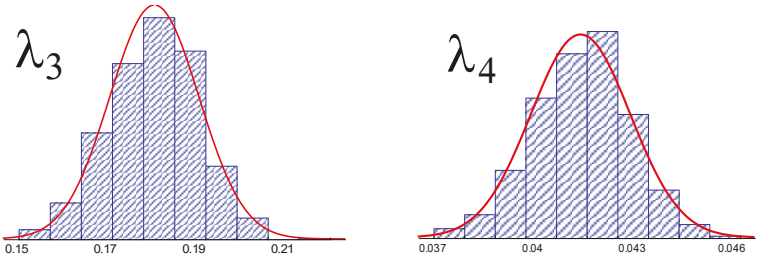

Figure 5. Plots of the probability density functions of the four GLD parameters obtained from 1000 bootstraps for the Hurst exponent of $H = 0.5$.

3.2. Maximal Pressure Probability Density Functions

3.2.1. Formulation

The density function, P_{max}, of the maximal pressure distribution corresponding to the GLD (Equation (8)) is given by the inverse distribution function of this distribution, Q_{max}:

$$Q_{max}(v) = \lambda_1 + \frac{\left(v^{1/n}\right)^{\lambda_3} - \left(1 - v^{1/n}\right)^{\lambda_4}}{\lambda_2} \tag{11}$$

With density function, f is:

$$f(x) = \frac{1}{Q'_{max}(F(x))} \tag{12}$$

where Q' is the derivative of Q and F the cumulative distribution function (CDF) of the Q PDF (i.e., $F = Q^{-1}$). Thus, the P_{max} function is evaluated for any pressure value x by numerically inverting the Q_{max} function as well as the density function P_{max}. To plot the P_{max} function, one first computes the quantile function Q_X with set of y lying in [0, 1] interval. The probability to have a maximal pressure less than $f\left(p_l^{max}\right)$ then equals $\Pr\left(p < p_l^{max}\right) = y^n\left(p_l^{max}\right)$. To obtain the density function $f\left(p_l^{max}\right)$, one can finally numerically derive:

$$f\left(p_l^{max}\right) = \frac{\partial y}{\partial y^n\left(p_l^{max}\right)} \tag{13}$$

As it can be observed on Figure 6, when the fractal dimension of the surface increases, the maximal local pressure increases. This is due to the fact that peaks become smaller for low Hurst exponents which drastically increase the local pressure and then the local probability of damage. Bowden and Tabor [29], assumed that in order for the bodies to slide relative to each other, the asperities are plastically deformed; i.e., the mean pressure corresponds to its hardness (and also near three times the yield pressure of the material). If one supposes for example that the hardness of the material is equal to 2050 MPa, then for $H = 1$, the probability of damage is impossible, for $H = 0.5$ this probability is equal to 1% and for $H = 0$ the probability of surface damage is one meaning that damage is certain.

3.2.2. Numerical Validation

To validate the proposed protocols, one hundred surfaces are simulated and the experimental extreme values are extracted and compared to the PDF distributions of the maximal pressure. The Figure 7 represents the 90% confidence intervals of modeled data by the Lambda distribution versus the experimental values.

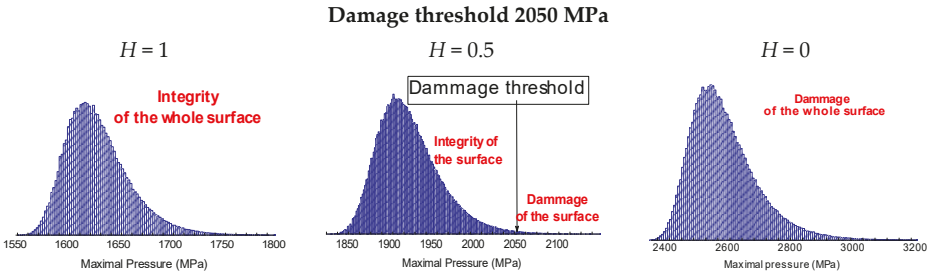

Figure 6. Plots of the GLD probability density functions and empirical histograms parameters for the three local maximal pressures corresponding to the Hurst exponent of H = 0, 0.5 and 1.

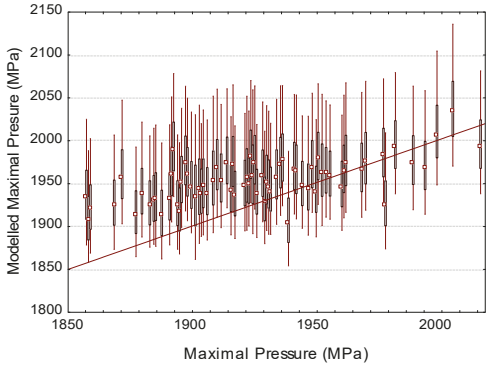

Figure 7. The 90% confidence intervals of modeled data by the Lambda distribution for the maximal pressure versus the pressure data values. The straight line represents y = x.

If the lambda distribution correctly fits the data, then the difference between the experimental data will be statistically equal to zero. To appreciate this hypothesis, the histograms of these differences are plotted for 100 surfaces (Figure 8). As is often the practice in statistics, the threshold of 95% is chosen to test the null value of the difference. Over all the one hundred surfaces, the null values is never rejected meaning that the lambda distribution describe correctly the extreme surface pressure.

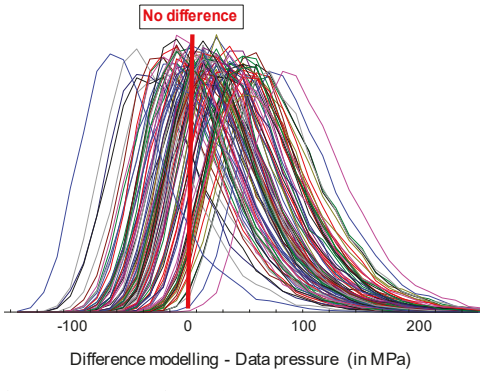

Figure 8. The 90% confidence intervals of modeled data by the Lambda distribution for the maximal pressure versus the values predicted by the local contact model.

4. Experimental Validation

It is quite problematic to validate the proposed model experimentally. Indeed, the principle of our modeling of extreme pressure values is to look at the distribution of local pressures obtained from discretized mapping, then to search a polymorphic density model that then allows us to evaluate extreme pressure value. This extreme pressure value then gives a lower limit of the yield strength of the future material guaranteeing no plasticification on the investigated contact area. In our simulation, in order to stabilize the high variability of the probability density of pressures, 100 contact simulations are performed to determine a robust density of the GLD parameters of the contact pressures and its associated bootstrap estimators (see Figure 5). Numerically the convergence and robustness seem to be achieved with these 100 simulations on 100 different topographies. This clearly shows that it is necessary, in order to validate the proposed model, to perform 100 plane/contact surface indentation experiments, which will then give us a correct estimate of the maximum plastification stress. It should be noted that in the bibliography, many authors limit themselves to measuring only one surface to determine the average contact pressure, which cannot be enough to determine the maximum contact pressure. The experimental determination of extreme values will, therefore, require an automated process of plane/rough surface indentation. Indentations experiments will not directly estimate local contact pressure, but an average pressure and an estimate of the first contact of the peak of maximum amplitude and its spatial location. Beyond this metrological problem, another problem, often encountered in the bibliography proposing plane/rough surface indentation is the difficulty of morphologically quantifying whether a peak has plastified. Admittedly, if the surface has a fairly high percentage of plastified peaks, it becomes possible to estimate statistically the rate of plastification (Dowson reference), but it remains difficult to determine experimentally the peak that has the first plastified (flatness problem, elastic return, metrological errors of the topographic measurement . . .).

However, it is essential to validate the proposed methodology. In fact, our model is based on the probability of having the first peak that plastifies and to associate its contact pressure. The criticisms of our methodology that can be formulated are on the one hand, a simplistic model of contact simulation (justified by the large number of high-resolution simulations, discretization necessary to capture the morphology of the highest peaks) and on the other hand the difficulty of validating this methodology by a reasoned approach. To have a less critical modeling of the material's behavior, finite element simulation seems tempting but remains complex at the level of elementary numerical operations. Even if this would prove possible in a reasonable time of calculations with the resolutions proposed in this article, it would prohibit us from future investigations on larger topographic resolutions (e.g., multi-fractal surfaces). Therefore, it is necessary to validate our approach without having to simulate our methodology by replacing our semi-analytical calculation with an MEF method. It is therefore necessary to build a methodology independent of the contact simulation method to validate the plasticification of extreme roughness and to associate them with a localized contact pressure without recourse to numerical calculation. For this purpose, we will have recourse to the nano-indentation test with of a Berkovich indentor. The nano-indenter continuously monitors the evolution of the tip depression with the indentation charge during the charging and discharging phases to observe the plastic and elastic response of the material. The tip used on our equipment is a Berkovich tip (pyramidal geometry with a triangular base). The indenter Berkovich is a three-sided pyramid, whose base is an equilateral triangle. The faces have an inclination of 65.3° with respect to the vertical axis. This homothetic geometry, therefore, makes it easy to identify the plasticized area by indentation. This homothetic geometry therefore makes it easy to identify morphologically the plastic area. A sample of the TA6V (MTS NanoIndentor) previously polished with 80 grade abrasive paper to obtain a rough surface is indented. Then the indentation print is recorded by atomic force microscopy (Bruker). Figure 9 (left) shows the topography where the angles of the indenter in plastic contact are visible. The non-indentated roughness has an Sa of 36 nm and the side of the impression in contact is equal to 18 µm.

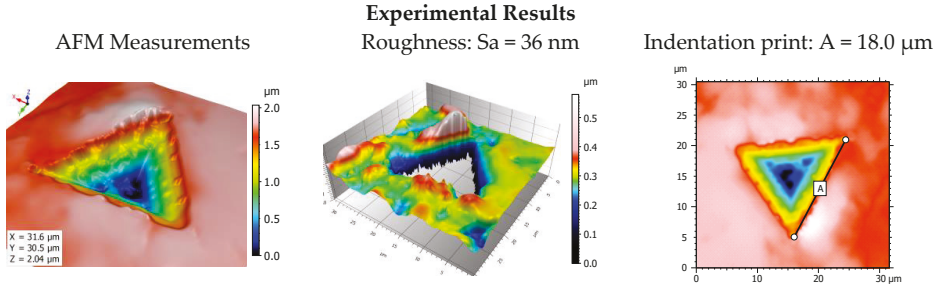

Figure 9. Nano-Indentation of TA6V samples (**left**), roughness extraction (**center**), indentation print measurements (**right**).

To carry out the simulation, we calculated the fractal dimension as well as the roughness (Sq), it was then possible to simulate a rough surface with the same property. Note that the summation of the function is limited in high frequencies to represent the beginning of the fractal regime of the roughness measured by AFM. Then the nano indentation test was simulated by an elasto-plastic model. Figure 10 shows the simulation of the indentation on the simulated rough surface (plastic zone is raised on the topographical map). The Sa of the simulated surface is closed to the experimental surface (Sa = 38 nm against Sa = 36 nm). This result shows that topographical simulation by the Weierstrass function leads to realistic rough surfaces. The elasto-plastic simulation shows a similar value on the indentation length 17 µm which validates our simulation model approach.

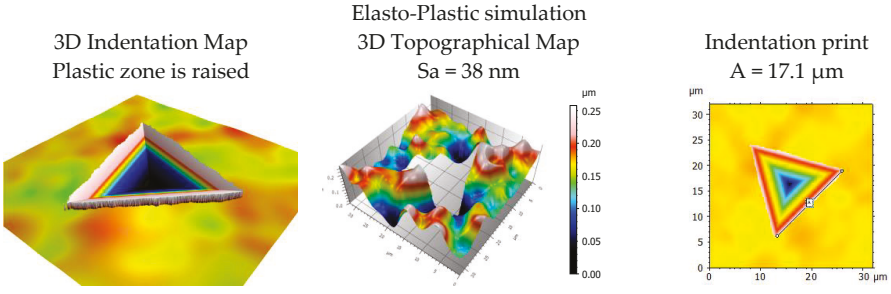

Figure 10. Elasto-plastic simulation of TA6V material (**left**). To visualize the plastified area and frontier elastic/plastic deformations, the plastic area is raised through the elastic area. At the **center**, roughness extraction simulated by the 3D Weierstrass function and indentation print of simulated indentation print is shown on the **right**.

We will then postulate that at the elastoplastic transition boundary (see Figure 11 left) the pressure field is continuous due to the given shape between the surface and the indenter. This means that this boundary defines the transition zone and, therefore, the contact pressure is equal to the elastic limit of the materials. As a result, this boundary topography allows us to calculate the probability density function of asperities height at the beginning of plasticification. Figure 11 (center) represents this probability density function for the simulated and experimental plasticification frontiers for a given roughness height. As can be observed, the densities between the experimental and simulated measurement are quite close. It then becomes possible to determine the probability density of surface integrity (Figure 11, right). The experimental and simulated data are consistent, which validates the robustness of the simulation on a rough surface to detect local areas of first plastification.

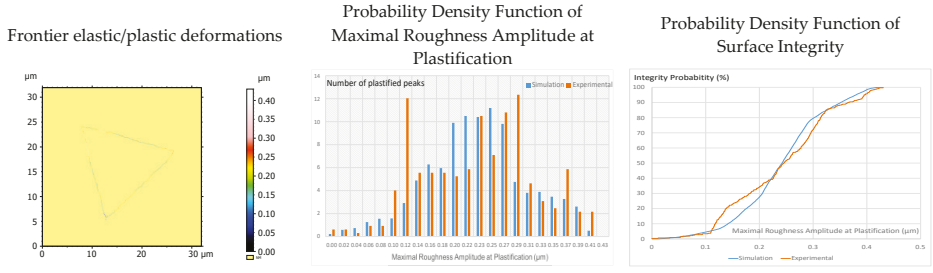

Figure 11. Frontier elastic/plastic deformations from elasto-plastic simulation of TA6V material (**left**). Probability density function of maximal roughness amplitude at plastification obtained from both simulated and experimental nano-indentations (**center**). Probability density function of surface integrity (**right**). 100% of integrity means that pass over a maximal peak amplitude of 0.43 µm, no plastification will occur).

5. Conclusions

In this paper, we proposed and exposed the principle of a statistical workflow to be applied to the analysis of rough surfaces in order to predict the statistics of contact pressure from roughness analysis. By means of the proposed functions, a statistical protocol allows us to extract the density of probability of the maximal pressure of a rough surface. This estimate is based upon a classical hypothesis of local elastic response of roughness peaks. The detailed validation of the proposed methodology could either involve contact pressure experimental measurements or numerical simulations taking into account the elastic interactions between peaks in future developments. The probability density of local contact pressure is described well by a GLD density function. Then, it is possible to determine the probability that the pressure of contact generates a plastic deformation from the analysis of the roughness statistics. The proposed methodology has been applied to numerically generated surfaces, but could also be adapted to the topography analysis of experimental ones. The influence of the sample size on this probability distribution variation can then be taken into account. From a statistical consideration, it should then become possible to plan the failure density of probability at a higher scale than the one use for scanning the sample. However, the uncertainties of measurements must be integrated to build a reliable probability density function of failure. The more experimental scanned surfaces, the better the prediction. Conversely, if the number of scanned surfaces is too weak, the elastic limit of the material must be increased to guarantee, with a fixed probability, the integrity of the structure, in order to get no damage of the structure by plastic deformation. The choice of the number of surfaces to be measured will become a compromise between the cost of the measure, the charge of the over-quality and the failure price. The workflow proposed in this paper, could contribute to finding the best traid-off and search for an optimal strategy in material elaboration.

Author Contributions: Conceptualization, Funding Acquisition, Writing and Formal Analysis, M.B.; Software, A.J.; validation, A.F.; investigation, F.P.; Nano Indentation and AFM measurements, F.R. All authors have read and agreed to the published version of the manuscript.

Funding: This research was funded by The ELSAT2020 project, co-financed by the European Union with the European Regional Development Fund, the French state and the Hauts de France Region.

Conflicts of Interest: The authors declare no conflict of interest.

Appendix A. The MultiScale Formulation of the Probability of Failure

The probability of failure will depends of the apparent surface area. If a one increases area, one increases the probability of having a higher pressure. If one suppose that the surface is ergodic, then double the surface area is equivalent to double the number of points of pressure in the pressure lambda

PDF that stay unchanged according to ergodicity assumption. However, the extreme value PDF that depends on the number of sample points will change and becomes:

$$\Pr\left(p < p_l^{max}\right) = y^{kn}\left(p_l^{max}\right) \tag{A1}$$

where $k > 0$ is the surface magnification factors, i.e., the predicted surfaces such $S = kS_0$ where $S = kS_0$ is the initial surface from which pressure PDF is evaluated.

Let $\Pr(S_0, k, P_d)$ the probability of surface integrities, then one computes by integration on the initial PDF that is $y(P_d)$ and one finally get the multiscale PDF of surface integrities:

$$Ln(\Pr(S_0, k, P_d)) = nkLn(y(P_d)) \tag{A2}$$

The Figure A1 (left) represents the multi-scale probabilities function of surface integrity versus surface area. This means that increasing the area of investigation compared to initial area increase the probability to find a higher maximal pressure. It becomes then possible to predict the maximal pressure assuring the integrity of a fixed area at a critical level α with only a measure on a lower surface area (Figure A1 right).

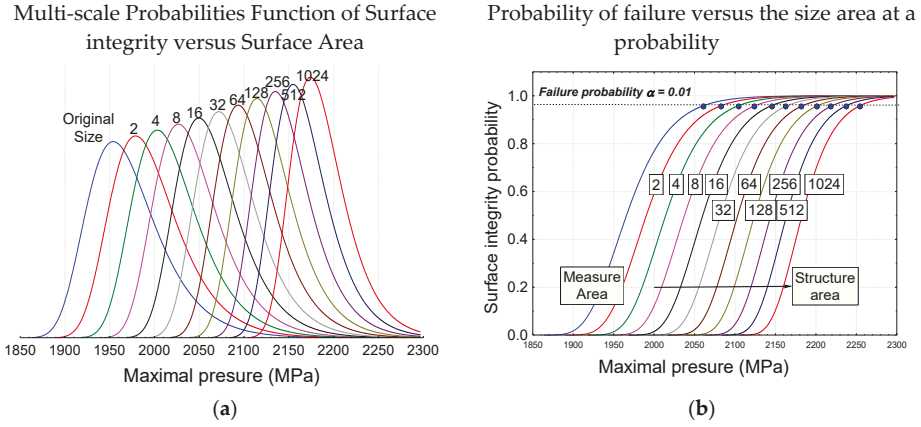

Figure A1. (**a**) Multi-scale Probabilities Function of Surface integrity versus Surface Area; (**b**) Probability of failure versus the size area at a probability.

References

1. Shen, J.; Liu, S.; Yi, K.; He, H.; Shao, J.; Fan, Z. Subsurface damage in optical substrates. *Opt. Int. J. Light Electron Opt.* **2005**, *116*, 288–294. [CrossRef]
2. Fine, K.R.; Garbe, R.; Gip, T.; Nguyen, Q. Non-destructive, real time direct measurement of subsurface damage. In Proceedings of the SPIE, Orlando, FL, USA, 19 May 2005; Volume 5799, pp. 105–110.
3. Stolz, C.J.; Menapace, J.A.; Schaffers, K.I.; Bibeau, C.; Thomas, M.D.; Griffin, A.J. Laser damage initiation and growth of antireflection coated S-FAP crystal surfaces prepared by pitch lap and magnetorheological finishing. In Proceedings of the SPIE, Boulder, CO, USA; 2005; Volume 5991, pp. 449–455.
4. Campbell, J.H.; Hawley-Fedder, R.A.; Stolz, C.J.; Menapace, J.A.; Borden, M.R.; Whitman, P.K.; Yu, J.; Runkel, M.; Riley, M.O.; Feit, M.D.; et al. NIF optical materials and fabrication technologies: An overview. In Proceedings of the SPIE, San Jose, CA, USA, 28 May 2004; Volume 5341, pp. 84–101.
5. Greenwood, J.A.; Williamson, J.P. Contact of nominally flat surfaces. In Proceedings of the Royal Society of London; Series A, Mathematical and Physical Sciences. Royal Society: London, UK, 1966; Volume 295, pp. 300–319.
6. Greenwood, J.A.; Tripp, J.H. The contact of two nominally flat rough surfaces. *Proc. Inst. Mech. Eng.* **1970**, *185*, 625–633. [CrossRef]

7. Tsukasa, T.; Anno, Y.; Fumio, K. Analysis of the deformation of contacting rough surface. *Bull. JSME* **1972**, *15*, 982–1003. [CrossRef]
8. Van Zwol, P.J.; Svetovoy, V.B.; Palasantzas, G. Distance upon contact: Determination from roughness profile. *Phys. Rev. B Condens. Matter Mater. Phys.* **2009**, *15*, 996–1003. [CrossRef]
9. Broer, W.; Palasantzas, G.; Knoester, J.; Svetovoy, V.B. Roughness correction to the Casimir force at short separations: Contact distance and extreme value statistics. *Phys. Rev. B Condens. Matter Mater. Phys.* **2012**, *85*, 155410. [CrossRef]
10. Ponthus, N.; Scheibert, J.; Thøgersen, K.; Malthe-Sørenssen, A.; Perret-Liaudet, J. Statistics of the separation between sliding rigid rough surfaces: Simulations and extreme value theory approach. *Phys. Rev. E* **2019**, *99*, 023004. [CrossRef] [PubMed]
11. Malekan, A.; Rouhani, S. Model of contact friction based on extreme value statistics. *Friction* **2019**, *7*, 327–339. [CrossRef]
12. Bigerelle, M.; Najjar, D.; Iost, A. Multiscale functional analysis of wear: A fractal model of the grinding process. *Wear* **2005**, *258*, 232–239. [CrossRef]
13. Bhushan, B.; Majumdar, A. Elastic-plastic contact model for bifractal surfaces. *Wear* **1992**, *153*, 53–64. [CrossRef]
14. Lopez, J.; Hansali, G.; Le Bossa, J.C.; Mathia, T. Caractérisation fractale de la rugosité tridimensionnelle d'une surface. *J. Phys. III* **1994**, *4*, 2501–2519. [CrossRef]
15. Jourani, A.; Dursapt, M.; Hamdi, H.; Rech, J.; Zahouani, H. Effect of the belt grinding on the surface texture: Modeling of the contact and abrasive. *Wear* **2005**, *259*, 1137–1143. [CrossRef]
16. Johnson, K.L. *Contact Mechanics*; Cambridge University Press: Cambridge, UK, 1985.
17. Jourani, A.; Bigerelle, M.; Petit, L.; Zahouani, H. Local coefficient of friction, sub-surface stresses and temperature distribution during sliding contact. *Int. J. Mater. Prod. Technol.* **2010**, *38*, 44–56. [CrossRef]
18. Jourani, A.; Hagege, B.; Bouvier, S.; Bigerelle, M.; Zahouani, H. Influence of abrasive grain geometry on friction coefficient and wear rate in belt finishing. *Tribol. Int.* **2013**, *59*, 30–37. [CrossRef]
19. Gumbel, E.J. *Statistical Theory of Extreme Values and Some Practical Applications*; Applied Mathematics; National Bureau of Standards: Washington, DC, USA, 1954.
20. Karian, Z.A.; Dudewicz, E.J. *Fitting Statistical Distributions: The Generalized Lambda Distribution and Generalized Bootstrap Methods*; Chapman & Hall: London, UK; CRC Press: Boca Raton, FL, USA, 2000.
21. Karian, Z.A.; Dudewicz, E.J. *Handbook of Fitting Statistical Distributions with R*; Chapman & Hall: London, UK; CRC Press: Boca Raton, FL, USA, 2010.
22. Najjar, D.; Bigerelle, M.; Lefebvre, C.; Iost, A. A new approach to predict the pit depth extreme value of a localized corrosion process. *ISIJ Int.* **2003**, *43*, 720–725. [CrossRef]
23. Bigerelle, M.; Najjar, D.; Fournier, B.; Rupin, N.; Iost, A. Application of lambda distributions and bootstrap analysis to the prediction of fatigue lifetime and confidence intervals. *Int. J. Fatigue* **2006**, *28*, 223–236. [CrossRef]
24. Bigerelle, M.; Gautier, A.; Iost, A. Roughness characteristic length scales of micro-machined surfaces: A multi-scale modeling. *Sens. Actuators B Chem.* **2007**, *126*, 126–137. [CrossRef]
25. Fournier, B.; Rupin, N.; Bigerelle, M.; Najjar, D.; Iost, A.; Wilcox, R. Estimating the parameters of a generalized lambda distribution. *Comput. Stat. Data Anal.* **2007**, *51*, 2813–2835. [CrossRef]
26. Fournier, B.; Rupin, N.; Bigerelle, M.; Najjar, D.; Iost, A. Application of the generalized lambda distributions in a statistical process control methodology. *J. Process Control* **2006**, *16*, 1087–1098. [CrossRef]
27. Efron, B. Bootstrap methods: Another look at the Jackknife. *Ann. Stat.* **1979**, *7*, 1–26. [CrossRef]
28. Efron, B.; Tibshirani, R. *An Introduction to the Bootstrap*; Chapman & Hall: New York, NY, USA, 1993.
29. Bowden, F.P.; Tabor, D. *The Friction and Lubrication of Solids*; Oxford University Press: Oxford, UK, 2001.

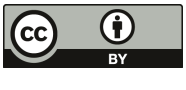

coatings

MDPI

Article

Corrosion and Wear Resistance of Fe-Based Amorphous Coatings

Guang Li [1,2,3], Youyi Gan [2], Chenheng Liu [2], Yu Shi [2,*], Yanchun Zhao [2] and Shengzhong Kou [2]

1 State Key Lab for Strength and Vibration of Mechanical Structures, Department of Engineering Mechanics, Xi'an Jiaotong University, Xi'an 710049, China; lg_xian@126.com
2 State Key Laboratory of Advanced Processing and Recycling of Non-ferrous Metal, Lanzhou University of Technology, Lanzhou 730050, China; ganyy_lz@163.com (Y.G.); lchlch2010@163.com (C.L.); Yanchun_zhao@163.com (Y.Z.); koushengzhong@163.com (S.K.)
3 Centre for Applied Dynamics Research, School of Engineering, University of Aberdeen, Aberdeen AB24 3UE, UK
* Correspondence: shiyu@lut.cn; Tel.: +86-0931-297-6702

Received: 31 October 2019; Accepted: 10 January 2020; Published: 14 January 2020

Abstract: Fe-based amorphous coatings were prepared on the surface of 45 steel substrates via supersonic plasma spraying and laser cladding. The corrosion and wear behavior of the two different coatings were investigated. Compared with supersonic plasma spraying, laser cladding resulted in coatings with a relatively denser structure, lower porosity, less cracks, and a good metallurgical bond with the substrate. Thanks to these properties, coatings produced by laser cladding exhibit a higher ability to resist uniform corrosion and better friction and wear performance than plasma-sprayed coatings.

Keywords: amorphous coating; laser cladding; supersonic plasma spraying; microstructure; corrosion resistance; wear resistance

1. Introduction

Amorphous materials exhibit excellent properties compared to crystalline materials because they do not have crystal defects, such as grain boundaries and dislocations [1]. Among metallic glasses (MGs), Fe-based MGs have attracted worldwide interest since the discovery of their high strength and hardness, excellent corrosion resistance and wear resistance, and relatively low material cost [2]. However, their engineering application is limited by their brittleness at room-temperature, size impact, and limited amorphous forming ability [3–5]. Amorphous coatings based on Fe-based MGs systems prepared via different methods on substrates can overcome some drawbacks, especially improving corrosion resistance and wear resistance of some materials [6]. Compared with 316 stainless-steel and Ni-based super-alloys, Fe-based amorphous coatings display corrosion resistance in complex and harsh marine environments [7–11]. These studies clearly indicate that Fe-based amorphous coatings can provide a higher and broad resistance to both general and localized corrosion, which is promising for their applications in ships in a marine environment, in nuclear fuel containers, in the oil and gas industries, in power stations, etc. [12,13].

Fe-based amorphous coatings fabricated using the supersonic plasma spraying technology and laser cladding technology are promising materials because of their low cost, high hardness, and good abrasive wear and corrosion resistance and may thus be developed to provide both corrosion and wear protection [14]. However, Fe-based amorphous coatings prepared via these two methods have different properties. It has been found that the thickness of Fe-based amorphous coatings prepared via plasma spraying can reach 200 μm, the bonding strength can be 60 MPa, and the porosity, related

to the flow of argon during spraying, can be 2%–3% [15–17]. Laser cladding as a method to prepare amorphous coating is characterized by laser energy concentration, low heat input, and rapid melting and cooling. It has been shown that laser cladding produces coatings with a complete amorphous structure in the middle of the cladding layer, hardness of 1270 HV, and good corrosion resistance. As the laser scanning speed increases, the cooling rate of the coating increases, and the amorphous content of the coating increases. When the scanning speed exceeds 45 mm/s, the amorphous content in the cladding layer reaches about 45% [18–21]. Ye et al. [22] used the laser cladding technology to prepare amorphous coatings on the surface of 304 stainless steel with high amorphous content. The wear resistance of the amorphous coatings was 10 times higher than that of crystalline materials.

In a previous study on corrosion and wear, some different properties of Fe-based amorphous coatings were reported. Amorphous coatings prepared via supersonic plasma spraying technology show higher amorphous content, but the bonding strength is low, and pores and microcracks are present inside the coatings, which seriously affect their application [15–17,23]. Preparing amorphous coatings with laser cladding can solve the problems of low bonding strength and high porosity. However, since laser cladding completely melts amorphous powders and then cools and solidifies them to form coatings, the amorphous content of the coatings is low, and thermal stress and residual stress present inside the coatings easily generate cracks during rapid cooling [24,25]. This affects the development and application of amorphous coatings.

In this paper, supersonic plasma spraying and laser cladding were used to prepare Fe-based amorphous composite coatings on the surface of 45 steel substrates. We studied the microstructure, corrosion resistance, and friction wear of the coatings and compared and analyzed the performances of the two processes. Our results provide a basic guide for their practical application.

2. Experimental Materials and Methods

The substrate material was 45 steel with gauge dimensions of $100 \times 80 \times 8$ mm^3. The composition of the 45 steel is shown in Table 1. The alloy powder was amorphous FeCrMoCB produced by Liquidmetal Company, Lake Forest, CA, USA, with a particle size of 26–70 μm. The nominal composition of the amorphous powder is shown in Table 2. The structures of the FeCrMoCB amorphous powder and the coatings were investigated via X-ray diffractometry (XRD, PHILIPS X' Pert MPD, Amsterdam, The Netherlands) with Cu-Kα radiation. A continuous scan mode was used to scan in a 2θ range of 20°–80°. The morphologies of the samples were established via a Quanta450FEG scanning electron microscope (SEM, FEI Company, Hillsboro, OR, USA) equipped with an energy-dispersive spectroscope (EDS).

Table 1. Chemical composition of the 45 stainless-steel substrate (wt %).

Element	C	Si	Mn	P	Cu	Ni	Cr	S	Fe
wt %	0.44	0.21	0.53	0.028	0.02	0.01	0.03	0.007	Bal.

Table 2. Chemical composition of the cladding material (wt %).

Element	Cr	Mo	C	B	Fe
wt %	25	20	3	3	Bal.

Figure 1 shows the particle size of the powder particles, and the diffuse peak (inset) represents the amorphous phase, indicating that the powder used in this experiment was completely amorphous.

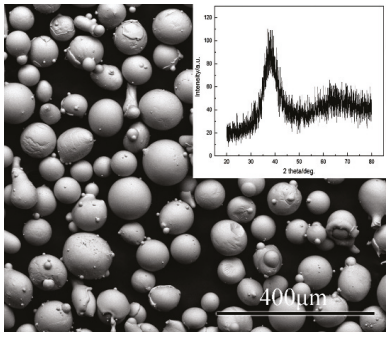

Figure 1. Typical SEM image and XRD analysis (inset) of FeCrMoCB amorphous metallic alloy powder.

Before plasma spraying, the substrate was smoothed with sandpaper, cleaned with acetone to remove oil pollution on the surface, and finally dried in air. DH-2080 supersonic plasma spraying equipment (Shanghai Dahao Dahao Company, Shanghai, China) was used for the experiment. Table 3 lists the plasma spraying parameters used in this study. After spraying, the sample was cut into a block with a size of $10 \times 10 \times 8$ mm^3.

Table 3. Plasma spraying parameters.

Argon Flow (L/min)	Hydrogen Flow (L/min)	Voltage (V)	Current (A)	Powder Feed (g/min)	Spray Distance (mm)	Spray Thickness (mm)
160	20	140	370	30	120	0.2

The laser cladding heat source used a 4000 W high-power fiber-optic laser and a coaxial powder feeding method for single-layer single-pass cladding. Table 4 lists the laser cladding parameters. Argon protection was applied during the cladding process with a gas flow rate of 25 L/min. After completing the cladding, a $10 \times 10 \times 8$ mm^3 sample was cut along the laser scanning direction. The surface of each specimen was mechanically polished to a mirror finish. The morphology of the corrosion of the sample was analyzed with a Quanta450FEG SEM.

Table 4. Laser cladding parameters.

Laser Wavelength (nm)	Laser Power (W)	Scanning Speed (mm/s)	Spot Diameter (mm)	Argon Flow (L/min)
1070	2500	20	3	25

Electrochemical polarization was conducted in a three-electrode cell using a platinum counter electrode and a saturated calomel reference electrode (SCE). The specimens for the corrosion test were closely sealed with epoxy resin, leaving an end-surface (with a cross-sectional area of about 100 mm^2) exposed for testing. The specimens were tested in a 3.5 wt % NaCl solution. Before testing, the testing surface of each specimen was mechanically polished to a mirror finish, then degreased in acetone, washed in distilled water, and dried in air. Electrochemical polarization curves were determined at a potential sweep rate of 2.0 mV/s in a potential range from −1.0 to 1.0 V, after holding the samples in the electrolyte at the steady open circuit potential (OCP) for a period of 600 s. Once the polarization tests were finished, the corroded samples were immediately taken out, cleaned in distilled water using ultrasonic treatment, and finally dried in air.

In this experiment, the UH4000 multifunctional hardness tester (ITM, Lake bluff, IL, USA) was used to measure the microhardness of the coatings obtained by plasma spray and laser cladding. The

hardness tester used a conical diamond indenter with a loading load of 1 kgf and a loading residence time of 10 s.

Table 5 shows the parameters of the friction and wear test. The friction and wear test was carried out on the UMT-2MT universal friction and wear tester produced by CETR, USA. The friction data were determined via the reciprocating friction test method. During the test, the samples were fixed, and the friction pair reciprocated at a certain speed to achieve wear. Before the friction and wear test, the samples were cut into $19 \times 12 \times 5$ mm^3 specimens via wire cutting, carefully polished with SiC paper up to 2500 grit, and then ultrasonically cleaned with an acetone solution to remove impurities and oil stains from the surface. After the friction and wear test, the friction and wear morphology of the coatings were analyzed with a MiroXAM-800 non-contact optical profilometer (KLA-Tencor Company, Milpitas, CA, USA) and an SEM to explore the wear mechanism of the amorphous coatings.

Table 5. Friction and wear test parameters for the analysis of Fe-based amorphous coatings.

Loading Force (N)	Sliding Speed (m/s)	Sliding Frequency (Hz/s)	Sliding Total Stroke (m)	Friction Pair (mm)	Friction Time (s)
25	0.1	20	250	5	2400

3. Experimental Results and Analysis

3.1. Structural Characterization of the Coatings

Figure 2a presents the cross-sectional microstructure of the laser cladding layer. It can be clearly seen that the coating consisted of a cladding layer, a heat-affected zone, and the substrate. The average thickness of the laser cladding coatings was about 150 μm. As shown, the coating did not have defects such as porosities and cracks and was well bonded to the substrate.

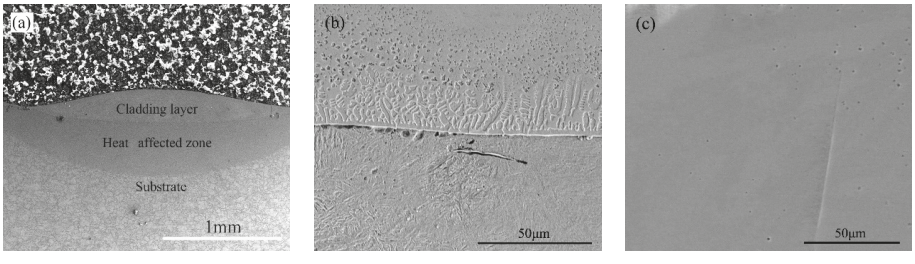

Figure 2. Microstructure of a coating produced by laser cladding: (**a**) Morphology of the cladding cross section; (**b**) microstructure of the bottom of the cladding layer; (**c**) microstructure of the surface of the cladding layer.

Figure 2b is an enlarged view of the bottom of the cladding layer in Figure 2a. It shows a dendrite region of about 20 μm at the junction of the coating and the substrate. This dendrite region is a columnar crystal that formed by propelling straight forward at a lower rate, as a consequence of the large temperature gradient between the substrate and the coating. The presence at the bottom of the coating of this typical epitaxial-growth columnar crystal region indicates that the coating and the substrate had a good metallurgical bond. According to the liquid solidification theory, a crystal growth morphology is mainly determined by the solid–liquid interface stability factor G/R (G is the temperature gradient, and R is the solidification rate). When the liquid phase begins to solidify, the temperature at the bottom of the molten pool differs greatly from the temperature of the substrate material, and the solidified structure grows along the maximum heat dissipation direction of the molten pool. Along the bottom of the molten pool to the surface of the coating, the temperature gradient G gradually decreases, and the solidification rate R gradually increases, which hampers the tendency of

the columnar crystal to continue growing upward. The growth of the columnar crystal is interrupted, resulting in the formation of an equiaxed crystal region.

Figure 2c is a magnified image of the surface of the cladding layer in Figure 2a. It shows that hardly any dendritic crystal region with a finer grain size was present. This suggests that the surface of the cladding layer was still amorphous. The fast heat loss of the surface layer limited the growth of nucleation sites.

Figure 3a shows the cross-sectional morphology of a coating obtained by supersonic plasma spraying. It can be seen that the coating thickness was about 400 μm, and the coating was well formed.

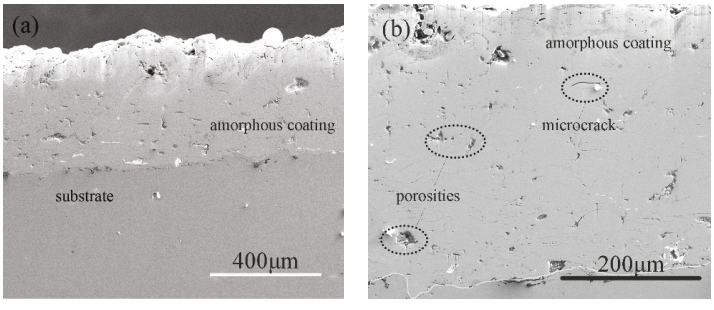

Figure 3. Microstructure of a coating produced by supersonic plasma spraying: (**a**) Morphology of a cross section of the plasma-sprayed coating; (**b**) magnified view of the coating.

Figure 3b is an enlarged view of the interface between coating and substrate. It can be observed that there was a mechanical bond between the coating and the substrate, and some pores were present at the bonding surface. A small number of unmelted particles, pores, and microcracks appeared in the coating due to the large Ar flow introduced into the air during the spraying process. On the other hand, pores and microcracks formed in a relatively loose layered structure when the particles hit the substrate at a high speed, which led to a severe splash phenomenon, so that the boundaries of some droplets could not be tightly fused together.

3.2. Phasse of the Coatings

Figure 4a shows the XRD pattern of the coating obtained by laser cladding. It consists of several sharp diffraction peaks appearing at approximately 40°–50°, which represent the crystalline phase, indicating that the coating contained a crystalline phase. After analyzing the results, these crystal phases appeared to consist mainly of Fe–Cr, Fe_2B, $(CrFe)_7C_3$, and other compounds. These hard phases significantly increase the microhardness of the coating. Therefore, the coating was not composed of complete Fe-based amorphous materials but contained crystal phases.

Figure 4b shows the XRD pattern of the supersonic plasma-sprayed coating. It can be seen that a diffuse peak of the amorphous phase appeared between 40° and 50°, indicating that the coating had a higher amorphous content compared to the one produced by laser cladding. However, a distinct sharp peak appeared at 44°, which corresponded to a Cr–Fe and $C_{0.09}Fe_{1.91}$ compound. This could be due to the fact that the powder contained 3% of carbon, and the carbon atoms, characterized by a higher melting point than the Fe atoms, formed a compound with the Fe atoms in the coating.

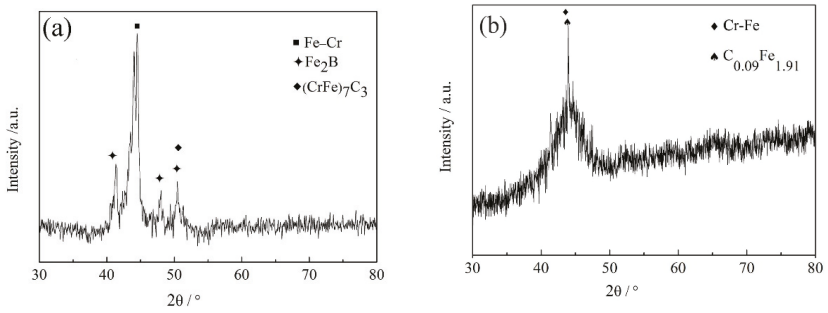

Figure 4. XRD diagram of the coatings. Coatings produced by (**a**) laser cladding; (**b**) supersonic plasma spraying.

3.3. Corrosion Resistance of the Coatings

Figure 5 shows the electrochemical polarization curves of the 45 steel substrate, a coating produced by laser cladding, and a supersonic plasma-sprayed coating in a 3.5 wt % NaCl solution. Table 6 shows the fitting results of the polarization curves in Figure 6. Compared with the substrate, the corrosion potential (E_{corr}) of the laser cladding-produced coating increased by about 148 mV, the corrosion potential (E_{corr}) of the supersonic plasma-sprayed coating increased by about 115 mV, and the corrosion current density (I_{corr}) was reduced by an order of magnitude. Thus, corrosion resistance was significantly improved. Compared with supersonic plasma-sprayed coatings, coatings produced by laser cladding showed a higher corrosion potential and a smaller corrosion current density. Therefore, coatings produced by laser cladding have better corrosion resistance than supersonic plasma-sprayed coatings.

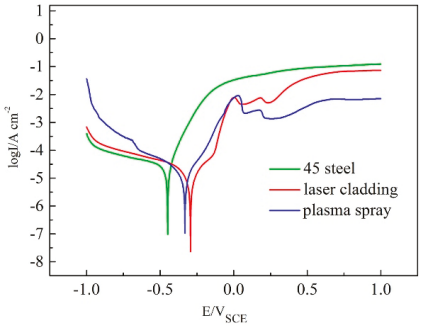

Figure 5. Polarization curves of the 45 steel substrate and the coatings produced by laser cladding and supersonic plasma spraying.

Table 6. Polarization parameters of substrate and coatings.

Substrate and Coating	E_{corr}/mV	I_{corr}/A·cm^{-2}
45 steel	−448.5	1.049×10^{-4}
Laser cladding-produced coating	−300.8	3.583×10^{-5}
Plasma-sprayed coating	−332.8	5.218×10^{-5}

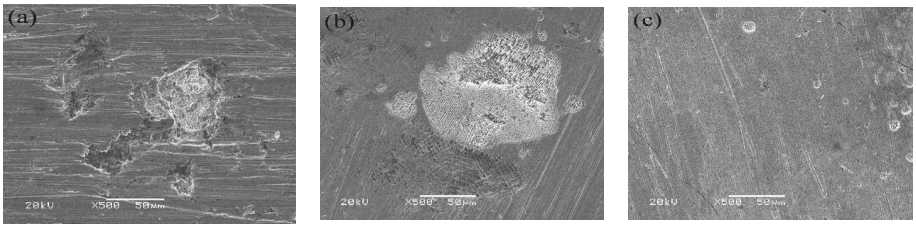

Figure 6. SEM micrographs of corrosion damages: (**a**) 45 steel; (**b**) supersonic plasma-sprayed coating; (**c**) coating produced by laser cladding.

Although the amorphous content of the supersonic plasma-sprayed coatings is higher than that of the coating produced by laser cladding, the supersonic plasma-sprayed coatings contain pores and microcracks, which provides an erosion path for corrosive media and reduces the corrosion resistance performance of the coatings. The coatings produced by laser cladding have a dense structure with no cracks and other obvious defects and high corrosion resistance.

Figure 6 shows the characteristic morphologies of corrosion damages generated on the surface of the substrate and coatings. Figure 6a shows deep corrosion pits in the untreated 45 steel substrate, indicating that severe corrosion occurred on the surface of 45 steel. Compared with the 45 steel substrate, the coatings showed good corrosion resistance. Figure 6b shows the micromorphology of the surface of the supersonic plasma-sprayed coating. It can be observed that many small pores appeared in the corroded area. This suggests that the plasma-sprayed coating had a low density. Figure 6c shows the micromorphology of the surface of the coating produced by laser cladding. It can be observed that there were few pits on its surface, and the corroded area was small. This indicates that coatings produced by laser cladding have a better corrosion resistance than plasma-sprayed coatings.

3.4. Microhardness of the Coatings

Figure 7 shows the microhardness of the laser cladding layer and supersonic plasma-sprayed coating at different depths of the coatings. It can be seen that microhardness of the laser cladding layer was significantly higher than that of the substrate and gradually decreased along the direction from the surface of the cladding layer to the substrate. The surface of the coating was relatively hard because small dendritic crystals and amorphous material coexist in this area. Near the fusion line, the hardness of the cladding layer was significantly reduced because of the penetration of the substrate into the cladding layer, which changed the composition of the cladding layer. This adversely affects the performance of coatings.

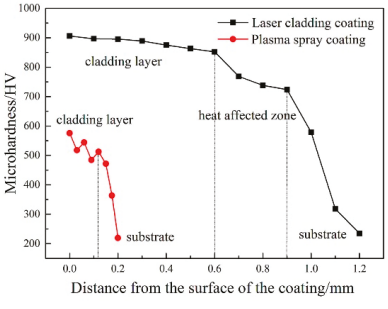

Figure 7. Microhardness of the coatings.

Compared with the coating produced by laser cladding, the supersonic plasma-sprayed coating has a lower hardness. This is because supersonic plasma-sprayed coatings are formed by molten

or semimolten particles impacting on the surface of the substrate at high speed; this results in superimposed disc-shaped particles that combine with each other and solidify on the surface of the substrate. However, gaps remain between the particles, decreasing the hardness of the coating.

3.5. Wear Performance of the Coatings

Table 7 shows the average coefficient of friction for the 45 steel substrate, plasma-sprayed coatings, and coatings produced by laser cladding. It indicates that the average coefficients of friction of the amorphous coatings prepared by the two processes re smaller than that of the substrate. Therefore, the coatings have better wear resistance. The average coefficient of friction of the plasma-sprayed coating was lower than that of the coating produced by laser cladding because of a lower value of the coefficient of friction of the plasma-sprayed coating in the first 350 s.

Table 7. Average friction coefficients of the 45 steel substrate, the coating produced by laser cladding, and the plasma-sprayed coating.

	45 Steel	**Laser Cladding Coating**	**Plasma-Sprayed Coating**
Average Friction Coefficient	0.2992	0.2915	0.2778

Figure 8 shows the friction coefficients of the 45 steel substrate, plasma-sprayed coating, and coating produced by laser cladding. It shows that the friction coefficients of the coating produced by laser cladding and the plasma-sprayed coating were not much different from that of the substrate, but the fluctuation of the friction coefficient of the substrate was large, indicating that the amorphous composite coatings had better anti-wearing properties than the substrate. The friction coefficient curve of the coating produced by laser cladding did not show a wide range of pulsation, indicating that the coating did not show severe wear failure during the entire friction test. Therefore, coatings produced by laser cladding show excellent and stable friction and wear properties. The plasma-sprayed coating had a low coefficient of friction in the first 350 s, which then suddenly increased. The change of the friction coefficient was obvious, as indicated by the partial peeling of the coating after the first 350 s of friction.

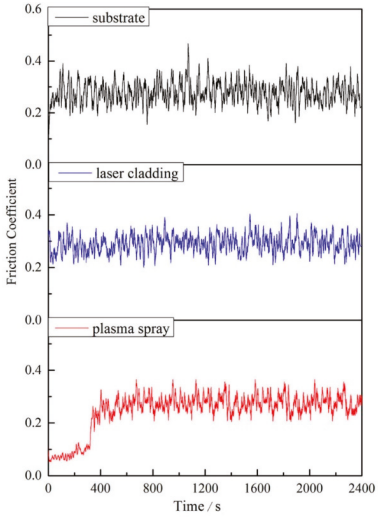

Figure 8. Coefficient of friction of the 45 steel substrate, the coating produced by laser cladding, and the plasma-sprayed coating.

Figure 9 shows the wear volumes of the 45 steel substrate, the coating produced by laser cladding, and the plasma-sprayed coating. Compared with the 45 steel substrate, the wear areas of the coatings prepared by the two processes were reduced by about 10 times. The wear volumes of the coatings were significantly reduced, suggesting that the abrasion resistance of the coatings was improved. The main reason for a higher wear resistance of the coating produced by laser cladding compared to the plasma-sprayed coating is that there pores and microcracks were present in the plasma-sprayed coating, which caused the coating to peel off during the friction and wear process and reduced the coating wear resistance.

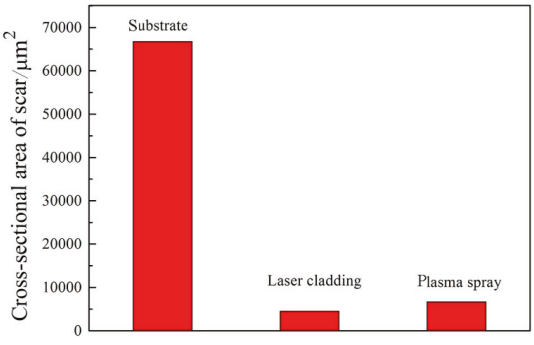

Figure 9. Wear scar volumes of the 45 steel substrate, the coating produced by laser cladding, and the plasma-sprayed coating.

Morphological observations on the wear of Fe-based amorphous coatings can provide useful information on the wear mechanisms; therefore, scanning and electron microscopy analysis of the friction and wear morphology of coatings produced by laser cladding and plasma spraying was carried out.

Figure 10 shows the wear profile of the coatings produced by laser cladding and plasma spraying. It can be seen from Figure 10a that there was a partial peeling pit in the wear region of the coating produced by laser cladding. This is because this coating contained a hard crystalline phase consisting of Fe_2B and dendritic crystals. The anti-cutting ability of the coating was reduced during wear, which caused the formation of the peeling pits. In addition, there was a clear furrow in the non-flaking pit area, which was formed by the friction of the hard phase in the coating. It can be seen from Figure 10b that a large amount of flaking occurred on the surface of the plasma-sprayed coating. The reason is that this coating is a layered structure formed by particles are stacked on each other, which leave pores and microcracks inside the coating. As the wear process progresses, cracks will gradually expand, shearing the surface of the coating when they reach a critical dimension. The depth and width of the wear scar of the plasma-sprayed coating were significantly larger than those of the coating produced by laser cladding, indicating that the wear resistance of the latter is better. The reason is that the coating produced by laser cladding possesses a dense structure, characterized by metallurgical bonding between the coating and the substrate, high bonding strength, and cohesive bonding strength, in addition to amorphous and fine crystalline phases in its interior. These crystals promote fine-grain strengthening and dispersion strengthening. These factors improve the wear resistance of the coating produced by laser cladding.

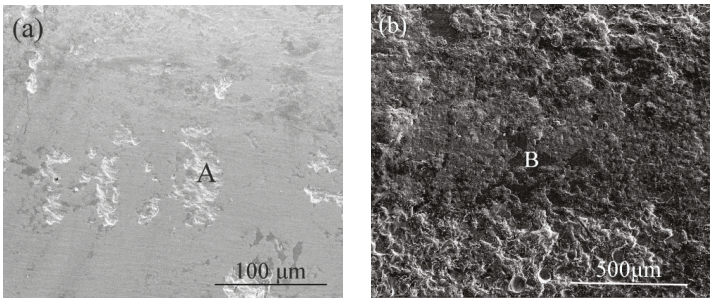

Figure 10. Wear scar morphology of coatings produced by laser cladding and plasma spraying: Coating produced by (**a**) laser cladding; (**b**) plasma spraying.

4. Conclusions

Fe-based amorphous coatings produced by laser cladding and plasma-spraying were analyzed. Fe-based amorphous coating prepared by laser cladding presented better qualities than plasma-sprayed coatings.

The electrochemical behaviors of the coatings produced by laser cladding and plasma spraying in a 3.5 wt % NaCl solution were studied through electrochemical polarization. It was shown that Fe-based amorphous coatings prepared via the two processes have higher corrosion resistance than the 45 steel substrate, and the corrosion resistance of the coatings produced by laser cladding is superior to that of plasma-sprayed coatings. It was found that the corroded region in the plasma-sprayed coatings exposed many small pores, indicating that these coatings are not dense. Additionally, the supersonic plasma-sprayed coatings contain pores and microcracks, which affect their corrosion resistance. In contrast, the structure of coatings produced by laser cladding is dense and can thus protect the substrate from corrosive media.

The friction and wear properties of the coatings produced by laser cladding and plasma spraying were measured to analyze the friction coefficients and wear performances of the coatings. The wear resistances of Fe-based amorphous coatings prepared via the two processes were higher than that of the 45 steel substrate. The wear resistance of coatings produced by laser cladding is better than that of the plasma-sprayed coatings because the former are dense and contain several hard phases. In addition plasma-sprayed coatings more easily peel off during friction, because they form a mechanical bond with the substrate and have a layered structure. In contrast, coatings produced by laser cladding do not have many defects, have a dense structure, and contain some crystalline phases, all properties that improve their friction and wear resistance.

Author Contributions: Conceptualization, G.L. and Y.S.; Validation, G.L., Y.G., C.L., Y.S., Y.Z. and S.K.; Investigation, G.L. and Y.S.; Resources, G.L., Y.S., Y.Z., and S.K.; Data Curation, G.L. and Y.S.; Writing—Original Draft Preparation, Y.G., C.L. and G.L.; Writing—Review and Editing, G.L., Y.G. and C.L.; Supervision, G.L.; Project Administration, Y.S.; Funding Acquisition, G.L., Y.S., Y.Z. and S.K. All authors have read and agreed to the published version of the manuscript.

Funding: This work was supported by NSFC (Nos. 51961022, 51675256, 51661017, 51571105), China Postdoctoral Science Foundation (No. 2017M623153), and Basic Research of Gansu Province (No. 17JR5RA107).

Acknowledgments: Guang Li acknowledges the support from China Scholarship Council.

Conflicts of Interest: The authors declare no conflict of interest.

References

1. Inoue, A. Stabilization and high strain-rate superplasticity of metallic supercooled liquid. *Mater. Sci. Eng. A* **1999**, *267*, 171–183. [CrossRef]
2. Trexler, M.M.; Thadhani, N.N. Mechanical properties of bulk metallic glasses. *Prog. Mater. Sci.* **2010**, *55*, 759–839. [CrossRef]
3. Gu, X.; Poon, S.J.; Shiflet, G.J. Mechanical properties of iron-based bulk metallic glasses. *J. Mater. Res.* **2007**, *22*, 344–351. [CrossRef]
4. Gu, X.; Poon, S.J.; Shiflet, G.J.; Widom, M. Ductility improvement of amorphous steels: Roles of shear modulus and electronic structure. *Acta Mater.* **2008**, *56*, 88–94. [CrossRef]
5. Keryvin, V.; Hoang, V.; Shen, J. Hardness, toughness, brittleness and cracking systems in an iron-based bulk metallic glass by indentation. *Intermetallics* **2009**, *17*, 211–217. [CrossRef]
6. Inoue, A.; Kong, F.; Zhu, S.; Shalaan, E.-S.; Al-Marzouki, F. Production methods and properties of engineering glassy alloys and composites. *Intermetallics* **2015**, *58*, 20–30. [CrossRef]
7. Zhou, H.; Zhang, C.; Wang, W.; Yasir, M.; Liu, L. Microstructure and mechanical properties of Fe-based amorphous composite coatings reinforced by stainless steel powders. *J. Mater. Technol.* **2015**, *31*, 43–47. [CrossRef]
8. Zhu, Y.; Li, Z.; Li, R.; Li, M.; Daze, X.; Feng, K.; Wu, Y. Microstructure and property of Fe–Co–B–Si–C–Nb amorphous composite coating fabricated by laser cladding process. *Appl. Surf. Sci.* **2013**, *280*, 50–54. [CrossRef]
9. Farmer, J.; Haslam, J.; Day, S.; Lian, T.; Saw, C.; Hailey, P.; Choi, J.-S.; Rebak, R.; Yang, N.; Payer, J.; et al. Corrosion resistance of thermally sprayed high-boron iron-based amorphous-metal coatings: $Fe_{49.7}Cr_{17.7}Mn_{1.9}Mo_{7.4}W_{1.6}B_{15.2}C_{3.8}Si_{2.4}$. *J. Mater. Res.* **2007**, *22*, 2297–2311. [CrossRef]
10. Zhang, S.; Zhang, W.; Wang, S.; Gu, X.; Wang, J. Characterisation of three-dimensional porosity in an Fe-based amorphous coating and its correlation with corrosion behaviour. *Corros. Sci.* **2015**, *93*, 211–221. [CrossRef]
11. Zhang, C.; Zhang, Z.-W.; Chen, Q.; Liu, L. Effect of hydrostatic pressure on the corrosion behavior of HVOF-sprayed Fe-based amorphous coating. *J. Alloy. Compd.* **2018**, *758*, 108–115. [CrossRef]
12. Nie, G.M.; Huang, C.; Li, B.; Zhong, J.; Wang, S. Fabrication and application status of Fe-based amorphous alloy coatings. *Surf. Technol.* **2017**, *46*, 18–26.
13. Zhang, C.; Guo, R.; Yang, Y.; Wu, Y.; Liu, L. Influence of the size of spraying powders on the microstructure and corrosion resistance of Fe-based amorphous coating. *Electrochim. Acta* **2011**, *56*, 6380–6388. [CrossRef]
14. Stoica, M.; Eckert, J.; Roth, S.; Zhang, Z.; Schultz, L.; Wang, W. Mechanical behavior of Fe65.5Cr4Mo4Ga4P12C5B5.5 bulk metallic glass. *Intermetallics* **2005**, *13*, 764–769. [CrossRef]
15. Zhou, Z.; Wang, L.; He, D.Y.; Wang, F.C.; Liu, Y.B. Microstructure and electrochemical behavior of Fe-based amorphous metallic coatings fabricated by atmospheric plasma spraying. *J. Therm. Spray Technol.* **2011**, *20*, 344–350. [CrossRef]
16. Kobayashi, A.; Yano, S.; Kimura, H.; Inoue, A. Fe-based metallic glass coatings produced by smart plasma spraying process. *Mater. Sci. Eng. B* **2008**, *148*, 110–113. [CrossRef]
17. Zhou, Y.-Y.; Ma, G.-Z.; Wang, H.-D.; Li, G.-L.; Chen, S.-Y.; Wang, H.-J.; Liu, M. Fabrication and characterization of supersonic plasma sprayed Fe-based amorphous metallic coatings. *Mater. Des.* **2016**, *110*, 332–339. [CrossRef]
18. Zhu, Y.; Li, Z.; Li, R.; Li, M.; Feng, K.; Wu, Y.; Wada, T.; Kato, H. High power diode laser cladding of Fe–Co–B–Si–C–Nb amorphous coating: Layered microstructure and properties. *Surf. Coat. Technol.* **2013**, *235*, 699–705. [CrossRef]
19. Katakam, S.; Kumar, V.; Santhanakrishnan, S.; Rajamure, R.; Samimi, P.; Dahotre, N.B. Laser assisted Fe-based bulk amorphous coating: Thermal effects and corrosion. *J. Alloy. Compd.* **2014**, *604*, 266–272. [CrossRef]
20. Mojaver, R.; Mojtahedi, F.; Shahverdi, H.R.; Torkamany, M.J. Study on feasibility of producing an amorphous surface layer of $Fe_{49}Cr_{18}Mo_7B_{16}C_4Nb_3$ by pulsed Nd:YAG laser surface melting. *Appl. Surf. Sci.* **2013**, *264*, 176–183. [CrossRef]
21. Wu, X.; Hong, Y. Fe-based thick amorphous-alloy coating by laser cladding. *Surf. Coat. Technol.* **2001**, *141*, 141–144. [CrossRef]
22. Ye, X.; Shin, Y.C. Synthesis and characterization of Fe-based amorphous composite by laser direct deposition. *Surf. Coat. Technol.* **2014**, *239*, 34–40. [CrossRef]

23. Koga, G.; Schulz, R.; Savoie, S.; Nascimento, A.; Drolet, Y.; Bolfarini, C.; Kiminami, C.; Botta, W. Microstructure and wear behavior of Fe-based amorphous HVOF coatings produced from commercial precursors. *Surf. Coat. Technol.* **2017**, *309*, 938–944. [CrossRef]
24. Lu, Y.; Huang, G.; Wang, Y.; Li, H.; Qin, Z.; Lu, X. Crack-free Fe-based amorphous coating synthesized by laser cladding. *Mater. Lett.* **2017**, *210*, 46–50. [CrossRef]
25. Chew, Y.; Pang, J.H.L.; Bi, G.; Song, B. Thermo-mechanical model for simulating laser cladding induced residual stresses with single and multiple clad beads. *J. Mater. Process. Technol.* **2015**, *224*, 89–101. [CrossRef]

coatings

MDPI

Article

Sensitivity Analysis of Rotor/Stator Interactions Accounting for Wear and Thermal Effects within Low- and High-Pressure Compressor Stages

Florence Nyssen * and Alain Batailly

Department of Mechanical Engineering, École Polytechnique de Montréal, Montréal, QC H3T 1J4, Canada; alain.batailly@polymtl.ca

* Correspondence: florence.nyssen@polymtl.ca

Received: 20 December 2019; Accepted: 11 January 2020; Published: 15 January 2020

Abstract: In the current design of turbomachines, engine performance is improved by reducing the clearances between the rotating components and the stator, which allows for loss decrease. Due to these clearance reductions, contact events may occur between the rotor and the stator. An abradable coating is deposited along the stator circumference as a sacrificial material to lower the contact severity. However, experiments highlighted the occurrence of rotor/stator interactions with high wear depth on the abradable coating as well as high temperature increases within the abradable coating following contacts. This work focuses on the sensitivity analysis of rotor/stator interactions with respect to the rotor angular speed and the initial clearances between the rotor and the stator, taking into account thermal effects within the abradable coating. Convergence analyses are first conducted to validate the numerical model. Then, after a calibration of the thermal model of the abradable coating based on two experimental test cases, the numerical model is used to investigate the cross effects of the angular speed and the initial clearances on the obtained rotor/stator interactions.

Keywords: turbomachinery; contacts; rotor/stator interactions; abradable coating; thermal effects

1. Introduction

To respect increasingly stringent environmental constraints and to lower operating costs, turbomachine manufacturers are focusing on the improvement of engine performance to decrease fuel consumption [1]. A common solution to lower aerodynamic loss and increase overall performance of an engine consists of the reduction of nominal clearances between rotating bladed disks (rotor) and the surrounding casings (stator). However, this clearance reduction may lead to rotor/stator unilateral contacts and hazardous interaction phenomena [2,3]. In order to reduce the severity of such contact events, an abradable coating is often deposited along the casing contact surface as a sacrificial material [4–6]. A variety of works have been carried out on the numerical simulation of rotor/stator interactions taking into account abradable coating wear [7–9]. Previous work of the authors [10] proposed a numerical strategy to model temperature evolution within the abradable coating following contact events and wear. In this article, this numerical model is improved focusing on two aspects: (1) the definition of the blade heat flux is refined, the latter is now proportional to the friction forces—i.e., therefore also proportional to the contact forces—between the blade and the abradable layer, and (2) a dependence of the mechanical properties of the abradable coating on the temperature is included. In this work, the focus is made on the validation of the contact forces magnitude using two independent experimental data sets. Using the previous definition of the heat flux, an accurate prediction of temperature levels within the structure for two test cases means that contact forces are predicted with a relevant order of magnitude for each configuration.

The first test set-up consists of a rotating high-pressure (HP) compressor's bladed disk, on which the calibration of the numerical model is performed. The focus is made on a 22-lobe torsion interaction, with 22 high temperature areas recorded by an infrared camera localized behind the experimental set-up. The numerical model is calibrated to obtain the same temperature increases than in the experiments. Then, the calibrated model is used to simulate experimental tests carried out on a second experimental test, on a low-pressure (LP) compressor's bladed disk, focusing on a 7-wear-lobe interaction involving the first bending mode. The predicted temperatures using the calibrated model are compared with experimental data of this second test set-up.

The fact that the numerical model—calibrated on the first experiments only—also allows similar temperature increases in the second configuration validates the order of magnitude of the predicted heat flux, and therefore of the predicted contact forces. Based on this conclusion, a detailed sensitivity analysis of the dynamical responses of the system with the clearance between the tip of the blade and the casing is conducted. In particular, the evolution of wear and temperature profiles are analyzed in detail, as well as the effect of the rotor/stator clearances and the angular speed on the observed interactions.

The second section of the article details the numerical model, with a description of each component and of the time integration strategy. Convergence analyses are carried out in the third section with respect to space and time discretization parameters to validate the numerical model. In the fourth section, the calibration of the blade heat flux is performed based on the first considered experimental set-up. Then, the calibrated model is used to simulate the second test case. In the fifth section, an in-depth analysis of the effect of the initial clearance and of the angular speed on the observed rotor/stator interaction is carried out.

2. Numerical Model

The numerical model consists of a single rotating blade and a casing on which an abradable layer is deposited. A detailed description of these three components is presented below, along with the employed time integration algorithm.

2.1. Blade

The blade finite element mesh yields $\mathbf{M}$, $\mathbf{D}$ and $\mathbf{K}(\Omega)$ matrices, respectively the mass, damping and stiffness matrices, with Ω the angular speed. To decrease the size of the model, a modal reduction of the structural matrices is conducted using an existing component mode synthesis method embedding centrifugal effects detailed in [11]. The reduced structural matrices are noted $\mathbf{M}_r$, $\mathbf{D}_r$ and $\mathbf{K}_r(\Omega)$, and the reduction matrix, $\mathbf{\Phi}$, reads:

$$\mathbf{\Phi} = \begin{bmatrix} \mathbf{I} & \mathbf{0} \\ \mathbf{\Phi}_R(0) & \mathbf{\Psi} \end{bmatrix} \tag{1}$$

with:

$$\mathbf{\Psi} = \begin{bmatrix} \mathbf{\Phi}_R\left(\frac{\Omega_{\max}}{2}\right) - \mathbf{\Phi}_R(0) \\ \mathbf{\Phi}_R(\Omega_{\max}) - \mathbf{\Phi}_R(0) \\ \mathbf{\Phi}_L(0) \\ \mathbf{\Phi}_L\left(\frac{\Omega_{\max}}{2}\right) \\ \mathbf{\Phi}_L(\Omega_{\max}) \end{bmatrix}^{\mathsf{T}} \tag{2}$$

in which $\mathbf{\Phi}_R(\Omega)$ and $\mathbf{\Phi}_L(\Omega)$ denote respectively the n_c constraint modes and the first η fixed interface modes computed for a given angular speed Ω. In order to avoid potential rank-deficiency due to similarities between the constraint modes, an orthonormalization of matrix $\mathbf{\Psi}$ is performed. In the

reduced order model, the retained physical degrees of freedom are localized along the blade tip to manage contact interactions. The reduced equation of motion of the blade is given by:

$$\mathbf{M}_r\ddot{\mathbf{q}} + \mathbf{D}_r\dot{\mathbf{q}} + \mathbf{K}_r(\Omega)\,\mathbf{q} + \mathbf{F}^c(\mathbf{q}) = \mathbf{F}^e \tag{3}$$

in which $\mathbf{q}$ contains the reduced degrees of freedom, $\mathbf{F}^c$ denotes the contact forces and $\mathbf{F}^e$ the external forces. An explicit time integration procedure based on the central finite-differences method is used to compute the blade displacement at each iteration $n+1$ as follows [9]:

$$\mathbf{x}^p_{n+1} = \left[\frac{\mathbf{M}}{h^2} + \frac{\mathbf{D}}{2h}\right]^{-1}\left(\left[\frac{2\mathbf{M}}{h^2} - \mathbf{K}\right]\mathbf{x}_n + \left[\frac{\mathbf{D}}{2h} - \frac{\mathbf{M}}{h^2}\right]\mathbf{x}_{n-1}\right) \tag{4}$$

with h the time step of the time integration scheme (referred to as mechanical time step in the following). If blade/abradable coating contacts occur, predicted displacements are corrected using:

$$\mathbf{x}_{n+1} = \mathbf{x}^p_{n+1} + \left[\frac{\mathbf{M}}{h^2} + \frac{\mathbf{D}}{2h}\right]^{-1}\mathbf{F}^c(\mathbf{q}) \tag{5}$$

2.2. Casing

The casing is assumed perfectly rigid, meaning that it remains insensitive to blade contacts. In order to initiate contact, a progressive deformation is applied on the casing at the beginning of the simulation until it reaches a deformed configuration with two lobes, i.e., two privileged contact areas, as illustrated in Figure 1. This two-lobes deformation aims to model the casing ovalization resulting from a thermal imbalance within the engine at rest due to the up motion of the hot gas [12].

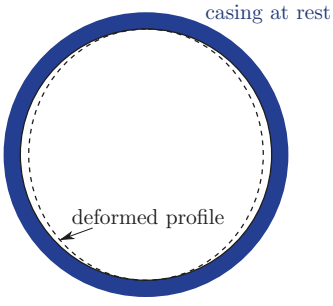

Figure 1. 2-lobe casing deformation.

2.3. Abradable Coating

The abradable coating model is composed of two distinct meshes: (1) a mechanical mesh composed of one-dimensional rod elements to compute wear, and (2) a two-dimensional cylindrical thermal mesh for temperature computation. A weak thermo-mechanical coupling is assumed: thermic influences the system mechanics, but the mechanical deformation of the abradable layer elements has no effect on the computed temperatures. The assumption of weak thermo-mechanical coupling is relevant in the context of rapid dynamics using small time steps and an explicit resolution scheme [13]. It conveniently allows separate solving of the mechanical and the thermal problem. Only heat transfer by conduction is considered.

2.3.1. Mechanical Mesh

The mechanical mesh of the abradable layer consists of one-dimensional two-node rod elements mechanically independent of their neighbors, governed by a plastic constitutive law detailed in [9]. Contact forces resulting from blade/abradable layer contact events cause an elastic deformation of the

rod elements as well as permanent plastic deformations which represents numerically the abradable layer's wear, as illustrated in Figure 2. The evolution of the wear profile of the abradable layer can therefore be computed at each time iteration using this mechanical mesh.

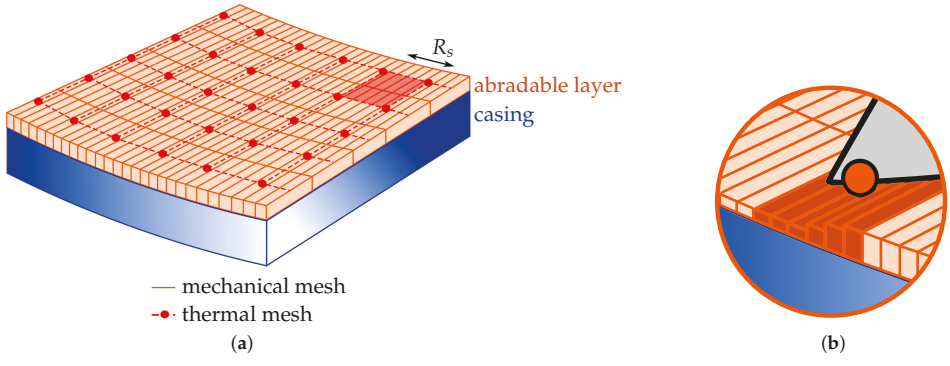

Figure 2. Abradable coating wear mechanism following blade/abradable coating contact event (**a**) and zoom on the abradable layer's wear (**b**).

2.3.2. Thermal Mesh

To compute the temperature evolution within the abradable layer following contact events, a second mesh is added. The latter consists of a two-dimensional thermal mesh superimposed to the mechanical one, as illustrated in Figure 3, with one degree of freedom per node, the nodal temperatures. Along the circumferential direction, one thermal element is considered every R_s mechanical elements, and a contact on any of the R_s mechanical elements will provide a heat flux for the corresponding thermal element, see Figure 3.

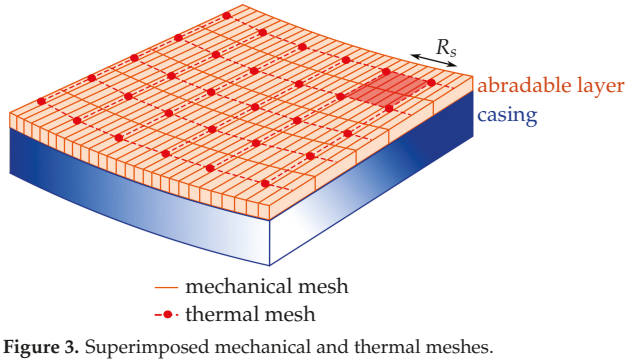

Figure 3. Superimposed mechanical and thermal meshes.

The heat equation, solved on the thermal mesh, is given by [14]:

$$\mathbf{C}_T\dot{\mathbf{T}} + \mathbf{K}_T\mathbf{T} = \mathbf{F}_T \tag{6}$$

in which $\mathbf{T}$ contains the nodal temperatures, $\mathbf{C}_T$ denotes the thermal capacity matrix, $\mathbf{K}_T$ is the thermal conductibility matrix, and the nodal heat flux vector $\mathbf{F}_T$. Thermics and mechanics have different time scales: while the explicit time integration scheme typically requires a time step of 10^{-7} s, thermal problems can be solved with time steps as large as 1 s. Therefore, this equation and the blade equation of motion (Equation (3)) are solved using different time discretizations: the heat equation is

solved every R_t mechanical time steps. The use of these two different space discretization significantly lowers computation times.

The heat flux $\mathbf{F}_T$ in Equation (6) is assumed proportional to the friction forces between the abradable coating and the blade, or if all the abradable coating is removed, between the casing and the blade. At each thermal iteration, the sum of the heat flux generated during the R_t last mechanical time steps is considered, such as:

$$\mathbf{F}_T = \sum_{R_t} q_T \mu \mathbf{t}_n \|\mathbf{v}_t\| \tag{7}$$

in which μ is the friction coefficient (between the abradable coating and the blade or between the casing and the blade depending of the contact components), $\mu\mathbf{t}_n$ the friction forces, $\mathbf{v}_t$ the relative tangential abradable layer/blade velocity (which is approximated here by the blade angular speed Ω) and q_T is a coefficient that will be calibrated in the following using experimental results.

The heat equation (Equation (6)) is solved at each thermal time step, i.e., every R_t mechanical time steps. The evolution of the temperature within the abradable layer is computed at each thermal iteration $t+1$ by solving the system of equations [14]:

$$\mathbf{T}(t+1) = \mathbf{T}(t) + \bar{\mathbf{K}}_T^{-1} \bar{\mathbf{F}}_T(t) \tag{8}$$

with:

$$\begin{aligned} \bar{\mathbf{K}}_T &= \mathbf{C}_T + \alpha' \, \Delta t \, \mathbf{K}_T \\ \bar{\mathbf{F}}_T(t) &= \Delta t \left(\mathbf{F}_T(t) - \mathbf{K}_T \mathbf{T}(s) \right) \end{aligned} \tag{9}$$

where α' is the integration scheme parameter and $\Delta t = R_t h$ is the thermal time step. One can demonstrate [14] that, in a linear framework, the integration scheme is stable if $\Delta t < \frac{2}{(1-2\alpha')\omega_{max}}$, unconditionally stable for $\alpha' \geq \frac{1}{2}$, and stable without oscillation for $\Delta t < \frac{2}{(1-\alpha')\omega_{max}}$, where ω_{max} denotes the largest eigenfrequency of $\mathbf{C}_T^{-1}\mathbf{K}_T$. In this work, the value of α' is set to $\frac{1}{2}$ such that the scheme is unconditionally stable.

2.3.3. Thermo-Mechanical Coupling

Thermal and mechanical problems are coupled according to two aspects: (1) the thermal expansion of the abradable layer, and (2) the modification of its material properties with temperature. Based on the temperature computed using the thermal mesh, the thermal expansion of each mechanical abradable layer's element at a given iteration t is computed as followed, assuming a linear thermo-elastic constitutive law:

$$\varepsilon_T(t) = \alpha_T \left(\mathbf{T}(t) - \mathbf{T}(t-1) \right) \tag{10}$$

with ε_T the thermal deformation and α_T the thermal expansion coefficient. For the dependence of material properties with temperature, a linear variation of the Young's modulus E and plastic modulus K of the abradable coating with temperature is assumed in the model. This law can be used as first approximation for aluminum-silicium alloys [15].

2.4. Summary

The blade model, the casing model and the mechanical mesh of the abradable layer are modeled using an existing strategy detailed in [9]. A thermal mesh of the abradable layer is added here to compute temperature increases following contact events. In order to compute temperature elevations within the abradable layer, the heat flux provided by the blade to the abradable layer is assumed proportional to the friction forces between these two components. Two discretization parameters—the spatial and time discretization parameters, denoted R_s and R_t respectively—are involved in the thermal model.

3. Convergence Analysis

In this section, the convergence of the results with respect to both space and time discretization parameters, R_s and R_t respectively, is analyzed. More particularly, the convergence is presented in terms of the abradable layer's wear and temperature profiles at both the leading (LE) and the trailing edges (TE) as well as in terms of blade stresses. Simulations are carried out using the high-pressure (HP) compressor blade's finite element model shown in Figure 4a, and the retained nodes in the reduced order model are marked as red dots.

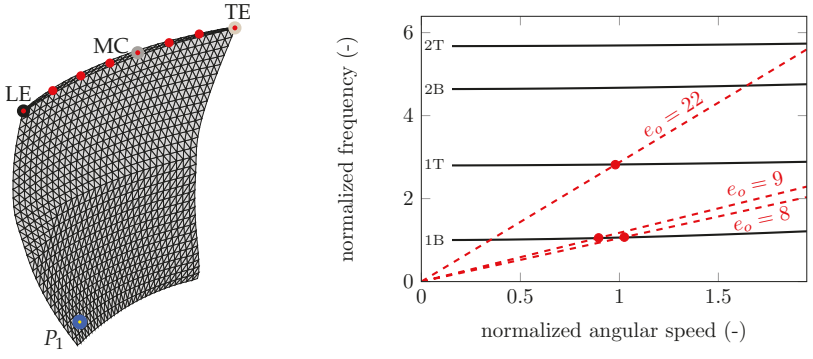

(**a**) (**b**)

Figure 4. Finite element model (**a**) and Campbell diagram (**b**) of the HP compressor blade.

The simulations are run over 100 blade revolutions, at constant angular speed. The chosen angular speed, denoted $\Omega^{\text{HP}}_{\text{exp}}$, corresponds to the excitation of the first torsion (1T) mode with the 22nd engine order (e_o), see the Campbell diagram in Figure 4b [3]. In particular, the selected angular speed is slightly higher than the one corresponding to the curve's intersection because of contact stiffening. The angular speed axis in Figure 4b is normalized using $\Omega^{\text{HP}}_{\text{exp}}$ as reference. The contact is initiated by a 2-lobe casing deformation (see Figure 1). For all simulations, 20,000 mechanical abradable layer elements are considered along the circumferential direction, which ensures that convergence has been reached. The mechanical time step is fixed to h of 10^{-7} s for all simulations. The used value for the friction coefficient μ is 0.1.

Convergence of wear and temperature profiles at both leading and trailing edges at the end of the simulation is shown in Figures 5 and 6, respectively in terms of space and time discretizations. Results show an accurate description of wear and temperature profiles within the abradable layer for $R_s > 100$ (see Figure 5). Small differences appear in temperature profiles for the lowest R_s values, which correspond to a coarser thermal mesh (see the curve referring to $R_s = 100$ in Figure 5c,d).

However, results obtained for all R_t values are perfectly superimposed (see Figure 6). This is due to the different time scales between mechanical and thermal phenomena: considering $R_t = 5000$ leads to a thermal time step of $\Delta t = R_t h = 5000 \times 10^{-7} = 5 \times 10^{-4}$ s, which remains much lower than typical thermal time scales. Simulations with $R_t = 5000$ leads therefore an accurate solution of the heat equation.

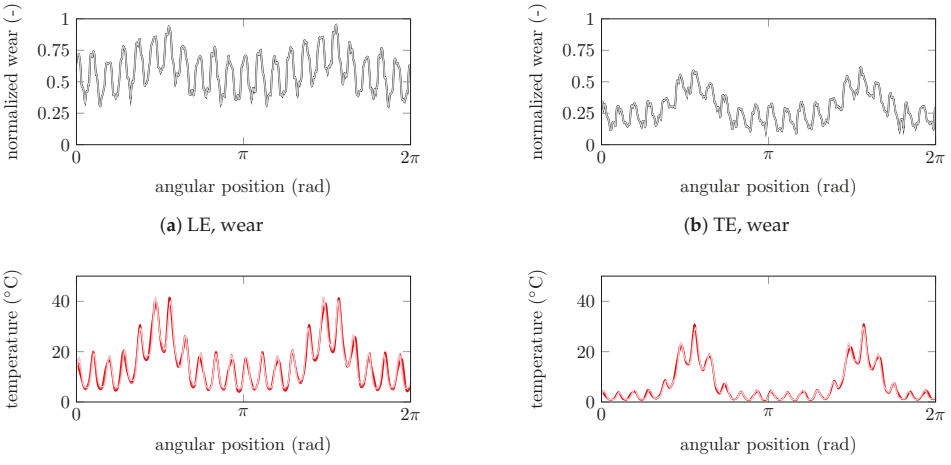

(**a**) LE, wear (**b**) TE, wear

(**c**) LE, temperature (**d**) TE, temperature

Figure 5. Convergence analysis of the wear and temperature profiles at the end of the simulation at the leading and trailing edge with the number of thermal abradable coating elements $n_{ab,th}$: $n_{ab,th} = 80$ or $R_s = 250$ (——/——), $n_{ab,th} = 100$ or $R_s = 200$ (——/——), $n_{ab,th} = 200$ or $R_s = 100$ (——/——), $n_{ab,th} = 250$ or $R_s = 80$ (——/——).

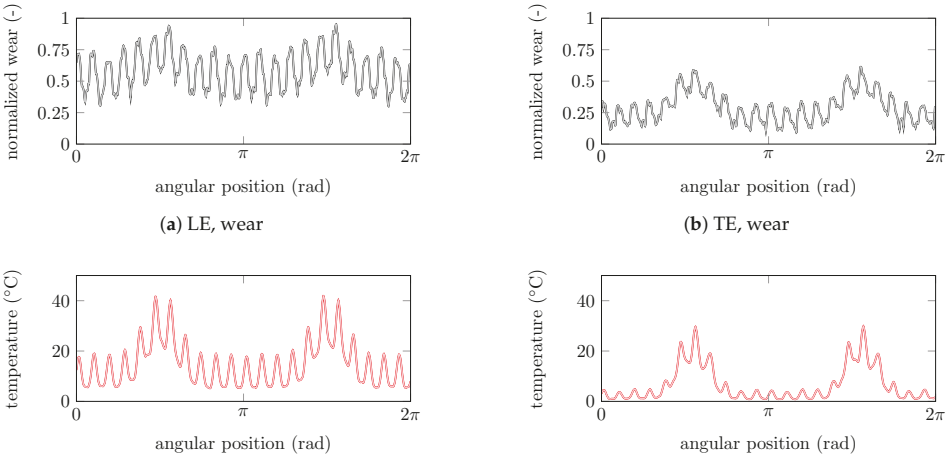

(**a**) LE, wear (**b**) TE, wear

(**c**) LE, temperature (**d**) TE, temperature

Figure 6. Convergence analysis of the wear and temperature profiles at the end of the simulation at the leading and trailing edge with R_t: $R_t = 1$ (——/——), $R_t = 500$ (——/——), $R_t = 1000$ (——/——), $R_t = 5000$ (——/——).

Convergence of blade related quantities is verified in terms of stresses at node P_1, shown in blue in Figure 4a, close to the blade root. This quantity is indeed very sensitive since it relies on predicted blade dynamics and abradable profile evolution. Figure 7 shows the time evolution of the blade stress at node P_1 for several R_s and R_t values. Stresses are computed at the initiation of the interaction. Curves are perfectly superimposed for all R_s and R_t values. This perfect superimposition comes from

the superimposition of the abradable wear profile—the latter indeed directly influences the blade dynamics—for all R_s and R_t values (see Figures 5a,b and 6a,b).

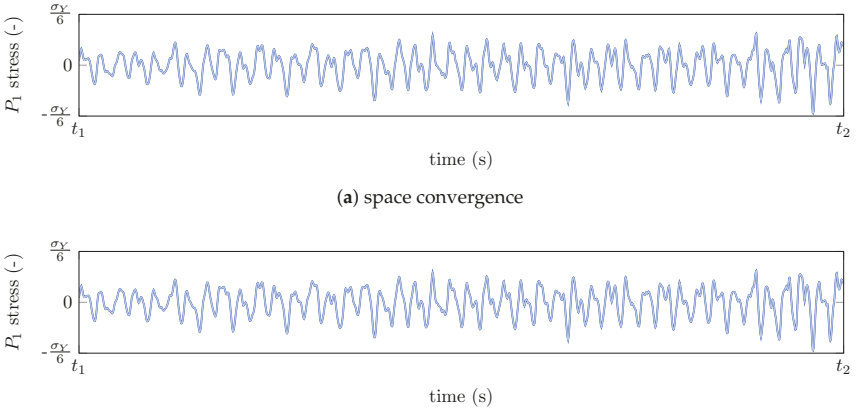

Figure 7. Time evolution of blade stresses (**a**) with R_s: $R_s = 80$ (——), $R_s = 100$ (——), $R_s = 200$ (——), $R_s = 250$ (——), and (**b**) R_t: $R_t = 1$ (——), $R_t = 500$ (——), $R_t = 1000$ (——), $R_t = 5000$ (——).

The stress field within the full blade finite element mesh at the same time step $t = t_2$ is shown in Figure 8 for different R_s values, and in Figure 9 for different R_t values. The used color code goes from white—no stress—to dark blue—highest stress level, i.e., $\frac{\sigma_Y}{6}$, with σ_Y the yield stress of the blade. Almost identical stress fields are retrieved for all R_s and R_t values. This observation is consistent with the perfect superposition of the stresses time evolution in Figure 7. The dynamical behavior of the blade is therefore identical for all tested R_s and R_t values.

Finally, computation times associated with each simulation are depicted in Figure 10. The horizontal dotted line refers to the simulation time without computing temperatures. All simulations have been performed on a standard computer with an i7-processor. The chosen trade-off between results accuracy and computation times yields 200 thermal abradable coating elements along the circumferential direction (i.e., $R_s = 100$) and $R_t = 1000$. The value of these two parameters is fixed for the following simulations.

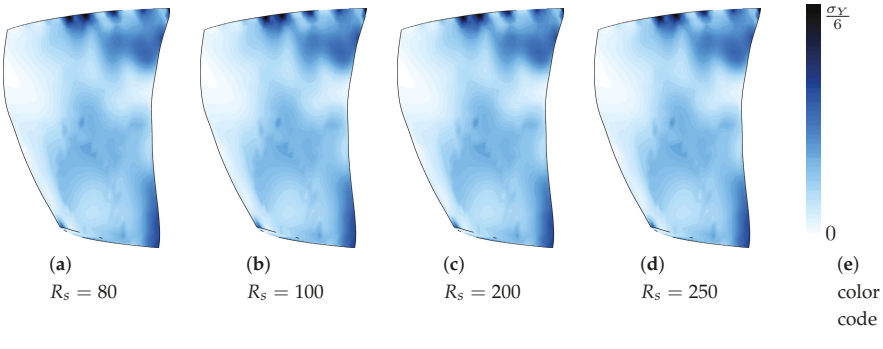

Figure 8. Blade stress fields for different R_s values.

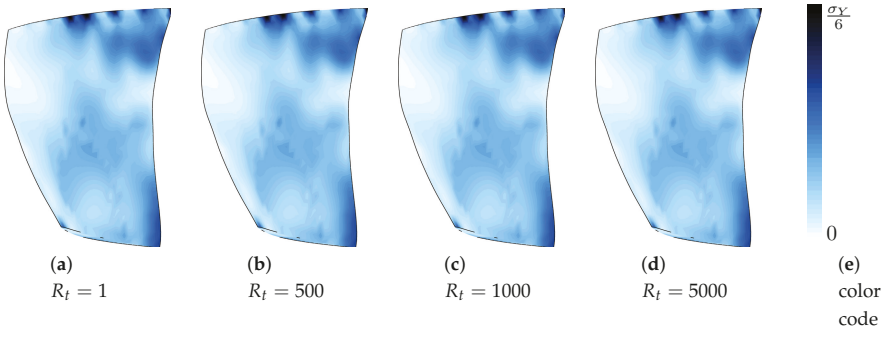

Figure 9. Blade stress fields for different R_t values.

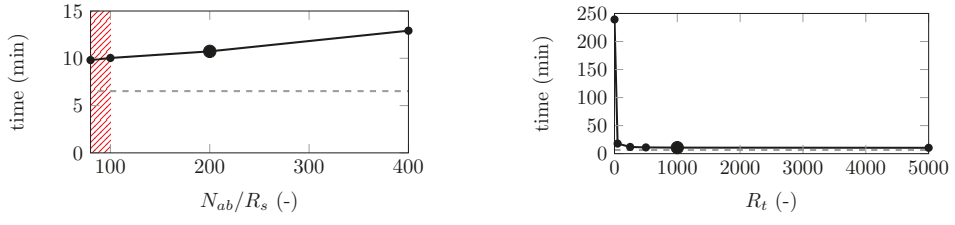

Figure 10. Evolution of the computation time with (**a**) the number of thermal abradable coating elements, and (**b**) with R_t.

4. Experiments

The previously described model is applied here on two experimental data sets: (1) a high-pressure (HP) compressor's bladed disk, and (2) a low-pressure (LP) compressor's bladed disk. Both experimental set-up are first detailed. Then, the temperature field recorded on the first experiment set-up is used to calibrate the numerical thermal model. Finally, the second test is simulated using the calibrated model, and the obtained temperatures are compared with the experiments.

4.1. Calibration of the Thermal Model

The aim of this section is to calibrate the thermal model based on previously published experimental data [3]. The set-up consists of a rotating bladed disk that undergoes contact events with an abradable layer deposited onto a simplified casing. Both the bladed disk and the casing are made of titanium materials, and the abradable layer is made an AlSi alloy. An infrared camera in front of the test set-up recorded temperature increases [3]. The color code ranges from white—no temperature increase—to red—high temperatures. The targeted angular speed is $\Omega_{\text{exp}}^{\text{HP}}$, which corresponds to the 22nd engine order excitation of the first torsion mode, see Figure 4b. 22 hot spots are observed along the casing circumference, and temperatures above 80 °C have been recorded experimentally, as depicted in Figure 11a. A more detailed description of the test set-up and data analyses can be found in [3].

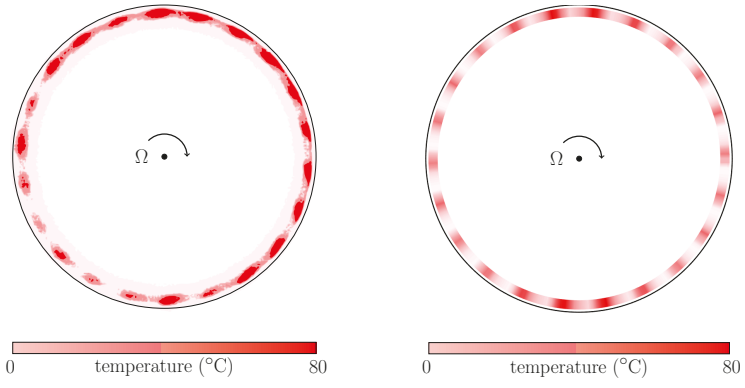

(**a**) experimental [3] (**b**) numerical

Figure 11. Temperature profile for the HP compressor test case.

Simulations are carried out over 100 blade revolutions at constant angular speed corresponding to the experimental value. The values for R_s and R_t parameters are fixed to the values selected in the convergence analysis. The value of the heat flux parameter q_T is calibrated to retrieve the same order of magnitude of temperature increase. The blade displacements at the leading edge (LE), mid-chord (MC) and trailing edge (TE), obtained using the calibrated model, are depicted in Figure 12. The blade displacement exhibits an increasing amplitude (for $t \in [0 - 0.51]$ s) followed by a decreasing amplitude of vibration (for $t > 0.51$ s). Displacements are similar to the ones obtained in [3] without taking into account thermal effects. This similarity in blade displacements is expected because of the low temperature increases during this test (80 °C): the thermal expansion of the abradable layer remains limited and does not significantly affect the blade dynamics.

The corresponding temperature profile at the leading-edge side at $t = 0.51$ s along the abradable layer circumference is plotted in Figure 11b. The 22 high temperature points are retrieved, with the same order of magnitude then the experimental temperature field, i.e., 80 °C (see Figure 11b) which was the calibration point of the thermal model.

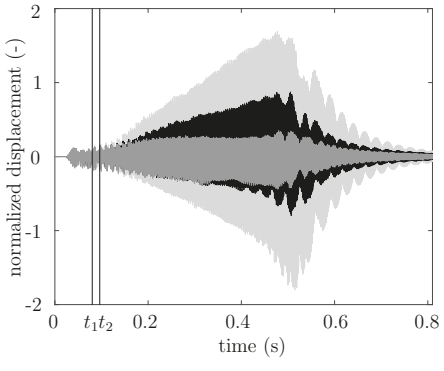

Figure 12. Time evolution of the blade displacement at the leading edge (——), mid-chord (——), and trailing edge (——) for the HP compressor test case.

The obtained wear profile at the leading edge, mid-chord and trailing edge at $t = 0.51$ s is shown in Figure 13. 22-wear lobes are observed at the leading and trailing edges because of the excitation of

the 22-engine order. At mid-chord, 2-wear lobes are obtained, corresponding to the casing deformation applied at the beginning of the simulation to initiate contacts. Because the responding mode is the first blade torsion (1T) mode, the blade has a low amplitude of vibration at mid-chord, and the 22 wear lobes are not visible (see Figure 13b). The temperature profile along the surface of the abradable layer can also be visualized with the red line along the wear profile (therefore, the temperature field in Figure 11b is retrieved in Figure 13a along the wear profile). The high temperature areas—in red in Figure 13a—are localized in front of the 22 wear lobes, as in the experiments, because the heat flux injected within the abradable layer is assumed proportional to the blade/abradable layer friction forces. Moreover, due to heat conduction within the abradable layer from the mid-chord location to the leading and trailing edge sides and to the initial 2-lobe casing deformation, higher temperature levels are achieved in the vicinity of angular positions $\frac{\pi}{2}$ and $\frac{3\pi}{2}$.

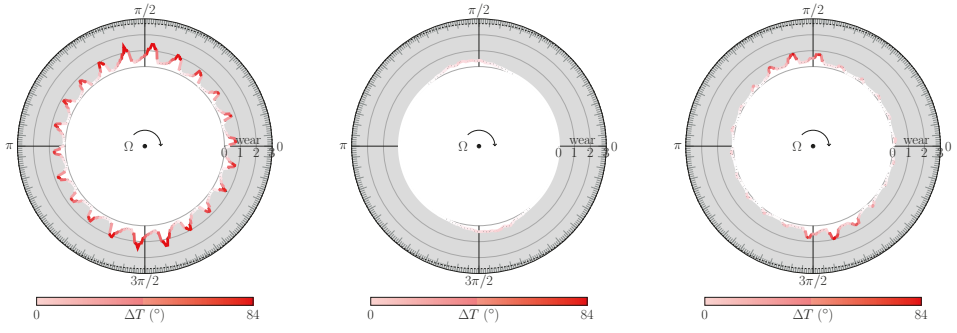

(**a**) LE (**b**) MC (**c**) TE

Figure 13. Wear and temperature profiles at 0.51 s for the HP compressor test case.

The numerical model allows prediction of the blade dynamics and wear profiles, with an order of magnitude for the temperatures which is consistent with experimental data. The calibrated model is therefore assumed relevant and is used in the next section to simulate the second test case.

4.2. Application of the Calibrated Model

The previously calibrated model is used in this section to predict the temperature elevation for the second experimental set-up [2]. This second test is carried out on a single stage of a LP compressor's bladed disk. The finite element model of the LP compressor blade can be seen in Figure 14a. A detailed description of the test and acquired signals can be found in [2]. One blade of the bladed disk is longer than the others to ensure that the contact between the rotor and the casing occurs on this blade. A strain gauge is located on the center of the blade to record its dynamical response. The bladed disk is mounted on a shaft and in a vacuum chamber to avoid aerodynamical loadings and temperature elevation by heat convection. Accelerometers and thermocouples are placed on the external surface of the casing, which is initially ovalized due to assembly conditions. The angular speed is chosen using the Campbell diagram shown in Figure 14b such as the first eigenfrequency—corresponding to the first bending (1B) mode—is excited by the 7th engine order. More precisely, the angular speed is slightly higher than the one corresponding to the intersection of the 1B mode with the 7th engine order due to contact stiffening. During the test, the angular speed is progressively increased to achieve the targeted speed, denoted $\Omega_{\text{exp}}^{\text{LP}}$.

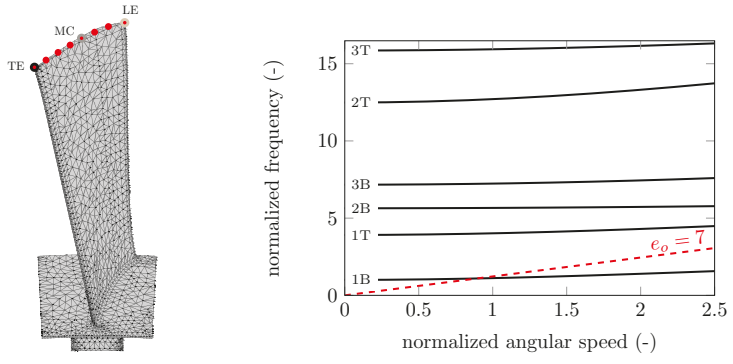

(**a**) (**b**)

Figure 14. Finite element model (**a**) and Campbell diagram (**b**) of the LP compressor blade.

The available data acquired during the experiments are: (1) the time evolution of the blade stresses recorded by the strain gauge, (2) the *post-mortem* wear profile, measured at the end of the experiments, and (3) temperatures on the outer surface of the casing recorded by the temperature probes at eight different angular positions. The detailed analysis of the time evolution of the blade stresses recorded by the strain gauge during the experimental test can be found in [2]. Contrary to the first test case on the HP compressor (see Section 4.1), the time response of the blade displacement always increases with time during the test, leading to a diverging blade motion.

The post-mortem wear profile is measured at the leading edge, mid-chord and leading edge at the end of the experiments using a coordinate measuring machine, every 10° along the circumferential direction. They are pictured in Figure 15. Seven deep wear lobes are observed on the trailing edge's side, with a high wear depth (see Figure 15c). Seven lobes are also observed at mid-chord (see Figure 15b), while almost no wear appears at the leading edge (see Figure 15a). The low wear level at the leading edge is due to the initial ovalization of the casing at the beginning of the test. These differences in the LE, MC and TE wear depths can be explained by the excitation of the 1B mode, which exhibit a large vibration amplitude at the TE and MC and a lower amplitude at the LE. Finally, temperature probes, located on the outer surface of the casing in front of the blade mid-chord at different angular positions, recorded the temperatures during the test. Temperatures measured at the end of the diverging motion are given in Figure 15b. They ranged from +15 to +125 °C. These temperatures seem to be higher at the middle of wear lobes, but data are very sensitive to the angular position. Nevertheless, this allows obtaining of an order of magnitude of the temperature level on the outer surface of the casing. Within the abradable layer, the achieved temperatures will logically be higher than the probe values.

Numerical simulations are conducted to reproduce the test conditions using the calibrated model. The simulation is carried out over 40 blade revolutions at constant angular speed $\Omega_{\text{exp}}^{\text{LP}}$. The space and time discretization parameters, R_s and R_t respectively, are kept the same than the one chosen in Section 3. The convergence of the results for these two parameters has been verified, but the results are not shown here for the sake of brevity. The finite element model of the instrumented blade is shown in Figure 14a. The red dots at the blade tip correspond to nodes retained in the reduced order model. The location of the leading edge (LE), mid-chord (MC), and trailing edge (TE) is also shown.

The obtained time evolution of the blade displacement at the leading edge, mid-chord and trailing edge is shown in Figure 16. As observed in the experiments, amplitude of vibration always increases with time, leading to a divergent interaction. Therefore, stresses within the blade reach the yield stress of the blade material thus leading to crack initiation, in agreement with experimental observations [2]. Also, amplitudes of the blade displacement are higher at the trailing edge and mid-chord, while the

vibration amplitude remains small at the leading edge. The dynamical behavior of the system is therefore well predicted by the numerical model.

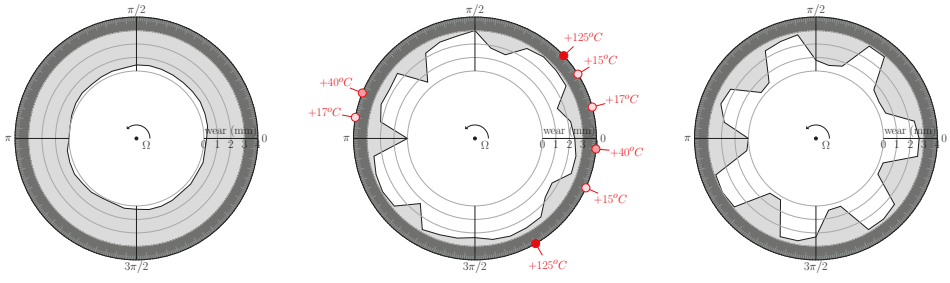

(**a**) LE (**b**) MC (**c**) TE

Figure 15. Experimental wear and temperature profiles for the LP compressor test case [2].

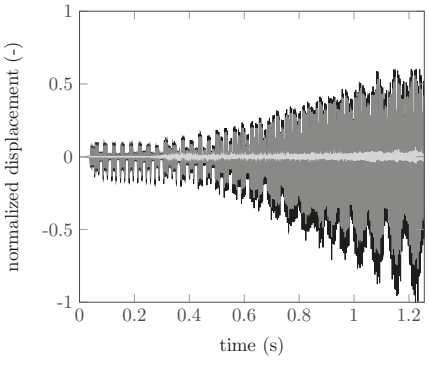

Figure 16. Time evolution of the blade displacement at the leading edge (——), mid-chord (——), and trailing edge (——) for the LP compressor test case.

Figure 17 shows the wear profile at the leading edge, mid-chord and trailing edge at the end of the simulation. These wear profiles obtained numerically can be directly compared with the experimental ones, shown in Figure 15. As in the experiments, seven deep wear lobes are observed at the trailing edge, because of the high blade amplitude of vibration. The abradable layer is removed over all its thickness at the angular positions of the seven wear lobes, and the blade may be in contact with the casing. Seven wear lobes are also observed at mid-chord, and two wear lobes are obtained numerically at the leading edge due to the initial ovalization of the casing. The temperature profile at the end of the simulation is also superimposed along the wear profile in Figure 17. The color code goes from white color—that corresponds to no temperature increase—to red—highest temperature increases. High temperature points are observed in the vicinity of wear lobes. The maximum temperature reached numerically within the abradable layer is 274 °C. This value is higher than the experimental observation (125 °C), but the temperature probes are located on the outer surface of the casing. It seems reasonable to expect higher temperature levels within the abradable layer, considering the heat localization and diffusion time. The order of magnitude of the temperature obtained using the calibrated model to simulate this second experimental test is therefore realistic.

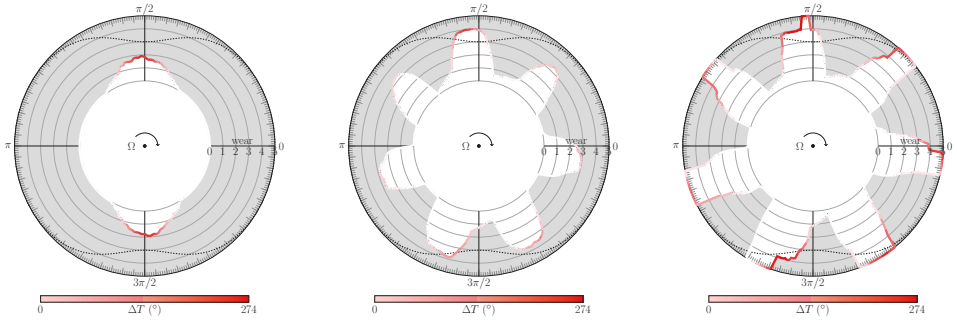

(**a**) LE (**b**) MC (**c**) TE

Figure 17. Numerical wear and temperature profiles for simulations on the LP compressor's blade.

4.3. Partial Conclusion

The numerical model calibrated using the first experimental test case provides realistic temperature values for both experimental test cases. Variations in the abradable coating's material properties or in the probe localization can explain the observed differences between numerical and experimental results. Nevertheless, the order of magnitude of the numerically predicted temperature is coherent with the experiments. Since the thermal flux is modeled as proportional to friction forces—and therefore proportional to the contact forces—the agreement between the temperatures for the two test cases can be directly related to coherent order of magnitudes for numerically predicted contact forces.

Additionally, for both investigated cases, the predicted blade dynamics is similar to experimental observations: (1) for the HP compressor case, a non-diverging interaction on the torsion mode with the 22nd engine order is retrieved, and (2) for the LP compressor blade, a diverging interaction with the first bending mode and the 7th engine order is obtained as in the experiments.

As a conclusion, thanks to the verification of the order of magnitude of contact forces for independent set-ups, the numerical model is assumed predictive in different configurations. Therefore, further detailed investigations on the system dynamical behavior and on the resulting rotor/stator interactions can be performed with confidence in the numerical predictions.

5. Sensitivity Analysis

In this section, a detailed sensitivity analysis of the observed interactions is carried out for both the HP and LP compressor blades. More particularly, the effect of the angular speed and the initial clearance between the blade and the abradable layer is investigated. Indeed, previous work showed that a precise modeling of the blade/casing clearances is key to accurately predict contact interaction phenomena [16]. Due to intrinsic nonlinearity of the system, a small change in the engine working conditions may lead to completely different amplitudes of vibration and dynamical behavior.

5.1. High-Pressure Compressor Blade

A sensitivity analysis in terms of the angular speed and the initial clearance is performed here on the HP compressor blade shown in Figure 4a. The calibrated model is used for all simulations. First, the influence of the angular speed is studied on its own. Indeed, due to contact stiffening and to the intrinsic nonlinear nature of the studied phenomena, the angular speed at which interactions may occur is difficult to predict *a priori*. The dynamical response of the system is very sensitive to the angular speed. Simulations are therefore carried out over a range of angular speeds in the vicinity of the targeted interaction speed. Then, the same analysis is performed with a variation of the initial clearance since this parameter is key for contact interaction initiation. Finally, their coupled influence is analyzed.

5.1.1. Influence of the Angular Speed

Simulations are performed over a wide range of angular speeds around the experimental angular speed, denoted Ω_{exp}^{HP}. Each simulation is carried out at constant angular speed over 100 blade revolutions.

The evolution of the wear profile for different angular speeds at both leading and trailing edges along the circumference of the abradable coating taking into account thermal effects is shown in Figure 18. Dark areas refer to high wear levels while white color correspond to no wear. Depending on the angular speed, different interactions are observed: 9-wear lobes are identified with a high wear level around 0.95 Ω_{exp}^{HP} (excitation frequency corresponding to crossing between 9th engine order and the first blade bending mode, see Figure 4b), 22-wear lobes around Ω_{exp}^{HP} (crossing between 22nd engine order and the first blade torsion mode in Figure 4b), and 8-wear lobes around 1.05 Ω_{exp}^{HP} (crossing between 8th engine order and the first blade bending mode, see Figure 4b). Between these interaction areas, the observed 2-wear areas at angular positions $\frac{\pi}{2}$ and $\frac{3\pi}{2}$ are due to the initial casing deformation. Figure 19 shows the temperature profiles for different angular speeds at both leading and trailing edges along the circumference of the abradable coating. High temperature areas are observed in the vicinity of wear lobes because of the definition of the heat flux which is proportional to the blade/abradable layer friction forces. The two observed bending interactions (with engine orders 9 and 8) respond over a large angular speed range. The wear depth and the temperature increase are also higher, with all the abradable layer removed and localized high temperature points. When starting the engine, the angular speed progressively increases up to the nominal value. This wide interaction area will therefore be crossed. The torsion interaction occurs for a limited angular speed range. The wear depth is also lower than for the bending interaction, and the temperature is more uniform along the casing circumference.

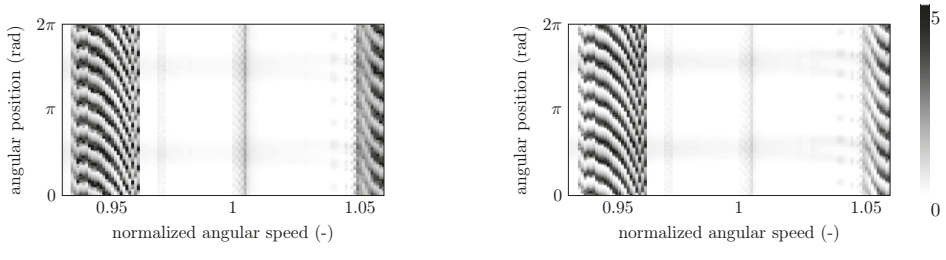

(**a**) LE (**b**) TE

Figure 18. Evolution of the wear profile with the angular speed for the HP compressor blade.

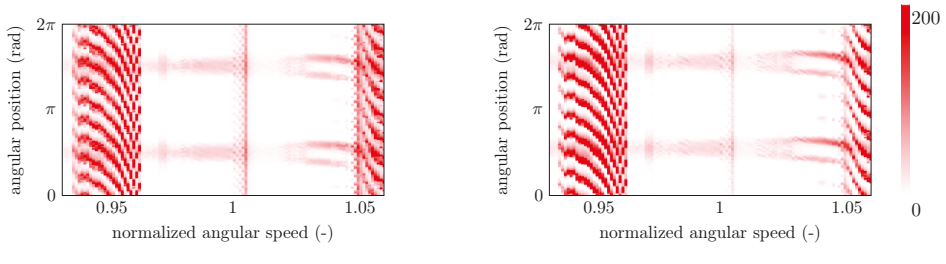

(**a**) LE (**b**) TE

Figure 19. Evolution of the temperature profile with the angular speed for the HP compressor blade.

A succession of blade/casing interactions are observed as the angular speed increases, with both bending and torsion modes. Abrupt changes of dynamical behavior are observed, with higher

wear depth for bending interactions. The angular position $\frac{\pi}{2}$ and $\frac{3\pi}{2}$ are privileged areas for high temperatures.

5.1.2. Influence of the Initial Clearance

Various research has been conducted to quantify the effect of the clearance between the tip of the blades and the casing from the aerodynamical point of view because of its high influence on the engine performance [17–20]. In this section, a sensitivity analysis to the clearance between the blade and the abradable coating is carried out in terms of structural dynamics and rotor/stator interaction.

The evolution of the frequency response function of the blade displacement at constant angular speed, equal to Ω_{exp}^{HP}, for an increasing initial clearance is shown in Figure 20. Three distinct areas can be identified, for which different modes respond. Area 1 corresponds to an interaction with the first bending mode. Area 2 is related to the 22-lobe interaction with the torsion mode. In area 3, for which the initial gap is larger ($>$0.38), the bending mode is again excited but with lower amplitude and a different engine order. The abrupt changes observed between the different areas, especially between areas 2 and 3, are due to the nonlinear intrinsic characteristic of contact interactions. The differences in the initial conditions lead to a system response along different modes.

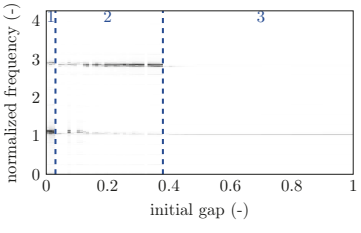

Figure 20. Evolution of the frequency response function of the blade displacement with the initial clearance for the HP compressor blade.

The evolution of the wear profile at the leading and trailing edge with the initial clearance is shown in Figure 21, and the corresponding evolution of the space Fourier transform of the wear profile is depicted in Figure 22. The same three areas can be distinguished. In area 1, 17-wear lobes are observed at both leading and trailing edges, with a high wear level. Wear level is slightly higher at the leading edge than the trailing edge. In area 2, 22-wear lobes can be identified. This corresponds to the 22-lobe interaction experimentally observed (see Section 4.1). This interaction is obtained over a large range of initial clearance ($[0.05 - 0.38]$). In area 3, which corresponds to larger initial gaps, even harmonics and 2 wear lobes are obtained. These 2-wear lobes are due to the initial deformation of the casing (see Figure 1), and no interaction occurs for high clearance values. The wear level is also lower in the area.

The associated temperature maps are shown in Figure 23. As expected, the three areas can also be observed, with respectively 17, 22 and 2 high temperature spots. However, in the second area, two high temperature areas can be additionally shown. This is because the first torsion mode is mainly excited, and at the middle of the blade, only two contact areas are observed (related to the 2-wear-lobe initial casing deformation) instead of 22. The diffusion within the abradable coating in these two areas leads to higher temperatures.

These results suggest that a clearance reduction may lead to unexpected effects on the engine dynamics in terms of rotor/stator interactions. On the contrary, a small increase of the initial clearance completely eliminates the interaction of interest, which would be beneficial for the engine blade dynamics if this gap increase does not affect the overall aerodynamic performance. Moreover, the clearance reduction does not have the same effect than an angular speed increase. Even if these two variations of configuration both lead to a blade-tip/abradable layer distance

reduction—centrifugal loadings are taken into account in the model—the 17-wear lobes interaction is initiated only at low clearance values.

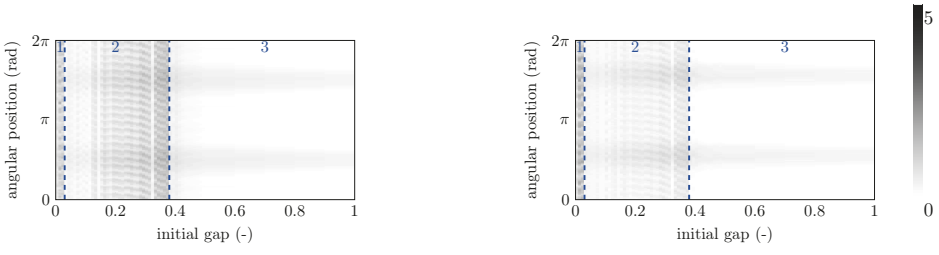

(**a**) LE (**b**) TE

Figure 21. Evolution of the wear profile with the initial clearance for the HP compressor blade.

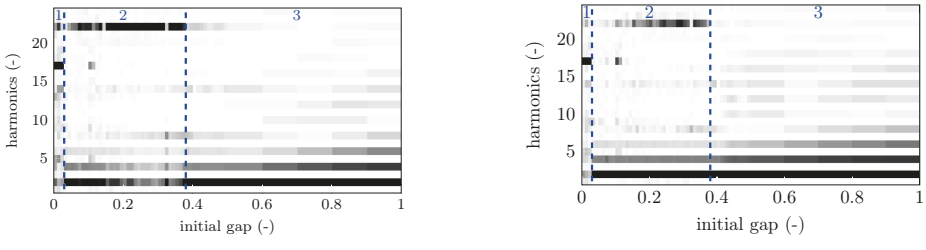

(**a**) LE (**b**) TE

Figure 22. Evolution of the space Fourier transform of the wear profile with the initial clearance for the HP compressor blade.

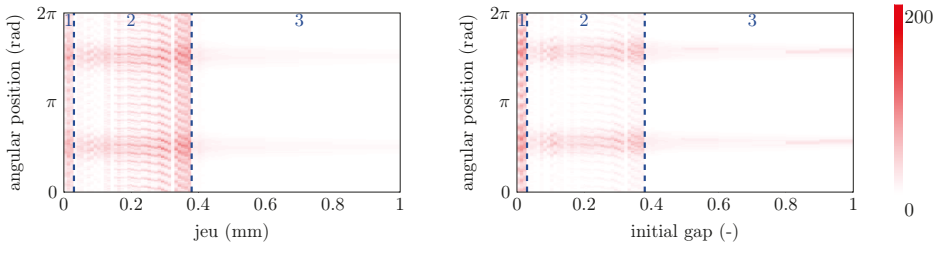

(**a**) LE (**b**) TE

Figure 23. Evolution of the temperature profile with the initial clearance for the HP compressor blade.

5.1.3. Cross Analysis

Depending on the angular speed and the initial clearance, different interactions have been observed. A coupled influence of both parameters is carried out in this section. In particular, Figure 24 summarizes the number of wear lobes obtained depending on the angular speed and the initial clearance. The angular speed axis is normalized using the experimental value as reference. Three different interactions are observed: 5 wear lobes (■) at higher angular speed for low initial gap values, 17 wear lobes (■) at low initial gap values, and 22 wear lobes (■) for intermediate gap values.

The experimentally observed 22-wear-lobe interaction occurs for smaller initial clearance values as the angular speed increases. This can be explained by the centrifugal loading that increases with the

angular speed. Indeed, the effective gap between the blade and the casing is equal to the initial gap reduced by the centrifugal displacement of the blade at the considered angular speed. For the smallest values of the initial gap, a 17-wear-lobe interaction appears but it is initiated for some distinct gap values. The initiation of this interaction is therefore very sensitive to initial conditions. For angular speeds above 1.1 Ω_{exp}^{HP}, the clearance reduction leads to 5 wear lobes. For high initial clearance values, no interaction is observed for any angular speed. Therefore, the effect of the initial clearance leads to a more complex dynamics than the angular speed variation.

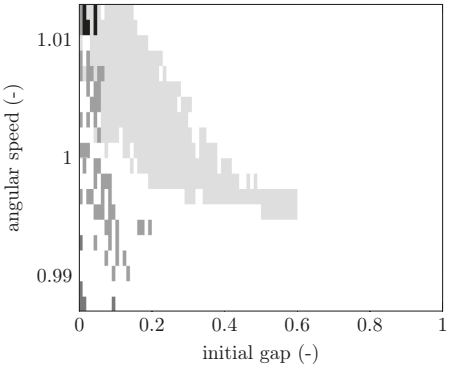

Figure 24. Number of wear lobes depending on the angular speed and the initial clearance for the HP compressor blade. (■): 5 wear lobes, (■): 17 wear lobes, (■): 22 wear lobes.

5.2. Low-Pressure Compressor Blade

The same three analyses are performed for the LP compressor blade in this section: the influence of the angular speed, of the initial clearance, and the coupled influence on the observed interactions.

5.2.1. Influence of the Angular Speed

The wear maps obtained over a range of angular speeds centered around the experimental angular speed (considered to be reference) at the LE and TE are shown in Figure 25, and the corresponding temperature maps are given in Figure 26. Abrupt changes in the blade behavior are observed. For the considered angular speed range, two interaction areas—with 8 and 7 wear lobes—are observed, both at the blade trailing edge only. These two interactions are due to the crossing between the first bending frequency with the different engine order curves. As for the HP compressor case, deeper wear lobes are observed for bending interactions. All the abradable layer is removed in front of lobes angular position. This means that higher blade amplitudes of vibrations are generated for these interactions. Between these two strong interaction areas, different numbers of lobes are observed: 4 lobes in the angular speed range $[0.9 - 1]\ \Omega_{exp}^{LP}$, 6 lobes for $\Omega > 1.05\ \Omega_{exp}^{LP}$, and an interaction with 13 wear lobes is also locally observed at the angular speed $\Omega = 1.1\ \Omega_{exp}^{LP}$.

High temperature points are observed in Figure 26 at high wear angular positions, especially for the interaction with the 8th and 7th engine orders. Indeed, deeper wear lobes are related to higher friction forces, and higher heat flux. In the angular speed range $[0.9 - 1]\ \Omega_{exp}^{LP}$, two high temperature areas are observed due to the casing ovalization. Heat conduction from the leading edge to the trailing edge exacerbates the two high temperature strips. For $\Omega > 1.05\ \Omega_{exp}^{LP}$, 4 high temperature bands are shown at angular positions $\frac{\pi}{2}$ and $\frac{3\pi}{2}$ again because of the high contribution of heat from the leading edge's side. For the same reason, the wear lobes at angular positions 0 and π leads to lower temperature levels because no contribution from the leading edge. At the angular speed $\Omega = 1.1\ \Omega_{exp}^{LP}$, 13 high temperature points are observed at the position of the wear lobes.

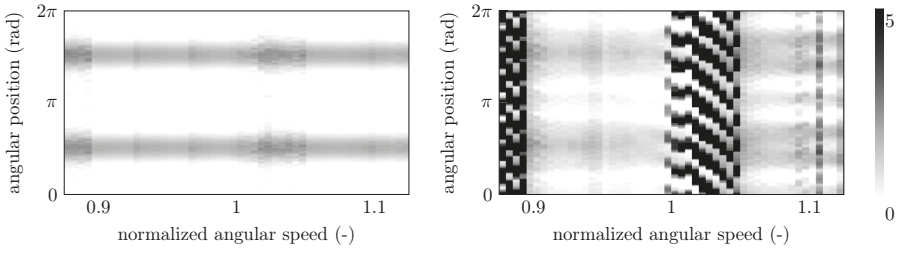

(**a**) LE (**b**) TE

Figure 25. Evolution of the wear profile with the angular speed for the LP compressor blade.

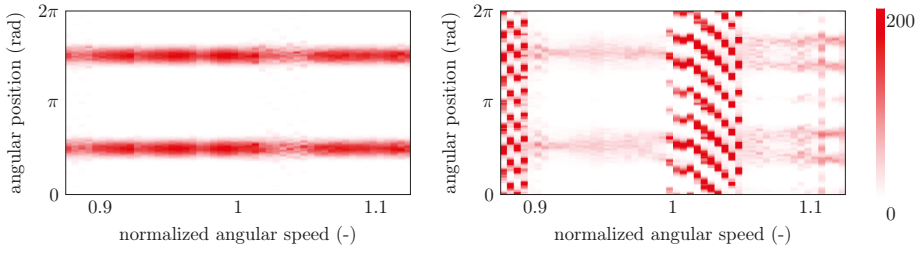

(**a**) LE (**b**) TE

Figure 26. Evolution of the temperature profile with the angular speed for the LP compressor blade.

5.2.2. Influence of the Initial Clearance

As for the HP compressor's blade, the influence of the initial clearance on the observed interaction is detailed. Higher gap values are studied since LP compressor blade are taller than blades within a HP compressor and have higher centrifugal displacements. Figure 27 show the evolution of the wear profile along the casing circumference while increasing the initial gap between the blade and the casing. The space Fourier transform of the wear maps with respect to the initial clearance is depicted in Figure 28. The evolution of the temperature profiles along the casing circumference with the initial gap is shown in Figure 29. On these graphs, three distinct areas can be identified. For low values of the initial gap, an unclear 7-wear lobes interaction is observed. When increasing the initial clearance, 7 deep wear lobes are obtained on the wear map at intermediate values. Finally, at higher values of the initial clearance, an abrupt change of behavior occurs, and no more interaction is observed. The 2 wear lobes correspond to the initial deformation of the casing. For all values, the interaction remains localized on the trailing edge only. The structure responds along its first bending mode, which exhibits a larger amplitude of vibration at the trailing edge. Contrary to the HP compressor case, deeper wear lobes are observed in area 2, while area 1 does not exhibits strong interactions. Therefore, reducing the initial clearances does not generate here unexpected and potentially damaging rotor/stator interactions. In Figure 29, high temperature points follow the wear profiles with a dominance (especially at low initial clearance) in the 2-wear-lobe areas because of the heat conduction within the blade. Because the wear depth is significant in area 2 at trailing edge, the heat transfer from the leading to the trailing edge is less pronounced than for the two other areas.

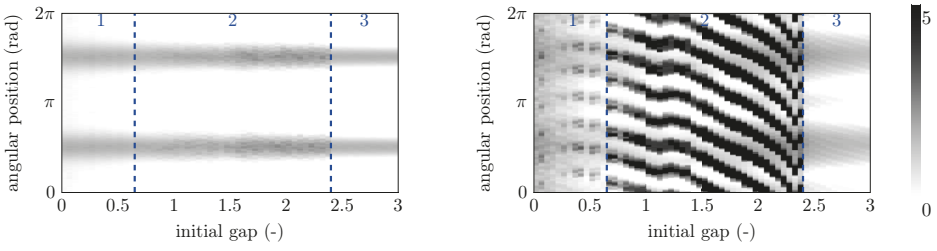

(**a**) LE (**b**) TE

Figure 27. Evolution of the wear profile with the initial clearance for the LP compressor blade.

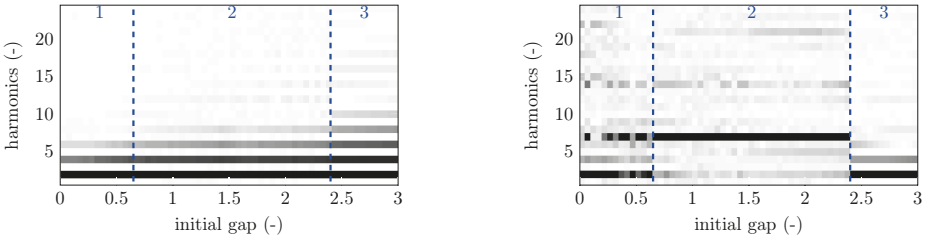

(**a**) LE (**b**) TE

Figure 28. Evolution of the space Fourier transform of the wear profile with the initial clearance for the LP compressor blade.

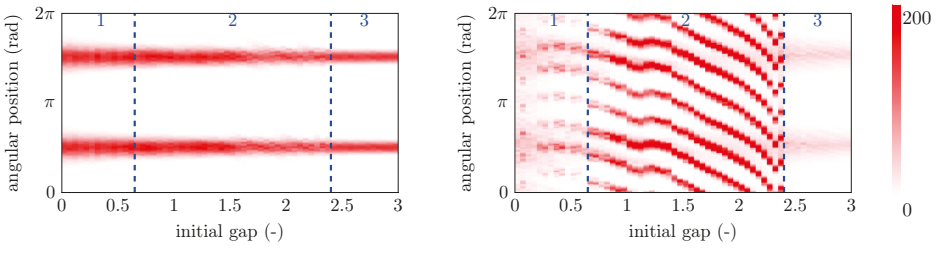

(**a**) LE (**b**) TE

Figure 29. Evolution of the temperature profile with the initial clearance for the LP compressor blade.

5.2.3. Cross Analysis

The interactions observed with respect to the initial blade-tip clearance and the angular speed are summarized in Figure 30. The angular speed axis is normalized using the experimental value as reference. Two different interactions are observed when varying the initial clearance and angular speed: 7 wear lobes (■), and 15 wear lobes (■). As for the HP compressor blade, the higher the angular speed, the lower initial clearance interactions occur. However, the two interaction areas are here well separated, with a more stable initiation of the interaction with the initial conditions. The 15 wear lobes is observed only at lower angular speed while the 7th engine order interaction responds for a large range of angular speeds and initial clearances. This cross analysis shows that depending on the engine nominal angular speed, a reduction of the nominal clearances in the engine design in order to improve the aerodynamic performance can lead to a risk of occurrence of interactions with other engine orders.

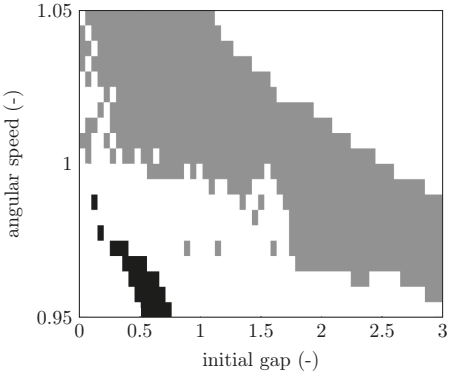

Figure 30. Number of wear lobes depending on the angular speed and the initial clearance for the LP compressor blade. (▪): 7 wear lobes, (■): 15 wear lobes.

6. Conclusions

This paper uses a numerical model taking into account thermal effects in the abradable coating to validate contact forces prediction through the comparison of two experimental set-up. The numerical modeling of the abradable layer consists of (1) a mechanical mesh made of independent two-node rod elements with elasto-plastic constitutive law to compute the abradable wear, and (2) a thermal mesh added to compute the evolution of the temperature in the abradable layer following blade contacts. The blade heat flux is assumed to be proportional to the friction forces between the blade and the abradable coating. A dependence of the mechanical properties of the abradable coating with temperature is also included. To reduce computation times, distinct space and time discretizations are used to solve the thermal and mechanical problems. A convergence analysis is performed, which shows that the space and time discretization has low effects on the obtained wear and temperature profiles as well as for the blade response.

A calibration of the blade heat flux has been carried out using experimental data acquired on a high-pressure compressor blade. The aim of the calibration was to retrieve the same temperature increases as observed in the experiments. This calibrated value has been kept to predict temperature levels for another set of experimental data, obtained from a low-pressure compressor blade. Because of the definition of the heat flux, proportional to the friction forces, the fact that realistic temperatures are obtained for two independent test cases with two distinct structures gives confidence in the numerically predicted contact forces.

Based on this calibrated model, further analyses in terms of the effect of the initial clearances—which is a key parameter in the initiation of contact interactions—and of the rotor angular speeds have been carried out. Both low-pressure and high-pressure compressor test cases have been investigated. A coupled influence of the angular speed and the initial clearance has also been conducted. It has been found that interactions occur for smaller initial clearance values as the angular speed increases. This is explained by the centrifugal load of the blade. But when decreasing the initial clearance at a given angular speed, unexpected interactions may appear, which were observed for the studied high-pressure compressor blade in particular. Different interactions for low gap values appear for this blade. However, for the low-pressure compressor blade, the studied interactions were more robust. Reducing the initial clearances is a common solution to improve aerodynamical engine performance. However, a detailed analysis of this clearance reduction is recommended since it may lead, for some blades, to detrimental dynamical behavior.

Author Contributions: Conceptualization, F.N. and A.B.; methodology, F.N.; validation, F.N.; formal analysis, F.N.; investigation, F.N.; writing—original draft preparation, F.N.; writing—review and editing, F.N. and A.B.; supervision, A.B.; project administration, A.B.; funding acquisition, A.B. All authors have read and agreed to the published version of the manuscript.

Funding: This research was supported by the Fonds de Recherche du Quebec—Nature et Technologies (FRQNT) and the Natural Sciences and Engineering Research Council of Canada (NSERC).

Conflicts of Interest: The authors declare no conflict of interest. The funders had no role in the design of the study; in the collection, analyses, or interpretation of data; in the writing of the manuscript, or in the decision to publish the results.

References

1. Williams, R.J. Simulation of blade casing interaction phenomena in gas turbines resulting from heavy tip rubs using an implicit time marching method. In Proceedings of the ASME Turbo Expo 2011 Conference, GT2011-45495, Vancouver, BC, Canada, 6–11 June 2011.
2. Millecamps, A.; Brunel, J.; Dufrénoy, P.; Garcin, F.; Nucci, M. Influence of thermal effects during blade-casing contact experiments. In Proceedings of the ASME 2009 IDETC & CIE Conference, ASME, San Diego, CA, USA, 30 August–2 September 2009.
3. Batailly, A.; Agrapart, Q.; Millecamps, A.; Brunel, J.F. Experimental and numerical simulation of a rotor/stator interaction event within an industrial high-pressure compressor. *J. Sound Vib.* **2016**, *375*, 308–331. [CrossRef]
4. Muszynska, A.; Bently, D.; Franklin, W.; Hayashida, R.; Kingsley, L.; Curry, A. *Influence of Rubbing on Rotor Dynamics—Part 1*; Technical Report NAS8-36179; NASA: Washington, DC, USA, 1989.
5. Borel, M.; Nicoll, A.; Schlapfer, H.; Schmid, R. The wear mechanisms occurring in abradable seals of gas turbines. *Surf. Coat. Technol.* **1989**, *39*, 117–126. [CrossRef]
6. Mandard, R.; Witz, J.F.; Boidin, X.; Fabis, J.; Desplanques, Y.; Meriaux, J. Interacting force estimation during blade/seal rubs. *Tribol. Int.* **2015**, *82*, 504–513. [CrossRef]
7. Salles, L.; Blanc, L.; Thouverez, F.; Gouskov, A. Dynamic analysis of fretting wear in friction contact interfaces. *Int. J. Solids Struct.* **2010**, *48*, 1513–1524. [CrossRef]
8. Baïz, S. Etude expérimentale du contact aube/abradable: contribution à la caractérisation mécanique des matériaux abradables et de leur interaction dynamique sur banc rotatif avec une aube. Ph.D. Thesis, Ecole Centrale de Lille, Villeneuve-d'Ascq, France, 2011.
9. Legrand, M.; Batailly, A.; Pierre, C. Numerical investigation of abradable coating removal through plastic constitutive law in aircraft engine. *J. Comput. Nonlinear Dyn.* **2011**, *7*, 011010. [CrossRef]
10. Nyssen, F.; Batailly, A. Thermo-Mechanical Modeling of Abradable Coating Wear in Aircraft Engines. *J. Eng. Gas Turbines Power* **2019**, *141*, 021031. [CrossRef]
11. Sternchüss, A.; Balmès, E. On the reduction of quasi-cyclic disks with variable rotation speeds. In Proceedings of the International Conference on Advanced Acoustics and Vibration Engineering (ISMA), Leuven, Belgium, 18–20 September 2006; pp. 3925–3939.
12. Palfrey-Sneddon, H.; Neely, A.J.; Smith, E.O. The influence of descent and taxi profiles on the thermal state of a jet engine at shutdown. In Proceedings of the ISABE 2017 Conference, Manchester, UK, 3–8 September 2017.
13. Adam, L. Modélisation du comportement thermo-élasto-viscoplastique des métaux soumis à grandes déformations. Application au formage superplastique. Ph.D. Thesis, Université de Liège, Liège, Belgium, 2003.
14. Debard, Y. *Méthode des éléments finis: thermique*; Université du Mans: Le Mans, France, 2011.
15. Jeong, C.Y. Effect of Alloying Elements on High TemperatureMechanical Properties for Piston Alloy. *Mater. Trans.* **2012**, *53*, 234–239. [CrossRef]
16. Batailly, A.; Legrand, M.; Millecamps, A.; Garcin, F. Conjectural bifurcation analysis of the contact-induced vibratory response of an aircraft engine blade. *J. Sound Vib.* **2015**, *348*, 239–262. [CrossRef]
17. Layachi, M.Y.; Bölcs, A. Effect of the axial spacing between rotor and stator with regard to the indexing in an axial compressor. In Proceedings of the ASME Turbo Expo 2001 Conference, GT2017-64342, New Orleans, LA, USA, 4–8 June 2001.

18. Ameli, A. Numerical simulation of rotor/stator interaction and tip clearance flow in centrifugal compressors. Master's Thesis, Lappeenranta University of Technology, Lappeenranta, Finland, 2015.
19. Gourdain, N.; Wiassow, F.; Ottavy, X. Effect of Tip Clearance Dimensions and Control of Unsteady Flows in a Multi-Stage High-Pressure Compressor. *J. Turbomach.* **2012**, *134*, 051005. [CrossRef]
20. Feng, J.; Luo, X.; Guo, P.; Wu, G. Influence of tip clearance on pressure fluctuations in an axial flow pump. *J. Mech. Sci. Technol.* **2016**, *30*, 1603–1610. [CrossRef]

coatings

MDPI

Article

The Influence of Disc Surface Topography after Vapor Blasting on Wear of Sliding Pairs under Dry Sliding Conditions

Andrzej Dzierwa [1,*], Pawel Pawlus [1] and Wieslaw Zelasko [2]

[1] Faculty of Mechanical Engineering and Aeronautics, Rzeszow University of Technology, Powstancow Warszawy 8 Street, 35-959 Rzeszow, Poland; ppawlus@prz.edu.pl

[2] Faculty of Mechanics and Technology, Rzeszow University of Technology, Kwiatkowskiego Street, 37-450 Stalowa Wola, Poland; w.zelasko@prz.edu.pl

* Correspondence: adzierwa@prz.edu.pl; Tel.: +48-17-743-2546

Received: 11 December 2019; Accepted: 21 January 2020; Published: 23 January 2020

Abstract: Wear tests were performed using a ball-on-disc tribological tester. In this study, 42CrMo4 steel disc of hardness 40 HRC co-acted with 100Cr6 steel ball with hardness of 60 HRC. Disc surfaces were created using vapor blasting to obtain values of the Sq parameter close to 5 μm. However, other disc surface topography parameters varied. Dry friction tests were carried out. Wear levels of discs and balls were measured using a white light interferometer Talysurf CCI Lite. It was found that the surface topography had a significant impact on tribological properties under dry sliding conditions. The research also allowed to identify significant dependencies between surface topography parameters and wear.

Keywords: wear; friction; surface topography

1. Introduction

The surface topography is one of the most important factors determining the quality of a surface layer. It defines a set of all overlapping irregularities of surface resulting from the machining processes and wear of materials. The use of all parameters [1] to assess the surface topography in terms of its functional characteristics is not entirely possible. A large simplification, however, is the attempt to assess the surface topography using only one parameter, that often happens in the industrial practice.

Despite the fact that a significant number of works have been made in the field of relationships between surface texture and tribological parameters, dependencies between surface topography parameters and friction and wear are not yet clearly defined [2–6].

The results obtained by the authors of papers [7,8] showed that the roughness amplitude had a significant impact on the transition between various friction regimes. The results of the ball-on-disc studies presented in papers [9,10] indicate the existence of a correlation between surface topography parameters (in particular Rsk and Rku) and the friction force. The Rsk parameter (skewness of the assessed profile) is the third order moment. It characterizes symmetry of the height distribution. The Rku parameter, which is fourth order moment described sharpness of the ordinate distribution. The Ssk and Sku parameters are three-dimensional extensions of the Rsk and Rku parameters, respectively. The coefficient of friction under dry conditions was lower for higher surface height. However, wear was not investigated in these works. The dependencies between the Ssk and Sku parameters and volumetric wear are presented in [11]. Larger values of the Sku parameter and smaller, negative Ssk parameters led to the reduction of wear volume of smooth steel discs. Grabon et al. [12] also found that the wear of a cylinder liner with a negative skewness was smaller compared to a

cylinder liner with a skewness close to 0 with the same value of the Sq parameter (root mean square deviation of the surface height) for both liners.

The influence of the surface topography on the frictional resistance in conditions of fretting wear was studied by, among others, authors of papers [13,14]. They received a lower coefficient of friction for rougher disc. Different results were obtained by the authors of reference [15], in which higher values of surface height corresponded to higher values of the friction coefficient. The results of the study of the effect of surface texture on fretting in dry friction conditions are presented in reference [16]. The tests revealed that the initial surface roughness had a significant effect on the obtained results. Especially tribological effects of spatial properties of the surface texture were significant.

Nyman et al. [17] pointed out that by characterizing the surface texture and calculating the several surface topography parameters like the average summit curvature Ssc and rms slope Sdq is possible to predict the remaining lifetime of a sintered friction material in a wet clutch. The authors of [18] showed that the average value of the coefficient of friction in lubricated sliding strongly depended on the mean arithmetical slope of the profile. The authors of paper [19] indicated that the standard deviation of surface height Sq and the summit density Sds were important from the point of view of the frictional resistance. The authors of [20] found a linear relationship between the roughness height of cylinder surface and friction of the cylinder liner–piston ring assembly.

One can see from a literature review that the effect of the surface topography of contacting elements on tribological performances of sliding pairs is uncertain. The aim of this study is to investigate the effect of the disc surface texture after vapor blasting on tribological properties of a disc–ball assembly under dry friction conditions

2. Materials and Methods

Tribological tests were carried out using the tribological tester T-11 made by Institute for Sustainable Technologies—National Research Institute in Radom (Poland) in a ball-on-disc configuration (Figure 1). The tribological system contained a stationary ball made of 100Cr6 steel with a hardness of 62 ± 2 HRC and a rotating steel disc of 40 ± 2 HRC hardness. Disc material was 42CrMo4 steel. Discs and balls diameters were 25 mm and 6.35 mm, respectively. Vapor blasting using the KIS-900 equipment was the finishing treatment of all discs. Its fundamental technical parameters are as follows:

- Working pressure: 0.3–0.7 MPa;
- Nozzle diameter: 5 mm;
- Abrasive granulation: 0.2–1.0 mm.

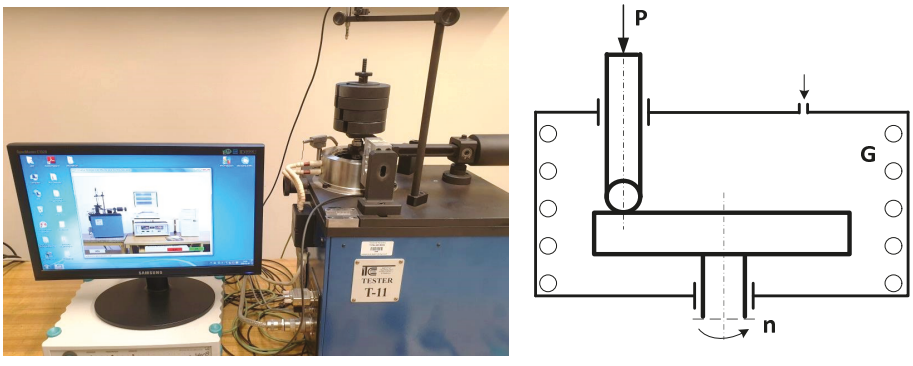

(**a**) (**b**)

Figure 1. Photo of tribological tester T-11 (**a**) and scheme of frictional pair; P—load, G—heater, n—rotational speed (**b**).

During vapor blasting the pressure of the feeding system was set to 0.6 MPa, and the initial flux angle was 60°. Aloxite 95A-60-J was an abrasive material. Its chemical composition included 95% of Al_2O_3; 2.5% of TiO_2; 1.1% of SiO_2; 0.3% of Fe_2O_3, and 1.1% of CaO. Aloxite 95A diameter was 0.3 mm. Duration of vapor blasting for each sample was 4 min. This treatment was performed in such a way to obtain a value of the Sq parameter (root mean square height of the surface) close to 5 μm, while other surface topography parameters varied. Different values of other surface topography parameters were obtained by slight changes of flux angle (between 55° and 65°). Tribological tests were carried out in dry friction conditions at an ambient temperature of 20–22 °C. The sliding speeds were: 0.16; 0.32; 0.48, and 0.64 m/s, the sliding distance—282.6 m, and the normal load—9.81 N. During tribological tests, wear products were removed from the test chamber using compressed air. The number of test repetitions was three. The friction force was recorded during each test, while after its completion the amount of wear was determined using a white light interferometer Talysurf CCI Lite [21]. The measuring area was 3.29 mm × 3.29 mm, the sampling interval in perpendicular directions was 3.3 μm. The measurements of the wear tracks were taken at four positions 90° apart. Then, the profiles were extracted perpendicularly to the wear tracks and the wear cross-sectional areas were calculated using TalyMap Gold 6.0 software. The calculation of volumetric wear of the disc according to Equation (1) was the next step.

$$VD = \pi ds \quad (1)$$

where: d—diameter of the wear track [mm], s—cross-sectional area of the wear track [mm^2].

Sq is the standard deviation for the amplitudes of the surface. This parameter characterizes averaged surface amplitude, its sensitivity on the measurement errors is low. The Ssk (skewness of the assessed surface topography) and Sku (kurtosis of the surface topography) are also height parameters, however, they describe the shape of the ordinate distribution. The combination of the skewness and kurtosis allow to identify steep slopes and deep valleys on the surface. The fastest—decay autocorrelation length Sal, belonging to spatial parameters, describes the character of the surface autocorrelation function. It is a shortest autocorrelation length for which the autocorrelation function decays to 0.2 value in any possible direction. The peak density Spd, which is the feature parameter, is the number of peaks on a unit sampling area. The hybrid parameter Sdq is the root-mean-square value of the surface slope within the sampling area. Both Spd and Sdq are frequently used in contact mechanics. The remaining functional parameters Spk (reduced peak height), Sk (core roughness depth), and Svk (reduced valley depth) characterize heights of three profile parts: Peak, core, and valley, respectively [1]. They are obtained on the basis of the material ratio curve (Figure 2). These parameters are important from the tribological point of view.

Table 1 presents selected surface topography parameters according to [1] of tested discs, and Figure 3 isometric views of some of them.

Table 1. Surface topography parameters of disc samples.

Parameter	Designation of Tested Discs								
	S1	**S2**	**S3**	**S4**	**S5**	**S6**	**S7**	**S8**	**S9**
Sq (μm)	4.89	5.11	4.97	5.21	4.93	4.98	4.91	5.17	4.94
Ssk	−0.767	−0.654	−0.856	−0.324	−0.419	−0.328	−0.847	−0.182	−0.061
Sku	8.78	4.72	6.9	3.97	4.02	3.34	6.79	3.36	3.82
Sal (mm)	0.0245	0.0267	0.0294	0.0401	0.0321	0.0883	0.0247	0.0682	0.0332
Spd ($1/mm^2$)	404	387	307	315	935	639	404	729	1181
Sdq	0.826	0.752	0.718	0.644	0.951	0.745	0.804	0.839	1.19
Sk (mm)	6.79	10.5	6.42	12.1	10.5	10.4	6.97	11.3	11.2
Spk (mm)	5.99	4.74	6.08	4.59	4.45	3.77	6.14	4.39	4.6
Svk (mm)	8.34	7.98	9.52	6.52	6.82	5.75	9.69	5.79	5.59

The texture aspect ratio of the disc surfaces Str, not shown in Table 1, which is the ratio of the fastest to the slowest decays of the autocorrelation function to 0.2 value, was between 0.808 and 0.919, indicating the isotropic character of the tested surfaces. Vapor blasted disc samples were also characterized by the negative skewness Ssk and the value of the kurtosis Sku between 3.34 and 8.78.

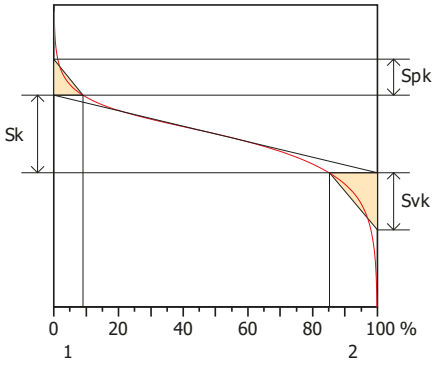

Parameters	Value	Unit
Sk	4.88	µm
Spk	2.27	µm
Svk	3.59	µm

Figure 2. Graphical interpretation of the Spk, Svk, and Sk parameters.

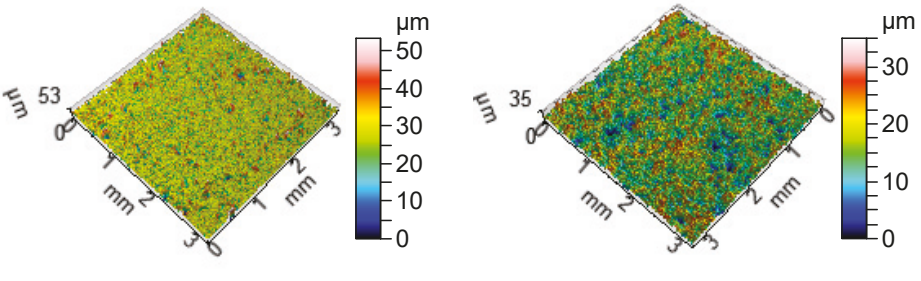

(**a**) (**b**)

Figure 3. Isometric views of selected discs: S1 (**a**), S8 (**b**).

3. Results and Discussion

Figure 4 shows the results of the volumetric wear calculation of the discs (VD), while Table 2 presents the other tribological parameters. For all frictional pairs, volumetric wear of the ball (VB), the friction distance necessary to obtain a stable value of the friction force (DSS), the average value of the friction force (Fav), as well as the value of the friction force obtained for the sliding distance equal to 35 m (F_{35}) are presented The running-in process of all tested frictional pairs was finished for sliding distances between 65 and 109 m. After running-in, the friction force obtained the stable value. The sliding distance of 35 m was chosen to analyze progress of running-in of tribological systems. Figure 5 shows the cross-sectional areas of wear tracks of selected discs.

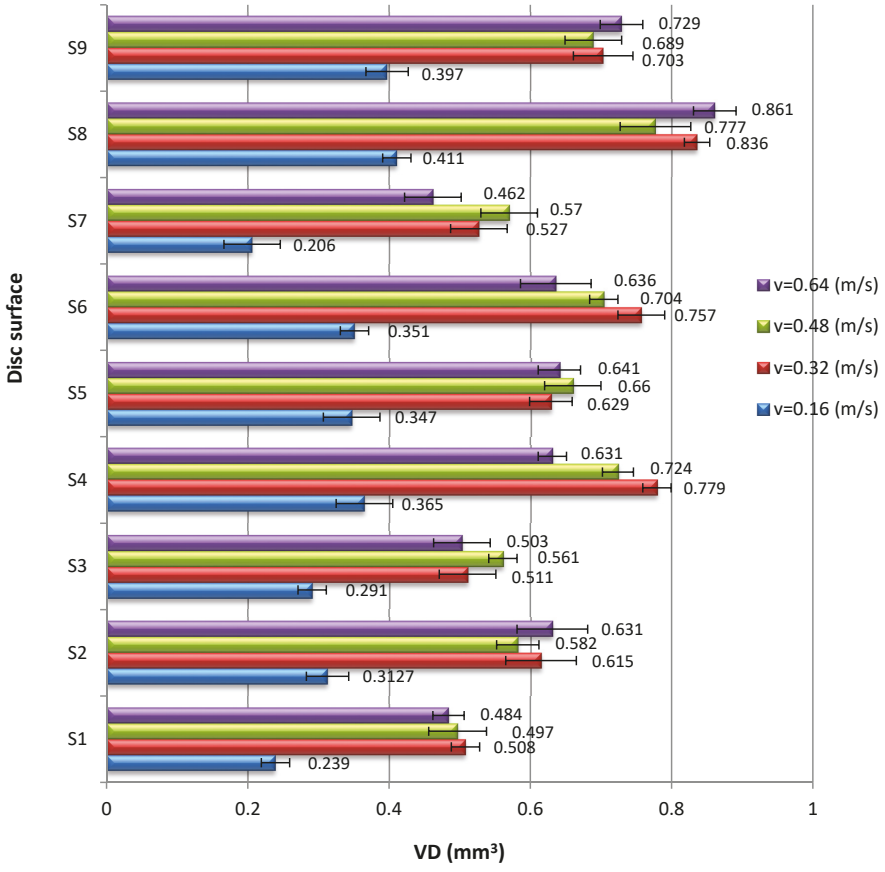

Figure 4. Volumetric wear levels of disc samples.

Table 2. Results of tribological tests.

v [m/s]	Parameter	Disc Surface								
		S1	**S2**	**S3**	**S4**	**S5**	**S6**	**S7**	**S8**	**S9**
0.16	VB (μm^3)	0.0315	0.0346	0.0318	0.0382	0.0344	0.0375	0.0338	0.0392	0.0385
	DSS (m)	109	97	98	112	94	129	95	106	98
	Fav (N)	8.480	8.293	8.146	8.695	8.156	8.176	8.134	8.208	8.191
	F_{35} (N)	3.576	3.888	4.074	4.058	3.906	3.252	3.66	4.338	4.121
0.32	VB (μm^3)	0.0396	0.0382	0.0411	0.0468	0.0459	0.0496	0.0477	0.0502	0.0481
	DSS (m)	112	96	82	115	112	73	81	82	74
	Fav (N)	8.760	8.277	8.570	8.172	8.141	8.228	8.361	8.213	8.156
	F_{35} (N)	5.892	6.414	4.974	6.744	4.206	7.122	5.568	6.156	5.256
0.48	VB (μm^3)	0.0381	0.0366	0.0401	0.0439	0.0425	0.0466	0.0452	0.0489	0.0456
	DSS (m)	98	92	92	88	91	89	95	78	82
	Fav (N)	7.946	8.006	7.967	8.168	7.989	8.201	8.102	8.099	7.987
	F_{35} (N)	4.513	4.698	4.899	5.821	4.609	4.108	5.404	4.556	4.502
0.64	VB (μm^3)	0.0379	0.0392	0.0391	0.0408	0.0415	0.0422	0.0354	0.0469	0.0454
	DSS (m)	96	88	80	92	96	92	98	74	78
	Fav (N)	7.811	7.969	7.906	7.856	7.988	8.065	7.803	8.084	8.006
	F_{35} (N)	5.635	6.211	4.747	6.565	4.609	6.621	5.403	4.598	5.152

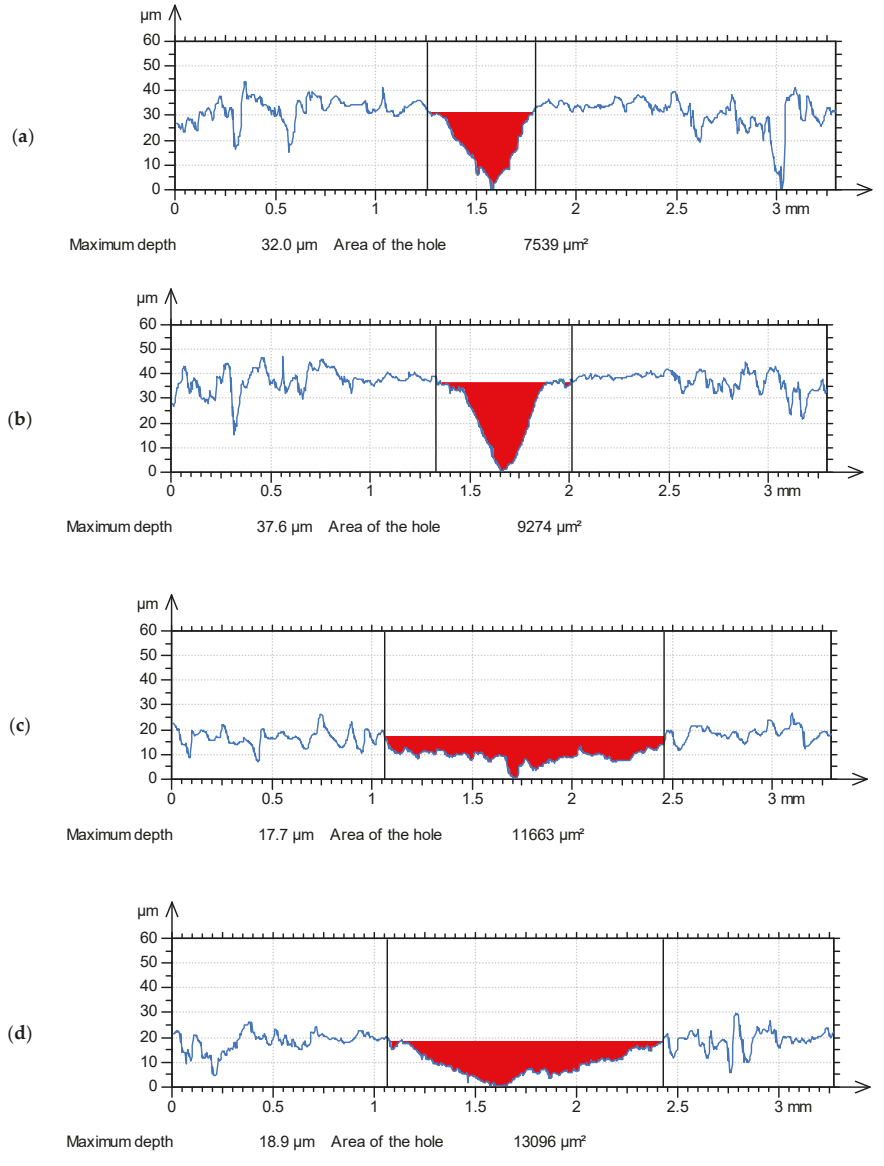

Figure 5. Cross-sectional areas of worn discs: S1 (**a**), S3 (**b**), S4 (**c**), S8 (**d**) at the sliding speed of v = 0.16 m/s.

The highest value of wear volume of the discs (VD = 0.411 mm^3) at a sliding speed of v = 0.16 m/s was observed for the S8 sample. It corresponded to the highest value of F_{35} parameter. The value of the friction force obtained after a sliding distance of 35 m was 4.338 N. On the other hand, the smallest value of the VD parameter for the frictional pair with S7 disc was equal to 0.206 mm^3. In this case the smallest value of the DSS parameter (apart from the S5 disc) was also found. The coefficient of friction µ ranged from 0.83 (disc S7) to 0.89 (disc S4).

An increase in the sliding speed to 0.32 m/s caused an increase in the wear volume of the discs. Similar to the sliding speed of v = 0.16 m/s, the highest value of the VD parameter was obtained for the

tribological system with the S8 disc, and it was 0.836 mm^3. The smallest value of volumetric wear was observed when the frictional pair contained S1 disc, and it was 0.508 mm^3. This value corresponded to the longest distance necessary to obtain a stable value of the friction force (112 m). In this case, the highest average value of the friction force Fav was also observed. At a sliding speed of 0.32 m/s the coefficient of friction μ achieved values from 0.83 (disc S5) to 0.89 (disc S1).

An increase in the sliding speed from 0.32 to 0.48 and 0.64 m/s did not lead to an increase in the volumetric wear of the discs. Moreover, in most cases the VD and VB parameters were slightly reduced. The smallest VD values were calculated for S1 disc (at v = 0.48 m/s) and S7 disc (at v = 0.64 m/s) and they were 0.497 and 0.462 mm^3, respectively. In both cases, the tribological systems were characterized by the highest values of the DSS parameter among other friction pairs and in both cases the value of the DSS parameter achieved 98 m. The sliding pair with the highest wear volume for both sliding speeds contained S8 disc sample. In this case the VD parameter obtained 0.777 mm^3 at v = 0.48 m/s and 0.861 mm3 at v = 0.64 m/s.

At a sliding speed of 0.48 m/s, the friction coefficient μ ranged from 0.81 (disc S1) to 0.84 (disc S6), while at 0.64 m/s from 0.79 (disc S7) up to 0.82 (disc S8).

The wear tracks visible on the cross-sectional areas of the discs Figure 5c, d don't have spherical shapes. This may indicate that during the co-acting of the elements, the initial non-conformal contact changed into a conformal [22]. The wear volume of discs was proportional to the volumetric wear of balls; the linear coefficient of correlation was between 0.69 and 0.94.

Surface topography analysis showed the formation of a one-directional (radial) texture after wear tests. The values of the Str parameter obtained after tribological tests were in the range of 6.2%–11.1% being characteristic for the surfaces after abrasive wear. Figure 6 presents isometric views of S4 and S6 discs after investigations and details of worn surfaces of these discs. The Str parameter of the S4 sample was 6.7%, and for the S6 it equaled to 9.9%. Figure 7 presents isometric views of balls co-acting with S4 and S6 discs after tribological tests, as well as slices of worn surfaces of those balls. The Str parameter of the ball co-acted with the S4 disc was 12.6%, while of the ball contacted with the S6 disc was 10.9%. The values of the Str parameter of all balls did not exceed 15%, creating a surface texture similar to that of the discs. The mean square deviation of the surface height Sq was 2.51 μm for the ball co-acting with the S4 disc and 2.34 μm for the ball co-acting with the S6 disc (Figure 7c,d).

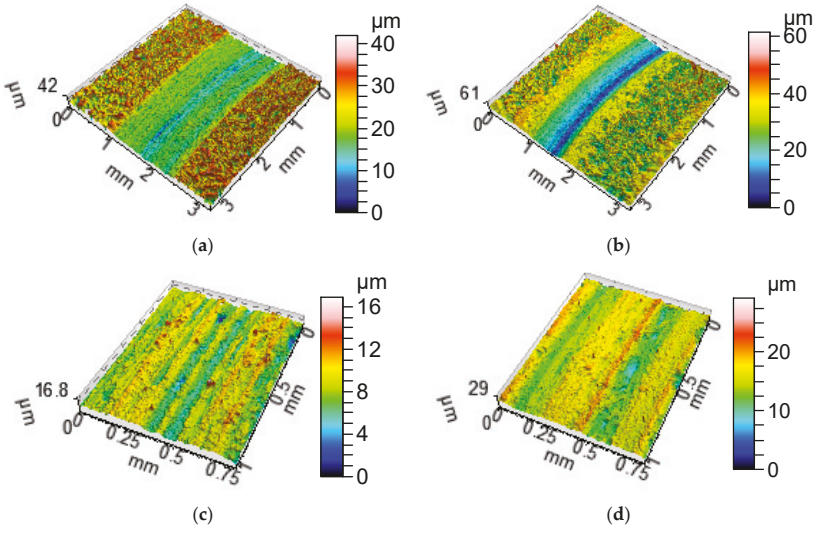

Figure 6. Isometric views of the discs S4 (**a**) and S6 (**b**) after tribological tests and details of their worn surfaces S4 (**c**), S6 (**d**).

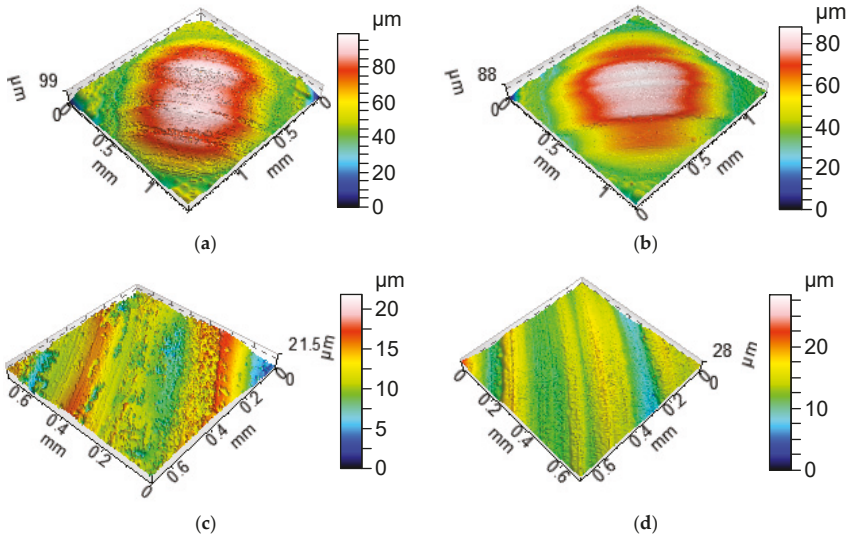

Figure 7. Isometric views of worn balls co-acting with the discs S4 (**a**) and S6 (**b**) and details of their worn surfaces co-acting with the discs S4 (**c**), S6 (**d**).

Similar to discs with a small surface height [11], abrasion was the dominant wear mechanism (Figure 8) which can be also related to high disc amplitudes. As a result of the co-action between sliding elements, truncation of the summits of the disc surfaces took place, which resulted in the creation of a new anisotropic surface texture. The craters appearing on the disc surfaces were slightly larger compared to the discs with a small surface height [11].

One can also see smooth areas with longitudinal grooves resulting from plastic deformation of disc surfaces. The increase in sliding speed did not cause significant changes of tested disc topographies. Wear of balls was significantly lower than wear of discs. This was caused by higher hardness of balls compared to that of discs. Ball surfaces were very smooth, but the presence of some abrasive particles aligned in the direction of sliding was visible. This indicated three-body mode of abrasive wear where worn material was not removed completely from the contact zone.

The coefficient of the linear correlation R was used to search for relationships between tribological and surface topography parameters. The value of the correlation coefficient is in the range [−1,1]. The higher absolute values of R point out the stronger linear relationship between the variables. A strong linear relationship occurring at all sliding speeds was found for the VD-Ssk (skewness) and VD-Sku (kurtosis) pairs. The Ssk parameter informs about the nature of the surface and it is sensitive on occasional deep valleys or high peaks. Zero skewness indicates a symmetrical height distribution [23]. The value of the skewness depends on whether the material is above (negative skewed) or below (positive skewed) the mean plane. The Sku parameter informs about the sharpness of the surface topography ordinate distribution. A value of Sku of 3 indicates a normal height distribution, if Sku < 3 surface has relative few high peaks and deep valleys; whereas if Sku > 3, it has many high peaks and deep valleys [24].

The coefficient of the linear correlation R between volumetric wear of discs and the Ssk parameter ranged from 0.88 (for v = 0.48 m/s) to 0.92 (for v = 0.16 m/s), while between VD and Sku, from −0.87 (for v = 0.24 m/s) to −0.91 (for v = 0.48 m/s).

Examples of dependencies between wear volume VD and Ssk and Sku parameters at different sliding speeds are shown in Figure 9.

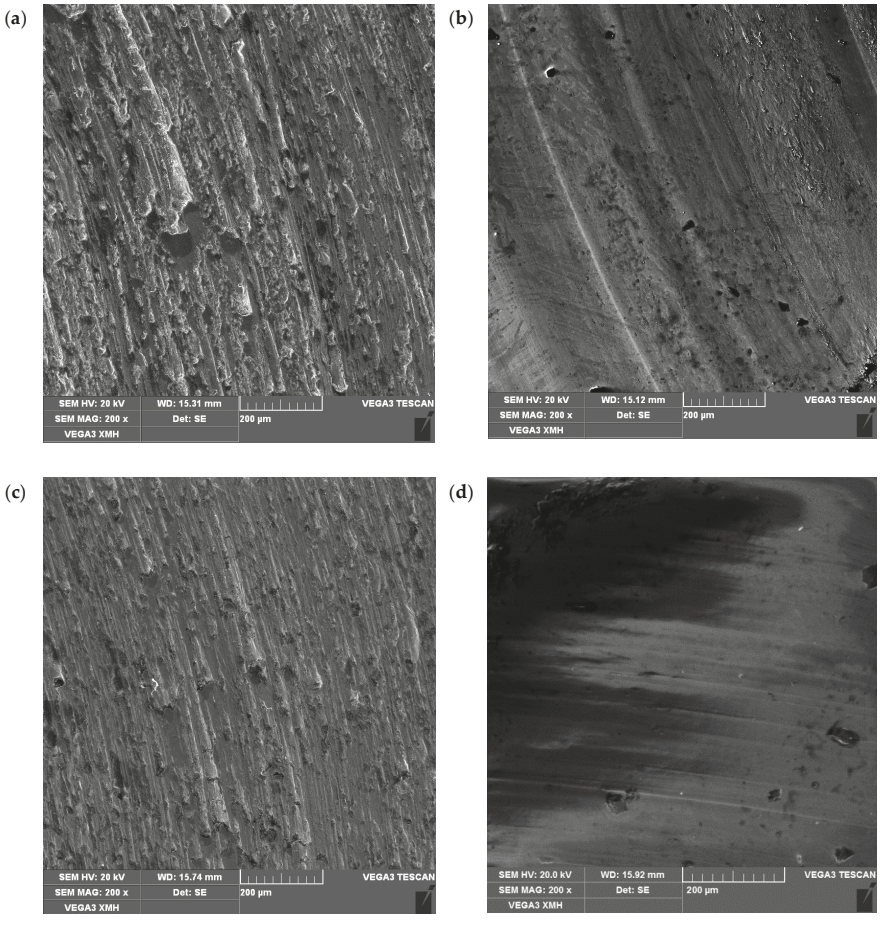

Figure 8. Worn surface of S4 disc (**a**,**c**) and co-acting ball (**b**,**d**) at the sliding speed of v = 0.16 m/s (**a**,**b**) and v = 0.64 m/s (**c**,**d**).

The lowest values of volumetric wear of the discs were achieved for the minimum values of the Ssk parameter and the maximum values of the Sku parameter. The Sku parameter of the discs was inversely proportional to the Ssk parameter. The coefficient of linear correlation between these parameters was −0.97. This relationship is characteristic for stratified surfaces like plateau honed cylinder texture—the negative skewness Ssk typically corresponds to the high kurtosis Sku [6]. The negative skewness can improve contact conditions by reducing the plasticity index, which in turn can cause the reduction of wear volume. The skewness Ssk is more tribologically important than the kurtosis Sku. The kurtosis is more sensitive to individual peaks or grooves presences [25]. Therefore, the dependence Ssk–VD seems to be more substantial than Sku–VD. Similar results were obtained in [11] and partially in [22] under dry friction conditions and in [12] under lubricated regime.

A strong linear dependency occurring at all sliding speeds was also found between volumetric wear of the discs and parameters characterizing the areal material ratio: Sk (core roughness depth), Spk (reduced peak height), and Svk (reduced valley depth). The Svk parameter characterizes the performance of surface in a regime of lubrication while the Spk parameter can provide information on the surface's wear resistance during the running-in (the lower value of the Spk, the greater wear

resistance). The roughness height Sk, however, determines the roughness height after running-in and characterizes surface properties in a steady-state period [26]. Depending on the sliding speed, the values of the coefficient of linear correlation R oscillated in the ranges: From 0.82 to 0.88 (for VD and Sk), from −0.76 to −0.85 (for VD and Spk), and from −0.84 to −0.89 (for VD and Svk).

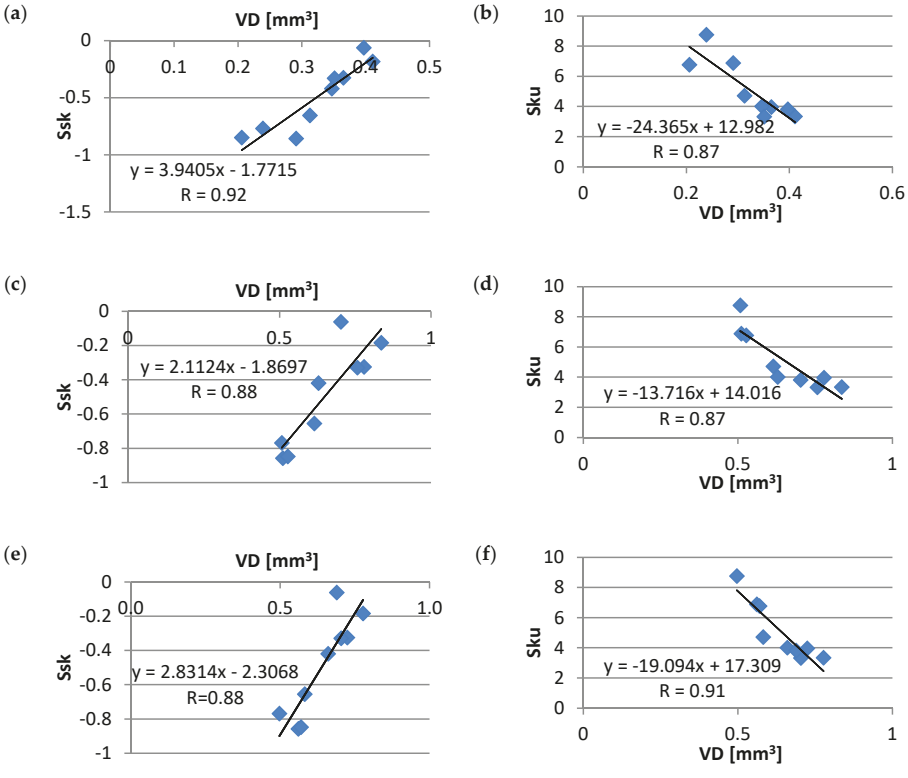

Figure 9. Dependencies between wear volume VD and Ssk (**a**,**c**,**e**) and Sku parameters (**b**,**d**,**f**) at the sliding speed of: (**a**,**b**) v = 0.16 m/s; (**c**,**d**) v = 0.32 m/s; (**e**,**f**) v = 0.48 m/s.

Figure 10 shows dependencies between parameters Spk and Svk and volumetric wear VD at sliding speeds v = 0.16 m/s (a), v = 0.32 m/s (b), and v = 0.48 m/s (c). Areas marked in red indicate higher values of the VD parameter, while green color presents areas corresponding to less wear on the discs. Dependencies between the core roughness height Sk and the volumetric wear are shown in Figure 11.

After analysis of the obtained results, one can see that increases in the values of Spk and Svk parameters corresponded to a decrease in the wear volume of the disc (Figure 9). However, the effect of the Spk and Svk parameters on the disc volumetric wear seems to be not substantial. The effect of the Spk parameter is important only during running-in and the Svk parameter is related to starved lubrication. The proportionality between the Sk parameter and volumetric wear of disc is probably substantial. The Sk parameter governs tribological properties of machined elements in a steady-state period. One can see from the analysis of Figure 4 that wear depth of disc is a little higher than initial surface height, so the effect of the Sk parameter on disc wear can be important. For all surfaces tested the Svk parameter was higher than the Spk parameter, which is related to the negative skewness Ssk.

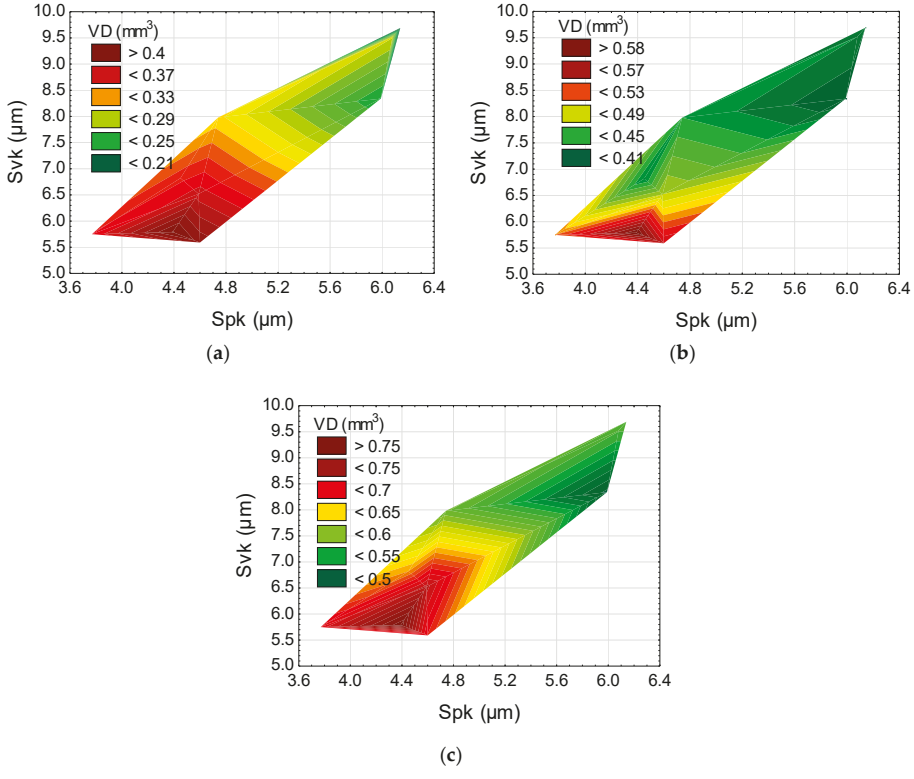

Figure 10. Dependencies between wear volume VD and Spk and Svk parameters at the sliding speed of v = 0.16 m/s (**a**), v = 0.32 m/s (**b**), v = 0.48 m/s (**c**).

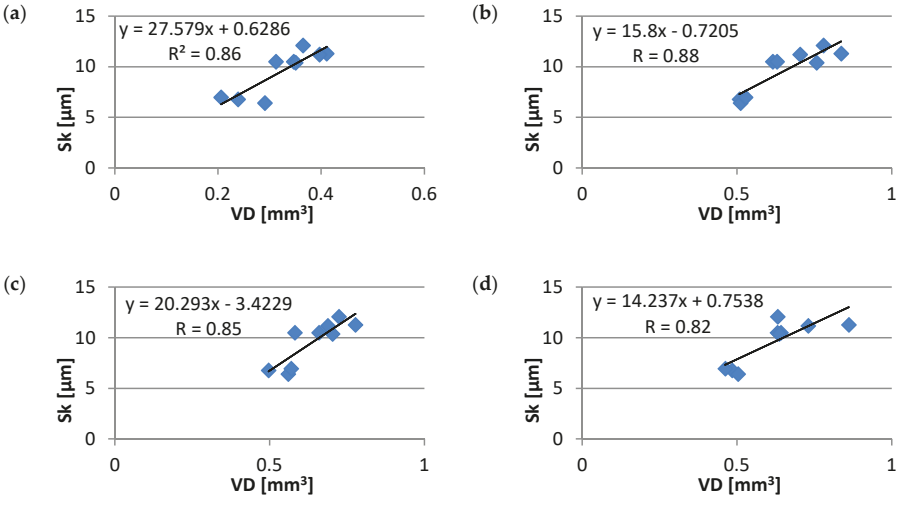

Figure 11. Dependencies between wear volume VD and Sk at the sliding speed of (**a**) v = 0.16 m/s; (**b**) v = 0.32 m/s; (**c**) v = 0.48 m/s; (**d**) v = 0.64 m/s.

The disc volumetric wear VD was proportional to the correlation length Sal (R was between 0.54 and 0.84). This dependence can be explained by the tendency to obtain the higher Sal parameter for the bigger surface height, determined by the Sk parameter. The remaining surface texture parameters: The rms slope Sdq and the peak density Spd were not strongly correlated with tribological parameters.

The volumetric wear levels were typically not correlated with parameters characterizing the friction force DSS, Fav, and F35. Only for the highest sliding speed v = 0.64 m/s the average friction force Fav was proportional to wear levels of disc VD and balls VB; the coefficients of the linear correlation R amounted to 0.83 and 0.94, respectively.

4. Conclusions

The results of the conducted research indicated many significant relationships between surface topography parameters and the tribological properties of tested samples.

Ssk and Sku parameters characterizing the shape of the surface ordinate distribution had significant impacts on the volumetric wear. A decrease in the value of the Ssk parameter and an increase in the value of Sku led to a reduction in the wear volume.

The wear volume of discs was also strongly correlated with the parameters characterizing the areal material ratio curve. It was shown that an increase in the value of the parameter Sk caused an increase in the volumetric wear level.

Wear of balls was proportional to wear of disc. An increase in the sliding speed resulted in a reduction in the coefficient of friction of the tribological system.

Author Contributions: Conceptualization: A.D., P.P., W.Z.; methodology: A.D., P.P., W.Z.; investigation and formal analysis: A.D., P.P., W.Z.; writing—original draft preparation: A.D., P.P., W.Z.; writing—review and editing: A.D., P.P., W.Z. All authors have read and agreed to the published version of the manuscript.

Funding: This research received no external funding.

Conflicts of Interest: The authors declare no conflict of interest.

References

1. *Geometrical Product Specifications (GPS)—Surface texture: Areal—Part 2: Terms, Definitions and Surface Texture Parameters*; ISO 25178-2:2012; International Standardization Organization: Geneva, Switzerland, 2012.
2. Svahn, F.; Kassaman-Rudolphi, A.; Wallen, E. The influence of surface roughness on friction and wear of machine element coatings. *Wear* **2003**, *254*, 1092–1098. [CrossRef]
3. Tayebi, N.; Polycarpou, A.A. Modeling the effect of skewness and kurtosis on the static friction coefficient of rough surfaces. *Tribol. Int.* **2004**, *37*, 491–505. [CrossRef]
4. Chang, W.R.; Hirvonen, M.; Gronqvist, R. The effects of cut-off length on surface roughness parameters and their correlation with transition friction. *Safety Sci.* **2004**, *42*, 755–769. [CrossRef]
5. Reizer, R.; Galda, L.; Dzierwa, A.; Pawlus, P. Simulation of textured surface topography during a low wear process. *Tribol. Int.* **2011**, *44*, 1309–1319. [CrossRef]
6. Grabon, W.; Pawlus, P.; Wos, S.; Koszela, W.; Wieczorowski, M. Effects of honed cylinder liner surface texture on tribological properties of piston ring-liner assembly in short time tests. *Tribol. Int.* **2017**, *113*, 137–148. [CrossRef]
7. Wang, S.; Hu, Y.-Z.; Tan, Q.-C. Frictional behaviour of engineering surfaces in overall lubrication regimes of point contacts. *Proc. Inst. Mech. Eng. J J. Eng.* **2011**, *225*, 1071–1080. [CrossRef]
8. Wang, S.; Hu, Y.-Z.; Wang, W.-Z.; Wang, H. Transition of frictional states and surface roughness affects in lubricated contacts. *Proc. Inst. Mech. Eng. J J. Eng.* **2008**, *222*, 407–414. [CrossRef]
9. Sedlacek, M.; Podgornik, B.; Vizintin, J. Correlation between standard roughness parameters skewness and kurtosis and tribological behaviour of contact surfaces. *Tribol. Int.* **2012**, *48*, 102–112. [CrossRef]
10. Sedlacek, M.; Podgornik, B.; Vizintin, J. Influence of surface preparation on roughness parameters, friction and wear. *Wear* **2009**, *266*, 482–487. [CrossRef]
11. Dzierwa, A. Influence of surface preparation on surface topography and tribological behaviours. *Arch. Civ. Mech. Eng.* **2017**, *17*, 502–510. [CrossRef]

12. Grabon, W.; Pawlus, P.; Sep, J. Tribological characteristics of one-process and two-process cylinder liner honed surfaces under reciprocating sliding conditions. *Tribol. Int.* **2010**, *43*, 1882–1892. [CrossRef]
13. Kubiak, K.J.; Bigerelle, M.; Mathia, T.G.; d'Hardivilliers, W. Roughness of interface in dry contact under fretting conditions. In Proceedings of the 13th International Conference on Metrology and Properties of Engineering Surfaces, Twickenham Stadium, UK, 12–15 April 2011; pp. 99–102.
14. Kubiak, K.J.; Liskiewicz, T.E.; Mathia, T.G. Surface morphology in engineering applications: Influence of roughness on sliding and wear in dry fretting. *Tribol. Int.* **2011**, *44*, 1427–1432. [CrossRef]
15. Pawlus, P.; Michalczewski, R.; Dzierwa, A.; Lenart, A. The effect of random surface topography height on fretting in dry gross slip conditions. Proceedings of the Institution of Mechanical Engineers. *Proc. Inst. Mech. Eng. J J. Eng.* **2014**, *228*, 1374–1391. [CrossRef]
16. Lenart, A.; Pawlus, P.; Dzierwa, A.; Sep, J.; Dudek, K. The effect of surface topography on dry fretting in the gross slip regime. *Arch. Civ. Mech. Eng.* **2017**, *17*, 894–904. [CrossRef]
17. Nyman, P.; Maki, R.; Olsson, R.; Ganemi, B. Influence of surface topography on friction characteristics in wet clutch applications. *Wear* **2006**, *261*, 46–52. [CrossRef]
18. Menezes, P.L.; Kailas, S.V. Kishore Influence of roughness parameters on coefficient of friction under lubricated conditions. *Sadhana* **2008**, *33*, 181–190. [CrossRef]
19. Singh, R.; Melkote, S.N.; Hashimoto, F. Frictional response of precision finished surfaces in pure sliding. *Wear* **2005**, *258*, 1500–1509. [CrossRef]
20. Ma, Z.; Henein, N.A.; Bryzik, W.; Glidewell, J. Break-in liner wear and piston ring assembly friction in a spark-ignited engine. *Tribol. Trans.* **1998**, *41*, 497–504. [CrossRef]
21. *Talysurf CCI 3D Non-Contact Surface Profiler System. User's Guide*; K505/70-01 Issue 5.2; Taylor Hobson: Leicester, UK, 2005; pp. 1–154.
22. Dzierwa, A.; Pawlus, P.; Zelasko, W.; Reizer, R. The study of the tribological properties of one-process and two-process textures after vapour blasting and lapping using pin-on-disc tests. *Key Eng. Mater.* **2013**, *527*, 217–222. [CrossRef]
23. Sedlacek, M.; Gregorcic, P.; Podgornik, B. Use of the roughness parameters S sk and Sku to control friction—A method for designing surface texturing. *Tribol. Trans.* **2017**, *60*, 260–266. [CrossRef]
24. Gadelmawla, E.S.; Koura, M.M.; Maksoud, T.M.A.; Elewa, I.M.; Soliman, H.H. Roughness parameters. *J. Mater. Process. Technol.* **2002**, *123*, 133–145. [CrossRef]
25. Pawlus, P.; Wieczorowski, M.; Mathia, T.G. *The Errors of Stylus Methods in Surface Topography Measurements*; ZAPOL: Szczecin, Poland, 2014; pp. 1–267.
26. Johansson, S.; Nilsson, P.H.; Ohlsson, R.; Anderberg, C.; Rosen, B.G. New cylinder liner surfaces for low oil consumption. *Tribol. Int.* **2008**, *41*, 854–859. [CrossRef]

coatings

MDPI

Article

Lubricating Properties of Cyano-Based Ionic Liquids against Tetrahedral Amorphous Carbon Film

Shouhei Kawada [1,*], Hikaru Okubo [1], Seiya Watanabe [1], Chiharu Tadokoro [2], Ryo Tsuboi [3], Shinya Sasaki [1] and Masaaki Miyatake [1]

[1] Department of Mechanical Engineering, Tokyo University of Science, 6-3-1 Niijyuku, Katsushika-ku, Tokyo 125-8585, Japan; 4516701@alumni.tus.ac.jp (H.O.); s-watanabe@rs.tus.ac.jp (S.W.); s.sasaki@rs.tus.ac.jp (S.S.); m-miyatake@rs.tus.ac.jp (M.M.)

[2] Department of Mechanical Engineering, Saitama University, 255 Shimo-Okubo, Sakura-ku, Saitama-shi, Saitama 338-8570, Japan; tadokoro@mail.saitama-u.ac.jp

[3] Department of Mechanical Engineering, Daido University, 10-3 Takiharu-cho, Minami-ku, Nagoya-shi, Aichi 457-8530, Japan; r-tsuboi@daido-it.ac.jp

* Correspondence: s-kawada@rs.tus.ac.jp

Received: 31 December 2019; Accepted: 7 February 2020; Published: 8 February 2020

Abstract: Ionic liquids have unique characteristics, which render them ideal candidates as new base oils or additives. In particular, there are great expectations from the combination of diamond-like carbon and cyano-based ionic liquids. Lubricating properties of cyano-based ionic liquids have been studied on specific tetrahedral amorphous carbon (ta-C) films. After lubrication, ta-C film/ta-C film contact interface exhibits exceedingly low friction. Therefore, it is necessary to understand this low friction phenomenon. The current study evaluated the lubricating mechanism of cyano-based ionic liquids against ta-C films. 1-Butyl-3-methylimidazolium dicyanamide ((BMIM)(DCN)) and 1-butyl-3-methylimidazolium tricyanomethane ((BMIM)(TCC)) were used as lubricants, with the latter exhibiting low friction coefficient of 0.03. Steel cylinders and disks with ta-C films were used as test specimens. Raman spectroscopy, matrix-assisted laser desorption/ionization time-of-flight mass spectrometry, and thermogravimetric analysis (TGA) helped us understand the mechanism of low friction induced by (BMIM)(TCC). Graphitization of the ta-C film at high temperatures might have caused the reduction in friction between the films. Similarly, anion adsorption on the worn surface at high temperatures also led to reduced friction. However, the TGA result showed a different trend than that of the sliding test. Our results indicate that the cyano-based ionic liquids underwent tribo-decomposition at low temperatures. Further, a minimum temperature was required for the adsorption of anions onto the sliding surface.

Keywords: friction reduction; ionic liquid; lubrication; surface chemistry; tetrahedral amorphous carbon

1. Introduction

"Ionic crystal" is a solid-state material consisting of cations and anions, such as sodium chloride, sodium acetate, and ammonium chloride. Despite being a salt, ionic liquids exist in the liquid phase at a temperature of 100 °C or lower [1–3]. They are good candidates as new lubricant oils or additives because of their unique characteristics, including their non-volatility, low vapor pressure, the ability to remain in the liquid phase over a wide temperature range, low viscosity, and an infinite number of ion combinations [4–8]. Kondo et al. reported the use of ionic liquids as adsorption films for magnetic thin films inspired by the use of ionic liquids in the tribology field [9–11]. Ionic liquids that include elemental fluorine exhibit low friction at steel/steel contacts due to the generation of ferrous fluoride. However, severe corrosion occurs on the worn surface, and hazardous hydrogen fluorine is

produced through reaction with moisture [12–14]. This corrosion can be prevented with the use of ionic liquids under inert atmosphere, but the corrosion may occur after the atmospheric relief [15]. From the viewpoint of environmental conservation, the usage of halogen-free ionic liquids is desirable. There are various types of halogen-free ionic liquids. The sulfate- and phosphate-based ionic liquids form reaction films on the worn surface at steel/steel contacts, thereby leading to low friction coefficient or small wear volume [16]. The cyano-based ionic liquids exhibit low friction via the formation of an adsorption film of their anions [17–20]. Boron-based ionic liquids also exhibit low friction; however, the detailed mechanism is still not clear [21]. Further, various cations are also being investigated, which include phosphonium and ammonium cations. They increase the solubility of the ionic liquids in the base oils and make it possible to study them as lubricant additives [22–25]. In addition, very low friction caused by the ionic liquids has been reported in recent years. One of the applications is their use as a swelling agent for polymer brushes [26–28]. These polymer brushes exhibit an ultra-low friction coefficient of less than 0.01 [27,28]. Diamond-like carbon (DLC) is also used as one of the effective friction materials for reducing friction between surfaces [29,30]. Lubricating properties of cyano-based ionic liquids in steel/DLC and DLC/DLC contacts have been evaluated, and these combinations have been reported to exhibit low friction [17,20,31–33]. Further, AISI52100/tetrahedral amorphous carbon (ta-C) film and ta-C film/ta-C film contacts exhibited very low friction of 0.02 and 0.018, respectively. The combination of a cyano-based ionic liquid and ta-C film has the potential to be a novel lubrication system. However, a detailed lubricating mechanism for this combination is poorly understood.

In this study, the lubricating properties of cyano-based ionic liquids against a ta-C film were evaluated using a reciprocating sliding friction and wear tester. We focused on the conditions at which low friction was observed and the relationship of the molecular structures of cyano-based ionic liquids and ta-C film. Two types of cyano-based ionic liquids, 1-butyl-3-methylimidazolium dicyanamide (BMIM)(DCN) and 1-butyl-3-methylimidazolium tricyanomethane (BMIM)(TCC), were used as lubricants. In order to clarify the reason for the low friction, various investigations were made using techniques including thermogravimetric analysis (TGA), Raman spectroscopy, and matrix-assisted laser desorption/ionization time-of-flight mass spectrometry (MALDI-TOF/MS).

2. Materials and Methods

2.1. Lubricants and Materials

In this study, (BMIM)(DCN) and (BMIM)(TCC) purchased from Merck (Darmstadt, Germany) were used as lubricants. The molecular structures and physical properties of these ionic liquids are listed in Tables 1 and 2, respectively. Their viscosities were measured with a tuning fork vibration viscometer (SV-1A, A&D Company, Tokyo, Japan). Their purity and melting points were catalog values.

Table 1. Molecular structures of cyano-based ionic liquids. 1-Butyl-3-methylimidazolium dicyanamide ((BMIM)(DCN)); 1-butyl-3-methylimidazolium tricyanomethane ((BMIM)(TCC)).

(BMIM)(DCN)
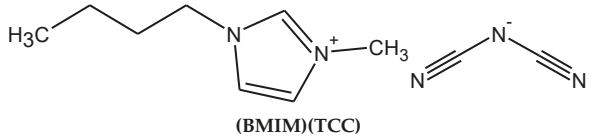
(BMIM)(TCC)
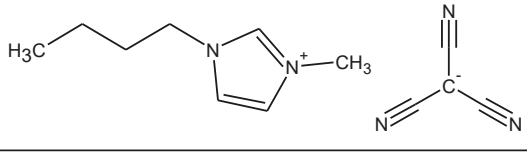

Table 2. Physical properties of the ionic liquids.

Name	(BMIM)(DCN)	(BMIM)(TCC)
Viscosity (50 °C)	11.6 [mPas]	11.1 [mPas]
Melting point	<−50 [°C]	<−50 [°C]
Purity	>98 [%]	>98 [%]

AISI 52,100 steel cylinders (diameter: 15 mm; length: 22 mm; HRC60) and AISI 52100 steel disks (diameter: 24 mm; thickness: 7.9 mm; HRC60) with a ta-C film coating were used as sliding materials. The cylinders and disks were procured from Test Materials (Tokyo, Japan). The ta-C film-coated steel disks were produced by the ITF Co. (Kyoto, Japan) by arc ion plating. Table 3 lists the properties of the ta-C film. The hardness of this film was measured with a tribo-indenter (Ti950, Hysitron, Minneapolis, MN, USA), and the coating thickness was measured with a coating thickness analyzer (Calotest, Anton Paar Tritec SA, Neuchâtel, Switzerland).

Table 3. Physical properties of the ta-C film.

Roughness	R_a = 0.01 [μm]
Hardness	73 [GPa]
Film thickness	1.0 [μm]
Hydrogen content	<1.0 [at%]
Interlayer	Cr

2.2. Sliding Tests

The lubricating properties were evaluated with a reciprocating sliding tester (SRV4, Optimol, Langenbach, Germany). Before testing, the specimens were ultrasonically cleaned with a mixed solution of petroleum benzine and acetone at 1:1 ratio for 10 min. Then, 90 μL of the ionic liquid was applied to the disk surface. The operating parameters for the sliding tests were as follows: temperature of 30–290 °C, programmed heating rate of 10 K per 5 min, air atmosphere, load of 50 N, reciprocating frequency of 50 Hz, and amplitude of 1 mm. The sliding test was stopped when a sharp increase in the friction coefficient was reached. Constant temperature sliding tests were conducted at approximately 30 °C, and the temperature at which a low friction coefficient was achieved was determined to study the mechanism of low friction. The operating parameters were as follows: load of 50 N, sliding time of 30 min, reciprocating frequency of 50 Hz, and amplitude of 1 mm. This sliding test was stopped when the friction reduction effect was observed. The tests were confirmed to be reproducible. After the sliding tests, the disk specimens were ultrasonically cleaned with a mixed solution of petroleum benzine and acetone for 10 min. The surface images of the disk specimens after the sliding tests were obtained using a laser microscope (VK-X150, Keyence, Osaka, Japan). Each surface profile was obtained by a surface profile meter (SURFCOM 1500SD3, ACCRETECH, Tokyo, Japan), with respect to the vertical direction of the wear track.

2.3. Raman Spectroscopy

The structural changes in the wear track of ta-C films were investigated by Raman spectroscopy (inVia Raman Microscope, Renishaw, Gloucestershire, UK). The Raman spectrometer used a 532 nm YAG laser with a maximum output power of 2.5 mW in conjunction with an objective lens at 50x magnification. The Raman spectra of the amorphous carbon showed some prominent features (D-peak at approximately 1300–1400 cm^{-1} and G-peak at 1500–1600 cm^{-1}) [34]. The increase in the ratio of the D-peak to G-peak intensities (I_D/I_G) indicates the degree of graphitization of the ta-C film [35]. Graphitization (increase in I_D/I_G) of the film is known to influence the friction behavior [36]. In this study, the degree of graphitization was estimated by calculating the I_D/I_G ratio.

2.4. MALDI-TOF/MS Analysis

The surface information for the worn surface of each disk was obtained by MALDI-TOF/MS analysis (autoflex speed, Bruker, Billerica, MA, USA). The wavelength of the laser was 337 nm, acceleration voltage was 20 kV, and step size was 100 μm. The measurement area was approximately 9 mm^2 (3 × 3 mm^2). The reflected mode was used for the analysis, and the laser beam diameter was 100 μm. The measured mass range was 1–3000 m/*e*. Before analysis, the sample surface was ultrasonically cleaned with a solution of petroleum benzine and acetone for 10 min.

2.5. Thermogravimetric Analysis

The thermal stability of the used ionic liquids was evaluated by TGA (TG-DTA2010SA, Bruker, Billerica, MA, USA). TGA of the samples was carried out in aluminum pans in nitrogen atmosphere in a temperature range of 30–500 °C at a programmed heating rate of 10 K/min.

3. Results

3.1. Friction Tests

Figure 1 shows the frictional behavior of each cyano-based ionic liquid at an elevated temperature. In the case of (BMIM)(DCN), the friction coefficient gradually increased with the temperature. A reduction in friction was observed at 170 °C. The friction coefficient was approximately 0.07. After this, a sharp increase in the friction coefficient was observed at 210 °C, because the ta-C film might have peeled from the substrate. When (BMIM)(TCC) was used, the friction coefficient gradually increased with the temperature. At 90 °C, the friction coefficient decreased to approximately 0.03. A sharp increase in the friction coefficient was then observed at 110 °C, which confirmed that the temperature affected the reactivity of the ionic liquids. We performed the sliding test at a constant temperature and confirmed the time-dependence of the friction coefficient to clarify the effect of temperature. Figure 2 shows the frictional behavior of the ionic liquids at 30 °C, and the temperature at which a low friction coefficient was achieved. To determine the temperature corresponding to the low friction coefficient of the ionic liquids, friction tests were conducted at 170 °C and 100 °C for (BMIM)(DCN) and (BMIM)(TCC), respectively. Figure 3 shows an image of the worn surface of the ta-C film obtained with a laser microscope. Figures 4 and 5 show the worn surface profiles of the ta-C film lubricated with each ionic liquid. At 30 °C, both ionic liquids showed stable friction behaviors and small surface wear. At the temperature corresponding to the low friction coefficient, the reduced friction of each ionic liquid was confirmed. Further, the progression of wear was confirmed in comparison with the results obtained at 30 °C.

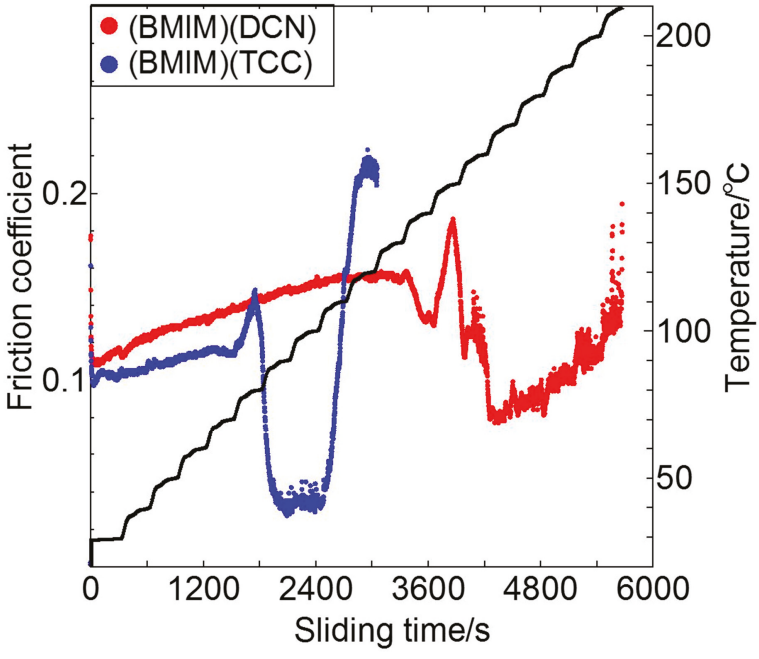

Figure 1. Friction behaviors of (BMIM)(DCN) and (BMIM)(TCC) at elevated temperatures.

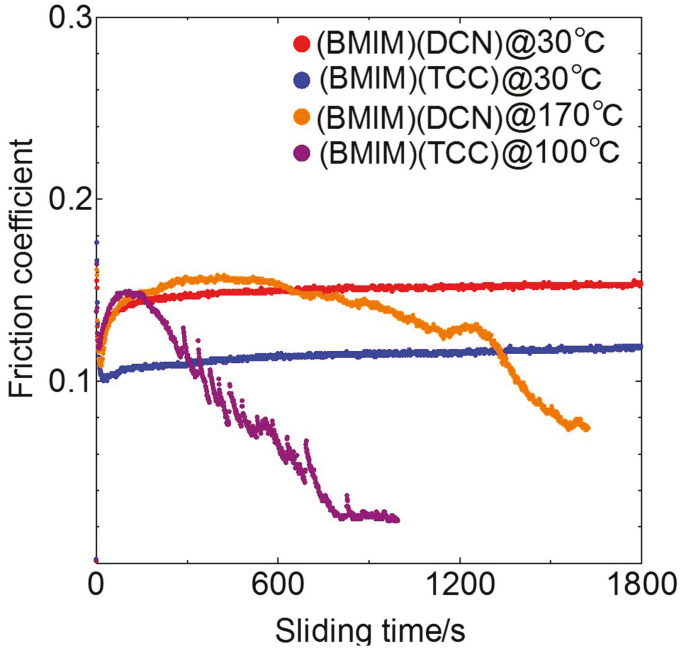

Figure 2. Frictional behavior of (BMIM)(DCN) and (BMIM)(TCC) at each temperature.

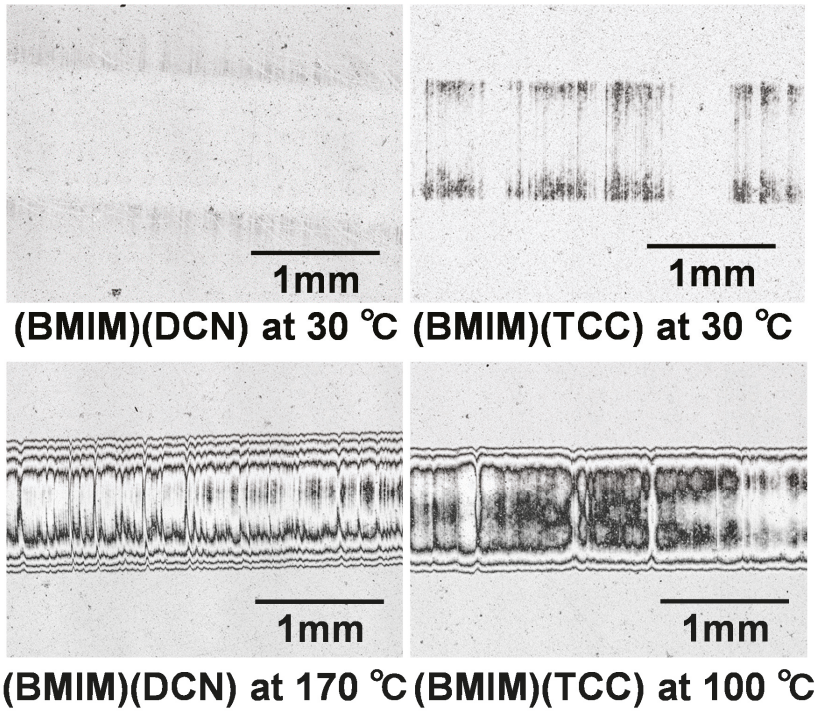

Figure 3. Images of the worn surfaces of ta-C films subjected to friction under different conditions.

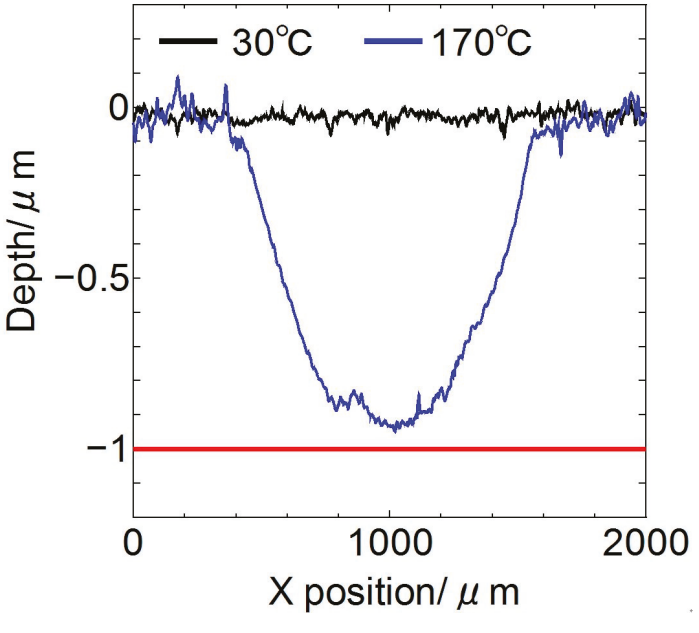

Figure 4. Surface profile of (BMIM)(DCN).

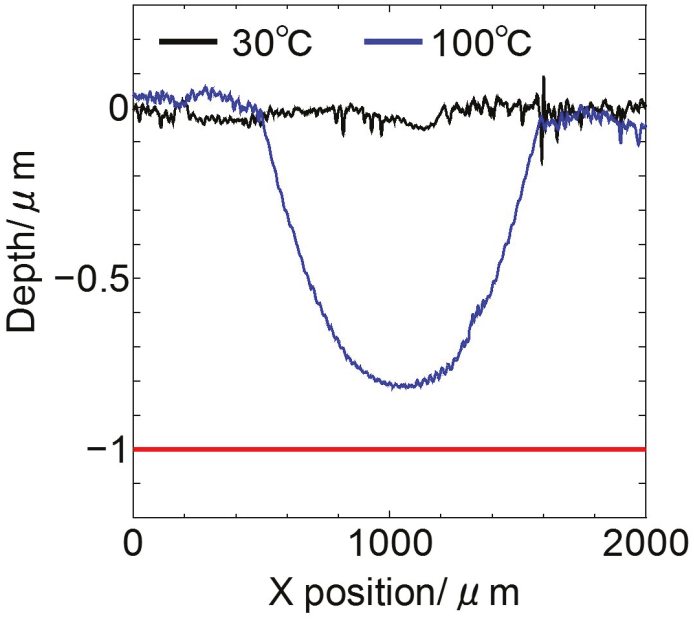

Figure 5. Surface profile of (BMIM)(TCC).

3.2. Raman Spectroscopy

Raman spectroscopy was performed to investigate the structural changes in the ta-C film. Figure 6 shows the Raman spectra of ta-C films after each sliding test when lubricated with (BMIM)(DCN) or (BMIM)(TCC). Figure 7 shows the I_D/I_G ratio of the ta-C films. The interior and exterior parts of the wear track of the ta-C films were analyzed. At 30 °C, no major difference was observed between the interior and exterior parts of the wear track. The graphitization proceeded on the worn surface at the temperature corresponding to the low friction coefficient. It is possible that the graphitization of the ta-C film was responsible for the reduced friction.

3.3. MALDI-TOF/MS Results

The surface information about the worn surface of the disks was obtained using MALDI-TOF/MS (autoflex speed, Bruker, Billerica, MA, USA) to determine the material that caused the reduction in friction. Selected cations and anions for the investigation are as follows: (EMIM) cation = 111, (BMIM) cation = 139, (DCN) anion = 66, and (TCC) anion = 90. In addition, no other matrix was used in this surface analysis because ionic liquids themselves are widely used as a matrix [37]. In other words, if the ions derived from the ionic liquids adsorb to the worn surface, the mass spectra and mapping images can be obtained. From the area where the ions of the ionic liquid are not adsorbed to the surface, no data should be obtained [37]. Figure 8 shows the mapping images of the disk specimens obtained by MALDI-TOF/MS. Few cations and anions were detected at 30 °C. However, anions were adsorbed on the worn surface at the temperature corresponding to the low friction coefficient. Further, the cation content was small compared to that of the anion.

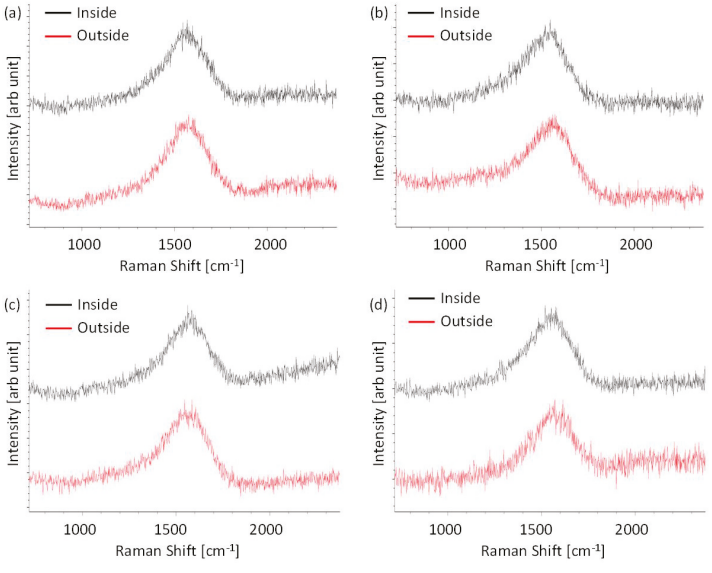

Figure 6. Results of the Raman spectroscopic analyses. (**a**) (BMIM)(DCN) 30 °C, (**b**) (BMIM)(DCN) 170 °C, (**c**) (BMIM)(TCC) 30 °C, and (**d**) (BMIM)(TCC) 100 °C.

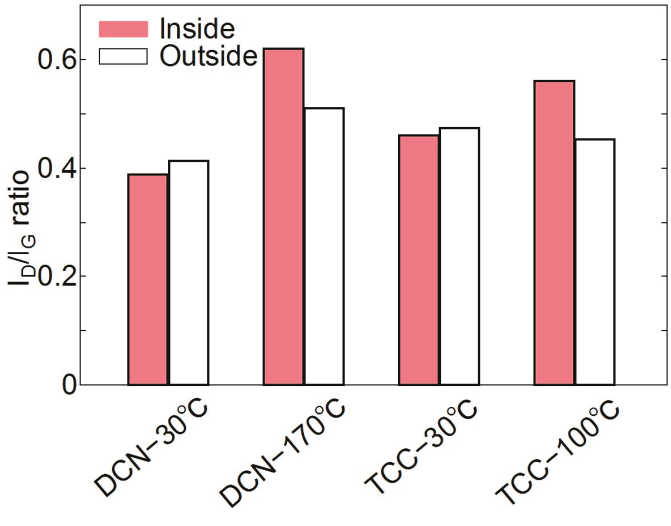

Figure 7. I_D/I_G ratio of (BMIM)(DCN) and (BMIM)(TCC).

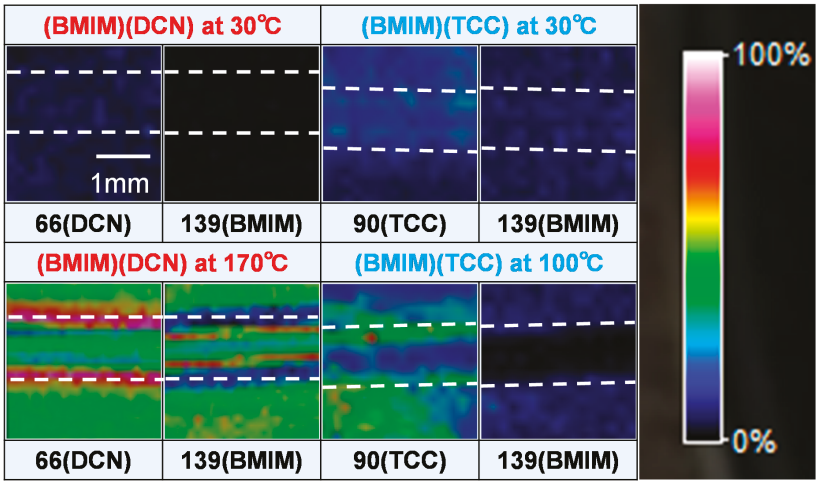

Figure 8. Mapping images of the ta-C film obtained using matrix-assisted laser desorption/ionization time-of-flight mass spectrometry (MALDI-TOF/MS).

3.4. Thermogravimetric Analysis

The ambient temperature affected the reaction of anions with the surface, whereas the cations did not strongly interact with the surface, as determined by MALDI-TOF/MS analysis. The interaction force between cations and anions in the ionic liquid is presumably an important factor. The stability of the ionic liquids was analyzed by TGA to investigate the ionic interaction as well. Figure 9 shows the TGA results. The temperatures corresponding to a weight loss of ~5% are 300 °C for (BMIM)(DCN) and 344 °C for (BMIM)(TCC). This result seems to contradict the results of the sliding test at elevated temperatures.

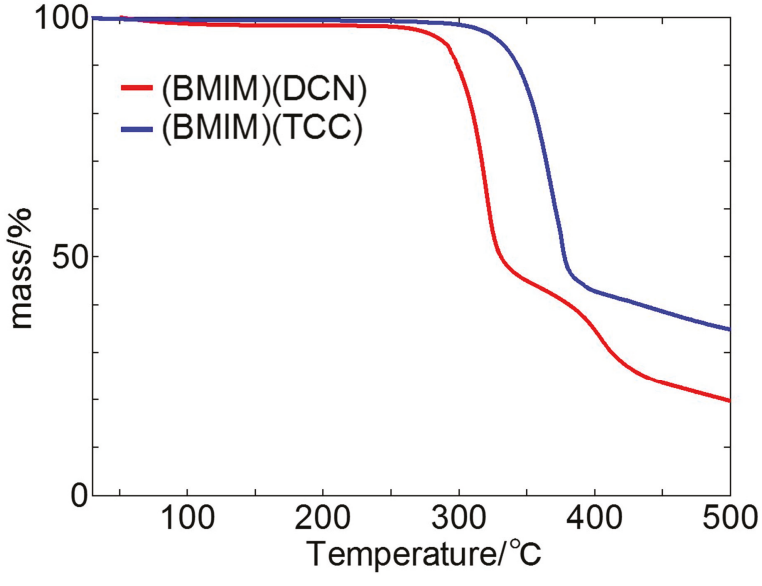

Figure 9. Thermal stability of (BMIM)(DCN) and (BMIM)(TCC).

4. Discussion

In this study, the reduction in friction between steel disks lubricated with (BMIM)(DCN) and (BMIM)(TCC) was confirmed at 90 °C and 170 °C, respectively. With regard to the friction reduction mechanism of DLC, graphitization of DLC at the friction interface has been pointed out as the cause [31–36]. The results of Raman spectroscopy indicated that the graphitization of the ta-C film progressed on the worn surface at the temperature corresponding to the low friction coefficient, which affected the friction behavior. Graphitization was likely caused by the combination of ambient temperature and friction heat. However, the temperature at which the friction was reduced was different for the two cyano-based ionic liquids studied, and another factor influencing the reduction in friction can be predicted. As another possible factor responsible for the reduction in friction, the adsorption of ionic liquids on the friction surfaces was considered. MALDI-TOF/MS analyses indicated that the anions from the ionic liquid adsorbed on the worn surface at the temperature corresponding to the low friction coefficient. The presence of anions on the worn surface and the reduction in friction due to the adsorbed anions have often been reported [19,20,32,37,38]. It has been reported that the ta-C film surface is reactive due to the presence of dangling bonds and reacts with the lubricants [31]. Thus, it is presumed that anions are adsorbed onto the dangling bonds of the ta-C film through covalent bonding, and that the adsorption of anions dominates the friction behavior. Further, as only anions are adsorbed on the worn surface at the temperature of low friction, we speculate that the decomposition temperature of the ionic liquids is an important factor determining the friction characteristics. However, the relationship between the ion interaction and lubricating property could not be obtained from the TGA results. Therefore, we believe that the ionic liquids underwent tribo-decomposition on the worn surface at 30 °C. The anion adsorption is likely to require a high ambient temperature. Thus, both ionic liquids showed low friction at the temperature corresponding to the low friction coefficient. Moreover, the (TCC) anion more easily reacted with the ta-C film than the (DCN) anion. The worn surface likely became brittle as a result in the latter case, leading to accelerated wear.

5. Conclusions

The lubricating properties of two cyano-based ionic liquids against the ta-C film were investigated using a reciprocating sliding tester. In addition, the lubricating mechanism was investigated using MALDI-TOF/MS, TGA, and Raman spectroscopy.

The main findings are as follows:

- The lubricating property of each cyano-based ionic liquid against the ta-C film was influenced by the anion structure and ambient temperature. (BMIM)(TCC) exhibited exceedingly low friction at 170 °C.
- Raman results indicated the occurrence of the graphitization of the ta-C films lubricated with (BMIM)(DCN) and (BMIM)(TCC) at the temperature corresponding to the low friction coefficient, which might have affected the friction behavior.
- MALDI-TOF/MS analyses indicated that anions were adsorbed on the worn surface at the temperature corresponding to the low friction coefficient. The cation content on the worn surface was small compared to the anion content. Therefore, it is speculated that the adsorption of anions also affects the friction behavior.
- We found a contrary trend to that of the sliding test at elevated temperatures with TGA. The ionic liquids might have experienced tribo-decomposition on the worn surface at 30 °C. Anion adsorption requires a high ambient temperature.

Author Contributions: S.K. designed the experiments and wrote the initial draft of the manuscript. S.K. and H.O. performed the experiments. H.O., S.W., C.T., R.T., S.S., and M.M. designed the experiments, contributed to data collection and interpretation, and critically reviewed the manuscript. All authors approved the final version of the manuscript and agree to be accountable for all aspects of the work in ensuring that questions related to the accuracy or integrity of any part of the work are appropriately investigated and resolved.

Funding: This research was funded by JSPS fellow grant, grant number 19K14862.

Acknowledgments: This research was supported by a JSPS fellow grant (No. 19K14862). We would like to thank Editage (www.editage.com) for English language editing.

Conflicts of Interest: The authors declare no conflict of interest.

References

1. Wilkes, J.S. A short history of ionic liquids—From molten salts to neoteric solvents. *Green Chem.* **2002**, *4*, 73–80. [CrossRef]
2. Rogers, R.D.; Seddon, K.R. Ionic liquids—Solvents of the future? *Science* **2003**, *302*, 792–793. [CrossRef] [PubMed]
3. Seddon, K.R. A taste of the future. *Nat. Mater.* **2003**, *2*, 363–365. [CrossRef] [PubMed]
4. Li, H.; Endres, F.; Atkin, R. Effect of alkyl chain length and anion species on the interfacial nanostructure of ionic liquids at the Au (111)–ionic liquid interface as a function of potential. *Phys. Chem. Chem. Phys.* **2013**, *15*, 14624–14633. [CrossRef] [PubMed]
5. Kamimura, H.; Kubo, T.; Minami, I.; Mori, S. Effect and mechanism of additives for ionic liquids as new lubricants. *Tribol. Int.* **2007**, *40*, 620–625. [CrossRef]
6. Gebbie, A.M.; Smith, M.A.; Dobbs, A.H.; Lee, A.A.; Warr, G.G.; Banquy, X.; Valtiner, M.; Rutland, W.M.; Israelachivili, N.J.; Perkin, S.; et al. Long range electrostatic forces in ionic liquids. *Chem. Commun.* **2017**, *53*, 1214–1224. [CrossRef]
7. Motobayashi, K.; Nishi, N.; Inoue, Y.; Minami, K.; Sakka, T.; Osawa, M. Potential-induced restructuring dynamics of ionic liquids on a gold electrode: Steric effect of constituent ions studied by surface-enhanced infrared absorption spectroscopy. *J. Electro. Chem.* **2017**, *800*, 126–133. [CrossRef]
8. Suzuki, A.; Shinka, Y.; Masuko, M. Tribological characteristics of imidazolium-based room temperature ionic liquids under high vacuum. *Tribol. Lett.* **2007**, *27*, 307–313. [CrossRef]
9. Kondo, H.; Seto, J.; Ozawa, K.; Haga, S. Novel lubricants for magnetic thin film media. *J. Magn. Soc. J.* **1989**, *13*, 213–218. [CrossRef]
10. Kondo, H.; Seki, A.; Watanabe, H.; Seto, J. Frictional properties of novel lubricants for magnetic thin film media. *IEEE Trans. Magn.* **1990**, *26*, 2691–2693. [CrossRef]
11. Kondo, H.; Seki, A.; Kita, A. Comparison of an amide and amine salt as friction modifiers for a magnetic thin film medium. *Tribol. Trans.* **1994**, *37*, 88–104.
12. Wamser, C.A. Hydrolysis of fluoboric acid in aqueous solution. *J. Am. Chem. Soc.* **1948**, *70*, 1209–1215. [CrossRef]
13. Swatloski, R.P.; Holbrey, J.D.; Rogers, R.D. Ionic liquids are not always green: Hydrolysis of 1-butyl-3-methylimidazolium hexafluorophosphate. *Green Chem.* **2003**, *5*, 361–363. [CrossRef]
14. Arias-Pardilla, J.; Espinosa, T.; Bermudez, M.D. *Electrochemistry in Ionic Liquids*; Springer: Berlin/Heidelberg, Germany, 2015; pp. 533–561.
15. Kondo, Y.; Yagi, S.; Koyama, T.; Tsuboi, R.; Sasaki, S. Lubricity and corrosiveness of ionic liquids for steel-on-steel sliding contacts. *Inst. Mech. Eng. J. Eng. Tribol.* **2012**, *226*, 991–1006. [CrossRef]
16. Kawada, S.; Watanabe, S.; Tadokoro, C.; Sasaki, S. Effects of alkyl chaing length of sulfate and phosphate anion-based ionic liquids on Tribochemical reactions. *Tribol. Lett.* **2018**, *66*, 8. [CrossRef]
17. Kondo, Y.; Koyama, T.; Tsuboi, R.; Nakano, M.; Miyake, K.; Sasaki, S. Tribological performance of halogen-free ionic liquids as lubricants of hard coatings and ceramics. *Tribol. Lett.* **2013**, *51*, 243–249. [CrossRef]
18. Minami, I.; Inada, T.; Okada, Y. Tribological properties of halogen-free ionic liquids. *Inst. Mech. Eng. J. Eng. Tribol.* **2012**, *226*, 891–902. [CrossRef]
19. Kawada, S.; Watanabe, S.; Tadokoro, C.; Tsuboi, R.; Sasaki, S. Lubricating mechanism of cyano-based ionic liquids on nascent steel surface. *Tribol. Int.* **2018**, *119*, 474–480. [CrossRef]
20. Kawada, S.; Watanabe, S.; Sasaki, S.; Miyatake, M. Evaluation of friction behavior and surface interactions of cyano-based ionic liquids under different sliding contacts and high vacuum condition. *Lubricatns* **2018**, *6*, 69. [CrossRef]
21. Shah, F.U.; Glavatskih, S.; Antzutkin, N.O. Boron in tribology: From borates to ionic liquids. *Tribol. Lett.* **2013**, *51*, 281–301. [CrossRef]

22. Zhou, Y.; Qu, J. Ionic liquids as lubricant additives: A review. *Appl. Mater. Interfaces.* **2017**, *9*, 3209–3222. [CrossRef] [PubMed]
23. Jiang, C.; Wang, Y.; Su, H.; Li, W.; Wang, Z. Synthesis and evaluation of a protic ionic liquid as a multifunctional lubricant additive. *Friction* **2019**, 1–9. [CrossRef]
24. Avilés, M.D.; Pamies, R.; Sanes, J.; Carrión, F.J.; Bermúdez, M.D. Fatty acid-derived ionic liquid lubricants. Protic ionic liquid crystals as protic ionic liquid additives. *Coatings* **2019**, *9*, 710. [CrossRef]
25. Guo, H.; Adukure, A.R.; Iglesias, P. Effect of ionicity of three protic ionic liquids as neat lubricants and lubricant additives to a biolubricant. *Coatings* **2019**, *9*, 713. [CrossRef]
26. Tadokoro, C.; Sato, K.; Nagamine, T.; Nakano, K.; Sasaki, S.; Sato, T.; Sakakibara, K.; Tsujii, Y. Concentrated polymer brush as reciprocating sear material for low leakage and low friction. *Tribol. Tans.* **2019**. [CrossRef]
27. Tujii, Y.; Nomura, A.; Okayasu, K.; Gao, W.; Ohno, K.; Fukuda, T. AFM studies on microtribology of concentrated polymer brushes in solvents. *J. Phys. Conf. Ser.* **2009**, *184*, 012031.
28. Sato, K.; Okubo, H.; Hirata, Y.; Tadokoro, C.; Nakano, K.; Tsujii, Y.; Sasaki, S. Macroscopic tribological properties of thick concentrated polymer brush on rough steel under lubrication with ionic liquid. *J. Tribologi.* **2019**, *20*, 97–113.
29. Bouabibsa, I.; Lamri, S.; Sanchette, F. Structure, mechanical and tribological properties of Me-doped diamond-like carbon (DLC) (Me = Al, Ti, or Nb) hydrogenated amorphous carbon coatings. *Coatings* **2018**, *8*, 370. [CrossRef]
30. Aijaz, A.; Ferreira, F.; Oliveira, J.; Kubart, T. Mechanical properties of hydrogen free diamond-like carbon thin films deposited by high power impulse magnetron sputtering with Ne. *Coatings* **2018**, *8*, 385. [CrossRef]
31. Okubo, H.; Kawada, S.; Watanabe, S.; Sasaki, S. Tribological performance of halogen-free ionic liquids in steel–steel and DLC–DLC contacts. *Tribol. Trans.* **2018**, *61*, 71–79. [CrossRef]
32. Kawada, S.; Watanabe, S.; Tsuboi, R.; Sasaki, S.; Prakash, B. Lubrication mechanism of halogen-free ionic liquids. *Tribol. Online* **2017**, *12*, 155–161. [CrossRef]
33. Kawada, S.; Sato, K.; Watanabe, S.; Sasaki, S. Lubricating property of cyano-based ionic liquids against hard materials. *J. Mech. Sci. Tech.* **2017**, *31*, 5745–5750. [CrossRef]
34. Ogwu, A.A.; Lamberton, R.W.; Morley, S.; Maguire, P.; McLaughlin, J. Characterization of thermally annealed diamond like carbon (DLC) and silicon modified DLC films by Raman spectroscopy. *Physica B Condensed Matter* **1999**, *269*, 335–344. [CrossRef]
35. Vengudusamy, B.; Green, J.H.; Lamb, G.D.; Spikes, H.A. Tribological properties of tribofilms formed from ZDDP in DLC/DLC and DLC/steel contacts. *Tribol. Int.* **2011**, *44*, 165–174. [CrossRef]
36. Liu, Y.; Erdemir, A.; Meletis, E.I. An investigation of the relationship graphitization and frictional behaviour of DLC coatings. *Surf. Coat. Tech.* **1996**, *86–87*, 564–568. [CrossRef]
37. Christoph, G.; Ernst, P.; Nicole, D.; Gunter, A. Imaging of a Tribolayer Formed from Ionic Liquids by Laser Desorption/Ionization-Reflectron Time-of-Flight Mass Spectrometry. *Anal. Chem.* **2012**, *84*, 10708–10714.
38. Liu, X.Q.; Zhou, F.; Liang, Y.; Liu, W. Tribological performance of phosphonium based ionic liquids for an aluminum-on-steel system and opinions on lubrication mechanism. *WEAR* **2006**, *261*, 1174–1179. [CrossRef]

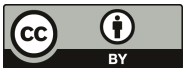

coatings

MDPI

Article

Friction Reduction in Unidirectional Lubricated Sliding Due to Disc Surface Texturing

Slawomir Wos, Waldemar Koszela, Andrzej Dzierwa and Pawel Pawlus *

Faculty of Mechanical Engineering and Aeronautics, Rzeszow University of Technology, Powstancow Warszawy 8 Street, 35-959 Rzeszow, Poland; wosslawomir@prz.edu.pl (S.W.); wkktmiop@prz.edu.pl (W.K.); adzierwa@prz.edu.pl (A.D.)

* Correspondence: ppawlus@prz.edu.pl; Tel.: +48-17865-1183

Received: 26 January 2020; Accepted: 27 February 2020; Published: 29 February 2020

Abstract: Surface texturing is an option of surface engineering resulting in reduction of friction due to the creation of isolated dimples or grooves on sliding surfaces. The purpose of this work is to find the effect of the groove bottom profiles on the reduction of the friction force. Investigations were conducted using an Optimol SRV5 tribotester equipped with a pin-on-disc module. A disc made of 42CrMo4 steel, with a 100 mm diameter acted as a sample. A counter-sample was made of the same material, however, its diameter was 20 mm. The sliding conditions were selected to be similar to those of a sliding crankpin bearing pad operating in a high-performance internal combustion engine. Surface texturing was found to be beneficial for a reduction in the friction coefficient up to 55% in comparison to the untextured disc. Tribological performances of discs with spiral groove patterns were better than those with a radial layout. In most cases the convergent profile of the groove bottom was superior to the dam shape.

Keywords: surface texturing; pin-on-disc; conformal contact; friction force; lubricated sliding

1. Introduction

Surface texturing is one of the fundamental methods of changing sliding conditions under lubrication. As a result of surface texturing a decrease in wear and better efficiency of mechanisms can be achieved [1–5]. Typically, beneficial effects of surface texturing in mixed and boundary lubrications are larger than those found under full film lubrication [4]. Many years ago a surface directionality was found to be a way to improve tribological performances of sliding elements [6]. Therefore, structures with parallel or cross-hatched grooves [7–10] were created. Textured surfaces with isolated dimples are also used [11–15].

The orientation of grooves to the sliding direction is very important from the tribological point of view. Petterson and Jacobson [16] found that in a regime of starved lubrication grooves positioned perpendicularly to the sliding direction led to smaller frictional resistance compared to their location parallel to the direction of motion. Perhaps when the ball slid along the grooves there was a small probability for a very small area of contact to cross an oil reservoir. Moronuki and Furukawa [17] obtained similar results after sliding tests between textured Si and planar Si in a low contact pressure regime. These results were caused by minimizing the adhesion force by the grooves perpendicular to sliding due to water capillary. The experimental research conducted by Yuan et al. [18] revealed that under a low contact pressure the grooves orthogonal to the movement direction caused more decrease in the coefficient of friction that those oriented along the sliding direction. Probably the strongest hydrodynamic lift was offered when the grooves were perpendicular to the sliding direction. Ren et al. [19] obtained the same reason of the results of tribological investigations. They achieved the beneficial effect of perpendicular orientation of grooves to the sliding direction on the frictional resistance

under a slide-to-roll contact [19]. According to Zum Gahr et al. [20] the grooves perpendicularly aligned to the direction of motion led to smaller friction force; this behavior is related to higher oil film thickness than obtained for grooves parallel to the sliding direction. According to Costa and Hutchings [21] and Duarte et al. [22] parallel textures guide the lubricant away from the contact leading to a smaller film thickness and, thus, higher coefficient of friction. The authors of papers [10,23,24] found that a decrease in the honing angle led to lower coefficient of friction of cylinder liner–piston ring pack. Probably a small honing angle enhanced hydrodynamic action.

Generally, for one-directional surfaces, the main direction should be oriented orthogonally to the direction of motion.

The effect of oil pockets orientation to the sliding direction for the chevron-shaped pattern was studied by the authors of papers: [25–28]. They found that chevron pattern pointing along the direction of motion could lead to film thickness growth. Wang [29] and Galda et al. [30] observed that orientation of triangle-shaped oil pockets and dimples of long drop shape, respectively, had a substantial effect on tribological behaviors of sliding pairs. The lowest friction force was achieved when one side border orthogonal to the sliding direction first entered the contact zone.

The optimization of the dimple bottom profiles was done experimentally. Lu et al. tested triangular [31] and squared [32] sloped dimples in lubricated line contact. The bottoms with the converging shapes helped to minimize friction by generating hydrodynamic lift. Galda et al. [30] obtained the same finding after testing dimples of the long drop shape with the sloped bottoms.

Various fabrication techniques were used for surface texturing [33]. Laser texturing is the most widely used, because this method seems to be the most flexible and efficient [1,11,13–15,34–36]. Abrasive jet machining can be an alternative to laser texturing [28,37–39]. The other methods include electrochemical etching, lithography [12], photochemical texturing, burnishing (embossing) [30,40] and some kinds of machining (honing [8–10] or grinding). A sharp tip can be also used for creating grooves [41]. This process can be facilitated using machines equipped with CNC.

The main aim of this work is to find the effect of the groove bottom profiles on the friction reduction, based on the diverging and converging characteristics of the textures. Similar experimental investigations were done rarely.

Surface texturing highly depends on the application; it should be dedicated to a special tribological system. The sliding conditions used in this work correspond to those of sliding crankpin bearing pad operating in a high-performance internal combustion engine. Such pads are typically threatened by severe wear, due to starved lubrication and high temperature in a race motorcycle engine. The attempt was done to achieve low friction, wear and heat generation due to surface texturing.

2. Materials and Methods

A disc made of 42CrMo4 steel with a 100 mm diameter acted as a sample. A counter-sample was made of the same material, however, its diameter was 20 mm. Samples and counter-samples were heat treated to receive hardness of 40 HRC for the sample and 35 HRC for the counter-sample. Textured discs had higher hardness than the counter-samples to increase their wear resistances. Due to it wear of the textured sample was lower than that of the counter-sample leading to smaller friction and prolonged life of the tribological system. The experiments were carried out using an Optimol SRV5 tribotester (produced by: Optimol Instruments Prüftechnik GmbH, Flößergasse 3, D-81369 München, Germany) equipped with a rotary module. The method of fixing the counter specimen was modified to ensure better aligning of the cooperating surfaces and eliminate fixing errors (Figure 1). The normal load was 50 N, the rotational speed was 500 rpm and the friction radius was 20 mm. The attempt was done to ensure the closest sliding parameters to those existed inside the motorcycle engine during start phase. Tests were carried out in temperature of 30 °C. Before each test the sample and the holder were heated up and hold in 30 °C for 5 min to stabilize the temperature. Temperature sensor was located under the rotating disc inside the holder. Therefore, the heat generated by friction force was

impossible to monitor precisely due to the heat dissipation. Surface textures of contacting elements were measured by a white light interferometer Talysurf CCI Lite.

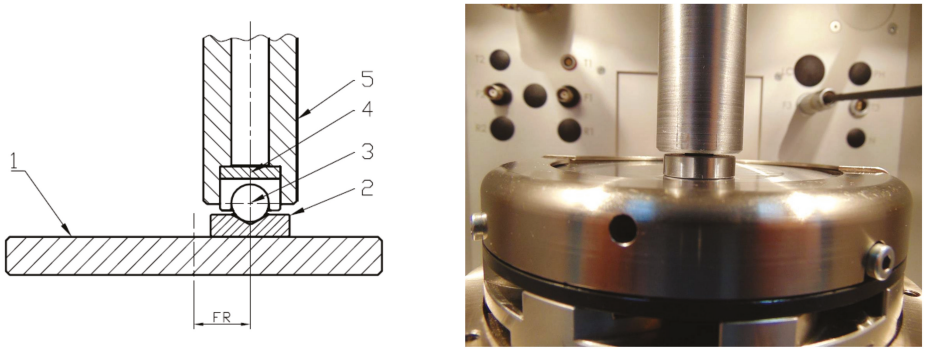

(**a**) (**b**)

Figure 1. Scheme of counter-sample mounting; 1—sample (rotating disc), 2—self-aligning counter-sample, 3—ball bearing, 4—ball bearing holder, 5—load transmitting rod, FR—friction radius (**a**); view of test chamber (**b**).

In the beginning of each test a volume of 5 mL of semisynthetic motorcycle oil 10W40 T4 was supplied to the test zone. There are the following parameters of a lubricant: kinematic viscosity 66 mm^2/s (66 cSt) at 40 °C, and 13.5 mm^2/s (13.5 cSt) at 100 °C, ignition temperature 180 °C, and a freezing point of −18 °C. This specific oil was selected due to its designation to high-performance motorcycle engines. Base surfaces of samples were ground and some of them were tested without texturing as reference samples, their roughness parameter Ra was 0.25 ± 0.01 µm. Surface texturing was made by precise milling. The milling process was chosen due to the great accessibility of CNC mills. We tried to present the possibilities of using standard CNC machines in surface texturing instead of using other techniques, like laser surface texturing, electrical discharge machining or etching, in which additional devices are required. Moreover, thanks to careful production process planning it is possible to create grooves by adding only one additional operation to CNC machine. That approach does not lead to a high increase in the production cost. Three types of the milling process was used. The first one required 5 axis CNC milling machine, where mounted disc was tilted by 0.5° from the horizontal direction. This approach helped to form a groove of with a sharp edge on one side and a convergent bottom on the other side (Figure 2).

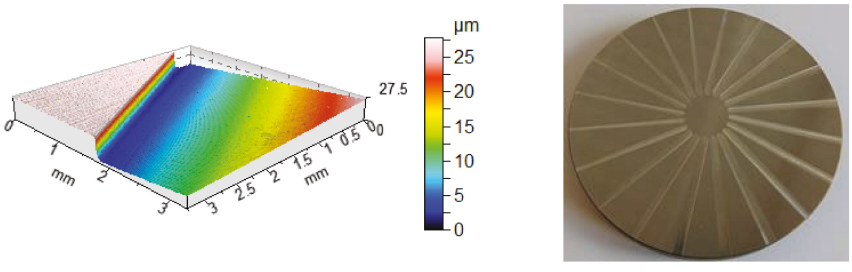

Figure 2. Isometric view of the bottom of the groove of a sharp edge on one side and a convergent bottom (**left**) and sample view with straight radial grooves of type 1 (**right**).

Other two types of created grooves were made with the use of sharp milling tool of 3 mm diameter and ball milling tool of 6 mm diameter. With application of sharp milling tool positioned vertically to a

sample the both sides sharp edge groove was obtained. This type acted in lubricated sliding conditions as the both side dam (divergent) (Figure 3a).

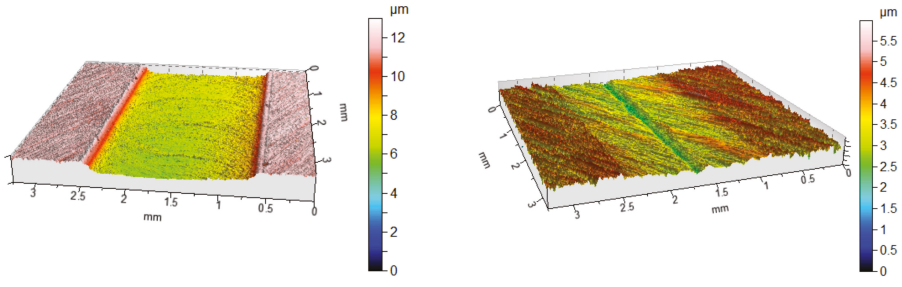

(**a**) (**b**)

Figure 3. Isometric view of a surface created: (**a**) using a sharp mill cutter with sharp edges from both sides and (**b**) made with the use of a ball mill cutter.

Other type of a groove was made using a ball mill cutter; due to spherical shape of the tool light slopes at the edges of the groove were obtained, its depth slowly increased from the sides to achieve maximum value at the groove center. This geometry was called both side convergent (Figure 3b).

Figure 4 shows schemes of bottom profiles of grooves with sliding direction of the counter-sample.

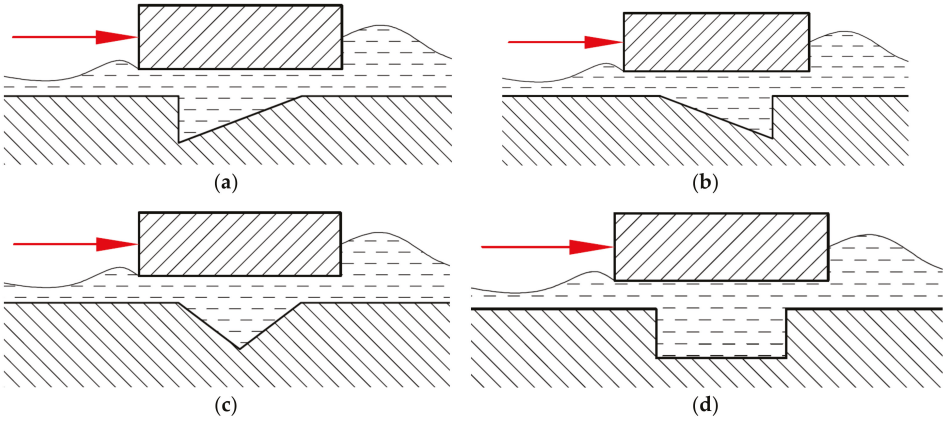

(**a**) (**b**)

(**c**) (**d**)

Figure 4. Schemes of bottom profiles of grooves with marked sliding direction of the counter-sample. (**a**) Convergent; (**b**) Dam; (**c**) Both side convergent; (**d**) Both side dam.

Discs with radial pattern of the grooves were called discs of type 1 (Figure 2). The spiral layout was created to gather the lubricant to the contact zone and then to minimize oil loss. Discs of types 2 and 3 originated from different parts of Archimedes curve; the starting point of the curve was located at a center of the disc. Discs of type 4 and 5 were made from the same parts of the curve, however, starting points of the grooves were spaced from the centers of discs by 10 mm.

Due to milling tool positioning during five-axis machining a problem with precision occurred. Shaping a spiral groove with an asymmetric profile was possible, however, in this case the groove had different depths at its whole length. This problem was caused by adding positioning accuracies of all five axes during simultaneous movement. This was the reason why spiral grooves had only two bottom shapes: both side convergent and both side dam. These shapes required simultaneous movement in only two axes, in the third axis the depth of material cut was set before spiral shape

milling. The bottom profiles of the textures were defined by the shape of used mills. The convergent bottom shapes were created to form lubrication wedges. The dam shapes are typically formed by laser surface texturing or etching, therefore they were also taken into consideration.

Figure 5 shows photos of discs with spiral patterns of grooves and dimensions of guiding lines of these grooves from the discs of types 2–4. There were 20 grooves on each disc. The number of test repetitions was at least 3.

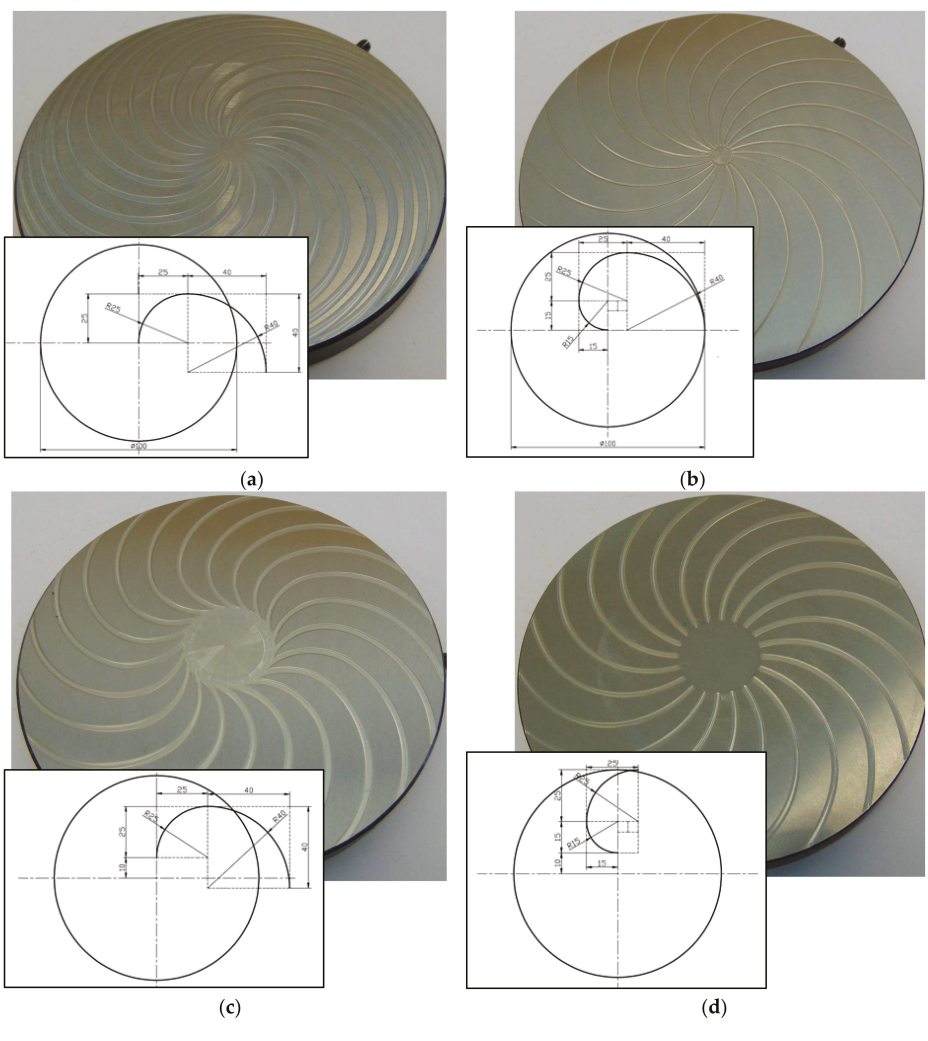

Figure 5. Views of discs of types 2 (**a**), 3 (**b**), 4 (**c**), and 5 (**d**) with dimensions of guiding lines.

Figure 6 shows isometric views of selected grooves from spiral discs. Table 1 presents dimensions of grooves from various textured discs.

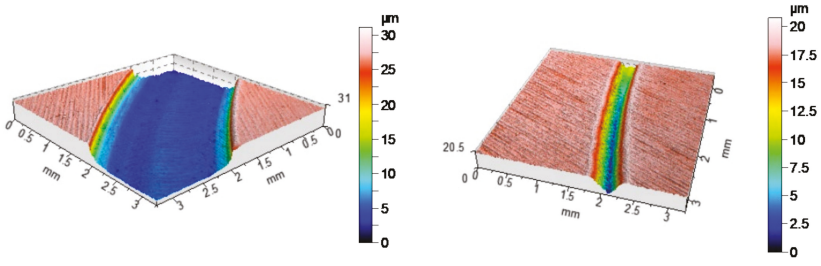

Figure 6. Isometric views of grooves from discs of type 2: both side dam (**left**) and both side convergent (**right**).

Table 1. Sizes of grooves from various textured discs.

Kind of the Groove	Width of the Groove [mm]	Depth of the Groove [µm]	Average Area of the Hole in the Cross Section [mm^2]
	Type 1		
Convergent	3.1 ± 0.1	24.7 ± 1.2	0.040900
Dam	3.15 ± 0.05	25.4 ± 1.4	0.041600
Both side convergent	1.6 ± 0.1	4.5 ± 0.4	0.001012
Both side dam	1.95 ± 0.05	28.8 ± 1.8	0.042000
	Type 2		
Both side convergent	0.61 ± 0.1	17.5 ± 3	0.003747
Both side dam	1.9 ± 0.05	23 ± 3	0.039697
	Type 3		
Both side convergent	0.6 ± 0.1	25.3 ± 1.8	0.003677
Both side dam	2.1 ± 0.05	30.4 ± 2.4	0.044300
	Type 4		
Both side convergent	0.6 ± 0.1	25.7 ± 1	0.003201
Both side dam	1.9 ± 0.05	30 ± 1	0.037354
	Type 5		
Both side convergent	0.56 ± 0.1	26.3 ± 2.2	0.002331
Both side dam	1.95 ± 0.05	16.9 ± 1.6	0.031540

One can see from the analysis of Table 1 that depths of the grooves were typically between 17 and 34 µm; both side convergent grooves from disc of type 1 of the lowest depth (4.5 µm) were the exceptions. For discs with spiral patterns of grooves the main difference between grooves called both side convergent and both side dam was width which was much larger in the latter case. The changes of width affected also the area of the hole in the cross-section. Due to a difference in depths this area of both side dam groove of disc 1 was also larger than that of both side convergent groove.

3. Results and Discussion

Figure 7 shows curves presenting friction forces versus time for the sliding pair containing the untextured disc. Due to instability of the friction force, the number of test repetitions was 4. One can see that the friction force after initial fluctuations increased as test progressed and obtained a stable value after about 170 seconds. The final value of the friction force was between 3 and 6 N. In the middle and final parts of tests large variations of the friction forces also occurred in most cases.

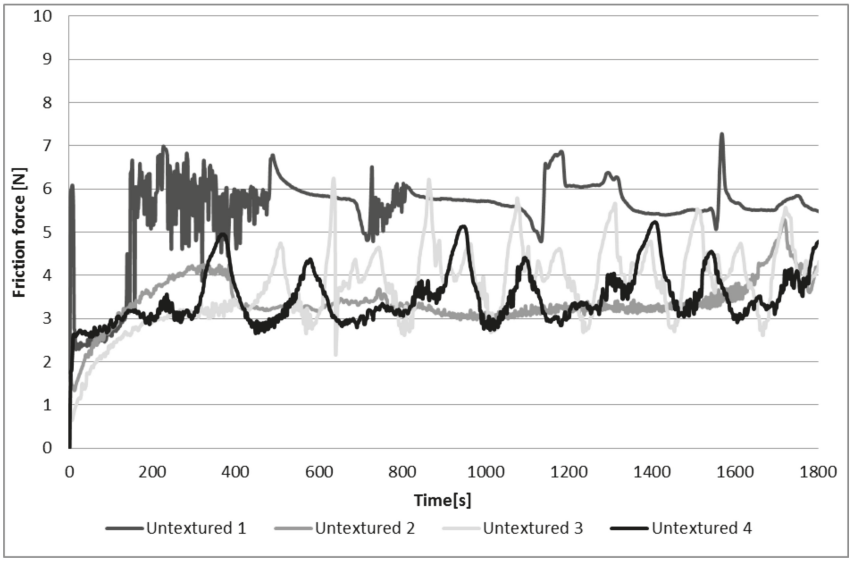

Figure 7. Friction force versus time for assembly with an untextured disc.

Figure 8 presents friction force runs for assemblies with textured disc of type 1.

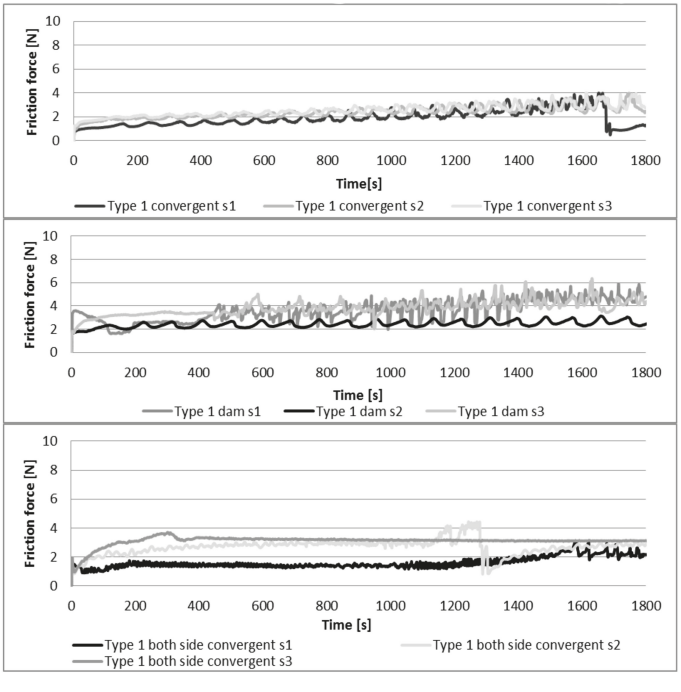

Figure 8. *Cont.*

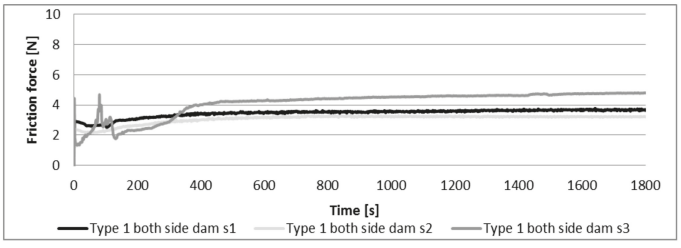

Figure 8. Friction force versus time for assemblies with a textured disc of type 1.

The course of the friction force curve for assembly with textured disc of type 1 with convergent bottom profile was different from that of sliding pair with untextured disc. The friction force initially sharply increased, obtained 1–1.5 N and then increased slowly. The final value of the friction force was 2.5–4 N. The scatters of the friction force between test runs and within the same test run were smaller than those obtained for untextured assembly. The fluctuations of the friction force versus time (of the shape similar to sinusoid) were probably caused by a rotation of the counter-sample (small disc).

The change of the bottom profile from convergent to dam caused higher scatter of the friction force. In one test run the friction force increased abruptly, obtained the value about 2 N and then increased very slowly – its final value was between 2.5 and 3 N. In two other runs, the friction forces after obtaining value of about 3 N increased, but more quickly than in the mentioned latter test run and finally obtained values between 4 and 6 N. In both cases scatters of the friction forces within test run were comparatively large.

When both sides of the groove bottom profile were convergent, the final values of the friction forces were comparatively small: 2–3 N. However the shape of the friction force curves varied. In one test run the friction force was stable after about 300 seconds. In other cases the friction forces after initial sharp growths slowly increased. The fluctuations of the friction forces within one test run were lower than in the analysed previously cases.

A low variation of the friction force within the same test run was also observed for sliding pairs containing both sides dam of the profile bottom in the middle and final parts of tests. The friction forces after initial changes slowly increased and obtained the final values between 3.2 and 4 N; they were higher compared to those obtained for the disc with convergent bottom shape from the both sides.

Figure 9 shows average friction coefficients with scatters for sliding pairs with untextured disc and discs with straight radial groves (of type 1) during the whole tests as well as at the beginning and at the end of tests. Values described as "the beginning of the test" were calculated as average values between 60 and 360 seconds of the test. Average values calculated between 1500 and 1800 s were described as "end of the test". Average values at "whole test" were calculated between 60 and 1800 seconds. The first 60 seconds of each test were discarded due to instabilities of the friction forces. One can see that the worst tribological performance was obtained for the assembly with untextured disc. In this case both the mean value and the scatter of the coefficient of friction were the largest. Textured discs led to lower frictional resistance particularly in the initial test parts. The convergent profile bottoms from one and both sides seem to be better solution than the profile bottom of dam shape. However, taking the scatter into consideration, there is difficult to find any difference between the behaviors of textured samples of type 1.

Figure 10 presents curves characterizing the friction force versus time for assemblies with spiral discs of types 2 and 3.

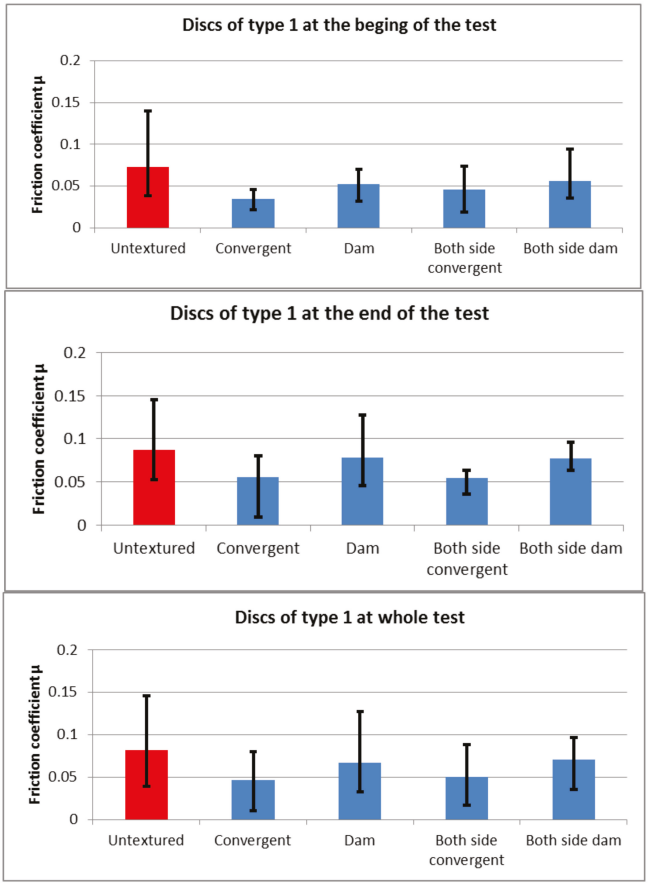

Figure 9. Average friction coefficients with scatters for assemblies with an untextured disc and discs with straight radial grooves (of type 1).

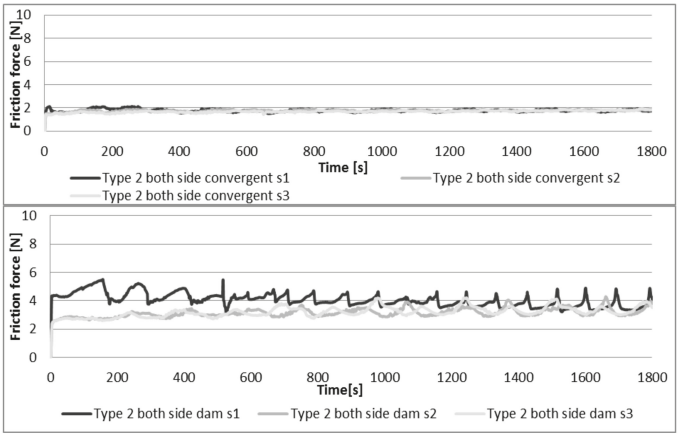

Figure 10. *Cont.*

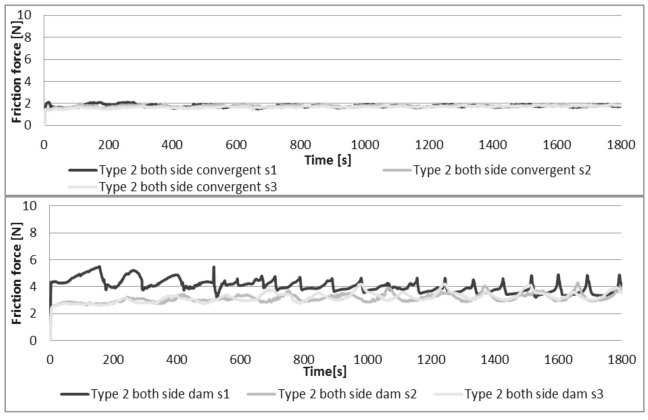

Figure 10. Friction force versus time for assemblies with a textured discs of type 2 and type 3.

A convergent disc of type 2 after initial sharp increase in a few seconds obtained stable value a little smaller than 2 N. The fluctuation of the friction force was low.

Changing the bottom profile from convergent to dam for the disc of type 2 caused an increase in the friction force, its variation also increased between and within test runs. After a few seconds the friction force obtained values of 3–4 N and then in two runs the friction force marginally increased, while in the third case – decreased. The final value of the friction force was between 3 and 5 N.

Beneficial results were achieved for both side convergent disc of type 3. In two cases the fiction force after obtaining a constant value was stable. Its final value was between 1.3 and 1.6 N. The fluctuations of the friction forces were small.

Changes of the shape of the groove bottom from convergent to dam led to increases in both the friction force values and scatters. The final value of the friction force was between 2 and 4 N.

In general the convergent bottom profile of the groove led to better results for discs of types 2 and 3 compared to dam bottom shape. The courses of the friction force curves in all analyzed cases were superior to those found for sliding pairs with untextured samples and with the disc of type 1.

Figure 11 shows graphs presenting the friction force versus time for assemblies with textured discs of types 4 and 5.

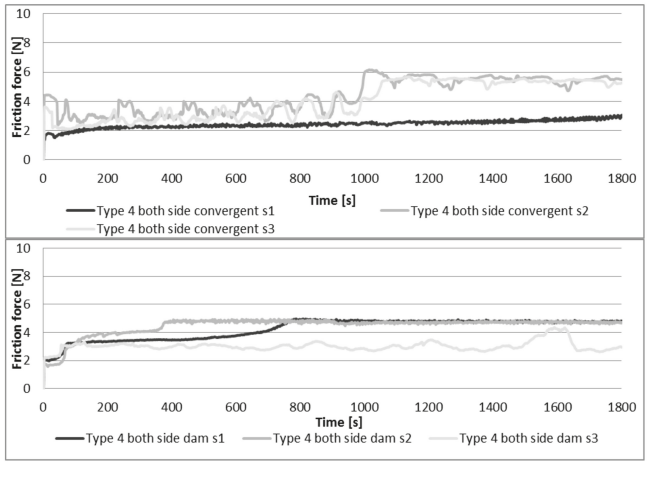

Figure 11. *Cont.*

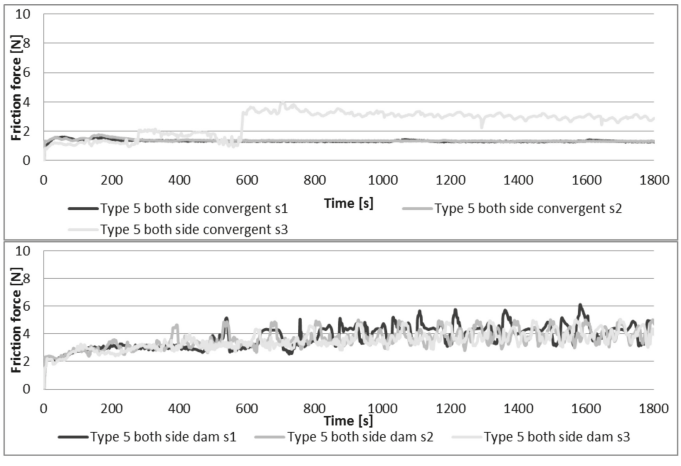

Figure 11. Friction force versus time for assemblies with textured discs of type 4 and type 5.

The disc of type 4 gave not good tribological results. For both profiles of the bottom of the groove scatters of the friction force were comparatively high. When this profile was convergent, the friction force increased with time. The final value of the friction force was between 2.8 and 5.5 N. When this bottom has dame shape after 800 seconds the friction force was constant, especially in two cases. The final friction force was between 2.7 and 4.8 N. Generally, both profiles of the bottom of grooves gave similar results.

The friction force corresponding to the disc with convergent groove bottom profile of type 5 after initial sharp increase in a few seconds obtained stable value near 1 N. In two cases the friction force increased to 1.3 N and was stable during the test; the fluctuation of the friction force was low. In the third run the friction force after about 300 seconds abruptly increased to 3.5 N and then slowly decreased. The final value of the friction force was between 1.3 and 3 N.

Changing the groove bottom profile from convergent to dam for the disc of type 5 caused an increase in the friction force values and scatters. After a few seconds the friction force obtained the value about 2 N and then it slowly increased and obtained the final value between 3.5 and 5 N. The convergent bottom profile of the groove was better for the disc of type 5.

Figure 12 shows average friction coefficients with scatters for textured discs with spiral grooves of types 2, 3, 4, and 5 during the whole test as well as at the beginning and at the end of tests. Since, in most cases, the friction force was nearly constant during the test, three graphs were similar. The smaller scatter of the friction force was obtained in the final parts of tests. The best results (the smallest friction forces values and scatters) were achieved for the discs of type 2 and 3 with convergent groove profile bottoms. For the disc of type 5 the convergent profile bottom of the groove led to better results, however, the scatter of the friction force was comparatively high. The worst results (high friction forces values and scatters) were obtained for the disc of type 4 independently of its groove bottom profile.

During tests the truncation of the highest asperities occurred. However, wear was smaller than the height of the original surface roughness - Figure 13. The wWear level was comparatively high for untextured samples and textured samples with dam groove bottom shapes, particularly for the radial pattern of grooves.

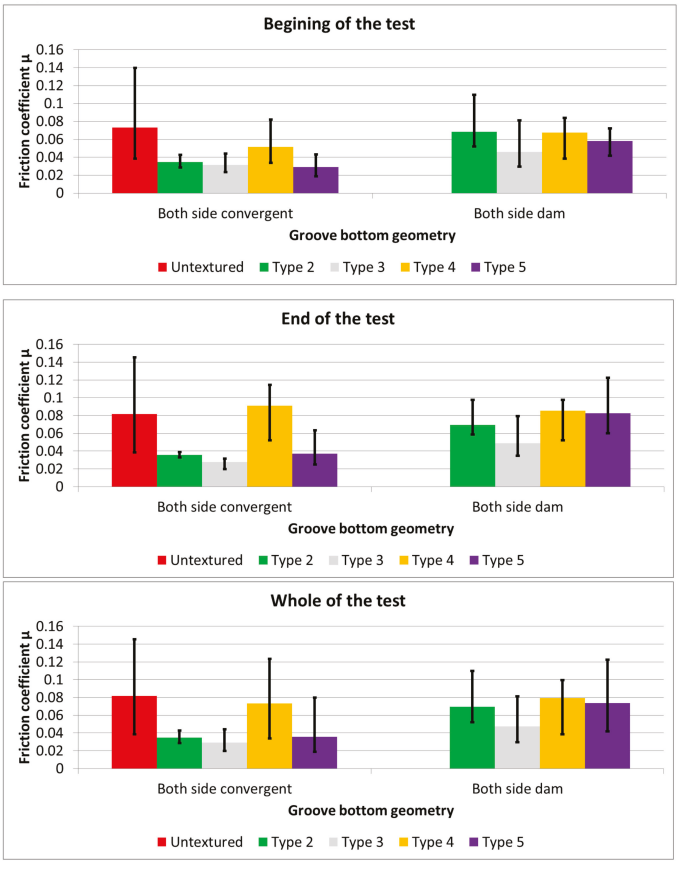

Figure 12. Average friction coefficients with scatters for assemblies with textured discs with spiral grooves (of types 2, 3, 4, and 5).

The untextured disc led to high values of the coefficient of friction values and, perhaps more importantly, the highest scatters both within the test run and between test runs. This performance was caused by disc surface topography after grinding. Because of the lack of oil pockets, the assembly with untextured disc operated in boundary lubrication conditions or in mixed lubrication conditions with dominance of boundary lubrication regions over full lubrication areas, in this case the formation of the hydrodynamic lift was not possible. An increase in the average temperature of tested assembly, due to friction force, was also the greatest for untextured discs (8 °C). For comparison, the average temperature increases of the assemblies with textured discs leading to the greatest and the lowest friction coefficients were 3.2 and 2.4 °C, respectively. However, due to the high distance between the friction region and the temperature sensor most of heat generated was dispersed. To gain more precise data a thermal imaging camera should be used.

Situation was improved after introducing radial grooves (disc of type 1). A reduction in the frictional resistance due to surface texturing was the largest in the initial part of the test. An increase in the friction force as test progressed obtained for sliding pairs with textured samples was a problem. This behavior was probably caused by the oil loss. During tests straight radial grooves presumably gathered the lubricant, which leaked out from the contact zone due to a centrifugal force presence. However, in this case a reduction of the resistance to motion and the smaller friction force variation occurred, compared to the assembly with untextured disc sample. The grooves with convergent bottom

profiles (one side and both sides) were slightly superior to those with the dam shape. The obtained values of the friction coefficient confirmed the known ability to decrease friction with the use of the convergent shape of the friction surfaces due to the formation of the lubrication wedge. During tests the amount of oil was sufficient to fill all the grooves; moreover, there was no visible wear debris entrapped inside the grooves after the test. Significantly longer tests could probably show a positive effect of the grooves as traps for wear debris.

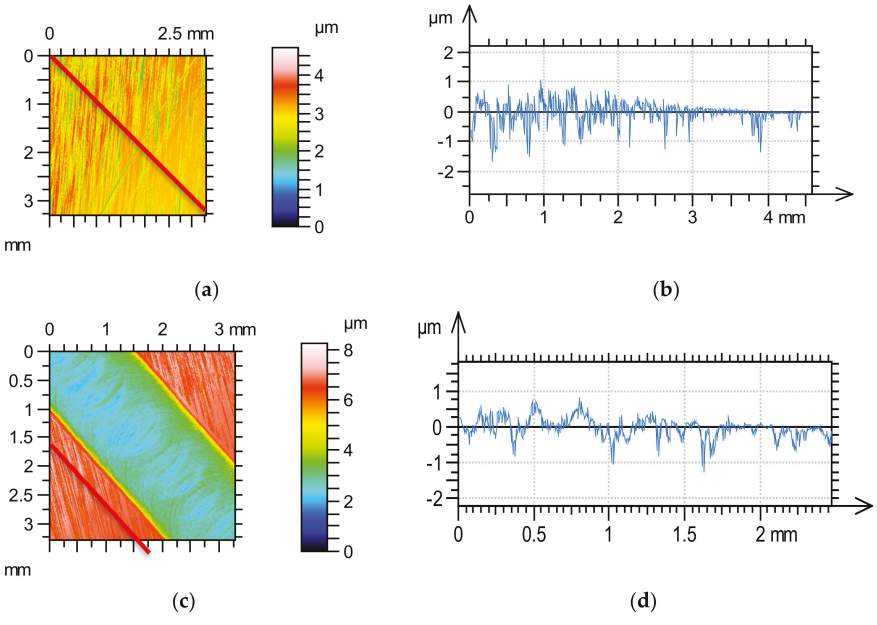

Figure 13. Contour plots (**a,c**) and extracted profiles (**b,d**) of worn untextured disc surface (**a,b**) and surface of type 1 with both side dam bottom shape of the groove (**c,d**).

Spiral discs of types 2, 3, 4, and 5 were created to gather the oil to the contact area and to reduce oil loss. Better tribological behaviors of spiral pattern of dimples than those of radial rows layout of oil pockets were also achieved in work [39]. In most cases the friction force did not increase during tests, especially for the convergent groove bottom profile. For discs of types 2, 3, and 5 the convergent profile bottom of the groove was superior to that of the dam bottom shape. The tribological performance of the disc of type 4 was independent of the shape of the disc texture bottom. The smallest frictional force and the best stability of results were achieved for the disc of type 2. The disc of type 3 of both side convergent groove bottom profile assured also stable and small resistance to motion. The disc of type 5 of both side convergent groove bottom shape also led to comparatively small friction force, but the scatter of the coefficient of friction was high. The worst results were obtained when the disc of type 4 was used: high resistance to motion and high fluctuations of the friction force occurred.

To explain the results of experimental investigations during the contact of discs with spiral grooves with the counter-samples, the additional analysis was conducted (Figure 14).

The spiral fragment located in the contact zone depends on the curvature of the spiral used. The texture of type 5 generated the equal flows of the lubricant inside the groove to the inner and outer sides of the disc (Figure 14a). When discs 2 and 3 were used, the flow inside the groove generated by rotational movement would be directed into the center of the disc (Figure 14b), this solution helps to decrease oil loss from the contact zone due to flow generated by the centrifugal force. The texture of type 4 generated the flow outside the disc (Figure 14c). One can see from this analysis that the

performance of discs of type 4 should be the worst, due to the largest oil loss. These assumptions were confirmed for assemblies containing textures with both side convergent bottoms of grooves. For grooves with both side dam bottoms the hydrodynamic force was not generated so easily and therefore the effect of spiral pattern vanished. Therefore, in most cases the convergent profile of groove bottom gave better results than dame bottom shape. These results are in accordance with other works; Galda et al. [30] and Lu et al. [31,32] achieved beneficial tribological effects of converging profiles of isolated dimples bottoms.

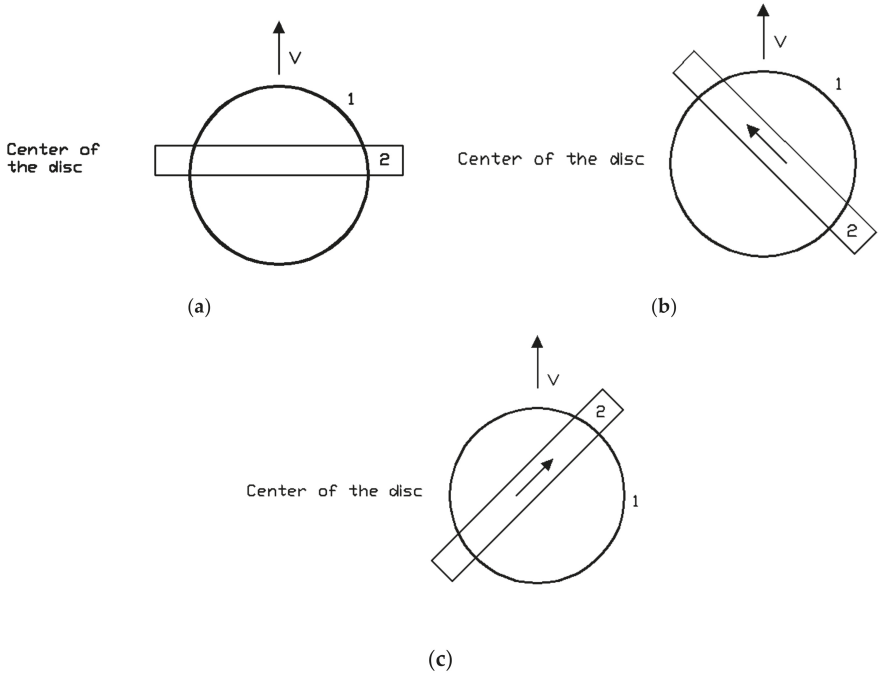

Figure 14. Scheme of oil flow inside the groove depending on the contact between the spiral fragment and the counter-sample; V- linear speed, 1–the contact area with the counter-sample, 2–the position of the spiral groove; (**a**) equal flows of the lubricant, (**b**) the flow directed to the center of the disc, and (**c**) flow outside the disc.

Although the shapes of spirals were created to gather oil in one direction of rotation, only the spiral fragments located in the friction zones affected oil gathering. Therefore, the triblogical performances of discs of types 4 and 5 were not so beneficial as presumed.

The effect of oil loss due to the presence of the centrifugal force on the coefficient of friction was found to be substantial in other research concerning surface texturing [28]. Grützmacher et al. [42] also noticed the increase in friction in lubricated sliding as a result of centrifugal force presence.

4. Conclusions

Surface texturing was found to be beneficial for the reduction of the friction coefficient up to 55% in comparison to untextured surface.

Convergent profile of the groove bottom was beneficial in most cases especially when is connected with the spiral pattern of the grooves. The best results were achieved for samples with both side convergent groove bottom and the disc patterns of types 2 and 3.

Simple shape of the groove (type 1) in most cases led to high scatter of the friction coefficient. This phenomenon was probably caused by constant losses of lubricant due to the presence of the centrifugal force. Spiral grooves helped to gather oil into the contact area, which led to decreases in the friction coefficient value and scatter at the end of test.

Author Contributions: Conceptualization: S.W., W.K., A.D., P.P.; methodology: S.W., W.K., A.D., P.P.; investigation, and formal analysis: S.W., W.K., A.D., P.P.; writing—original draft preparation: S.W., W.K., A.D., P.P.; writing—review and editing: S.W., W.K., A.D., P.P. All authors have read and agreed to the published version of the manuscript.

Funding: This research was partially funded by the National Science Centre (decision no. 2018/31/B/ST8/02946).

Conflicts of Interest: The authors declare no conflict of interest.

References

1. Etsion, I. State of the art in laser surface texturing. *J. Tribol. Trans. ASME* **2005**, *125*, 248–253. [CrossRef]
2. Nilsson, B.-G.; Rosen, T.R.; Thomas, D.; Wiklund. Oil pockets and surface topography: Mechanism of friction reduction. In Proceedings of the XI International Colloquium on Surfaces, Chemnitz, Germany, 2–3 February 2004.
3. Erdemir, A. Review of engineered tribological interfaces for improved boundary lubrication. *Tribol. Int.* **2005**, *38*, 249–256. [CrossRef]
4. Gachot, C.; Rosenkranz, A.; Hsu, S.M.; Costa, H.L. A critical assessment of surface texturing for friction and wear improvement. *Wear* **2017**, *372–373*, 21–41. [CrossRef]
5. Rosenkranz, A.; Grützmacher, P.G.; Gachot, C.; Costa, H.L. Surface texturing in machine elements-a critical discussion for rolling and sliding contacts. *Adv. Eng. Mater.* **2019**, *21*, 1900194. [CrossRef]
6. Anno, J.N.; Walowit, J.A.; Allen, C.M. Microasperity lubrication. *J. Tribol.* **1968**, *90*, 351–355. [CrossRef]
7. Li, T.; Lu, X.; Ma, X.; Xu, H.; Jiao, B.; Zou, D. Numerical and experimental analysis of the honing texture on the lubrication performance of piston ring–cylinder liner tribosystem. *Tribol. Trans.* **2019**, *62*, 991–1006. [CrossRef]
8. Anderberg, C.; Dimkovski, Z.; Rosén, B.-G.; Thomas, T.R. Low friction and emission cylinder liner surfaces and the influence of surface topography and scale. *Tribol. Int.* **2019**, *133*, 224–229. [CrossRef]
9. Mezghani, S.; Demirci, I.; Zahouani, H.; El Mansori, M. The effect of groove texture patterns on piston-ring pack friction. *Precis. Eng.* **2012**, *36*, 210–217. [CrossRef]
10. Grabon, W.; Pawlus, P.; Wos, S.; Koszela, W.; Wieczorowski, M. Effects of honed cylinder liner surface texture on tribological properties of piston ring-liner assembly in short time tests. *Tribol. Int.* **2017**, *113*, 137–148. [CrossRef]
11. Zeng, S.; Li, J.; Zhou, N.; Zhang, J.; Yu, A.; He, H. Improving the wear resistance of PTFE-based friction material used in ultrasonic motors by laser surface texturing. *Tribol. Int.* **2020**, *141*, 105910. [CrossRef]
12. Wang, M.; Zhang, C.; Wang, X. The wear behavior of textured steel sliding against polymers. *Materials* **2017**, *10*, 330. [CrossRef] [PubMed]
13. Kasem, H.; Stav, O.; Grützmacher, P.; Gachot, C. Effect of low depth surface texturing on friction reduction in lubricated sliding contact. *Lubricants* **2018**, *6*, 62. [CrossRef]
14. Braun, D.; Greiner, C.; Schnider, J.; Gumbsch, P. Efficiency of laser surface texturing in the reduction of friction under mixed lubrication. *Tribol. Int.* **2014**, *77*, 142–147. [CrossRef]
15. Xiong, D.; Qin, Y.; Li, J.; Wan, Y.; Tyagi, R. Tribological properties of PTFE/laser surface textured stainless steel under starved oil lubrication. *Tribol. Int.* **2015**, *82*, 305–310. [CrossRef]
16. Pettersson, U.; Jacobson, S. Friction and wear properties of micro textured DLC coated surfaces in boundary lubricated sliding. *Tribol. Lett.* **2004**, *17*, 553–559. [CrossRef]
17. Moronuki, N.; Furukawa, Y. Frictional properties of the micro-textured surface of anisotropically etched silicon. *CIRP Ann. Manuf. Technol.* **2003**, *52*, 471–474. [CrossRef]
18. Yuan, S.; Huang, W.; Wang, X. Orientation effects of micro-grooves on sliding surfaces. *Tribol. Int.* **2011**, *44*, 1047–1054. [CrossRef]
19. Ren, N.; Nanbu, T.; Yasuda, Y.; Zhu, D.; Wang, Q. Micro textures in concentrated-conformal-contact lubrication: Effect of distribution patterns. *Tribol. Lett.* **2007**, *28*, 275–285. [CrossRef]

20. Zum Gahr, K.H.; Wahl, R.; Wauthier, K. Experimental study of the effect of microtexturing on oil lubricated ceramic/steel friction pairs. *Wear* **2009**, *267*, 1241–1251. [CrossRef]
21. Costa, H.L.; Hutchings, M. Effects of die surface patterning on lubrication in strip drawing. *J. Mater. Process. Technol.* **2009**, *209*, 1175–1180. [CrossRef]
22. Duarte, M.; Lasagni, A.; Giovanelli, R.; Narciso, J.; Louis, E.; Mücklich, F. Increasing lubricant film lifetime by grooving periodical patterns using laser interference metallurgy. *Adv. Eng. Mater.* **2008**, *10*, 554–558. [CrossRef]
23. Michail, S.K.; Barber, G.C. The effects of roughness on piston ring lubrication—Part II: The relationship between cylinder wall surface topography and oil film thickness. *Tribol. Trans.* **1995**, *38*, 173–177. [CrossRef]
24. Bolander, N.W.; Sadeghi, H. Deterministic modeling of honed cylinder liner friction. *Tribol. Trans.* **2007**, *50*, 248–256. [CrossRef]
25. Costa, H.L.; Hutchings, I.M. Hydrodynamic lubrication of textured steel surfaces under reciprocating sliding conditions. *Tribol. Int.* **2007**, *40*, 1227–1238. [CrossRef]
26. Vladescu, S.-C.; Olver, A.V.; Pegg, G.; Reddyhoff, T. The effects of surface texture in reciprocating contacts-an experimental study. *Tribol. Int.* **2015**, *82*, 28–42. [CrossRef]
27. Shen, C.; Khonsari, M.M. Texture shape optimization for seal-like parallel surfaces: Theory and experiment. *Tribol. Trans.* **2016**, *59*, 698–706. [CrossRef]
28. Wos, S.; Koszela, W.; Pawlus, P. Comparing tribological effects of various chevron-based surface textures under lubricated unidirectional sliding. *Tribol. Int* **2020**. In Press. [CrossRef]
29. Wang, W.; Huang, Z.; Shen, D.; Kong, L.; Li, S. The effect of triangle-shaped surface textures on the performance of the lubricated point-contacts. *J. Tribol.* **2013**, *135*, 1–11. [CrossRef]
30. Galda, L.; Dzierwa, A.; Sep, J.; Pawlus, P. The effect of oil pockets shape and distribution on seizure resistance in lubricated sliding. *Tribol. Lett.* **2010**, *37*, 301–311. [CrossRef]
31. Lu, P.; Wood, R.J.K.; Gee, M.; Wang, L.; Pfleging, W. A novel surface texture shape for directional friction control. *Tribol Lett.* **2018**, *66*, 51. [CrossRef]
32. Lu, P.; Wood, R.J.K.; Gee, M.; Wang, L.; Pfleging, W. The use of anisotropic texturing for control of directional friction. *Tribol. Int.* **2017**, *113*, 169–181. [CrossRef]
33. Costa, H.L.; Hutchings, I.M. Some innovative surface texturing techniques for tribological purposed. *Proc. Inst. of Mech. Eng. Part J* **2015**, *229*, 429–444. [CrossRef]
34. Grützmacher, P.I.; Profito, F.J.; Rosenkranz, A. Multi-scale surface texturing in tribology—Current knowledge and future perspectives. *Lubricants* **2019**, *7*, 95. [CrossRef]
35. Ancona, A.; Joshi, G.; Volpe, A.; Scaraggi, M.; Lugarà, P.; Carbone, G. Non-uniform laser surface texturing of an un-tapered square pad for tribological applications. *Lubricants* **2017**, *5*, 41. [CrossRef]
36. Ancona, A.; Carbone, G.; De Filippis, M.; Volpe, A.; Lugarà, P.M. Femtosecond laser full and partial texturing of steel surfaces to reduce friction in lubricated contact. *Adv. Opt. Technol.* **2014**, *3*, 539–547. [CrossRef]
37. Nakano, M.; Korenaga, A.; Miyake, K.; Murakami, T.; Ando, Y.; Usami, H.; Sasaki, S. Applying micro-texture to cast iron surfaces to reduce the friction coefficient under lubricated conditions. *Tribol. Lett.* **2007**, *28*, 131–138. [CrossRef]
38. Wang, X.; Liu, W.; Zhou, F.; Zhu, D. Preliminary investigation of the effect of dimple size on friction in line contacts. *Tribol. Int.* **2009**, *42*, 1118–1123. [CrossRef]
39. Wos, S.; Koszela, W.; Pawlus, P. Determination of oil demand for textured surfaces under conformal contact conditions. *Tribol. Int.* **2016**, *93*, 602–613. [CrossRef]
40. Koszela, W.; Dzierwa, A.; Galda, L.; Pawlus, P. Experimental investigation of oil pockets effect on abrasive wear resistance. *Tribol. Int.* **2012**, *46*, 145–153. [CrossRef]
41. Tian, H.; Saka, N.; Suh, N.P. Boundary lubrication studies on undulated titanium surfaces. *Tribol. Trans.* **1989**, *32*, 289–296. [CrossRef]
42. Grützmacher, P.G.; Rosenkranz, A.; Rammacher, S.; Gachot, C.; Mücklich, F. The influence of centrifugal forces on friction and wear in rotational sliding. *Tribol. Int.* **2017**, *116*, 256–263. [CrossRef]

coatings

MDPI

Article

Additional Tribological Effect of Laser Surface Texturing and Diamond-Like Carbon Coating for Medium Carbon Steel at Near Room Temperature

Yanhu Zhang [1], Hao Fu [1], Xinwei Wang [2,*], Hongyu Liang [1], Julius Caesar Puoza [3], Jinghu Ji [4], Xijun Hua [4,*], Xiaojing Xu [1] and Yonghong Fu [4,*]

1 Institute of Advanced Manufacturing and Modern Equipment Technology, Jiangsu University, Zhenjiang 212013, China; tribo.zhang@gmail.com or zhyh@ujs.edu.cn (Y.Z.); fh0602@sina.com (H.F.); hyliang@ujs.edu.cn (H.L.); xjxu67@ujs.edu.cn (X.X.)
2 Laboratory for Space Environment and Physical Sciences, Harbin Institute of Technology, Harbin 150080, China
3 Department of Mechanical Engineering, Sunyani Technical University, P.O. Box 206, Sunyani, Ghana; deokaesar@yahoo.co.uk
4 School of Mechanical Engineering, Jiangsu University, Zhenjiang 212013, China; jijinghu@ujs.edu.cn
* Correspondence: xinweiwang@hit.edu.cn (X.W.); xjhua@ujs.edu.cn (X.H.); fyh@ujs.edu.cn (Y.F.)

Received: 30 August 2020; Accepted: 24 September 2020; Published: 28 September 2020

Abstract: Texture surface containing both micro-pits and a thin carbon coating was produced using laser surface texturing and magnetic-control vacuum sputtering. Tribological properties of the laser-textured surface coated with thin carbon were experimentally investigated at low-temperature (8–10 °C) under starved and lubricated conditions with a ring-on-ring test rig. The results indicated that the laser-textured surface combined with carbon coating (textured + coating) exhibited low wear intensity and friction coefficient under lubricated conditions, while moderate wear was observed under starved lubrication conditions as compared with the smooth, textured, and carbon-coated surfaces. The wear mechanisms of the lubricated, textured, coated surface under three working conditions (10 N and 1.25 m/s, 16 N and 0.25 m/s, and 50 N and 0.05 m/s) revealed plowing effect, corrosion, and adhesive wear, while oxidative and adhesive wears were observed under starved lubrication. Finally, the textured, coated surface was freely adaptable to different working conditions and exhibited additional effects for better tribological applications at low-temperature as compared with the smooth, laser-textured, and carbon-coated surfaces.

Keywords: sliding friction; surface topography; carbon-based coatings; laser surface texturing; low-temperature

1. Introduction

Inefficient systemic loss of energy in machinery can be minimized by a reduction of friction and wear in mechanical components [1,2]. For example, the indispensable cogs and bearings in the industrial machine are of interest, with the hope of bridging the gap between our desire for energy and adverse environmental effects [3]. Tribology design and surface engineering technologies are sought after for improving the effectiveness and reducing friction losses in mechanical systems. Available literature indicates that surface texturing is one potential strategy to improve energy efficiency and decrease waste disposal and emissions [2,4]. Textured surfaces, with some intricate microstructures (pits, craters, and grooves), have gained widespread acceptance in tribology because of their ability to achieve the micro-hydrodynamic bearing effect, acting as reservoirs for the continuous supply of

lubricants, and trapping of wear debris by eliminating or reducing plowing effects of the working surfaces [5,6].

Among the surface texture fabrication techniques, laser surface texturing (LST) has become an established manufacturing method [7], owing to its advantages of being extremely fast, clean to the environment, and provides excellent control on shape and size of micro-structures [8–11]. It has been proved that LST is valid for tribological applications in mechanical face seal [12,13], thrust bearings [14,15], cutting tools [16–18], cams/tappets [19], drill bit [20], and piston rings [9,21,22]. LST is also used for the reduction of friction (or stiction) in magnetic storage devices [23] and for the minimization of wear and mechanical losses for micro-electro-mechanical system (MEMS) devices [24]. However, LST is deficient in the new challenges of improving the performances of tribological systems. Importantly, it fails to timely exhibit good transitional process from boundary (and dry) lubrication to full-film lubrication, or vice-versa, though the true state of the tribological system is complicated and filled with uncertainties. An important but little-known problem is the friction and wear mechanisms of textured surfaces with different lubrication regions, as well as effective measures to improve the transitional behavior in various lubrication regimes. LST can increase the range of hydrodynamic lubrication regime in the Stribeck curve [25,26]. Meanwhile, it is stated that the bulges at the edge of the dimple need to be optimized to have the positive effect of LST on lubrication regime transitions [27]. The friction coefficient is an important parameter for tribological performance, followed by wear loss, friction force, efficiency, and reliability, which are all critical to the operation of a special tribological system. In addition, it is necessary to understand the detailed wear and durability of laser-textured surfaces for different regions and working conditions.

Sputtered carbon coatings have been reported to have excellent tribological properties and, therefore, have the potential to be used as a hard solid lubricant and wear-resistant coatings [28]. The coating film is recommended for laboratories and plants for their overt properties, such as chemical stability, morphology, and anti-friction. Specifically, coated surfaces have been amenable to playing an active role in dry friction cases for several decades [29,30]. There is limited literature about the exaltation of tribological performances using appropriate coating film, under mixed film lubrication and boundary lubrication. Though some investigations have shown that carbon film is perfect and can offer a series of attractive properties for many applications [31–33]. Arslan et al. [34] reported two approaches to generate low-wear surfaces with diamond-like carbon (DLC) coating by laser surface texturing. Their results suggested that the tribological performance of a cylinder on a coated plate tribo-pair could be enhanced. Yasumaru et al. [35] investigated the tribological properties of DLC films' nanostructured surfaces by femtosecond laser ablation, where a MoS_2 layer on the nanostructured surface improved the friction properties. The creation of small and shallow cavities with a laser lithography technique on a DLC layer has allowed a significant reduction of the friction coefficient of DLC/steel contact [36]. Recently, an interesting investigation by Ding et al. [37] on carbon film with micro-dots has suggested that the influences of laser textures on the tribological performance of amorphous carbon film are strongly dependent on the friction pairs. For instance, LST has not improved the tribological performance of the friction pairs consisting of Si_3N_4 balls, whereas it is effective for the reduction of friction for the steel ball. Further, the DLC/LST composite specimens can obtain a low friction coefficient, which has been accounted for by the combined action of dimple-induced graphitizing transformation [38].

Previously conducted tribological studies have mostly focused on the suitable room temperature conditions for human beings to the detriment of outdoor industrial equipment (such as ships, kowtows, and wind turbines) that operates below room temperature. For extreme low-temperature conditions, the tribological researches focus on space and cryogenic aspects, which does not encourage technology development and theoretical progress. In the present research work, the tribological properties of the textured surface with thin carbon coating was compared with three different surfaces (smooth surface, laser-textured surface, and carbon-coated surface) under starved and lubricated conditions at below room temperature (8–10 °C). The result provided fundamental insights to guide the design

and analysis of surface textures for wind turbine bearings, precision bearings, and precision actuators in places like northern China, Scandinavia, Alaska, and northern Russia, where temperatures often remain below room temperature for weeks or months during winter.

2. Materials and Methods

2.1. Preparation and Characterization

The material specimen utilized for the experimentation was industrially available 45 steel. The 45 steel material is used by numerous manufacturing industries for the fabrication of bearing because it has low friction properties. Before the laser surface texturing (LST), the front surfaces of the samples were ultrasonically cleaned with alcohol and polished by a self-created polishing machine with a diamond aerosol spray of W0.5 grid size for 10 min to a surface roughness of <0.56 μm. During the texturing process, a Q-switch Nd^{3+}: YAG laser oscillator of 50 Watts (OWL, New York, USA) was used to modify the pulse. The single pulse interval processing method was utilized, as reported by Fu et al. [39,40], in the laser texturing process. This process can effectively alleviate the negative heat accumulation effect to accomplish proficient, accurate, and controlled laser micro-textures. The working principle of this process is to coordinate the laser pulse with the mechanical movement of the workpiece to make the laser pulse from the same position separated. The laser beam was focused on the surface of the ablated materials at normal incidence (along the Z-axis) using a convex lens with a focal length of 60 mm and a beam spot diameter of 60 μm. The specimen (small ring) was fixed on a three grasping chuck, which was mounted on a motor controlled two-dimensional stage, and the laser head Z was adjusted to a position so that the focus position was 0.

Round dimples were created on the surface of the ring utilizing the single pulse laser for the tribological investigation. The dimples on the surface of the ring specimen were uniformly arranged in a rectangular array with dot pitch L_1 (circumferential space of the micro-pits) and the line pitch L_2 (radial space of the micro-pits) given as 150 μm. The desired micro-pits diameter was 60 μm with the design texture density (T_d) of 12.6 %. The lumps or burrs around the edges of the dimples amid the laser texturing process were expelled by a gentle polishing process. It has been tentatively exhibited that these hardened lumps or burrs around the edges of the dimples negatively affect the tribological performance of contacting surfaces [27].

Conventionally, magnetron sputtering is one of the physical vapor deposition (PVD) methods with high deposition rates and low equipment costs [30] employed in surface coating. After the surface texturing, the nano-carbon coating was then deposited on the target surface by the method of magnetron sputtering with an argon plasma using a turbo chromium coater K575 (Quorum Technologies Ltd., Lewes, UK). A flow chart of the carbon sputtering is shown in Figure 1. Four types of surfaces (i.e., smooth, coated, textured, and textured and coated) were processed for the friction and wear test, as illustrated and presented (Figure 2).

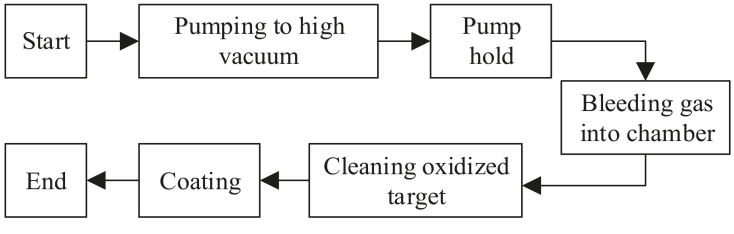

Figure 1. Flow diagram of preparation for carbon coating before tribological tests.

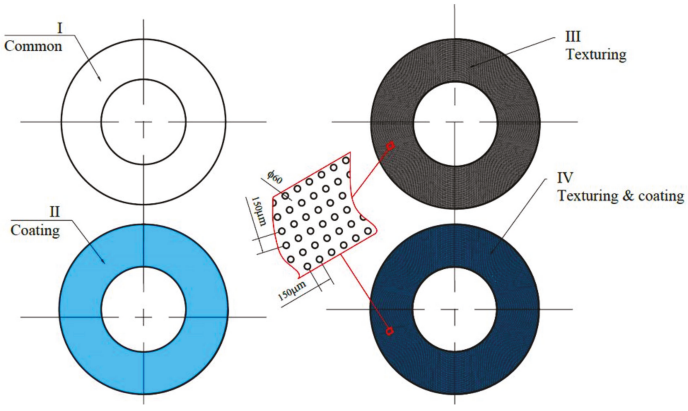

Figure 2. Illustration of a smooth surface (I), coated surface (II), textured surface (III), and textured and coated surface (IV).

Surface characterization has spontaneously been one meaningful issue in tribological analysis. The processed surfaces with micro-textures were characterized in 2D parameters and 3D topographies. Abbott curve is widely appreciated by many scientists and engineers, and thus such curves for different surfaces were plotted for comparison. A non-contact optical measuring instrument (WYKO NT1100 of Veeco, Tucson, AZ, USA) was used for the surface topography and characterization (Figure 3).

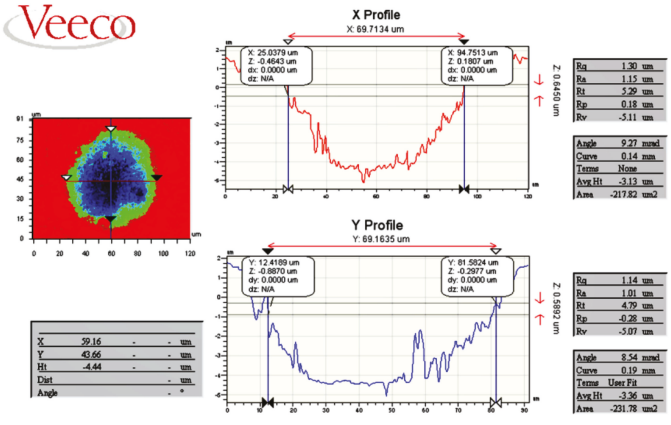

Figure 3. Diagram of dimple surface characterization using an optical profilometer.

The bulk 45 steel was finished by quenching in forced air to harden the surface at HRC40~43 and surface roughness of R_a < 0.56 μm. Dimples of depths 10~15 μm were produced on the surface of the quenched steel to form the textured sample with a roughness value of R_a < 0.8 μm and hardness value of HRC45~48 after the texturing process. A 0.12 μm thick layer of carbon was then coated on the surface of the quenched 45 steel to form the coated sample with a roughness of R_a < 0.5 μm. Finally, the quenched textured steel was coated with a 0.12 μm thickness layer of carbon to form a textured, coated sample. The technologies with technical parameters employed in preparing the various surfaces (smooth, LST, coating, LST + coating) for the friction and wear test are given in Table 1. Prior to the friction and wear tests, the contact surfaces of the rings were polished by fine silicon carbide paper (grit number P1000, Shanghai, China) to render the surface finish for all the test specimens at the same level.

Table 1. Details of the surface treating process and performance parameters.

Type	Material	Technology	Parameters	Note
Smooth	45# steel *	Quenching; Finishing	R_a < 0.56 μm (L = 120 μm) HRC 40~43	* parallel to 10455 of ASTM
LST	45#steel; Gas: N_2	Laser: 512 nm; Nd^{3+}:YAG; 50 Watts; 14 Ampere	Space: 150 μm × 150 μm; Diameter: 60 μm; Depth: 10~15 μm; R_a < 0.8 μm (L = 120 μm) HRC 45~48	TEM00; Q-switch; Frequency: 6.4 kHz; Pressure: 0.15 Mpa
Coating	45#steel; Target: carbon (TK8869)	Coater: K575; Current: 120 mA; Power: 110 W; Time:12 min	Thickness < 0.12 μm; R_a < 0.2 μm (L = 120 μm) HV 1800~2000	Argon: 40 mL/L, 99.99%; Delay: 4 min; No. cycles: 6
LST + coating	45# steel	Same as above	R_a < 0.5 μm (L = 120 μm)	Same as above

Note: "*" in the table reads that the steel is quenched before experiments.

2.2. Tribological Experiments

A configuration of a thrust washer and ring specimen as a friction pair on a whirling rig (MMW-1A, China) was utilized to investigate the tribological performances for the various surfaces, as shown in Figure 4. The upper sample (thrust washer, made of mid-carbon-steel after quenching) was set in the grip holder by a fastening screw. This holder is self-leveling to ensure face-to-face contact during the tests. The lower sample is a circular steel ring with an internal diameter of 16 mm and an external diameter of 32 mm. There are two symmetrically distributed holes on the lower sample for position limitation during the rotation of the principal axis of the testing rig. Besides, there is a small hole on the side surface of the lower sample (2.5 mm from the contact surface) for installing the thermocouple to indirectly test the temperature rise of the contact surface. During the experiment, SC40 (H100) engine oil with the society of automotive engineers (SAE) viscosity of 14.21 mm^2/s was applied. All the experiments were done at a temperature range of (8–10 °C) and relative humidity of 45 ± 3% for a test duration of 1 h.

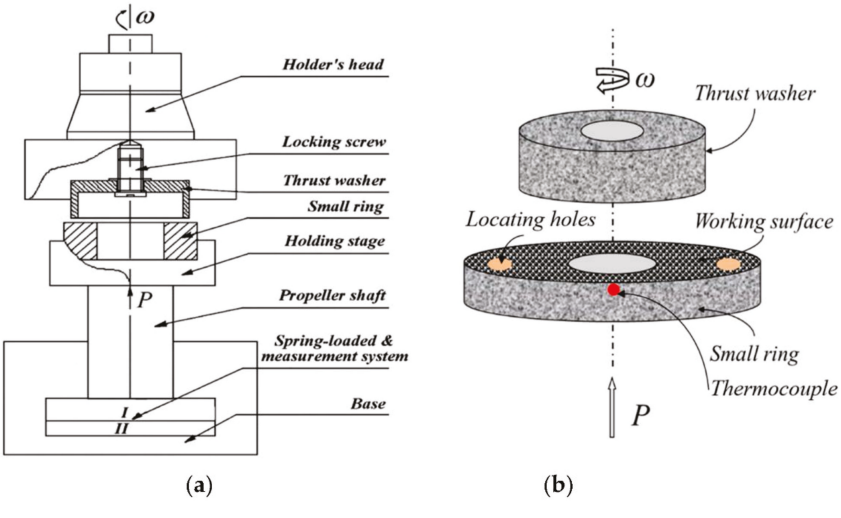

Figure 4. Apparatus for tribological tests of (**a**) the ring-on-ring test rig and (**b**) friction pair.

Three kinds of PV-values, which reads the load capacity of sliding bearings and is expressed the product of bearing pressure and sliding speed, were examined by the friction test. For simplicity, the bearing pressure was replaced by the normal force P. The test conditions are presented in Table 2.

Table 2. Tribo-test conditions referring to ASTM D3702-94 (R99).

Conditions	Speed (m/s)	Load (N)	Temperature (°C)	Humidity (%)	Viscosity (mm^2/s)
$(PV)_1$	1.25	10	8~10	45 ± 3%	14.21
$(PV)_2$	0.25	16	8~10	45 ± 3%	14.21
$(PV)_3$	0.05	50	8~10	45 ± 3%	14.21

Note: $(PV)_i$ (i = 1, 2, 3) show three typical loading conditions of friction couples, that is, high-speed and light-load condition, middle-speed and middle-load condition, and low-speed and heavy load condition.

During the experiments, the normal load P and friction torque T_f were recorded simultaneously to determine the coefficient of friction. The friction coefficient of the small thrust washer-ring pair was derived as follows.

$$f = F/P = T_f/(R_s \cdot P) \quad (1)$$

where F is the frictional force, R_s is the equivalent contact radius of the ring given by $R_s = (d_1 + d_2)/4$. d_1 and d_2 are the external and internal radius of the ring, respectively. Wear behaviors of the surfaces were evaluated by combining both qualitative and quantitative methods. The wear intensity I_w as an index was interpreted by expression (2).

$$I_w = \Delta m/[(P/A_a) \cdot L] \quad (2)$$

where Δm is the change in mass of the specimen before and after the friction test. The values were obtained by reading from an electric balance scale (Ohaus discovery, semi-micro, and analytical balances with 10 microgram readability). P is the normal load, A_a is the apparent area of contact during sliding, calculated from $A_a = \pi\left(d_1^2 - d_2^2\right)/4$, and L is the sliding distance during the whole test duration. The friction and wear test of each condition was repeated three times, and the average values were presented to ensure the repeatability of the results.

3. Results

3.1. Surface Characterization

Through analysis and comparison, a compound characterization of the 2D critical parameters and 3D topographies are presented. The R_a gives a general description of the surface amplitude, and R_q means the average of the measured height deviations taken within the evaluation length of the area. They are meant for traditional characterization in tribological applications. Specifically, they are critical in illustrating the friction stability and wear resistance. R_t is very sensitive to large deviations from the mean line and from scratches and also reads the uniformity of the surface roughness. In addition, R_{pk} indicates the top portion of the surface that is worn away in the run-in period, and R_{vk} reads the lowest part of the surface that retains the lubricant. Furthermore, the values of bearing ratios obtained from the bearing ratio curve (Abbott–Firestone curve) are M_{r1} and M_{r2}. The ideal value of M_{r1} is small, while the value of M_{r2} is large. After the analysis of the measured results, some useful parameters obtained are presented in Table 3. The surface characterization of the smooth surface is illustrated in Figure 5. It is observed that the smooth surface has a uniform roughness in horizontal and vertical directions, although it has a different waviness and texture after the characterization of the surface parameters. The Abbott–Firestone curve further supports this illustration for the bearing ratios of two sections (S_1 and S_3), which present a high consistency. The laser-textured surface has a higher roughness as compared with the smooth surface. Inversely, the surface roughness of the coated surface is lower than the smooth surface. The coated surface has the lowest roughness parameters (R_a, R_q,

R_t, R_{pk}, R_{vk}), while the textured surface has the highest roughness. The textured surface has a higher value of R_{vk} than the other surfaces. These values reveal that a given surface has excellent properties of abrasive resistance under uniform materials and working conditions.

Table 3. Roughness and Abbott–Firestone parameters of different surfaces before wear tests.

Parameters	Smooth	Textured	Coated	Textured + Coated
R_t (μm)	12.45	11.51	4.32	9.45
R_a (μm)	0.553	0.705	0.126	0.404
R_q (μm)	0.700	1.130	0.177	0.593
R_{pk} (μm)	0.592	0.728	0.154	1.287
R_{vk} (μm)	0.945	3.321	0.329	0.487
V_1 (nm)	21.29	17.36	5.75	56.4
V_2 (nm)	82.47	375.49	22.36	26.38
M_{r1} (%)	7.19	4.76	7.47	8.76
M_{r2} (%)	82.56	77.38	86.42	89.17

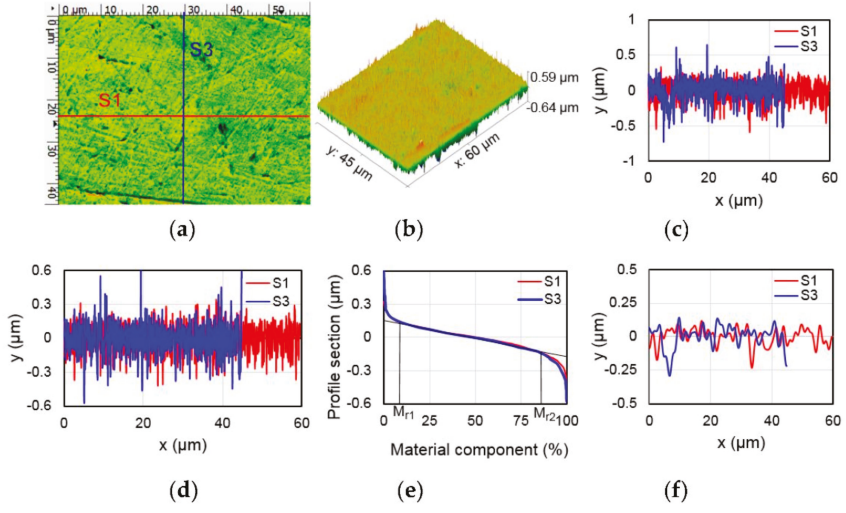

Figure 5. Surface characterization of the smooth surface of (**a**) 2D topography, (**b**) 3D topography, (**c**) texture, (**d**) roughness, (**e**) Abbott curve, and (**f**) waviness.

The working conditions of a friction pair usually change during operation. For comparison of surface topographies and parameters against the working conditions, three-dimensional topographies of the laser-textured surface with coating are presented after the wear tests under lubricated and starved conditions, respectively (Figures 6 and 7). The wear traces of the laser-textured surface with a coating under lubrication is clear and shallow. The asperity contact undergoes a light load, and the friction pair forms hydrodynamic lubrication. The surface roughness is rather high after the wear test. This means a laser-textured surface with the coating is reliable and durable for lubrication conditions. Abbott curves showing the coincidence of cross-sections (S1 and S2, Figure 7) direct that the wear loss of the non-textured regions is isotropic in the horizontal and vertical directions. The peak region of the worn away section of S3 is larger than that of the S1 and S2, while the core region of S3 is less than S1 and S2. This means the vertical asperities cannot bear the large load, and the life of the friction pair is short. However, the valley region acts as a lubricant reservoir (S3 > S1, S2).

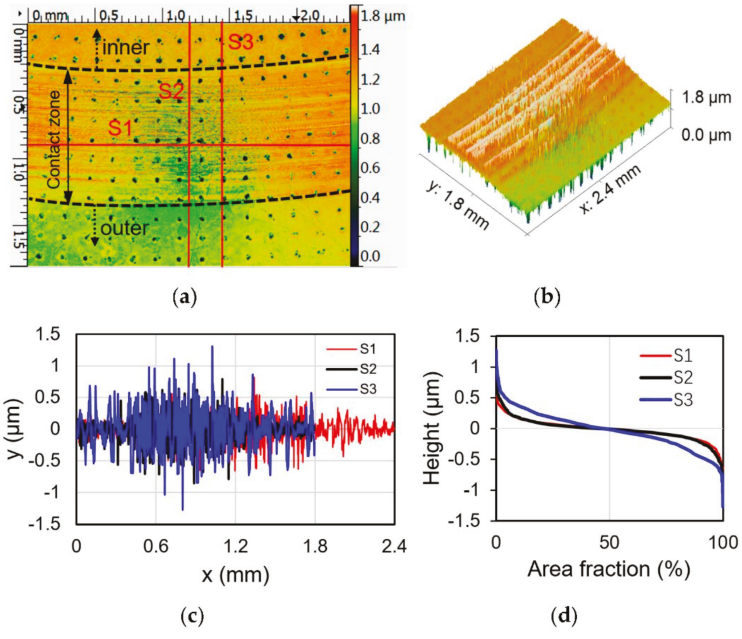

Figure 6. Surface characterization of the laser-textured and coated surface after wear test with 2D topography (**a**), 3D topography (**b**), section contour (**c**), Abbott curve (**d**) ($(PV)_2$: lubrication).

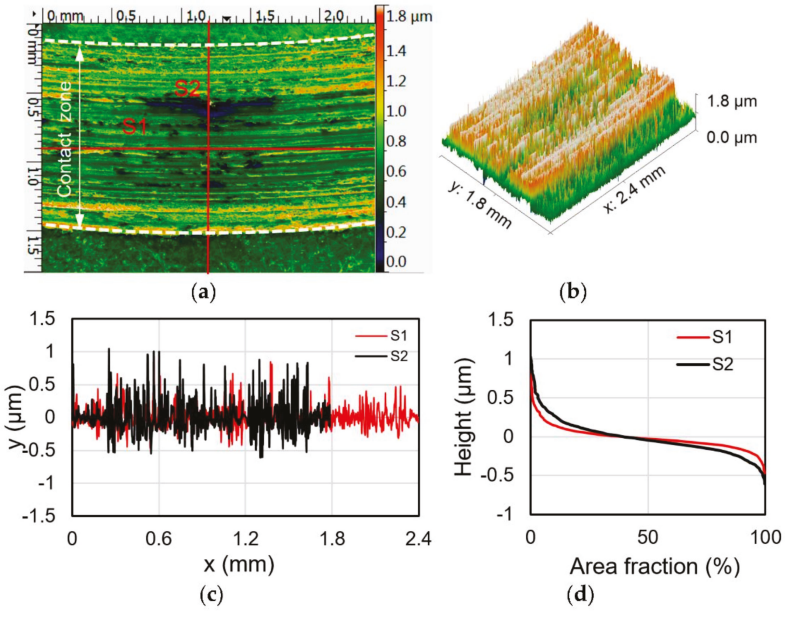

Figure 7. Surface characterization of the laser-textured and coated surface after wear test ($(PV)_2$: starvation): (**a**) 2D topography, (**b**) 3D topography, (**c**) section contour, (**d**) Abbott curve.

The wear trace width under lubrication is about 1 mm, whereas the width of the wear trace under starvation is about 1.35 mm. The roughness of the worn surface under starvation is lower than that of lubrication. The valley of the worn surface under starvation is shallow, which is due to the wear debris filling and the surface material flow during abrasive wear. In addition, the worn surface under starvation presents a complicated topography, which may be related to complicated wear mechanisms. Firstly, there is no lubricating medium between the friction pair, which can produce the so-called hydrodynamic lubrication and bearing force under dry friction. Importantly, the asperities of the friction pair on the LST surface are directly in contact, and the contact area is fairly small, resulting in high contact stress, which induces material deformation of the metal subsurface and the non-textured regions. Secondly, it is still the metal matrix material that plays a supporting role, although thin DLC coating on the contact surface. Under direct contact and shear action of the friction pair, material migration and accumulation deformation occur, and contact hot spots are formed in the rough friction area to cause local oxidation.

3.2. Friction Properties

The coefficients of friction of the different working surfaces are measured through friction tests, and the comparison is shown in Figure 8a. The smooth surface exhibits the highest friction coefficient and shows sustainable growth over the initial test period. The textured surface induced by the laser presents a stable friction coefficient trend during the test period. The laser texturing has some effects on the stable friction coefficient. The first aspect is the quenching effect and refinement of microstructure for a high quenching rate [41], which increases the surface hardness of the sample [42] and improves the abrasive resistance. According to the molecular-kinetic and mechanical model theories of the frictional behavior of elastic materials, the magnitude of the friction coefficient is inversely proportional to the hardness of steel surfaces [43]. The induced quenching effect by the laser increases the amount of martensite phase, which effectively decreases the surface friction coefficient and, consequently, improves the surface wear resistance. Secondly, the debris collection by the micro-pits hinders the attendance of the so-called third-body wear between the friction pair. Finally, the laser-material interaction on the surfaces and interfaces during the texturing process will result in recombination actions of the steel structure, which alter the surface chemistry, morphology, and crystal structure of the steel to form a new material structure with better tribological properties.

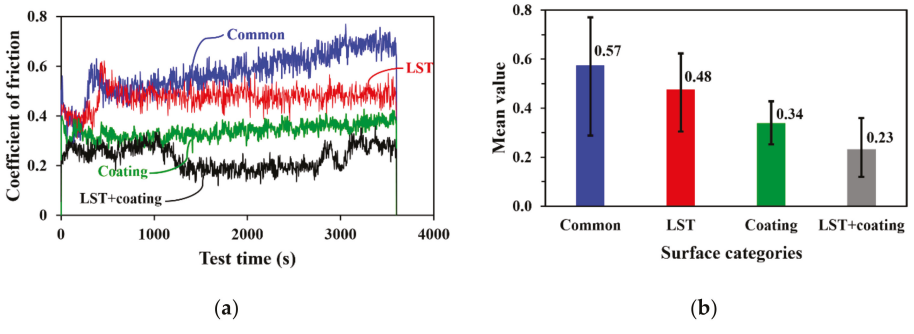

Figure 8. Friction coefficient vs. the sliding time (**a**) and the mean values (**b**) for four categories of surfaces under lubricated conditions at $(PV)_2$, i.e., P = 16 N, v = 0.25 m/s.

The carbon-coated surface exhibits a low friction coefficient as compared to the smooth and textured surface regardless of the test time. This is because of the carbon coating layer and the special full harden and steel surface through laser quenching. However, the friction coefficient shows a slowly growing trend. This might well be due to the failure of the carbon coating. Carbon coatings affect the plowing component of friction, while rough surfaces affect the degree of asperity penetration through

the coating into the substrate [44]. In addition, diamond-like carbon has an amorphous lattice structure, with sp^3, sp^2, and sp bonding type coexisting, and the hardness varies from 1500 HV to 6000 HV [45]. All of these make the phase transformation occurs easily when the local temperature gets up to 250 °C or even higher; graphitization is an unexpected result [46]. However, the changes in the carbon films' properties are beyond the recognition of engineering problems.

The friction coefficient of the textured surface with carbon coating shows more than one steady phase for the test duration. At the beginning of the test, the coefficient of friction shows a modest growing tendency. After 15 min, it goes into a steady-state with a considerable low value of about 0.17 for 20 min. The friction coefficient then passes into another steady-state after around 10 min. Theoretically, the friction binomial law indicates that the friction coefficient consists of two components. One is the mechanical interaction of the friction pair asperities on the macroscopic level, and the other is the molecular action of the surface film on the nanosomic scale. The in-depth mechanism of these components is considered in the analysis of the tribological performance. Laser surface texturing (LST) has a macro sense compared with the carbon thin film embedded on the flat surface. An attempt is made to search for a better tribological performance from a physiochemical standpoint. However, the result cannot fit comfortably with the superimposition of mechanical and molecular interpretation in this study because the water molecules play a prominent role in the frictional behavior of DLC films [47]. The friction coefficient of the four different samples in increasing order is as follows: textured + coating (0.2327), coating (0.339), textured (0.4746), and smooth (0.5744), as indicated in Figure 8b. Comparing with the smooth surface, the friction coefficient of textured, coated, and textured + coated surfaces are reduced by 17%, 41%, and 59%, respectively.

The curves of the friction coefficients for the textured surface with carbon-coated film for different working conditions are plotted in Figure 9a. In addition, the steady-state values are shown in, which are the average of the steady-state portion of the actual friction coefficient. The adulatory curve of friction coefficient provides a particularly sensitive monitor to an imperfect aspect of the carbon coating film. The data reveals that the coefficient of friction is fairly low under low-speed and heavy load conditions, referred to as $(PV)_3$. The value is hardly higher than 0.2, but for the transitory fluctuation, it has resulted from the mechanical inertia of the test rig. The comparison test suggests a greatly higher value of friction coefficient for the whole duration under high-speed and lightly loaded conditions, referred to as $(PV)_1$. However, it has a pretty good tendency to decrease following the test time. It is, therefore, easy to conclude that the textured surface with coated carbon thin film investigated in this study has a desirable performance under low-speed and heavy-load conditions in boundary lubrication for most engineering problems. For example, a piston in an internal combustion engine gets to the top dead center or bottom when the speed is very low, but carrying a heavy load. As discussed above, the coefficient of friction under the conditions of mid-velocity and moderate load, referred to as $(PV)_2$, shows a phased fluctuation, which may be due to the so-called three-body abrasion. During the rest, there may be some generation, variation, and transfer of abrasive particles, which are moving from one subdomain to another and change with the occurrence of squeezing effect and surface deformation. The temperature diachronic curve obtained by using a thermocouple sensor arranged in the side hole of the thrust ring specimen is shown in Figure 9b. Considering the same material matrix, it can be considered that the temperature diachronic curve is an indirect measurement result of the friction temperature rise. It can also be seen that the friction temperature rise is closely related to the working conditions. In the initial stage, the friction temperature rise is lower at low and high-speed conditions (i.e., $(PV)_1$, $(PV)_3$) and then increases to a higher degree (about 3 min). Interestingly, the temperature rise curve corresponding to working condition $(PV)_2$ is relatively high at the initial stage and then remains stable, which is different from the other two conditions. This indirectly reflects that the textured surface with carbon coating has good adaptability and application for medium-speed and medium-load conditions.

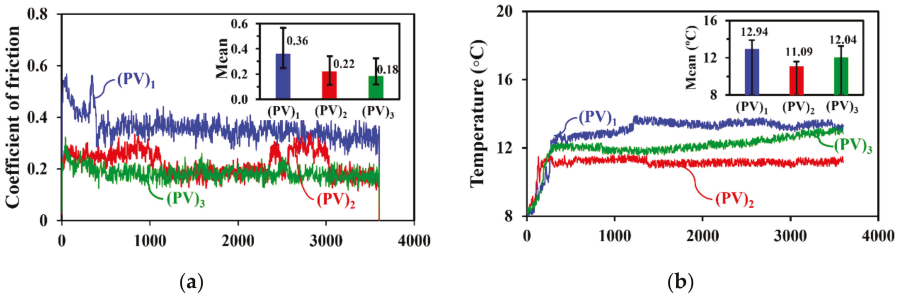

Figure 9. Friction coefficient curves (**a**) and temperature diachronic curves (**b**) for the laser-textured surfaces with carbon coating under lubricated conditions at $(PV)_1$, $(PV)_2$, and $(PV)_3$. Concretely, that is, v = 1.25 m/s, P = 10 N; v = 0.25 m/s, P = 16 N; v = 0.05 m/s, P = 50 N.

3.3. Wear Behavior

For the treated surfaces, a low coefficient of friction alone is insufficient to account for excellent tribological performance. Instead, extended humps for allowing adjacent carbon layers to slip over each other or over contacted material during the rubbing-in process, generally, have good wear-resistance. The wear intensities of the different surfaces are measured by an electronic balance with an accuracy of 0.01 mg, and the results are shown in Table 4 and illustrated graphically in Figure 10. Meanwhile, the wear scratches of the different surfaces under lubricated and starved conditions at different loads and velocities are tracked by SEM photos. To ensure that this is indeed the case, the energy-dispersive spectroscopy (EDS) (0~20 keV accelerating voltages) maps to study the inferred results on wear behaviors and mechanisms for textured and coated surfaces are illustrated. Although there is no significant reinforcement point in the SEM analysis, it is far from being a powerful surface analytical technique.

Table 4. Wear intensities for the four categories of surfaces under different test conditions.

Working Condition	Wear Intensity I_w, × 10^{-6} (mg/N·m)					
	Smooth	Textured	Coated	Textured + Coated		
Lubrication	2.8861	−3.2401	0.0476	0.9277	0.5542	−0.8515
Starvation	0.0959	−3.2742	−3.5881	2.4829	-	-
Note	$(PV)_2$	$(PV)_2$	$(PV)_2$	$(PV)_2$	$(PV)_3$	$(PV)_1$

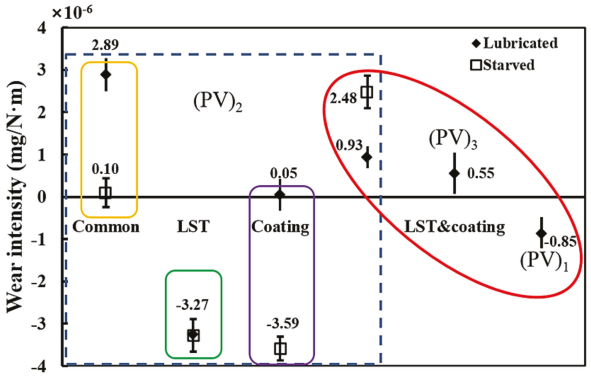

Figure 10. Wear intensities for the four categories of surfaces under different conditions.

It is interesting to note that there are differences in the wear loss of the various surfaces, both quantitatively and qualitatively. Firstly, as illustrated in Table 4, there is an increase in wear for the smooth surface, and the wear intensity values are positive. This phenomenon occurs under starved lubrication conditions on the ground that the friction pair consists of homogeneous medium-carbon steel with excellent elasticity in sliding friction. However, under lubricated conditions, the wear has reduced, as the oil film is enough to engulf the asperities and be replaced by viscous drag. The value of the wear intensity under full lubrication is 30 times more than that under starved lubrication conditions. SEM micrographs of worn surfaces of the smooth surfaces in sliding experiments at $(PV)_2$ are presented in Figures 11a and 12a.

As demonstrated, the plowing component of friction is weakened due to the separation of crests and peaks between the working surfaces by the viscous fluid under the lubricated condition. However, there are micro-cracks in the perpendicular direction of the sliding motion. When two rough surfaces are pressed together, the high pressure will give rise to elastic and plastic deformation at the tips of the surface asperities [48]. The wear patterns suggest that there is an accumulation of material near the two sides of the contact zone on the sliding surface, which may be due to the plastic deformation of the metal materials within the contact interface. The working surfaces embedded with hard particles always produce furrows and grooves in the process of sliding motion under starved conditions. The so-called three-body wear is produced by the two contact surfaces, and the hard particles are detached from the surfaces. As a result, the plowing effect is exacerbated, and the debris cannot stand the overwhelming local pressure other than been crushed at a high friction temperature. Some of the free-form abrasive particles are thereupon transferred timely between the contact surfaces, as indicated in Figure 12b. The tremendous heat from friction provides the right conditions for oxidation wear of the releasing particles during the instantaneous frictional contact with the partial working surface, resulting in the formation of black carbon. Additionally, the hardness of the contact surfaces of the friction pairs is approximately equivalent and prone to create adhesive wear mechanism.

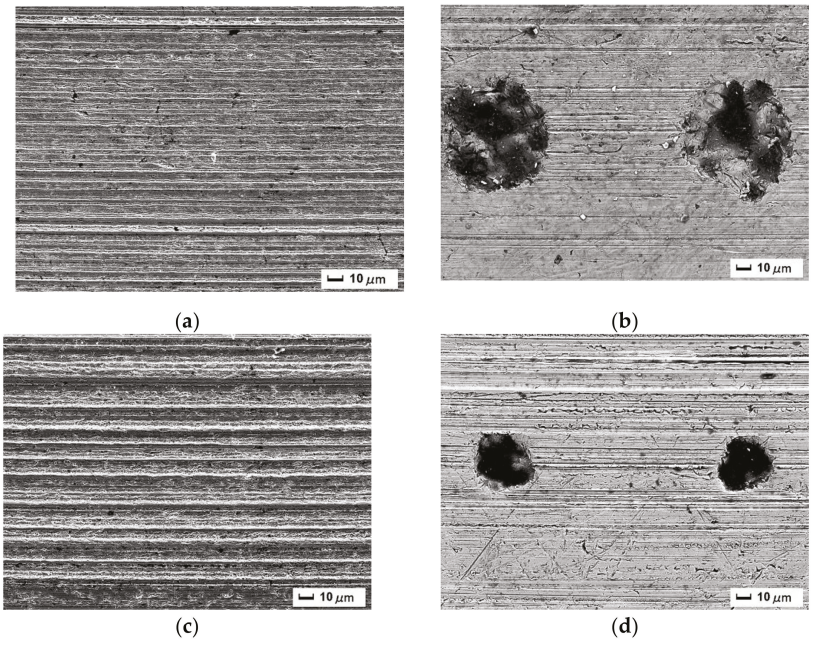

Figure 11. SEM micrographs of smooth (**a**), textured (**b**), coated (**c**), and textured + coated (**d**) worn surfaces under lubricated conditions in the sliding experiments at $(PV)_2$, (P = 16 N, v = 0.25 m/s).

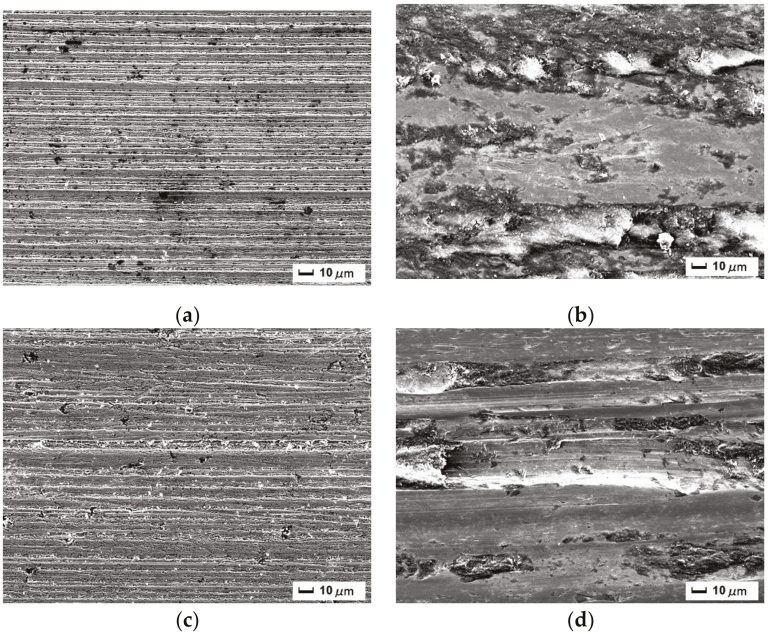

Figure 12. SEM micrographs of smooth (**a**), textured (**b**), coated (**c**), and textured + coated (**d**) worn surfaces under starved lubrication conditions in the sliding experiments at $(PV)_2$, (P = 16 N, v = 0.25 m/s).

The wear intensity of the textured surface is negative both under lubricated and starved conditions at $(PV)_2$, as illustrated in Figure 10. It can be inferred that the abrasive debris lost from the counter body with low surface hardness and adhesive action makes the grains fall into the micro-pits and on the nearby textured surface. SEM micrographs of worn surfaces of the textured surfaces in sliding experiments at $(PV)_2$ are displayed in Figures 11b and 12b. Under the lubricated conditions, the worn surface reveals light scratches on the textured surface with some free abrasion particles along with the sliding motion. This is attributable to the micro-bearings effects of the micro-pits array. The wear pattern demonstrates that the laser-textured surface has excellent skills to deal with lubricants and debris, with an interesting consequence for tribological behavior during the friction test under lubricated conditions. As presented, the carbon is no longer stable because of the increasing and accumulation of friction heat located in the contact zones under dry and loaded conditions.

Contrarily, the wear intensity of the coated surface under lubricated conditions is not negative. It confirms that carbon film could reduce the hardness of the working surface and then improve the abrasive resistance. Furthermore, the value is much less than the textured surface under the same conditions. SEM micrographs of worn surfaces of the carbon-coated surfaces in the sliding experiments at $(PV)_2$ are exhibited in Figure 11c. As presented, adhesive wear becomes a predominant mechanism for the carbon-coated surface due to the low surface hardness of the carbon-coated film. Meanwhile, the viscous effect of the lubricants increases evidently due to the wetting mechanism of the carbon film, and the friction increases with the exposed asperities on the counterpart surface. This results in serious wear particles that are turned out under lubricated conditions. As shown in Figure 12c, dissimilarly, carbon film plays the role of solid lubricant during the sliding motion, which actively alleviates the action of asperity-to-asperity contact, and the friction process is no longer uneven with contradictions. Consequently, wear and vibration have been reduced by the carbon thin film and the enclosed particles. However, there exist hard particles as foreign matters stored within the subsurface, which turns out and becomes free debris as soon as the thin carbon coating is worn out.

As suggested in Table 4, under lubricated conditions, there is little difference in the values of wear intensities under different loads and sliding speeds for the textured surface with a carbon coating. By comparison, the wear intensity with positive values $(PV)_3$ has been the smallest, while $(PV)_2$ has been the highest. However, under $(PV)_1$, the wear intensity is intermediate with a negative value. The wear intensity of the textured, coated surface with micro-pits array is positive, though its values are fairly high. From these values, we can induce that there are different wear mechanisms for the textured surface under different working conditions, as illustrated graphically in Figures 11d, 12d and 13.

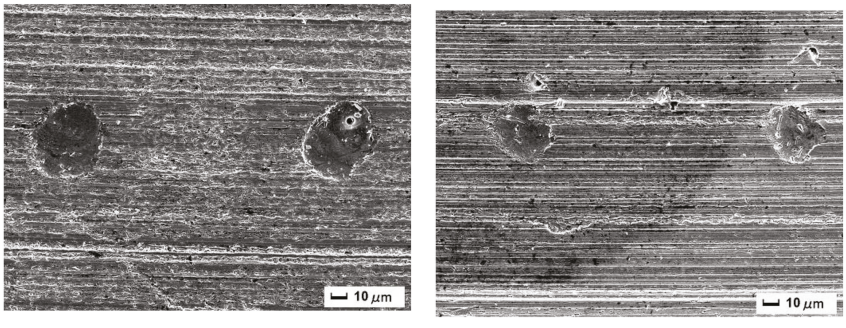

(**a**) (**b**)

Figure 13. SEM micrographs of worn surfaces of the laser-textured surfaces with carbon coating under a lubricated condition in the sliding experiments at (**a**) $(PV)_1$ and (**b**) $(PV)_3$ for 1 h.

Specifically, the wear tracks on the textured, coated surface under lubrication at $(PV)_1$ is illustrated in Figure 13a. It shows that the plowing effect under the conditions of the high-speed and light load is not dominant alone, but being accompanied by corrosion and adhesive wear. This may be as a result of the combined micro-plowing, micro-cutting, and micro-cracking mechanisms in the micro-texture during the friction test. The worn tracks on the textured surface with carbon coating under full lubrication at $(PV)_2$ is expressed in Figure 11d. As seen, shallow and burnished scratches on the friction surface denote that micro-plowing is the predominant wear mechanism. Furthermore, wear traces on the textured surface with coating and micro-pits under lubrication at $(PV)_3$ is expressed in Figure 13b. On the one hand, the plowing effect is the primary wear mechanism for the friction pair consisting of conformal surfaces; on the other hand, adhesive wear exists as a secondary mechanism. Unlike the preceding results at $(PV)_2$, there are wormlike wear particles along the sliding direction. Lastly, the wear tracks under starved conditions are exhibited in Figure 12d, which shows that there are oxidative and adhesive wears. Surprisingly, the micro-textured structure on the bulk material is buried with some deformation.

The energy-dispersive X-ray spectroscopy (EDS) examination spectrums of the novel laser-textured surfaces with carbon coating after the friction tests are presented in Figure 14. There are significant differences in the element intensity in the contact point within the wearable zones after the friction test under different working conditions. Specifically, the iron contents within the textured, coated surfaces decrease variably under different lubrication conditions, but the emerging oxygen seems to present some.

Comparing the three PV conditions under lubrication, the iron content is high under $(PV)_2$ (Figure 14b) condition but is decreased under $(PV)_3$ (Figure 14c), while the datum $(PV)_1$ (Figure 14a) condition does not offer any evident information. For the steel substrate, the decrease in iron content suggests that the friction and wear on the surface material are severe, while the increase in iron content shows that the novel surface is wearable. The added iron content illustrated on the material of the sliding counterpart may be lost and less on the treated surface. There are two illustrations for the causes of the unapparent change of iron content under $(PV)_1$ condition. One may be that the contact

surfaces of the friction pair are anti-friction. The other may be that the friction pair consisting of the same material has the same physicochemical properties, leading to the dissolution occurring on the contact surfaces of the pairs. It can clearly be seen that these cases are consistent with the results mentioned before the friction test.

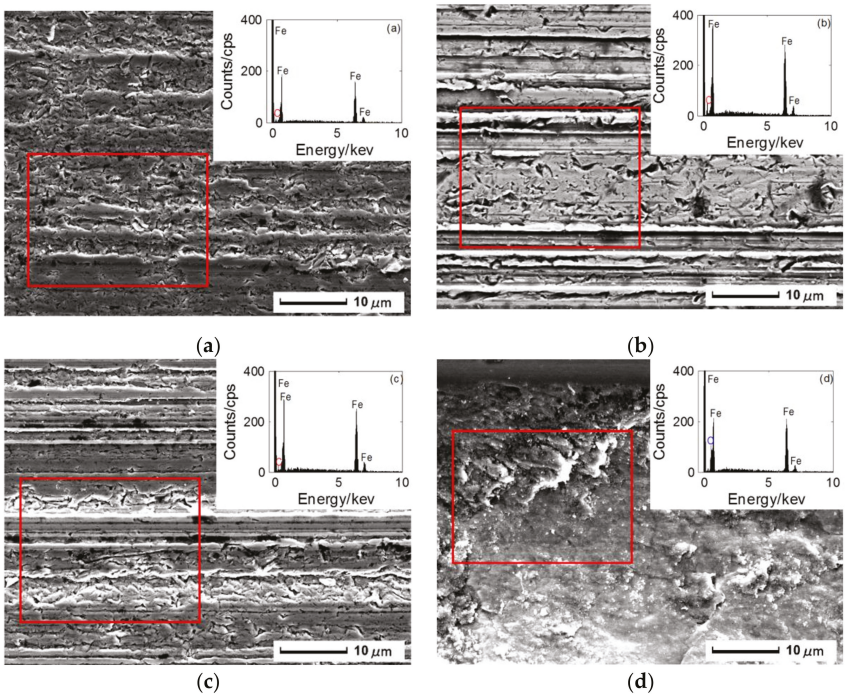

Figure 14. Local energy-dispersive X-ray spectroscopy (EDS) maps of the laser-textured surfaces with carbon coating after friction tests at different working conditions: (**a**) lubrication and $(PV)_1$, (**b**) lubrication and $(PV)_2$, (**c**) lubrication and $(PV)_3$, (**d**) starvation and $(PV)_2$.

4. Discussion

In this study, the laser-textured surface with DLC coating displays different tribological behaviors during the friction and wear test, and these behaviors are related to the bulk materials and micro-pits and the DLC-coated layer. Firstly, laser surface texturing can be seen as a partial laser machining on the surface of carbon steel by laser ablation gasification, accompanying laser transformation hardening (also known as laser quenching) [49]. The heating effects of the laser beam need some attention. The heat is absorbed rapidly (10^{-1}–10^{-7} s) in a small area on the surface of the workpiece, and the temperature rises sharply [50]. The solid phase transformation occurs between the melting point of the material and the critical temperature of austenite transformation. After self-quenching, martensite is obtained, and the transformation hardening of the workpiece surface is realized, resulting in the complete hardening of the 45 steel surface with partially quenched areas. The microstructure consists of fine needle-like martensite [51], although material structure, heating, and cooling speed are important factors for the transformation of hardening behavior [52]. This results in improved strength and hardness of the surface. Specifically, due to the steep temperature field distribution, there is a sharp transition from the laser hardened layer to the matrix and the second characteristic of local diffusion of carbon, and the hardness drop is as high as HV400–600 [50]. Besides the laser nitriding, other recombination actions might well exist during the surface texturing to improve the tribological properties for the nitrogen as

the assist gas during LST processing. The surfaces of the dimples also contribute to improving the tribological properties, especially for the contribution of low and steady friction [53]. Importantly, the hardness of hydrogenated DLC films, which is typically around 10–20 GPa depending on the sp^2 to sp^3 ratio and the hydrogen content, will act as anti-friction and anti-abrasion film [54]. Generally, TK8869, as a target material for carbon coatings, tends to be amorphous carbon material and is accepted as a soft coating for anti-friction and anti-abrasion. Therefore, the DLC carbon coating is adaptive to the boundary lubrication and mixed lubrication conditions for controlling friction and wear. Conclusively, emphasis should be placed on the effect of surface texture and coating on the surface friction properties. Regulation of the friction coefficient and the expansion of the Stribeck curve are available for the novel surface, treating with combined LST and DLC coating. After the tribological experimental data by Kalin et al. [55], the friction coefficients obtained are analyzed, and the results are shown in Figure 15. As shown, the friction coefficients increase initially with the Stribeck parameter and then decrease with a further increase of the parameter in the measurable range. LST and DLC are effective in regulating the behaviors of friction couples under different working conditions. Specifically, LST can expand the contact parameters for hydrodynamic lubrication and induce the friction transition on the Stribeck curve [27]. Meanwhile, DLC coating exhibits comfortable friction properties under boundary lubrication by forming a low friction film on the surface. Additionally, the friction properties can be highly improved by using extreme-pressure and anti-wear additives [56,57]. In this study, the experimental results, by considering the compound influence of LST and DLC coating, are far from that of the literature [55]; they may be accounted for the clear difference in the initial surface roughness and lubrication oil. However, compared with the LST surfaces, friction transitions occur on the Stribeck curve of the novel design LST surfaces with DLC coating.

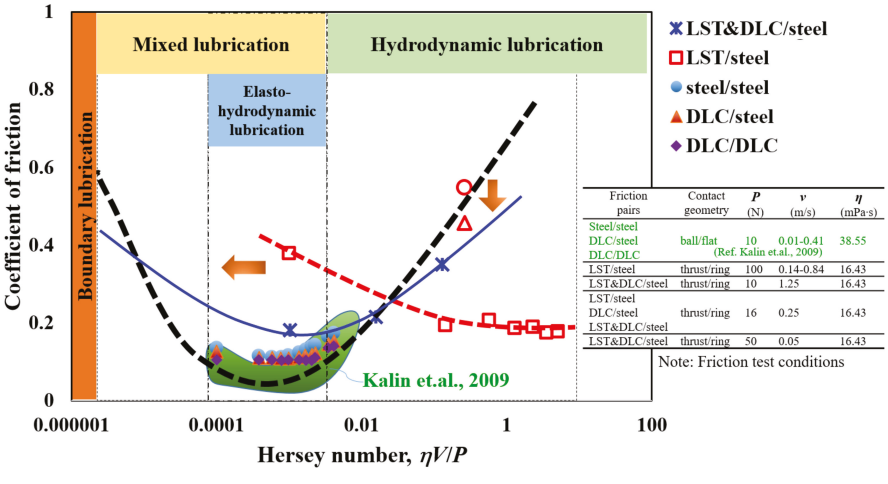

Friction pairs	Contact geometry	P (N)	v (m/s)	η (mPa·s)
Steel/steel DLC/steel DLC/DLC	ball/flat	10	0.01-0.41 (Ref. Kalin et.al., 2009)	38.55
LST/steel	thrust/ring	100	0.14-0.84	16.43
LST&DLC/steel	thrust/ring	10	1.25	16.43
LST/steel DLC/steel LST&DLC/steel	thrust/ring	16	0.25	16.43
LST&DLC/steel	thrust/ring	50	0.05	16.43

Figure 15. Illustration of the expansion of the Stribeck curve by laser surface texturing (LST) and diamond-like carbon (DLC) coating.

Wear mechanisms of LST surface with carbon coating is complicated for the given full-range lubrication and friction conditions. After the transformation of hardening through the LST process, the occurred grain refinement can improve the plastic deformation resistance and fracture strength, increase the stress caused by cracks, and increase the wear resistance [50]. Meanwhile, the DLC film is acknowledged for the low friction coefficient, good wear resistance, and high hardness [58]. However, the composite response of LST and DLC film is not usually comfortable during the friction and wear behavior by some working conditions, such as contact pressure, temperature [19], texture geometry [36], and lubricated medium [59]. Further, the combined investigation of LST and DLC film is far from the

universal conclusion for different engineering applications, although these works have been conducted by enough research teams [19,34–37,60–63]. Note that the order of surface texturing and DLC coating is different, and most of these investigations are conducted on the textured surface of DLC coating samples. For carbon steel samples, micro-cracking that results from tensile stress tends to occur within the smooth surface during sliding motion [64]. As known, micro-cracks are usually a bad sign of delamination wear, which consists of several basic steps, such as plastic deformation of the subsurface layer, subsurface crack nucleation, propagation, and generation of loose wear sheets [65]. Obviously, it is a fact that subsurface deformations, void elongation, and crack formation in medium-carbon steel are detrimental to the mating part and should be avoided by taking any surface protection measures. Thus, surface treatments, such as coating and texturing, are better methods of improving the tribological performance and properties of mechanical components [34,63,66], resulting in a clear difference in the worn surfaces after friction and wear experiments (see Figures 10 and 11).

After the LST, the hardness of the surface is enhanced by the laser action, while the substrate material of the counterpart is soft. Thus, both the laser-textured and non-textured zones of the contact surfaces of the friction couple will be in a mess due to frequent plowing and heating effects during the friction process. This results in the active surface been in the inhomogeneous state without harmonized interaction with each other, leading to heat accumulation, which enhances oxidation and friction. Lastly, as oxidation is exacerbated, the sheet scuff peels off, causing serious wear and tear. Conversely, apart from the solid film for the friction reduction of coating surfaces under the lean oil condition, soft carbon coatings undergo the action of plowing and squeezing mechanisms, and the surface roughness changes by the process of scratching and penetration concurrently. This generates new debris, which brings some additional mechanisms of friction and wear [67]. Differently, hard coating usually affects the load-carrying capacity through coating strength and substrate deformation [68]. Throughout the contact, the reduction of the actual area and the interlocking materials affects chiefly the surface roughness, while the asperity fatigue leads to the generation of wear debris. The bearing capacity and wear resistance of friction pairs under lubrication conditions can be improved by the hydrodynamic lubrication, micro-oil pool effect, and micro-lubrication of LST technology. At the same time, the tribological properties of friction couples under dry friction, and the boundary lubrication conditions can be enhanced by DLC coating. Through the coupling and synergy of these two mechanisms, comprehensive tribological properties of friction pairs can be improved, and the working conditions and application fields of specific friction pairs can be expanded. Thereafter, the lubrication design principle of the textured surface with carbon coating is illustrated and shown in Figure 16.

The wear traces shown by SEM photographs indicate different wear mechanisms for the different friction pairs with various treated surfaces. Specifically, the textured surface with coating presents oxidative and adhesive wear mechanism under starved lubrication conditions. The oxidation is not an incomprehensible result because amorphous carbon film cannot hold stable inertia at a fairly high temperature. The flashing temperature may get to hundreds Centigrade owing to the micro-contact with a heavy load during the dry friction condition. Thus, local carbonization occurs at the actual zone rather than the apparent region. Additionally, carbon film has certain mobility during micro-plowing and micro-cutting, which are micro-abrasive mechanisms of generating wear and material migration. Superficially, it is undesirable to improve the abrasion resistance of the working surface with micro-pits and carbon film. However, the truth of the matter is quite different because the periodic temperature rise may be higher in starved friction. Consequently, the carbon film is softened occasionally, and sound solid lubrication might well be realized, with no great loss of the bulk material and the counterpart after friction. Moreover, diamond and diamond-like carbon cannot produce protective oxide layers with oxidation and volatile CO_2. Additionally, for diamond-like carbon, H_2O is formed, which will emerge at the oxidation temperature [46], and a water-mediated hydrogen diffusion mechanism may exist on the oxide surface at a normal temperature or less.

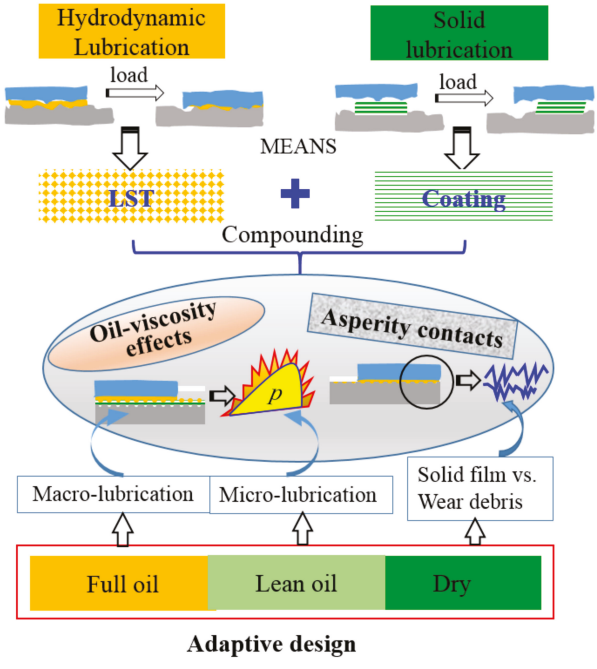

Figure 16. Illustration of the laser-textured surfaces for lubrication adaptive design.

Surface roughness is an important factor in scuffing failure, whether it occurs under conditions of boundary lubrication or mixed lubrication [48]. In this study, the surface of the bulk materials is not very smooth with some initial defects, which might have affected the result of the test. The micro-pits array of the laser-textured surfaces contains an error in depth and profile induced by the laser pulses. In addition, it is not easy to design the thickness of the carbon film to get an excellent tribological performance. A fairly thin film would lose its effects in dry and starved conditions, whereas a thick film would rather weaken the interface characteristic of the textured surface contact resistance and heat transfer. Moreover, the friction coefficients for several surfaces under starved conditions are not available, which are constrained by the weak resistance to shock for torque sensors. Consequent upon these problems and oversights, friction and wear behaviors carried out are quantitative to an extent, accompanied by qualitative analysis. This result could not be set aside without a grave responsibility for tribological performances and behaviors. Surface oxidization and van der Waals attractive energy over the carbon structures with nanoscale conformity [69] lead to a novel, critical, and unfolding surface treatment, yet some sagging problems with physicochemical actions demand further study.

5. Conclusions

This study illustrated the tribological performances of a laser-textured surface combined with carbon coatings compared with three typical surfaces (smooth surface, textured surface, and coated surface). The advantages of the textured surface with coating were demonstrated by surface characterization and tribological tests on a ring-on-ring rig. The analyzed results made us understand the relationship between material properties, surface topographies, and tribological behavior, as outlined below.

(1) Engineering surfaces after texturing and coating could be characterized using classical roughness and Abbott–Firestone parameters. Worn regions were isotropic in the horizontal (parallel to the sliding direction) and vertical directions. Changes in surface topography of worn traces were related to the wear behaviors and friction mechanism.

(2) Laser-textured surfaces with carbon coating significantly improved the friction and wear properties of the 45 steel under lubricated conditions, by consistently maintaining a steady-state friction coefficient. Comparing to the smooth surface, the stable friction coefficient under lubricated conditions (medium speed and load) of the textured surface, coated surface, and textured and coated surface were reduced by 17%, 41%, and 59%, respectively.

(3) The trend of temperature rise of the textured surface with coating was not consistent with that of the friction coefficient under different working conditions, which has accounted for the significant difference in the influence of the degree of working conditions (i.e., speed and load) on the friction coefficient and temperature rise.

(4) Under lubricated conditions, the plowing friction was weakened by the viscous shearing of lubricating oil, and the micro-cracks in the perpendicular direction of the sliding motion were present. The textured surface with a coating underwent the plowing friction accompanied by corrosion and adhesive wear under the conditions of high-speed and light load.

(5) Diamond-like carbon films, combined with microscopic bearing and pooling effects of surface textures, could significantly improve the hydrodynamic lubrication performance, whereas the available solid lubrication was available by the formation of low friction film under dry friction conditions. The additional effect provided a basis and scheme for lubrication adaptive design under complex working conditions.

Author Contributions: Conceptualization, Y.Z. and X.H.; methodology, Y.Z.; software, H.F.; validation, X.W., H.L., and X.X.; formal analysis, X.W.; investigation, H.F.; resources, Y.F.; data curation, J.J.; writing—original draft preparation, Y.Z.; writing—review and editing, J.C.P.; visualization, Y.Z.; supervision, X.H.; project administration, Y.F.; funding acquisition, Y.Z., H.F., X.W., H.L., and X.H. All authors have read and agreed to the published version of the manuscript.

Funding: This research was funded by the National Natural Science Foundation of China, grant No. 51705210, 51705211, 51705101, 51975252; Jiangsu Province Post-Doctoral Research Funding Scheme, grant No. 2019K195, 2019K233; State Key Laboratory of Mechanical System and Vibration Research Fund, grant No. MSV-2019-17; Key Laboratory of Micro-Systems and Micro-Structures Manufacturing (Harbin Institute of Technology), Ministry of Education, grant No. 2019KM009; Fundamental Research Funds for the Central Universities grant No. HIT. NSRIF. 2020043. The APC was funded by the Fundamental Research Funds for the Central Universities, grant No. 2020043.

Conflicts of Interest: The authors declare no conflict of interest.

References

1. Gualtieri, E.; Borghi, A.; Calabri, L.; Pugno, N.; Valeri, S. Increasing nanohardness and reducing friction of nitride steel by laser surface texturing. *Tribol. Int.* **2009**, *42*, 699–705. [CrossRef]
2. Spikes, H. Tribology research in the twenty-first century. *Tribol. Int.* **2001**, *34*, 789–799. [CrossRef]
3. Holmberg, K.; Andersson, P.; Erdemir, A. Global energy consumption due to friction in passenger cars. *Tribol. Int.* **2012**, *47*, 221–234. [CrossRef]
4. Rabuté, R.; Tian, T. Challenges involved in piston top ring designs for modern SI engines. *J. Eng. Gas Turbines Power* **2001**, *123*, 448–459. [CrossRef]
5. Arslan, A.; Quazi, M.M.; Masjuki, H.H.; Kalam, M.A.; Varman, M.; Zulkifli, N.W.M.; Jamshaid, M.; Mandalan, S.M.; Gohar, G.A.; Gulzar, M.; et al. Wear characteristics of patterned and un-patterned tetrahedral amorphous carbon film in the presence of synthetic and bio based lubricants. *Mater. Res. Express* **2018**, *6*, 036414. [CrossRef]
6. Wang, X.; Khonsari, M.; Li, S.; Dai, Q.; Wang, X. Experimental verification of textured mechanical seal designed using multi-objective optimization. *Ind. Lubr. Tribol.* **2019**, *71*, 766–771. [CrossRef]
7. Trdan, U.; Hocevar, M.; Gregorcic, P. Transition from superhydrophilic to superhydrophobic state of laser textured stainless steel surface and its effect on corrosion resistance. *Corros. Sci.* **2017**, *123*, 21–26. [CrossRef]
8. Etsion, I. State of the art in laser surface texturing. *J. Tribol.* **2005**, *127*, 248–253. [CrossRef]
9. Etsion, I.; Sher, E. Improving fuel efficiency with laser surface textured piston rings. *Tribol. Int.* **2009**, *42*, 542–547. [CrossRef]

10. Ronen, A.; Etsion, I.; Kligerman, Y. Friction-reducing surface-texturing in reciprocating automotive components. *Tribol. Trans.* **2001**, *44*, 359–366. [CrossRef]
11. Shinkarenko, A.; Kligerman, Y.; Etsion, I. The effect of elastomer surface texturing in soft elasto-hydrodynamic lubrication. *Tribol. Lett.* **2009**, *36*, 95–103. [CrossRef]
12. Antoszewski, B. Mechanical seals with sliding surface texture–model fluid flow and some aspects of the laser forming of the texture. *Procedia Eng.* **2012**, *39*, 51–62. [CrossRef]
13. Shi, L.; Wang, X.; Su, X.; Huang, W.; Wang, X. Comparison of the load-carrying performance of mechanical gas seals textured with microgrooves and microdimples. *J. Tribol.* **2016**, *138*, 021701. [CrossRef]
14. Lu, X.; Khonsari, M. An experimental investigation of dimple effect on the Stribeck curve of journal bearings. *Tribol. Lett.* **2007**, *27*, 169. [CrossRef]
15. Brizmer, V.; Kligerman, Y. A laser surface textured journal bearing. *J. Tribol.* **2012**, *134*, 031702. [CrossRef]
16. Sulaiman, M.H.; Christiansen, P.; Bay, N. The Influence of Tool Texture on Friction and Lubrication in Strip Reduction Testing. *Lubricants* **2017**, *5*, 3. [CrossRef]
17. Fang, S.; Llanes, L.; Bähre, D. Wear Characterization of Cemented Carbides (WC–CoNi) Processed by Laser Surface Texturing under Abrasive Machining Conditions. *Lubricants* **2017**, *5*, 20. [CrossRef]
18. Sharma, V.; Pandey, P.M. Geometrical design optimization of hybrid textured self-lubricating cutting inserts for turning 4340 hardened steel. *Int. J. Adv. Manuf. Technol.* **2017**, *89*, 1575–1589. [CrossRef]
19. Arslan, A.; Masjuki, H.H.; Varman, M.; Kalam, M.A.; Quazi, M.M.; Mosarof, M.H. Effect of change in temperature on the tribological performance of micro surface textured DLC coating. *J. Mater. Res.* **2016**, *31*, 1837–1847. [CrossRef]
20. Ling, T.D.; Liu, P.; Xiong, S.; Grzina, D.; Cao, J.; Wang, Q.J.; Xia, Z.C.; Talwar, R. Surface texturing of drill bits for adhesion reduction and tool life enhancement. *Tribol. Lett.* **2013**, *52*, 113–122. [CrossRef]
21. Grabon, W.; Koszela, W.; Pawlus, P.; Ochwat, S. Improving tribological behaviour of piston ring–cylinder liner, frictional pair by liner surface texturing. *Tribol. Int.* **2013**, *61*, 102–108.
22. Gu, C.; Meng, X.; Xie, Y.; Yang, Y. Effects of surface texturing on ring/liner friction under starved lubrication. *Tribol. Int.* **2016**, *94*, 591–605.
23. Baumgart, P.; Krajnovich, D.; Nguyen, T.; Tam, A.G. A new laser texturing technique for high performance magnetic disk drives. *IEEE Trans. Magn.* **1995**, *31*, 2946–2951.
24. Oka, T.; Itani, K.; Taguchi, Y.; Nagasaka, Y. Development of interferometric excitation device for micro optical diffusion sensor using laser-induced dielectrophoresis. *J. Microelectromech. Syst.* **2012**, *21*, 324–330.
25. Yu, H.; Wang, X.; Zhou, F. Geometric shape effects of surface texture on the generation of hydrodynamic pressure between conformal contacting surfaces. *Tribol. Lett.* **2010**, *37*, 123–130.
26. Akbarzadeh, S.; Khonsari, M. Effect of surface pattern on Stribeck curve. *Tribol. Lett.* **2010**, *37*, 477–486.
27. Kovalchenko, A.; Ajayi, O.; Erdemir, A.; Fenske, G.; Etsion, I. The effect of laser surface texturing on transitions in lubrication regimes during unidirectional sliding contact. *Tribol. Int.* **2005**, *38*, 219–225.
28. Kot, M.; Major, Ł.; Lackner, J.; Chronowska-Przywara, K.; Janusz, M.; Rakowski, W. Mechanical and tribological properties of carbon-based graded coatings. *J. Nanomater.* **2016**, *51*, 1–14.
29. Holmberg, K.; Mathews, A. Coatings tribology: A concept, critical aspects and future directions. *Thin Solid Films* **1994**, *253*, 173–178.
30. Tyagi, A.; Walia, R.; Murtaza, Q.; Pandey, S.M.; Tyagi, P.K.; Bajaj, B. A critical review of diamond like carbon coating for wear resistance applications. *Int. J. Refract. Met. Hard Mater.* **2019**, *78*, 107–122.
31. Wang, J.; Ma, J.; Huang, W.; Wang, L.; He, H.; Liu, C. The investigation of the structures and tribological properties of F-DLC coatings deposited on Ti-6Al-4V alloys. *Surf. Coat. Technol.* **2017**, *316*, 22–29. [CrossRef]
32. Han, X.; Zheng, J.; Hao, J.; Zhang, S. The microstructure, mechanical and tribological properties of aC: H films with self-assembled carbon nanohoops. *Surf. Coat. Technol.* **2017**, *311*, 27–34. [CrossRef]
33. Charitidis, C. Nanomechanical and nanotribological properties of carbon-based thin films: A review. *Int. J. Refract. Met. Hard Mater.* **2010**, *28*, 51–70. [CrossRef]
34. Arslan, A.; Masjuki, H.H.; Kalam, M.A.; Varman, M.; Mosarof, M.H.; Mufti, R.A.; Quazi, M.M.; Khuong, L.S.; Liaqat, M.; Jamshaid, M.; et al. Investigation of laser texture density and diameter on the tribological behavior of hydrogenated DLC coating with line contact configuration. *Surf. Coat. Technol.* **2017**, *322*, 31–37. [CrossRef]
35. Yasumaru, N.; Miyazaki, K.; Kiuchi, J. Control of tribological properties of diamond-like carbon films with femtosecond-laser-induced nanostructuring. *Appl. Surf. Sci.* **2008**, *254*, 2364–2368. [CrossRef]

36. Chouquet, C.; Gavillet, J.; Ducros, C.; Sanchette, F. Effect of DLC surface texturing on friction and wear during lubricated sliding. *Mater. Chem. Phys.* **2010**, *123*, 367–371. [CrossRef]
37. Ding, Q.; Wang, L.; Hu, L.; Hu, T.Y. The pairing-dependent effects of laser surface texturing on micro tribological behavior of amorphous carbon film. *Wear* **2012**, *274–275*, 43–49. [CrossRef]
38. Shamsul Baharin, A.F.; Ghazali, M.J.A.; Wahab, J. Laser surface texturing and its contribution to friction and wear reduction: A brief review. *Ind. Lubr. Tribol.* **2016**, *68*, 57–66. [CrossRef]
39. Fu, Y.; Liu, Q.; Ye, Y.; Hua, X.; Kang, Z.; Hao, F. Research on Laser Surface Micro Texturing Processing of Single Pulse Intervals. *Chin. J. Lasers* **2015**, *42*, 1203005.
40. Fu, Y.; Pan, G.; Hua, X.; Fu, H.; Gao, X. Study on the laser micro-manufacturing equipment of special micro-manufacturing technology. In Proceedings of the 2011 Second International Conference on Digital Manufacturing & Automation, Zhangjiajie, China, 5–7 August 2011; pp. 1176–1179.
41. Dutta Majumdar, J.I. Laser material processing. *Int. Mater. Rev.* **2011**, *56*, 341–388. [CrossRef]
42. Hu, T.; Hu, L.; Ding, Q. Effective solution for the tribological problems of Ti-6Al-4V: Combination of laser surface texturing and solid lubricant film. *Surf. Coat. Technol.* **2012**, *206*, 5060–5066. [CrossRef]
43. Moore, A.J.W.; Tegart, W.J.M.; Bowden, F.P. Relation between friction and hardness. *Proc. R. Soc. Lond. Ser. A Math. Phys. Sci.* **1952**, *212*, 452–458.
44. Sahoo, P.; Ali, S.M. Elastic-plastic adhesive contact of rough surfaces with soft coatings. *Tribol. Online* **2008**, *3*, 216–221. [CrossRef]
45. Vandevelde, T.C.S.; Vandierendonck, K.; Van Stappen, M.; Du Mong, W.; Perremans, P. Cutting applications of DLC, hard carbon and diamond films. *Surf. Coat. Technol.* **1999**, *113*, 80–85. [CrossRef]
46. Habig, K.H. Fundamentals of the tribological behaviour of diamond, diamond-like carbon and cubic boron nitride coatings. *Surf. Coat. Technol.* **1995**, *76*, 540–547. [CrossRef]
47. Andersson, J.; Erck, R.A.; Erdemir, A. Friction of diamond-like carbon films in different atmospheres. *Wear* **2003**, *254*, 1070–1075. [CrossRef]
48. Horng, J.H. Contact analysis of rough surfaces under transition conditions in sliding line lubrication. *Wear* **1998**, *219*, 205–212. [CrossRef]
49. Jianglong, L.; Zhirong, Z. A study of morphologies of residual austenite after laser transformation hardening. *Mater. Mech. Eng.* **1989**, *13*, 35–38. (In Chinese)
50. Ling, Z. The microstructure and the wear resistance of 45-steel after laser transformation hardening. *J. Chongqing Jiaotong Inst.* **1992**, *11*, 103–107. (In Chinese)
51. Jiandong, H.; Zhang, L. The observation on the lath martensite in the laser processing areas by TEM. *J. Chin. Electron. Microsc. Soc.* **1986**, *5*, 72–76. (In Chinese)
52. We, F.; Zhiqin, Y. Study on laser transformation hardening of metal surface. *Heat Treat. Met.* **1982**, *25*, 12–20. (In Chinese)
53. Grabon, W.A. A new approach to the description of height distribution of plateau honed cylinder liner surface texture during the initial stage of wear. *Wear* **2018**, *408*, 34–42. [CrossRef]
54. Moriguchi, H.; Ohara, H.; Tsujioka, M. History and applications of diamond-like carbon manufacturing processes. *Sei Tech. Rev.* **2016**, *82*, 52–58.
55. Kalin, M.; Velkavrh, I.; Vižintin, J. The Stribeck curve and lubrication design for non-fully wetted surfaces. *Wear* **2009**, *267*, 1232–1240. [CrossRef]
56. Podgornik, B.; Jacobson, S.; Hogmark, S. DLC coating of boundary lubricated components—Advantages of coating one of the contact surfaces rather than both or none. *Tribol. Int.* **2003**, *36*, 843–849. [CrossRef]
57. Topolovec-Miklozic, K.; Lockwood, F.; Spikes, H. Behaviour of boundary lubricating additives on DLC coatings. *Wear* **2008**, *265*, 1893–1901. [CrossRef]
58. Kovaci, H.; Yetim, A.F.; Baran, O.; Celik, A. Tribological behavior of DLC films and duplex ceramic coatings under different sliding conditions. *Ceram. Int.* **2018**, *44*, 7151–7158. [CrossRef]
59. Peng, R.; Zhang, P.; Tian, Z.; Zhu, D.; Chen, C.; Yin, B.; Hua, X. Effect of textured DLC coatings on tribological properties of titanium alloy under grease lubrication. *Mater. Res. Express* **2020**, *7*, 066408. [CrossRef]
60. Amanov, A.; Watabe, T.; Tsuboi, R.; Sasaki, S. Improvement in the tribological characteristics of Si-DLC coating by laser surface texturing under oil-lubricated point contacts at various temperatures. *Surf. Coat. Technol.* **2013**, *232*, 549–560. [CrossRef]
61. Shum, P.W.; Zhou, Z.F.; Li, K.Y. To increase the hydrophobicity, non-stickiness and wear resistance of DLC surface by surface texturing using a laser ablation process. *Tribol. Int.* **2014**, *78*, 1–6. [CrossRef]

62. Arslan, A.; Masjuki, H.H.; Varman, M.; Kalam, M.A.; Quazi, M.M.; Al Mahmud, K.A.H.; Gulzar, M.; Habibullah, M. Effects of texture diameter and depth on the tribological performance of DLC coating under lubricated sliding condition. *Appl. Surf. Sci.* **2015**, *356*, 1135–1149. [CrossRef]
63. He, D.; Zheng, S.; Pu, J.; Zhang, G.; Hu, L. Improving tribological properties of titanium alloys by combining laser surface texturing and diamond-like carbon film. *Tribol. Int.* **2015**, *82*, 20–27. [CrossRef]
64. Gu, D.; Hagedorn, Y.C.; Meiners, W.; Meng, G.; Batista, R.J.S.; Wissenbach, K.; Poprawe, R. Densification behavior, microstructure evolution, and wear performance of selective laser melting processed commercially pure titanium. *Acta Mater.* **2012**, *60*, 3849–3860. [CrossRef]
65. Suh, N.P. An overview of the delamination theory of wear. *Wear* **1977**, *44*, 1–16. [CrossRef]
66. Dufils, J.; Faverjon, F.; Heau, C.; Donnet, C.; Benayoun, S.; Valette, S. Combination of laser surface texturing and DLC coating on PEEK for enhanced tribological properties. *Surf. Coat. Technol.* **2017**, *329*, 29–41. [CrossRef]
67. Aghababaei, R. On the origins of third-body particle formation during adhesive wear. *Wear* **2019**, *426–427*, 1076–1081. [CrossRef]
68. Wang, C.T.; Hakala, T.J.; Laukkanen, A.; Ronkainen, H.; Holmberg, K.; Gao, N.; Wood, R.J.; Langdon, T.G. An investigation into the effect of substrate on the load-bearing capacity of thin hard coatings. *J. Mater. Sci.* **2016**, *51*, 4390–4398. [CrossRef]
69. Bhaskaran, H.; Gotsmann, B.; Sebastian, A.; Drechsler, U.; Lantz, M.A.; Despont, M.; Jaroenapibal, P.; Carpick, R.W.; Chen, Y.; Sridharan, K. Ultralow nanoscale wear through atom-by-atom attrition in silicon-containing diamond-like carbon. *Nat. Nanotechnol.* **2010**, *5*, 181–185. [CrossRef]

coatings

MDPI

Article

Improvement of the Tribological Properties and Corrosion Resistance of Epoxy–PTFE Composite Coating by Nanoparticle Modification

Lixia Ying [1], Yunlong Wu [1], Chongyang Nie [1,*], Chunxi Wu [1] and Guixiang Wang [2]

[1] College of Mechanical and Electrical Engineering, Harbin Engineering University, Harbin 150001, China; yinglixia@hrbeu.edu.cn (L.Y.); wuyunlong839153@163.com (Y.W.); wuchunxi789789@163.com (C.W.)
[2] College of Materials Science and Chemical Engineering, Harbin Engineering University, Harbin 150001, China; wangguixiang@hrbeu.edu.cn
* Correspondence: niechongyang@hrbeu.edu.cn; Tel.: +86-136-3362-5169

Abstract: In order to meet the requirements of high corrosion resistance, wear resistance, and self-lubrication of composite coatings for marine applications, epoxy matrix composite coatings containing PTFE and TiO_2 nanoparticles were prepared on the steel substrate. With silane coupling agent KH570 (CH_2=C(CH_3)$COOC_3H_6Si(OCH_3)_3$), titanium dioxide nanoparticles were modified, and organic functional groups were grafted on their surface to improve their dispersion and interface compatibility in the epoxy matrix. Then, the section morphology, tribological, and anticorrosion properties of prepared coatings, including pure epoxy, epoxy–PTFE, and the composite coating with unmodified and modified TiO_2, respectively, were fully characterized by scanning electron microscopy, friction–abrasion testing machine, and an electrochemical workstation. The analytical results show that the modified TiO_2 nanoparticles are able to improve the epoxy–PTFE composite coating's mechanical properties of epoxy–PTFE composite coating including section toughness, hardness, and binding force. With the synergistic action of the friction reduction of PTFE and dispersion enhancement of TiO_2 nanoparticles, the dry friction coefficient decreases by more than 73%. Simultaneously, modified titanium dioxide will not have much influence on the water contact angles of the coating. A larger water contact angle and uniform and compact microstructure make the composite coating incorporated modified TiO_2 nanoparticles show excellent anti-corrosion ability, which has the minimum corrosion current density of 1.688×10^{-7} A·cm^{-2}.

Keywords: composite coating; epoxy–PTFE; modified TiO_2; tribological properties; corrosion resistance

Citation: Ying, L.; Wu, Y.; Nie, C.; Wu, C.; Wang, G. Improvement of the Tribological Properties and Corrosion Resistance of Epoxy–PTFE Composite Coating by Nanoparticle Modification. *Coatings* **2021**, *11* , 10 . https://dx.doi.org/10.3390/coatings11010010

Received: 1 December 2020
Accepted: 22 December 2020
Published: 24 December 2020

1. Introduction

For the advantages of excellent friction, stable chemical property, and low cost [1–3], epoxy resin is one of the excellent polymer coating materials, which is widely applied in the metal protection, electronics, and medical equipment [4,5]. Especially, epoxy–PTFE composite coatings have low friction coefficient and anticorrosion ability as well as high temperature resistance [6]. Such coatings could increase the anticorrosion capacity of metals and the self-lubricity of bearings as well as modify the hydrophobic and ice-phobic properties for wind turbine blades [7–9].

However, due to the curing shrinkage and warpage deformation of epoxy, there are always a lot of micro-pores and cracks in the composite coating. Moreover, the low hardness of PTFE will also lead to the poor wear resistance of the epoxy–PTFE composite coating [10,11]. A viable solution is to add hard or inorganic particles, such as TiO_2, CuO, CuF_2, CuS, and Al_2O_3, which will improve the tribological properties of the coating [12–15].

Larsen et al. [14] obtained a composite coating containing CuO and PTFE by mixing CuO and PTFE with epoxy solution. The evidence shows that both CuO and PTFE particles are well dispersed in the epoxy. The incorporation of PTFE and CuO has a positive synergistic effect on the friction and wear properties when the content of CuO is in the range

of 0.1–0.4 vol.%. Hamad et al. [15] investigated the mechanical properties of toughened epoxy by utilizing two kinds of nanoparticles sizes of TiO_2 (17 and 50 nm) at different weight fractions (1%, 3%, 5%, and 10%). The results indicate that the addition of a small fraction of TiO_2 nanoparticles can bring an improvement in the mechanical properties of epoxy composite. Researchers also expect that the addition of some lubricating substances will have a good effect on the performance of the epoxy resin composite coating [16,17]. The tribological properties of epoxy composites were also studied by Chang et al. [18]. With different proportions of graphite, PTFE, short carbon fiber, and TiO_2 and their combinations as additions, the frictional coefficient, wear resistance, and contact temperature of composite coatings were tested in a dry sliding condition with different sliding velocities and contact pressures. Results show that TiO_2 works best in improving the wear resistance of epoxy.

On the other hand, in order to meet the requirements of a corrosive environment, the corrosion resistance of polymer coatings has received much interest recently. Shi et al. [19] reported two methods to improve the dispersing of nanoparticles in epoxy coatings, including silane treatment and preparing nano-oxide paste. Compared with nano-TiO_2 paste and silane-treated nano-SiO_2, the latter is better than the former in improving the corrosion resistance and hardness of epoxy. Fadl et al. [20] fabricated TiO_2 nanoparticles by a simple template-free sol-gel method and mixed them with poly-dimethylamino siloxane (PDMAS) to form a PDMAS/TiO_2 nanocomposite as a modifier for polyamine-cured epoxy coating. The corrosion resistance of PDMAS/TiO_2 epoxy coating versus unmodified epoxy was investigated by a salt spray accelerated corrosion test. The PDMAS/TiO_2 epoxy coating has better corrosion mitigation and a self-healing effect. Radoman et al. [21] obtained epoxy/TiO_2 nanocomposites by the incorporation of modified TiO_2 nanoparticles with gallic acid esters in epoxy. Due to the deoxidizing effect of modified TiO_2, the nanocomposites have better corrosion resistance than that of the pure epoxy. Therefore, it is possible to obtain better corrosion resistance of epoxy composite coating by incorporating and modifying nanoparticles.

From the perspective of comprehensive performance, TiO_2 nanoparticles were selected as the additive in this study. SiO_2 nanoparticles are mainly used to improve the mechanical properties and heat resistance of epoxy composites. Nano-zinc oxide has the characteristics of high activity, large specific surface area, easy agglomeration, and long dispersion time before preparation. Therefore, it is a difficult point to prepare nano-zinc oxide-modified epoxy resin. The surface of Al_2O_3 contains a large number of hydroxyl groups, which makes it difficult to evenly disperse in epoxy materials. On the contrary, TiO_2 nanoparticles not only have good chemical stability but also have excellent heat resistance and UV protection, so it is widely used in the fields of UV-resistant materials, packaging materials, and coatings. At the same time as rigid nanoparticles and its strong adhesion, TiO_2 is often used as a modified filler to improve the bending strength, tensile strength, and impact strength of epoxy resin. In the wear resistance test, TiO_2 nanoparticles can significantly improve the wear resistance of epoxy resin, because TiO_2 nanoparticles have a large specific surface area and a large contact surface with the substrate, which requires more external energy when sliding [22,23].

Overall, the current research shows that pure epoxy resin coating has good corrosion resistance, but the high friction coefficient and poor wear resistance could not meet the requirements for use under friction conditions. Adding PTFE can reduce the friction coefficient, but the hardness and wear resistance are still low. Generally, incorporating soft phase PTFE and hard phase TiO_2 is an effective way to improve the tribological performance of a coating. Nevertheless, due to agglomeration and the poor compatibility of nanoparticles in the coating, composite coatings that involve nanoparticles often show low corrosion resistance. In the paper, the research focused on the improvements of both the tribological property and corrosion resistance of epoxy composite coating. TiO_2 nanoparticles were modified by a silane-coupling agent to reduce their surface tension, avoid agglomeration, and improve the interfacial compatibility with epoxy firstly. Then, the influence of modified

TiO_2 on the tribological properties and corrosion resistance of an epoxy–PTFE composite coating were analyzed in detail.

2. Materials and Methods

2.1. Materials

The carbon steel SK85 was chosen as the substrate with dimensions of 30 × 12 × 1 mm^3 and with the nominal composition as follows: 0.80%–0.90% C, ≤0.35% Si, ≤0.50% Mn, ≤0.03% P, ≤0.03% S, ≤0.20% Cr, ≤0.25% Ni, and ≤0.30% Cu. Epoxy resin (E44) with viscosity range from 40,000 to 45,000 mPa·s at 25 °C was purchased from Nanjing Star Synthetic Materials Co., LTD., Nanjing, China. TiO_2 nanoparticles with an average diameter of 40 nm were purchased from Shanghai Macklin Biochemical Co., LTD., Shanghai, China. The silane coupling agent KH570 (CH_2=C(CH_3) $COOC_3H_6Si(OCH_3)_3$, ≥99%, Silica Co., LTD., Nanjing, China) was used as a modifier. The ethanol (CH_3CH_2OH, ≥99.7%, Fuyu Fine Chemical Co., LTD., Tianjin, China) was used as a dispersant. The acetic acid (CH_3COOH, ≥99.8%, Sinopharm Group Chemical Reagent Co., LTD., Beijing China) was used to adjust the pH value of the solution. Additionally, all reagents were used without further purification.

2.2. TiO_2 Modification

In this study, titanium dioxide nanoparticles were selected as the strengthening particles, the average diameter of which are 40 nm. They were modified by the silane coupling agent KH570 (CH_2=C(CH_3) $COOC_3H_6Si(OCH_3)_3$) to graft organic functional groups on the surface of TiO_2 nanoparticles. The unique method is described as follows.

Ethanol was used as the dispersant, and the pH value was adjusted by acetic acid to 6. The silane coupling agent KH570 and TiO_2 nanoparticles were added into a certain volume of dispersed solutions at a mass ratio of 15:100. Firstly, the configured modified liquid was sonicated by ultrasonic liquid processors for 10 min. Then, it was disposed with a magnetic stirrer at 50 °C for 240 min with a speed of 300 r/min. Subsequently, the modified powder was washed with ethyl alcohol and deionized water three times to remove excess organosilane. Finally, collected precipitates were dried at 80 °C in a drying oven and stored in vials for further testing. The presence of organic phase on the modified TiO_2 nanoparticles surface was tested with the FT-IR spectrum (PerkinElmer Co., LTD., Shanghai, China).

2.3. Coating Preparation

Four kinds of coatings were prepared, including epoxy, epoxy–PTFE, epoxy–PTFE/TiO_2 (unmodified), and epoxy–PTFE/TiO_2 (modified). Carbon tool steel (SK85) and *n*-butanol are chosen for the matrix material and diluent, respectively, and phenolic amine resin (T13) was the curing agent for epoxy resin (E44). The mass ratio of T13/*n*-butanol/E44 was 1:2:4. The mass content of PTFE and TiO_2 was controlled at 15% and 2%, respectively. During the preparation process, after stirring the mixture thoroughly, it was ultrasonicated for 10 min to allow complete defoaming. Subsequently, the as-cleaned steel panels were immersed in the mixture solution adequately for 20 min, and we used a small mold to ensure that the thickness of the samples were uniform at 52 ± 3 μm. Then, the drying was carried out in an oven at 90 °C for 180 min. Finally, samples were successfully prepared for evaluating their surface morphology as well as mechanical and corrosion properties.

2.4. Coating Performance Testing

The performance test of coatings mainly includes the surface morphology, hardness, bonding force, tribological properties, and corrosion resistance. The section morphology of the coatings was characterized by scanning electron microscopy (SEM, FEI, Quanta200, OR, USA). Shore durometers (Petey Testing Instrument Co., LTD., Guangzhou, China) were used for testing the micro-hardness. The average micro-hardness value was acquired by averaging the results of six measurements. The binding force of the coatings—the average

results of two sets of measurements—was tested by pull-off tester (DeFeLsko Co., LTD., Ogdensburg, NY, USA). The tribological properties of the coatings were examined by a friction-abrasion testing machine (SFT-2M, ZhongKe-kaihua, Lanzhou, China) at a load of 5.0 N and a stage rotated speed of 200 r/min. The friction counterparts were GCr15 steel balls with a diameter of 5.0 mm; the radius of the friction circle was set to 2 mm, the duration of each wear test was 10 min. Subsequently, the friction–wear behavior of the coatings was estimated by SEM. The corrosion resistance of the composite coatings was measured by an electrochemical workstation (CHI660B, Chenhua, Shanghai, China) after being soaked in 3.5% NaCl solution for 72 h. The samples were used as the working electrode, while a platinum sheet and a saturated calomel electrode (SCE) were the counter and the reference electrodes, respectively. The test frequency of electrochemical impedance spectroscopy (EIS) ranged from 1000 Hz down to 10 Hz, and the scanning voltage was 10 mV. The corrosion potential (E_{corr}) and corrosion current density (i_{corr}) were obtained from the potentiodynamic polarization curves. All corrosion tests were performed at room temperature.

3. Results and Discussions

3.1. The Modification of TiO_2 Nanoparticles

The transmission FT-IR spectra of TiO_2 nanoparticles with and without KH570 modification were compared, as shown in Figure 1. For unmodified TiO_2 nanoparticles, the absorption band between 3400 and 3500 cm^{-1} corresponds to the hydroxyl group (–OH) due to the partial electron–hole pairs migration on the surface of TiO_2 nanoparticles. The vibration absorption peak is situated in the wavenumber interval of 500–750 cm^{-1}, which demonstrates the presence of Ti–O–Ti groups. However, the new absorption bands appear in the FT-IR spectrum of modified TiO_2 nanoparticles in curve ***b***, and there are some characteristic absorption peaks of KH570 at 2917 cm^{-1} (–CH_3 and –CH_2), 1717 cm^{-1} (C=O), 1620 cm^{-1} (C=C), 500–750 cm^{-1} (Ti–O–Si), so it could be inferred that the organic functional group has been grafted onto the surface of TiO_2 nanoparticles successfully.

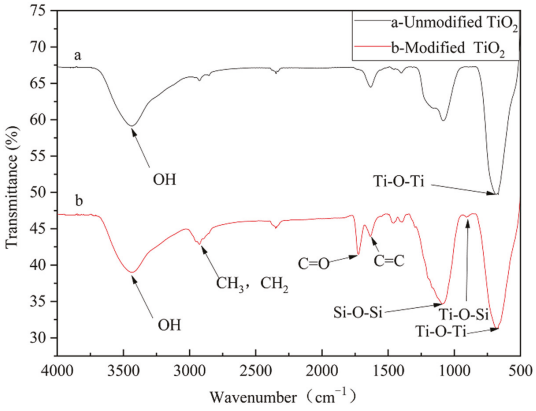

Figure 1. FT-IR results of unmodified TiO_2 and modified TiO_2.

Figure 2 is the energy-dispersive spectrometer (EDS) pattern of the TiO_2 nanoparticles before and after modification. The content of Si and C elements in Figure 2b is much higher than that in Figure 2a. The silane coupling agent molecule can be adsorbed on the surface of TiO_2 nanoparticles by its hydrophilic end and can react with the surface –OH groups on TiO_2 nanoparticles; therefore, the modified TiO_2 nanoparticles contain Si and C elements from KH570(CH_2=C(CH_3)$COOC_3H_6Si(OCH_3)_3$). All these experimental results demonstrate that the organic functional group of KH570 was successfully grafted onto the surface of TiO_2 nanoparticles.

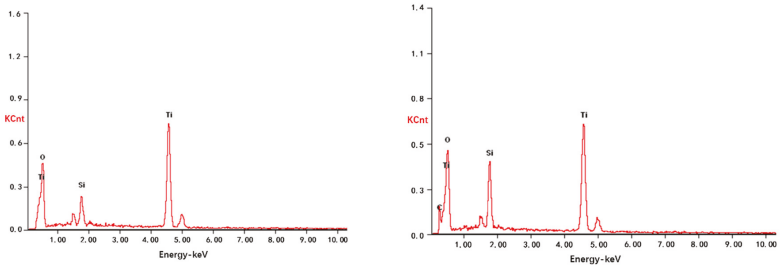

(**a**) (**b**)

Figure 2. The energy-dispersive spectrometer (EDS). (**a**) TiO_2 (unmodify), (**b**) TiO_2 (modify).

The fractured surface of four kinds of coatings was exhibited by scanning electron microscopy (SEM), as shown in Figure 3. It can be seen that the fractured surface of epoxy is very smooth (Figure 3a) even at 5000 times magnification. With the addition of PTFE and TiO_2 nanoparticles, the fractured surface of the composite coatings becomes much rougher than that of the pure epoxy coating. Furthermore, by comparing Figure 3b,c, it can be observed that there are still some flat areas and aggregated TiO_2 nanoparticles on the cross-section of the coating with unmodified TiO_2 nanoparticles (Figure 3c). However, with modified TiO_2 nanoparticles, the composite coating fracture surfaces are much rougher (Figure 3d), which can be attributed to the dispersive distribution of TiO_2 preventing crack propagation, and the excellent interfacial compatibility reducing the crack source. Generally, an increased section roughness means that the path at the crack tip is distorted, and the coating might absorb more section energy during the fracture process and possess better fracture toughness. Therefore, due to the grafting of organic functional groups adsorbed on the modified TiO_2 nanoparticles surface, the toughness of the composite coating is improved [24,25].

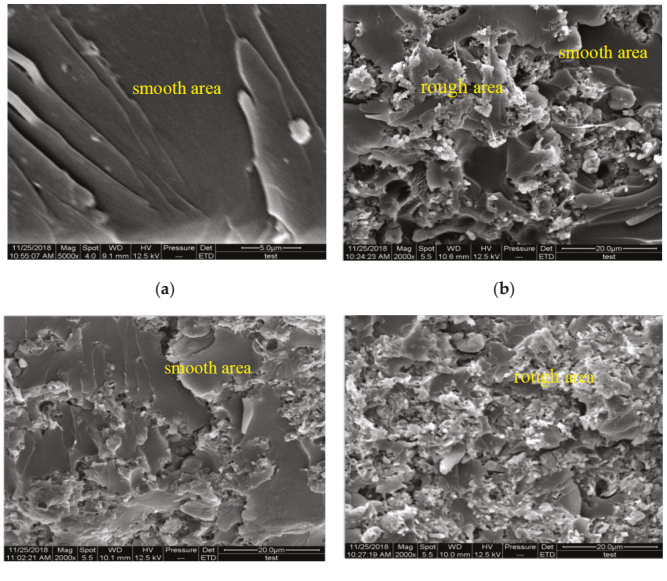

(**a**) (**b**)

(**c**) (**d**)

Figure 3. SEM images of section morphology of different coatings. (**a**) Unmixed epoxy, (**b**) epoxy-PTFE, (**c**) epoxy-PTFE/TiO_2(unmodify), (**d**) epoxy-PTFE/TiO_2(modify).

3.2. Hardness

Figure 4 shows the hardness values of different coatings. It indicates that the hardness of epoxy–PTFE–TiO_2 (modify), epoxy, epoxy–PTFE–TiO_2 (unmodify), and epoxy–PTFE coatings are arranged from high to low. The soft particles of PTFE improve the lubricity of the coating but also reduce its hardness. In contrast, modified hard TiO_2 nanoparticles can enhance the hardness of epoxy–PTFE composite coating better than unmodified hard TiO_2 nanoparticles. This is due to the modified TiO_2 nanoparticles dispersing more evenly in the coating, which has a dispersion strengthening effect in the coating.

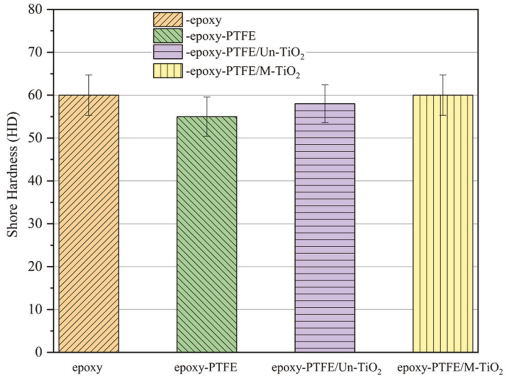

Figure 4. Hardness of different coatings.

3.3. Interfacial Adhesion

The interface bonding adhesion strength of different coatings is given in Figure 5. As Figure 5 shows, PTFE enhances the interfacial adhesion of epoxy coatings from 1.43 to 2.30 MPa. On the other hand, with the addition of modified TiO_2 nanoparticles, the bonding strength value of the composite coating reaches 2.70 MPa, which is higher than that of the coating containing unmodified TiO_2 nanoparticles. We interpreted that the introduction of organic functional groups on the surface of TiO_2 nanoparticles resulted in the formation of hydrogen bonds and Si–O bonds between the TiO_2 nanoparticles and the coating. The modified TiO_2 nanoparticles have a strong interfacial adhesion with the surrounding particles, and the van der Waals force attraction becomes stronger; therefore, the epoxy–PTFE–TiO_2 (modify) composite coating has the highest interfacial adhesion value. This corresponds to the improvement in section roughness and the hardness of the coating.

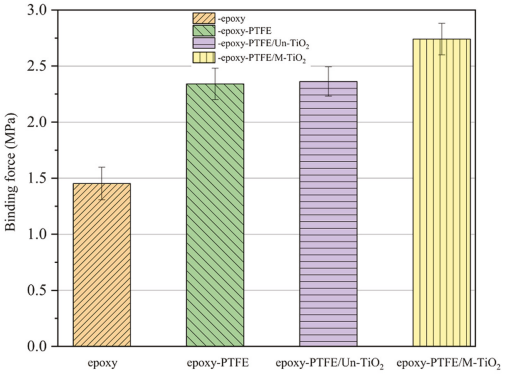

Figure 5. The results of interfacial adhesion.

3.4. Tribological Properties

Figure 6 shows the friction coefficient curves of different coatings versus the sliding time. As shown in Figure 6, with the addition of PTFE to epoxy, the friction coefficient decreases from 0.6 to about 0.16. Furthermore, compared to curve *C* of adding unmodified TiO_2 nanoparticles, the friction coefficient of the composite coating is less than 0.10 after adding modified TiO_2 nanoparticles, as shown in curve *D*.

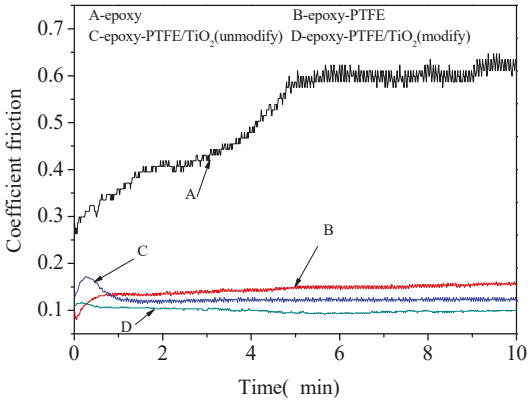

Figure 6. Friction coefficients of different coatings.

The SEM images of the worn surfaces are shown in Figure 7. After adding PTFE, the wear track width of the epoxy coating decreases from 634.21 (Figure 7a) to 321.56 μm (Figure 7b). Furthermore, with the addition of unmodified TiO_2 nanoparticles (Figure 7c), the width of the wear track narrows to 274.51 μm. With modified TiO_2 nanoparticles, the wear track becomes much smoother and narrower (Figure 7d). On the other hand, there are many micropores on the worn surface of epoxy, which indicates that the epoxy coating itself is not densification. When PTFE is incorporated, there are no obvious micropores. The PTFE with self-lubricating property spreads on the wear surface (as shown in curve A and curve B), reduces the friction coefficient, and brings a much smoother worn track (Figure 7b). When unmodified TiO_2 nanoparticles were added into the coating, particle agglomeration results in some micropores emerging on the worn surface (Figure 7c). However, there are seldom obvious micropores on the worn surface with modified TiO_2 nanoparticles (Figure 7d). Obviously, when modified TiO_2 nanoparticles coexist in the composite coating, uniformly dispersed nanoparticles and excellent interfacial compatibility lead to the narrowest and smoothest wear track. The composite coating D has the most excellent wear resistance.

Summing up, the friction coefficient of the composite coatings with PTFE is significantly improved because of the formation of PTFE lubricating transfer film on the wear surface. However, the wear resistance of a soft epoxy–PTFE composite coating is still weakened. With PTFE and TiO_2 coexisting in the epoxy–PTFE/TiO_2 (unmodify) composite coating, the combination of soft phase particles and hard phase particles leads to a higher wear resistance. In contrast, a relatively good interfacial compatibility brought by the modified TiO_2 nanoparticles decreases the furrow and adhesive effects, which leads to a lower friction coefficient, much smoother worn surface, and much higher wear resistance. Meanwhile, the addition of PTFE and TiO_2 nanoparticles may affect the mechanical properties, and the good interfacial compatibility of modified TiO_2 nanoparticles may improve the mechanical stability of the coating, which may also affect the tribological properties. As described by Homaeigohar et al., the uniform distribution of functionalized graphite nanofilaments can improve the mechanical stability of nanocomposite hydrogels, and the addition of tricalcium phosphate can affect the mechanical properties of

the polythylene [26,27]. All in all, the synergistic action of the friction reduction of PTFE and dispersion enhancement of modified TiO_2 nanoparticles of PTFE makes the epoxy–PTFE/TiO_2 (modify) composite coating show excellent friction reduction and anti-wear performance.

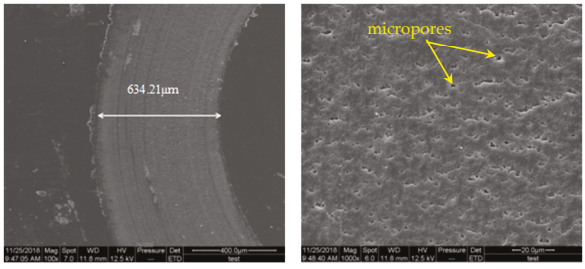

Wear scar profile Magnification of wear marks

(**a**)

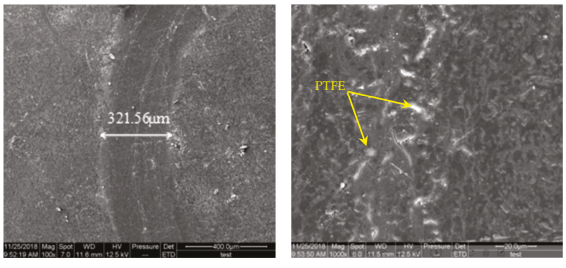

Wear scar profile Magnification of wear marks

(**b**)

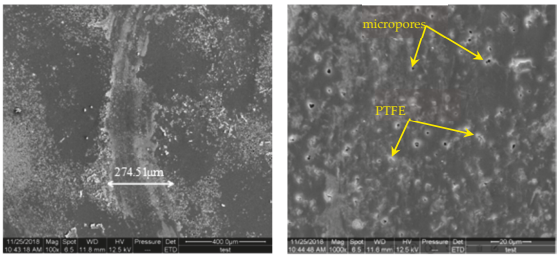

Wear scar profile Magnification of wear marks

(**c**)

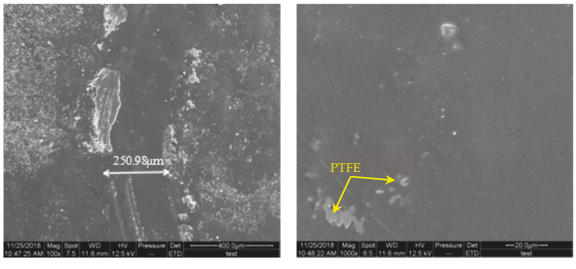

Wear scar profile Magnification of wear marks

(**d**)

Figure 7. Wear scar morphology of different coatings. (**a**) unmixed epoxy, (**b**) epoxy–PTFE, (**c**) epoxy–PTFE/TiO_2 (unmodify), (**d**) epoxy–PTFE/TiO_2 (modify).

3.5. Anti-Corrosion Properties

3.5.1. Hydrophobic Performance

The water contact angle of coatings was measured for evaluating their hydrophobic property, as shown in Figure 8. The water contact angles of the pure epoxy coating and epoxy/PTFE composite coating are 74.81° and 100.90°, respectively, which indicates that PTFE can improve the hydrophobic property of the coating. With the further addition of TiO_2 nanoparticles to the epoxy–PTFE coating, due to the presence of hydroxyl groups on the surface of TiO_2 nanoparticles, the water contact angle of the composite coating is reduced greatly to 56.84°, which is manifested as hydrophilic. The small contact angle of coating C will result in the worst corrosion resistance. In contrast, with adding the modified TiO_2 nanoparticles instead of unmodified TiO_2, the water contact angle of the composite coating approaches that of the pure epoxy coating, and the hydrophilicity of the coating decreased greatly. However, due to the steric hindrance effect, the hydroxyl groups on the surface of TiO_2 are not fully replaced by organic functional groups and still have a certain hydrophilicity.

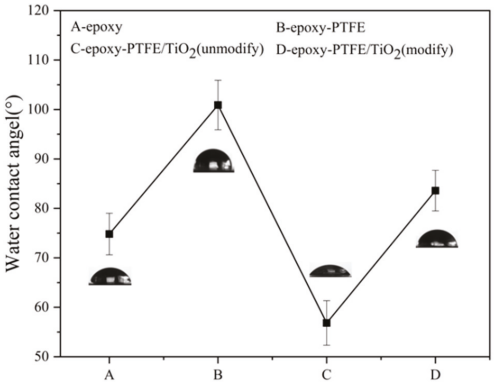

Figure 8. Water contact angles of four kinds of coatings.

When PTFE as hydrophobic particles were added to the epoxy coating, the water contact angle rose to 100.90°, showing hydrophobicity. Due to the presence of hydrophilic hydroxyl groups on the surface of TiO_2, the extremely poor interfacial compatibility between TiO_2 and epoxy coatings, resulting in easy agglomeration of TiO_2. Therefore, as shown in Figure 3c, there are still some flat areas on the cross-section of the coating, and the water contact angle of epoxy–PTFE/TiO_2 (modified) drops to 56.84° and shows hydrophilicity. Due to the influence of steric hindrance, part of the hydroxyl groups on the modified TiO_2 surface is replaced with organic functional groups. The interface compatibility between TiO_2 nanoparticles and the epoxy coating is enhanced, and the coating surface becomes rougher, as shown in Figure 3d. The water contact angle of the composite coating approaches that of the pure epoxy coating, while the hydrophilicity of the coating decreases greatly. All in all, the increase of the contact angle is beneficial to improve the corrosion resistance of the coating.The extremely poor interfacial compatibility between TiO_2 and epoxy coatings, resulting in easy agglomeration of TiO_2.

3.5.2. Potentiodynamic Polarization

The potentiodynamic polarization curves of different coatings are shown in Figure 9, and Table 1 exhibits the corrosion current density (i_{corr}) and corrosion potential (E_{corr}). Experimental results indicate that the corrosion current density decreases and the corrosion potential of the coating increases with the addition of PTFE.

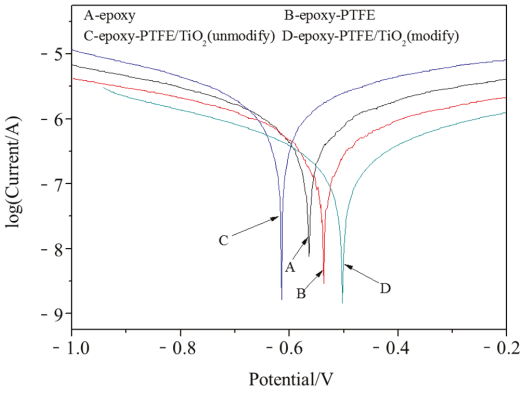

Figure 9. Potentiodynamic polarization curves of different coatings.

Table 1. Potentiodynamic polarization parameters of different coatings.

Coatings	Corrosion Current Density ($A \cdot cm^{-2}$)	Corrosion Potential (V)
epoxy	5.727×10^{-7}	−0.564
epoxy–PTFE	3.702×10^{-7}	−0.528
epoxy–PTFE/TiO_2 (unmodify)	8.725×10^{-7}	−0.614
epoxy–PTFE/TiO_2 (modify)	1.688×10^{-7}	−0.503

Due to the high hydrophilicity of TiO_2 nanoparticles, the containing corrosive medium of water molecules is more likely to penetrate the coating, get in the substrate, and reduce the corrosion resistance of the coating thereby. As shown in Figure 9, after adding unmodified TiO_2 nanoparticles into the epoxy–PTFE coating, the corrosion current density of the coating increases, and the corrosion potential decreases. In contrast, after adding the modified TiO_2 nanoparticles, the composite coating of epoxy–PTFE–TiO_2 (modified) has the minimum corrosion current density of 1.688×10^{-7} $A \cdot cm^{-2}$, and the corrosion potential increases to some extent (−0.503 V). In comparison, the corrosion resistance of the coating before the titanium dioxide modification is the worst. It can be speculated that the modified TiO_2 nanoparticles have better interfacial compatibility with epoxy, which prevents the immersion of corrosive media and thus improves the corrosion resistance of the epoxy–PTFE coating.

3.5.3. Electrochemical Impedance Spectroscopy

Figure 10 shows the test data of the electrochemical impedance spectroscopy (EIS). As can be seen from the results in Figure 10a,b, with PTFE and unmodified TiO_2 nanoparticles involved in the coating, the arc radius in the Nyquist figure and the impedance value of the low-frequency region in the Bode figure are very small; therefore, the addition of unmodified TiO_2 nanoparticles will reduce the corrosion resistance of the epoxy–PTFE coating. On the contrary, after adding modified TiO_2 nanoparticles into the epoxy–PTFE coating, both the arc radius in the Nyquist figure and the impedance value of low frequency in the Bode figure are larger, and the corrosion resistance of the epoxy–PTFE coating is greatly improved. The analysis results are consistent with the Tafel curve test results. Obviously, the poor corrosion resistance of coating C has been effectively addressed by the modification treatment of TiO_2 nanoparticles.

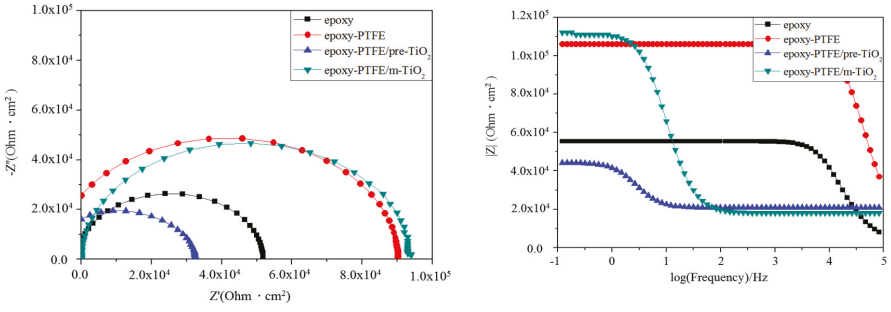

Figure 10. Electrochemical impedance of the coatings. (**a**) Nyquist, (**b**) Bode.

4. Conclusions

In order to meet the requirements of high corrosion resistance, wear resistance, and self-lubricating property of composite coatings for marine applications, the epoxy composite coatings containing PTFE and TiO_2 nanoparticles were prepared in this research. Through the modification treatment of TiO_2, the compactness of the coating is increased and the hydrophilicity is decreased, which leads to excellent tribological properties and corrosion resistance. The specific conclusions are as follows:

- Modifying the surface of TiO_2 nanoparticles grafted with organic functional groups can enhance their dispersion and further improve the interface compatibility with the epoxy matrix. Simultaneously, the bonding force between the coating and the matrix is increased. Compared with pure epoxy, epoxy–PTFE, and the composite coating with unmodified TiO_2, the epoxy–PTFE–TiO_2 composite coating with modified TiO_2 has the lowest friction coefficient and the most excellent wear resistance.
- With the incorporation of modified TiO_2 nanoparticles, the hydrophilicity of the epoxy–PTFE composite coating decreases significantly, which is beneficial to improve the corrosion resistance of the composite coating. Simultaneously, modified TiO_2 nanoparticles improve the interface compatibility and densification of the composite coating. There are very few micropores in the coating, so it is difficult for the water molecules containing corrosive media to penetrate the coating and get into the matrix. The composite coating including modified TiO_2 nanoparticles possesses better corrosion resistance than that of the coating with unmodified TiO_2. By the modification treatment of TiO_2 nanoparticles, the poor corrosion resistance of an epoxy–PTFE–TiO_2 composite coating has been effectively addressed.

Author Contributions: Conceptualization, L.Y. and G.W.; methodology, L.Y. and G.W.; validation, L.Y.; formal analysis, L.Y. and C.W.; investigation, L.Y. and Y.W.; writing—original draft preparation, L.Y., C.N., and Y.W.; writing—review and editing, L.Y., C.N., and Y.W. All authors have read and agreed to the published version of the manuscript.

Funding: The authors acknowledge the financial support from the Natural Science Foundation of Heilongjiang Province (JJ2019LH1520) and the Fundamental Research Funds for the Central Universities (3072020CF0705).

Data Availability Statement: Data is contained within the article.

Conflicts of Interest: The authors declare no conflict of interest.

References

1. Fei, J.; Li, H.J.; Fu, Y.W.; Qi, L.H.; Zhang, Y.L. Effect of phenolic resin content on performance of carbon fiber reinforced pa-per-based friction material. *Wear* **2010**, *269*, 534–540. [CrossRef]
2. Pourhashem, S.; Saba, F.; Duan, J.-Z.; Rashidi, A.; Guan, F.; Nezhad, E.G.; Hou, B. Polymer/Inorganic nanocomposite coatings with superior corrosion protection performance: A review. *J. Ind. Eng. Chem.* **2020**, *88*, 29–57. [CrossRef]
3. Rajesh, P.S.M.; Delaroa, C.; Gagné, M.; Klemberg-Sapieha, J.E.; Sirois, F.; Therriault, D. Continuous and selective-area coating of silver on fiber-reinforced polymer composites for aerospace applications. *Mater. Today Commun.* **2019**, *18*, 206–212. [CrossRef]
4. Liu, Y.; Lu, J.; Cui, Y. Improved thermal conductivity of epoxy resin by graphene–nickel three-dimensional filler. *Carbon Resour. Convers.* **2020**, *3*, 29–35. [CrossRef]
5. Culbreath, C.J.; Gaerke, B.; Taylor, M.S.; McCullen, S.D.; Mefford, O.T. Effect of infill on resulting mechanical properties of additive manufactured bioresorbable polymers for medical devices. *Materialia* **2020**, *12*, 100732. [CrossRef]
6. Zhang, F.; Yuan, Z.; Jia, X.; Wang, X.; Fu, G.; Yu-Er, C. Preparation and properties of a kind of corrosion resistant, self-cleaning and colored PTFE coating on metal surface. *Mater. Prot.* **2019**, *52*, 100–103.
7. Qin, C. (Chris); Mulroney, A.T.; Gupta, M.C. Anti-icing epoxy resin surface modified by spray coating of PTFE Teflon particles for wind turbine blades. *Mater. Today Commun.* **2020**, *22*, 100770. [CrossRef]
8. Shen, J.; Van Rijn, F.; Pei, Y.T.; De Hosson, J.T.M. On the abrasiveness and reinforcement of fillers in PTFE/epoxy composites. *Polym. Compos.* **2016**, *39*, 698–707. [CrossRef]
9. Shi, X.; Nguyen, T.A.; Suo, Z.; Liu, Y.; Avci, R. Effect of nanoparticles on the anticorrosion and mechanical properties of epoxy coating. *Surf. Coat. Technol.* **2009**, *204*, 237–245. [CrossRef]
10. McCook, N.; Burris, D.; Bourne, G.R.; Steffens, J.; Hanrahan, J.; Sawyer, W.G. Wear resistant solid lubricant coating made from PTFE and epoxy. *Tribol. Lett.* **2005**, *18*, 119–124. [CrossRef]
11. Liu, D.; Zhao, W.; Liu, S.; Cen, Q.; Xue, Q. Comparative tribological and corrosion resistance properties of epoxy composite coatings rein-forced with functionalized fullerene C60 and graphene. *Surf. Coat. Technol.* **2016**, *286*, 354–364. [CrossRef]
12. Sawyer, W.; Freudenberg, K.D.; Bhimaraj, P.; Schadler, L.S. A study on the friction and wear behavior of PTFE filled with alumina nanoparticles. *Wear* **2003**, *254*, 573–580. [CrossRef]
13. Friedrich, K.; Zhang, Z.; Schlarb, A.K. Effects of various fillers on the sliding wear of polymer composites. *Compos. Sci. Technol.* **2005**, *65*, 2329–2343. [CrossRef]
14. Larsen, T.Ø.; Andersen, T.L.; Thorning, B.; Horsewell, A.; Vigild, M.E. Changes in the tribological behavior of an epoxy resin by incorporating CuO nanoparticles and PTFE microparticles. *Wear* **2008**, *265*, 203–213. [CrossRef]
15. Al-Turaif, H.A. Effect of nano TiO_2 particle size on mechanical properties of cured epoxy resin. *Prog. Org. Coat.* **2010**, *69*, 241–246. [CrossRef]
16. Vattikuti, S.P.; Byon, C. Synthesis and characterization of molybdenum disulfide nanoflowers and nanosheets: Nanotribology. *J. Nanomater.* **2015**, *2015*, 710462. [CrossRef]
17. Vattikuti, S.P.; Byon, C.; Reddy, C.V.; Venkatesh, B.; Shim, J. Synthesis and structural characteri-zation of MoS_2 nanospheres and nanosheets using solvothermal method. *J. Mater. Sci.* **2015**, *50*, 5024–5038. [CrossRef]
18. Chang, L.; Zhang, Z.; Breidt, C.; Friedrich, K. Tribological properties of epoxy nanocomposites. *Wear* **2005**, *258*, 141–148. [CrossRef]
19. Shi, H.; Liu, F.; Yang, L.; Han, E. Characterization of protective performance of epoxy reinforced with nanometer-sized TiO_2 and SiO_2. *Prog. Org. Coat.* **2008**, *62*, 359–368. [CrossRef]
20. Fadl, A.; Abdou, M.; Hamza, M.; Sadeek, S. Corrosion-inhibiting, self-healing, mechanical-resistant, chemically and UV stable PDMAS/TiO_2 epoxy hybrid nanocomposite coating for steel petroleum tanker trucks. *Prog. Org. Coat.* **2020**, *146*, 105715. [CrossRef]
21. Radoman, T.S.; Dzunuzovic, J.V.; Jeremic, K.B.; Grgur, B.N.; Milicevic, D.S.; Popovic, I.G.; Dzunuzovic, E.S. Improvement of epoxy resin properties by incorporation of TiO_2 nanoparticles surface modified with gallic acid esters. *Mater. Des.* **2014**, *62*, 158–167. [CrossRef]
22. Liu, Y.; Wang, R. Study on nano-particles modified epoxy resin. *Technol. Dev. Chem. Ind.* **2016**, *45*, 22–24.
23. Tian, L.; Wang, X.; Wu, Y.; Wang, H.; Wei, Y. Research progress in the epoxy composites modified by nano-inorganic particles. *New Chem. Mater.* **2012**, *40*, 4–7.
24. Ahmetli, G.; Deveci, H.; Soydal, U.; Seker, A.; Kurbanli, R. Coating. Mechanical and thermal properties of epoxy toluene oli-gomer modified epoxy resin/sepiolite composites. *Prog. Org. Coat.* **2012**, *75*, 97–105. [CrossRef]
25. Sabzi, M.; Mirabedini, S.; Zohuriaan-Mehr, J.; Atai, M. Surface modification of TiO_2 nano-particles with silane coupling agent and investigation of its effect on the properties of polyurethane composite coating. *Prog. Org. Coat.* **2009**, *65*, 222–228. [CrossRef]
26. Homaeigohar, S.; Tsai, T.-Y.; Young, T.-H.; Yang, H.J.; Ji, Y.-R. An electroactive alginate hydrogel nano-composite reinforced by functionalized graphite nanofilaments for neural tissue engineering. *Carbohydr. Polym.* **2019**, *224*, 115112. [CrossRef]
27. Homaeigohar, S.; Sadi, A.Y.; Javadpour, J.; Khavandi, A. The effect of reinforcement volume fraction and particle size on the mechanical properties of β-tricalcium phosphate–high density polyethylene composites. *J. Eur. Ceram. Soc.* **2006**, *26*, 273–278. [CrossRef]

coatings

MDPI

Article

Structural Features and Tribological Properties of Detonation Gun Sprayed Ti–Si–C Coating

Bauyrzhan Rakhadilov [1,2], Dastan Buitkenov [1,*], Zhuldyz Sagdoldina [1], Bekbolat Seitov [3], Sherzod Kurbanbekov [3] and Meruyert Adilkanova [4]

[1] Research Center Surface Engineering and Tribology, Sarsen Amanzholov East Kazakhstan University, Ust-Kamenogorsk 070000, Kazakhstan; rakhadilovb@mail.ru (B.R.); sagdoldina@mail.ru (Z.S.)
[2] Plasma Science LLP, Ust-Kamenogorsk 070000, Kazakhstan
[3] Department of Physics, Khoja Akhmet Yassawi International Kazakh-Turkish University, Turkestan 161200, Kazakhstan; bekbolat.seitov@ayu.edu.kz (B.S.); sherzod.kurbanbekov@ayu.edu.kz (S.K.)
[4] The Faculty of Earth and Environmental Sciences, Daulet Serikbaev East Kazakhstan Technical University, Ust-Kamenogorsk 070000, Kazakhstan; milka160281@mail.ru
* Correspondence: buitkenovd@mail.ru; Tel.: +7-776-439-9994

Abstract: The paper considers the research results of structural-phase state and tribological characteristics of detonation coatings based on Ti–Si–C, obtained at different filling volumes of the explosive gas mixture barrel of a detonation gun. The results analysis indicates that the phase composition and properties of detonation coatings strongly depend on the technological parameters of spraying. With an increase of the explosive mixture in the filling volume of the detonation barrel up to 70% of the coatings consist mainly of the TiC phase, because high temperature leads to a strong decomposition of Ti_3SiC_2 powders. Thus, the XRD results confirm that at 70% of the explosive gas mixture's filling volume, partial decomposition and disintegration of the powders occurs after detonation spraying. We established that detonation coatings based on titanium carbosilicide obtained at the explosive gas mixture's filling volume at 60% are characterized by high wear resistance and adhesive strength. Thermal annealing was performed after spraying in the temperature range of 700–900 °C for 1 h to reduce microstructural defects and improve the Ti–Si–C coating characteristics. As a result of the heat treatment in the Ti–Si–C system at 800 °C, we observed that an increase in the volume fraction of the Ti_3SiC_2 and TiO_2 phases led to a 2-fold increase in microhardness. This means that the after-heat-treatment can provide a sufficient reaction time for the incomplete reaction of the Ti–Si–C (TSC) coating during the detonation gun spraying. Thus, annealing can provide an equal distribution of elements in the coatings.

Keywords: detonation gun spray; structure; carbolized titanium; hardness; wear resistance; phase; adhesion; heat treatment

Citation: Rakhadilov, B.; Buitkenov, D.; Sagdoldina, Z.; Seitov, B.; Kurbanbekov, S.; Adilkanova, M. Structural Features and Tribological Properties of Detonation Gun Sprayed Ti–Si–C Coating. *Coatings* **2021**, *11* , 141 . https://doi.org/10.3390/coatings11020141

Received: 26 December 2020
Accepted: 19 January 2021
Published: 28 January 2021

1. Introduction

Currently, carbides, silicides, and transition metals have aroused considerable interest due to increasing demand. In particular, the most frequently mentioned phases in the Ti–Si–C system are TiC, Ti_5Si_3, and Ti_3SiC_2. They attract considerable interest due to their unique metallic combination and ceramic properties. As metals, they have good electrical and thermal conductivity, high plasticity, good machinability and excellent thermal shock resistance. As ceramics, they have low density, high stiffness, high melting points, and good resistance to oxidation and corrosion [1–3]. Such exceptional properties result from the coexistence of strong covalent ionic MX bonds and weak metallic MA bonds within a layered hexagonal structure (space group P63/mmc) of MAX materials, which are created by repeating a three-layer structure (consisting of two Mn + 1xN layers intercalated by a single atomic layer A) [4]. A unique distinctive feature of these materials is the layered structure of their crystal lattice—the regular arrangement of layers of M and A atoms

of elements that have reduced binding energy between them. Tightly packed layers of titanium atoms alternate with layers of silicon atoms, and carbon atoms occupy octahedral interstices between titanium atoms [5,6]. These properties make the phase material Ti_3SiC_2 MAX ideal for extreme condition applications. In addition, system Ti–Si–C has good characteristics under conditions of abrasive wear and corrosion. However, production coatings based on Ti–Si–C production by traditional methods are associated with a high temperature and duration of their obtaining process. Sprayed coatings based on Ti_3SiC_2 are usually accompanied by phases TiC and Ti–Si. The short reaction time of powder mixtures and the decomposition of Ti–Si–C at high temperature are the main problems for the phase's purity. An analogous problem occurs with plasma spraying of coatings [7]. In addition, using heat treatment to improve the characteristics of the resulting coatings is not well studied. Considering their tribological application, the question of how to deposit Ti_3SiC_2-based coatings with high wear resistance is still undecided.

Among the coating methods, detonation spraying and high-velocity oxy-fuel (HVOF) spraying [8–11] have an obvious advantage in comparison to plasma spraying and other spraying methods because of high particle flight speed and lower operating temperature. Detonation spraying coatings from powder are based on the use of explosion energy of a fuel–oxygen mixture and are known as a promising method for obtaining coatings from various materials with good adhesion [12]. The higher velocity flow of particles allows providing higher density and adhesive strength of the detonation coating. The essential advantage of the detonation spraying method is the ability to accurately control the amount of explosive gas mixture used for each shot of the detonation gun, which allows changing the degree of thermal and chemical effects of detonation products on the particles of spraying powder [13]. Depending on the composition of the acetylene–oxygen explosive mixture, from a O_2/C_2H_2 ratio and from the nature of the gas carrier, chemical interactions may occur between the individual phases of the composite particles [14,15]. In this regard, the detonation method of coating is of considerable interest. Therefore, much attention is directed at obtaining detonation coatings from binary and ternary phases relevant to the Ti–Si–C system.

In connection with the above, the aim of this work is to study the structural features and tribological properties of coatings based on Ti–Si–C, which are obtained by the detonation method under various deposition modes, as well as to study the effect of thermal annealing on the structural and phase states of coatings based on Ti–Si–C.

2. Materials and Methods

By detonation spraying on the surface of steel U9 (with 0.94 wt.% C) Ti_3SiC_2 coatings were obtained. The chemical composition of the powder was Ti: 74 wt.%; SiC: 20 wt.%; C: 6.0 wt.%, and powder particle size was between 20 and 40 μm. Before spraying, the substrate was sandblasted to improve the adhesive strength of the coatings. The value of the surface roughness parameter after sandblasting was on average (Ra) 3.2 microns. The distance between the treated surface of the sample and the detonation barrel was 200 mm. The straight barrel diameter was 20 mm.

The CCDS2000 (LIH SB RAS, Novosibirsk, Russia) detonation set-up was used to obtain the coatings, which has a system of electromagnetic gas valves that regulate the supply of fuel and oxygen and control the system purging (Figure 1). The acetylene–oxygen mixture was used as a fuel gas, which is the most used fuel during detonation spraying of powder materials. Spraying was carried out at the ratio of the acetylene–oxygen mixture O_2/C_2H_2 = 1.856. The volume of the explosive gas mixture of the detonation gun barrel was varied from 50% to 70%. The average shot frequency of working gases at 4 Hz was: acetylene 4–7; propane–butane mixture 2 . . . 3, 5; oxygen 10 . . . 12; nitrogen 10 . . . 15 m^3/h. Nitrogen was used as a carrier gas.

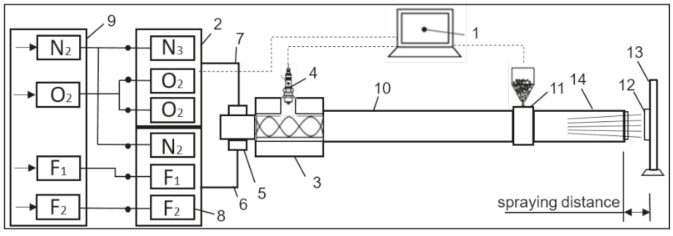

Figure 1. Schematic diagram of the CCDS2000 detonation complex: 1—control computer; 2—gas distributor; 3—mixing-ignition chamber; 4—spark plug; 5—barrel valve; 6—fuel line; 7—oxygen line; 8—gas valves; 9—gas supply unit; 10—indicated part of the barrel; 11—powder feeder; 12—workpiece; 13—manipulator; 14—the muzzle of the barrel; F_1—acetylene; F_2—propane–butane; O_2—oxygen; N_2—nitrogen.

The research phase composition of the samples was studied by X-ray diffractometer X'PertPro (Philips Corporation, The Nederlands) using CuKα radiation. The shooting was carried out in the following modes: tube voltage U = 40 kV; tube current I = 20 mA; exposure time 1s; shooting step $\Delta 2\theta \sim 0.02^\circ$ and 2θ = 10–90°. The surface morphology was studied by scanning electron microscopy using secondary (SEs) and backscattered electrons (BSEs) on a Vega3 (Tescan, Brno, Czech Republic) scanning electron microscope. Tribological tests for sliding friction were performed on a high-temperature tribometer TRB^3 (Anton Paar Srl, Peseux, Switzerland) using the standard "ball-disc" technique (international standards ASTM G 133-95 and ASTM G 99) [16,17]. A counterbody was used comprising a ball with a diameter of 3.0 mm made of SiC-coated steel. The tests were carried out at a load of 10 N and a linear velocity of 3 cm/s, a radius of wear curvature of 4 mm, the friction path was 41 m. Wear tracks were studied using a non-contact 3D profilometer MICROMEASURE 3D (STIL, France) station. The CSEM Micro Scratch Tester (Neuchatel, Switzerland) was used to study the adhesive characteristics of coatings by the "scratching" method. Scratch testing was performed at a maximum load of 30 N; the rate of change of normal loading on the sample was 29.99 N/min, the speed of movement of the indenter was 9.63 mm/min, the length of the scratch was 10 mm, the radius of tip curvature was 100 microns. To obtain reliable results, three scratches were applied to the surface of each coated sample. The obtained coatings with mechanical properties (Young's modulus, hardness) were studied by a NanoScan-4D Compact (FSBI TISNCM, Russia) nanohardometer. The tests were carried out at a load of 200 mN. Loading time, unloading time, and the time of supporting the maximum load were each 5 s. The dependence of the penetration depth on the applied force at the loading and unloading stages was determined by the Oliver–Pharr method. At least 10 measurements were carried out on each sample, the results of which were averaged. Sample tests for abrasive wear were carried out on an experimental stand (Figure 2a) against soft fixed abrasive particles according to the "rotating roller–flat surface" scheme in accordance with GOST 23.208-79, which conforms to the American standard ASTM C 6568 [18,19]. Sample tests for impact and abrasive wear were carried out on an experimental stand in accordance with GOST 23.207-79 (Figure 2b) [20]. For a comparative assessment of the wear resistance of detonation coatings, tests were carried out in the following modes: impact energy E = 3.3 J, impact velocity υ = 1 m/s, and impact frequency n = 200 min^{-1}. The samples tested for abrasive and impact-abrasive wear underwent 8–10 tests. After each test, the mass loss of the samples was determined and was given the average value with the standard deviation. The microhardness of the samples was measured by a diamond indenter on a PMT-3M (LOMO, Russia) device in accordance with GOST 9450-76 [21], at a load of 200 g and an exposure time of 10 s [22]. Thermal annealing of coated samples was carried out in a laboratory tubular electric furnace of resistance SUOL-0.4.4/12 (0.4.4—dimensions of working space, 40 × 400 mm; 12—the nominal temperature of the working space, 1200 °C) in a vacuum of 10^{-2} Pa at temperatures of 700 °C, 800 °C, and 900 °C for 1 h, followed by cooling in the furnace.

The temperature was measured and regulated by a precision high-precision temperature controller HTC-2 [23].

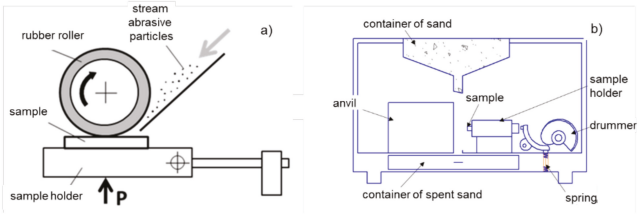

Figure 2. The experimental test stand for testing of samples: (**a**) abrasive wear according to the "rotating roller–flat surface" scheme; (**b**) impact and abrasive wear.

3. Results and Discussions

Figure 3 shows the diffractograms of Ti_3SiC_2 powder and Ti–Si–C coating obtained at the barrel filling volume of an explosive gas mixture from 50% to 70%. The results of powder XRD analysis showed that the powder consisted of Ti_3SiC_2 as the main phase and TiC as the secondary phase. The diffractograms of Ti–Si–C coatings showed a decrease in the intensity of Ti_3SiC_2 diffraction lines and an increase in TiC intensity, which indicated a partial decomposition of the Ti–Si–C system and agreed with the data [24–31]. A decrease in the intensity of diffraction lines in the Ti–Si–C system after detonation spraying was due to the deintercalation of silicon from Ti–Si–C lattice layers [25,26] since the silicon flatness had weak connections with Ti–C flatness. This occurred due to detonation spraying when the Ti–Si–C system lost a certain amount of silicon due to its high "fugacity" [27]. XRD analysis showed that when the barrel was filled with explosive mixtures to 50% and 60%, a low degree of Ti_3SiC_2 decomposition was achieved, and also after spraying the appearance of reflexes (100) and (106) of the Ti_3SiC_2 phase was detected. With an increase in the filling volume of the detonation barrel to 70%, a decrease in the intensity of the diffraction peaks of Ti_3SiC_2 was observed because of the decomposition of the powder into TiC. In the detonation wave flow, the Ti_3SiC_2 powder decomposed due to high-speed shock interaction heated to high temperatures. Thus, the XRD results confirmed that at 70% of the explosive mixture's filling volume, partial decomposition and disintegration of the powders occurred after detonation spraying.

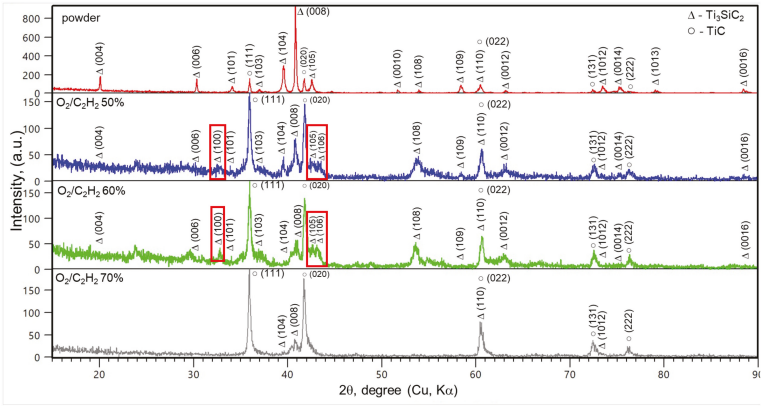

Figure 3. Diffractogram of Ti_3SiC_2 powder and Ti–Si–C coatings obtained at different filling volumes of the explosive gas mixture of the detonation gun barrel.

The SEM image shows that the cross section of the sprayed coating is not flat and continuous. From the image's analysis, it follows that the coating structure has an inhomogeneous structure with pores, a typical layered, wave-like arrangement of structural components. Significant pores (the dark area highlighted by a circle) can be seen in the image of the coating cross section (Figure 4b,d). The border between the coating and the base has a characteristic zigzag shape. The structure consists of small particles and several large flat spots with periodic observations of the morphology of terraces in certain areas (Figure 4a,c), the light gray area indicates mainly the Ti_3SiC_2 phase, highlighted by a rectangle, and the friable and dark gray area indicates the TiC phase. Dark areas have large volume fractions in the coatings. The surface roughness of coatings Ti–Si–C (Ra) comprises 2.5–2.65 μm.

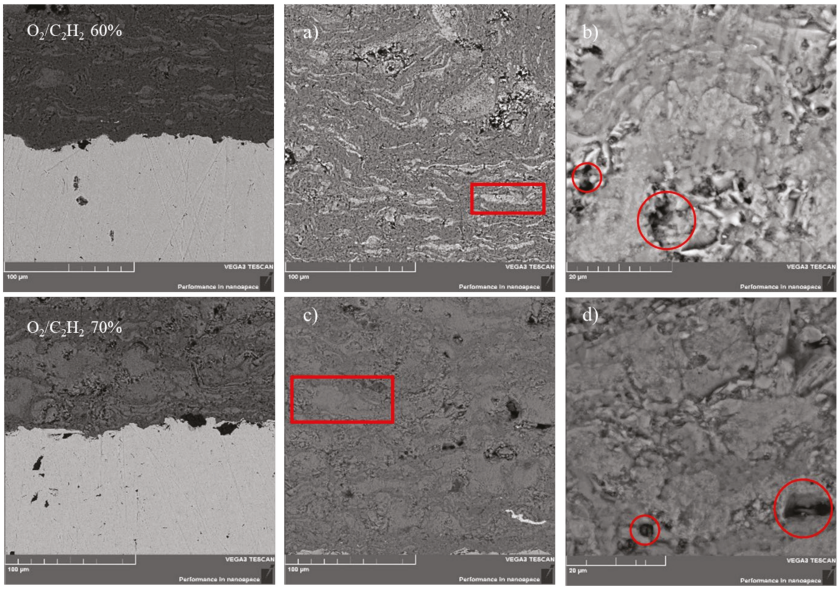

Figure 4. SEM images of the morphology of coating cross section: (**a**) Ti–Si–C $_{60\%}$ while 100 μm; (**b**) Ti–Si–C $_{60\%}$ while 20 μm; (**c**) Ti–Si–C $_{70\%}$ while 100 μm; (**d**) Ti–Si–C $_{70\%}$ while 20 μm.

One of the main factors determining the coating quality was adhesion. Figure 5 shows the adhesive strength testing results of scratch testing. The moment of coating adhesive or cohesive failure was fixed visually after testing using an optical microscope with a digital camera, also by changing two parameters: acoustic emission and friction force. It should be noted that not all recorded events associated with the destruction of the coating describe the actual adhesion of the coating to the substrate. Various registration parameters during testing processes allowed fixing different coating failure stages; so, L_{c1} means the moment of appearance of the first crack, L_{c2} the peeling of coating areas, and L_{c3} the plastic abrasion of the coating to the substrate [32]. According to the type of change in the acoustic emission (AE) amplitude, it was possible to judge the crack formation intensities and their development in the sample during scratching. The Ti–Si–C system coatings that occurred during the explosive gas mixture filling volumes of 50% and 60% were visible, the first crack was formed at a load of L_{c1} = 12 N. Then the process continued in a certain cycle. A corresponding peak of acoustic emission accompanied each crack formation (Figure 5a,b). Partial abrasion of the coating to the substrate was judged by a sharp change in the friction force growth intensity. This occurred at a load of L_{c3} = 29 N, which was also confirmed by visual observation, noting a change in the color of the sample material at the bottom of the scratch (Figure 5a,b). The L_{c3} value indicated a high adhesive strength of coating adhesion to the substrate.

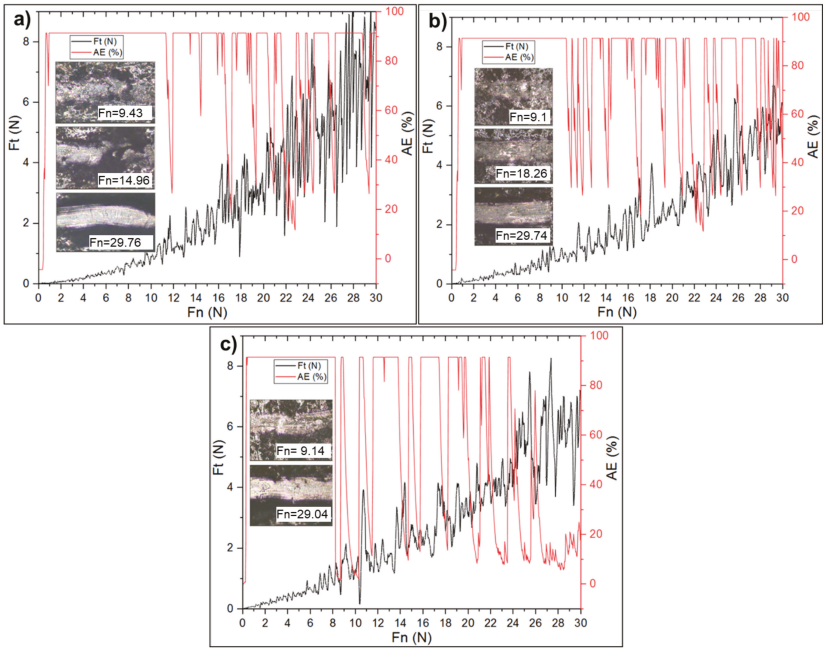

Figure 5. Results of the scratch test of Ti–Si–C coatings obtained at different filling volumes of the explosive gas mixture of the detonation gun barrel: (**a**) 50%, (**b**) 60%, and (**c**) 70%.

The Ti–Si–C system coating obtained at the explosive gas mixture filling volume of 70% shows appearance cracks (Figure 4c) observed at L_{c1} = 8 N load. According to adhesion tests, it can be argued that the cohesive destruction of the sample coating occurred at 8 N, and its adhesive destruction at 29 N. The Ti–C system has a higher stiffness, so it is natural to expect minimal elastic and intense plastic deformation during the adhesion test [33].

For coatings of this functional purpose, wear resistance is one of the most important exploitation properties, which is reflected both in the capacity of structures as a whole and in the conservation of the geometric dimensions of individual parts. The results of coating tribological tests showed that the filling volume of the explosive mixture and the coating structures had a significant impact on the value of the friction coefficient of the coating surface and wear resistance. Therefore, in the case of composite coatings Ti–Si–C obtained with the filling volumes of the explosive mixture at 50% and 60% in the detonation gun barrel, the friction coefficient at the initial stage of testing to 18.40 and 25.10, respectively, was 0.15–0.20 μ and slightly increased; subsequently the friction coefficient increased monotonously from 0.25 to 0.60 μ (Figure 6). The obtained coating Ti–Si–C system's friction coefficient at a filling volume of 70% was 0.60 μ. According to the XRD analysis results, the increasing wear resistance of the Ti–Si–C system coatings with detonation barrel filling volumes of 50% and 60% was related to a larger proportion of the Ti_3SiC_2 phase.

With the profilometer were taken images of the wear track of the studied samples (Figure 6). Assessing the samples' wear resistance based on the wear tracks' geometric parameters illustrated that the depth of the sample track at 70% of the explosive mixture's filling volume was significantly greater when compared with others. The detonation coatings based on titanium carbolized were characterized by high wear resistance.

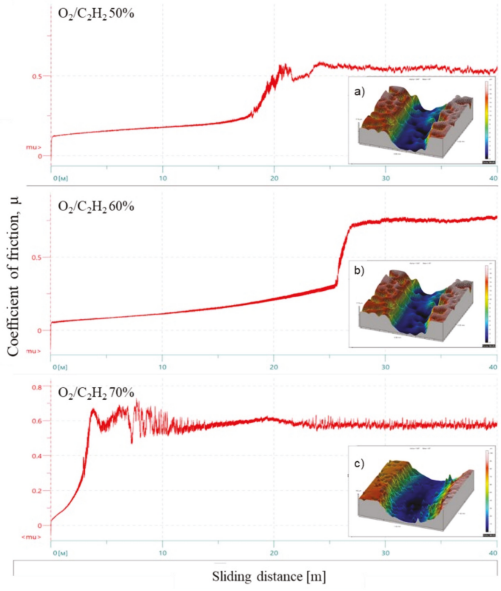

Figure 6. Tribological tests results of Ti–Si–C coatings obtained at different filling volumes of the explosive gas mixture of the detonation gun barrel and track profiles: (**a**) 50%; (**b**) 60%; (**c**) 70%

The study results of the mechanical characteristics of the obtained coatings were carried out by the Oliver–Pharr method, and typical dynamic loading–unloading diagrams are shown in Figure 7. From the analysis of the loading and unloading curves, it can be seen that the penetration depth of the nano-indenter in the cases of explosive gas mixture filling volumes of 50% and 60% was less than in the case of 70% filling volume. According to the analysis of the indentation curves, it can be concluded that the elastic stiffness of the coatings during 70% filling was higher (Figure 7b) when compared to the rest (Figure 7a,b). According to the XRD analysis results, when the filling volume of the explosive mixture in the detonation gun barrel increased to 70% a coating was formed with a high content of the TiC phase. Thus, the results of nano-indentation and scratch testing were in good agreement and confirmed the formation of TiC, which had a higher stiffness compared to Ti_3SiC_2.

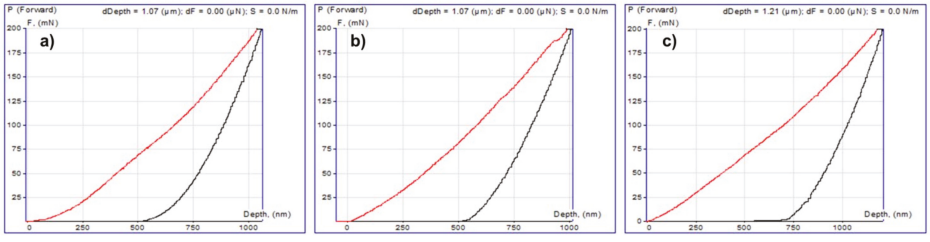

Figure 7. Loading–unloading curves for Ti–Si–C coatings obtained at a different explosive gas mixture filling volumes of the detonation gun barrel: (**a**) 50%; (**b**) 60%; (**c**) 70%.

The values of hardness and modulus of elasticity of the research samples obtained from the loading–unloading curve analysis are shown in Table 1. As visible from Table 1, coatings with a high content of Ti_3SiC_2 had higher hardness values compared to the coating with the prevailing TiC phase.

Table 1. Results of nano-indentation.

Coating	Filling Volume, %	HIT, GPa	Eeff, GPa
Ti–Si–C	50	10.07 ± 1.63	242.36 ± 51.61
	60	10.01 ± 2.31	235.96 ± 44.05
	70	7.51 ± 0.50	198.99 ± 17.70

The detonation spraying process is characterized by a significant number of technological parameters. The complexity and insufficient study of the phenomena underlying it makes it very difficult to trace the relationship of individual parameters to determine the process optimal modes, using one-factor experiments. Therefore, experimental and statistical methods of regressive analysis and the theory of experiment planning are used when optimizing the process. Abrasive and impact-abrasive wear are two of the main factors that limit working parts, machines, and equipment components for various purposes. To assess the resistance of Ti–Si–C coatings to abrasion and impact-abrasive wear, tests were carried out on special stands. Table 2 shows the test results of the abrasive and impact-abrasive wear. The coated samples' mass loss was less than that of the original sample, which indicates an increased resistance to impact and abrasive wear. This is due to the presence of a larger proportion of the hardening carbide phase TiC in the Ti_3SiC_2 coating. This is due to an increase of the strengthening phase TiC in the composition of the protective coating. There is a significant increase in internal stresses and a decrease in the amount of the more plastic phase, which ultimately decreases toughness.

Table 2. Abrasive and impact-abrasive wear test results.

No	Samples Name	Filling Volume, %	Mass Loss, g (Abrasive Wear)	Wear Coefficient, K (Abrasive Wear)	Weight Loss, g (Impact and Abrasive Wear)	Wear Coefficient, K (Impact and Abrasive Wear)
1	Steel 45	-	0.0302	1	0.0508	1
2	Sample without coating	-	0.0265	1.14 ± 0.14	0.0475	1.07 ± 0.13
3	Ti_3SiC_2 coating	50	0.0192	1.57 ± 0.19	0.0399	1.3 ± 0.16
4	Ti_3SiC_2 coating	60	0.0122	2.47 ± 0.3	0.0336	1.51 ± 0.18
5	Ti_3SiC_2 coating	70	0.0203	1.48 ± 0.18	0.04	1.27 ± 0.15

According to the determination results of the samples' mass loss after testing wear on the fixed abrasive (Figure 2), the greatest strength was found in a coating obtained by the 60% (0.0122 g) filling volume of the detonation gun barrel and the smallest was in the filling volume of 70% (0.0203 g), the wear resistance of all coatings was higher than the initial sample (0.0265 g). The detonation coatings based on titanium carbolized were characterized by high wear resistance.

Thus, in this work, we made the effort to obtain composite coatings based on Ti–Si–C with the Ti_3SiC_2 phase by detonation spraying. The analysis of the obtained experimental results indicated that the phase composition and properties of detonation coatings strongly depend on the technological parameters of spraying. With an increase of explosive gas mixture in the filling volume of the detonation barrel up to 70% of the coatings consisted mainly of TiC phases, since high temperature leads to a strong decomposition of Ti_3SiC_2 powders [34]. Consequently, the successful production of high-purity MAX-phase coatings by detonation spraying was not reported. Based on the analysis of literature sources [35,36] and preliminary studies, it was suggested that if gas–thermal deposition of substances of the Ti–Si–C system is carried out, it would be possible to obtain a multiphase coating containing such phases as carbides, silicides, and carbosilicides of titanium, and during subsequent heat treatment–regulation of its phase composition. Thermal annealing was performed in the temperature range 700–900 °C for 1 h.

The Vickers hardness of Ti–Si–C composite coatings before and after annealing is shown in Figure 8. The hardness of the composite coating increased significantly with increasing the annealing temperature: at T = 700 °C, the microhardness was 1150 HV; at T = 800 °C, the microhardness was 1400 HV; and at T = 900 °C, the microhardness decreased to 850 HV.

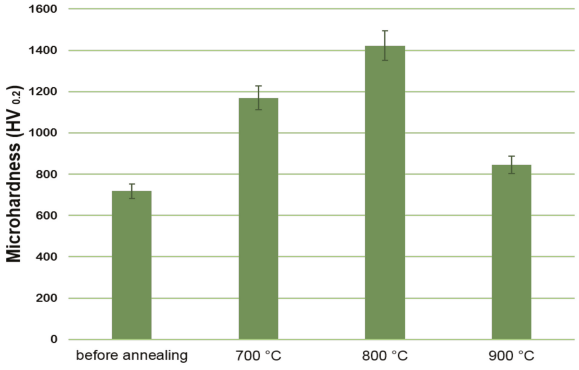

Figure 8. Effect of annealing temperature on the microhardness of coatings based on Ti–Si–C.

Aiming to identify the cause of the change in microhardness, we performed XRD analysis of coatings before and after annealing. The results of XRD analysis of coatings showed (Figure 9) that the coating before annealing consisted of TiC and Ti_3SiC_2 phases.

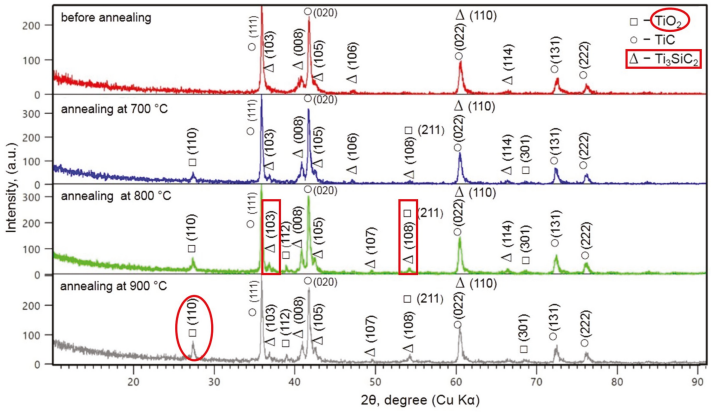

Figure 9. Diffractograms of Ti–Si–C coatings at different annealing temperatures.

After annealing, the formation of TiO_2 phases and an increase in the reflex intensities (103) and (108) of Ti_3SiC_2 phases were observed. Compared to the after-sprayed coatings, the phase fraction of the Ti_3SiC_2 phase in the after-annealing coatings increased significantly. A change in the fraction of phases indicated a solid-phase transformation during thermal activation. An increase in the TiO_2 line intensity was observed after annealing at T = 900 °C, which indicated an increase in the thickness of the oxide layer. The increase in microhardness after annealing was associated with an increase in the content of Ti_3SiC_2 phases in coatings. At the same time, after annealing at T = 900 °C, the decrease in microhardness was insignificant due to an increase in the oxide layer's thickness. After annealing at 800 °C, an increase in the Ti_3SiC_2 line intensity indicated an increase in the symmetric movements of C atoms in the Ti_3SiC_2 molecule. This means that subsequent heat treatment

provided sufficient reaction time for an incomplete reaction of the Ti–Si–C (TSC) coating during detonation spraying.

The microstructure of Ti–Si–C_{800} consisted of a titanium-rich region (light region) and a TiC_x region diluted by Si (light gray regions). Heat treatment can lead to the diffusion of C and Si atoms [37]. Thus, annealing can provide a more homogeneous distribution of atoms in coatings after annealing. This can be verified by displaying the Ti–Si–C and Ti–Si–C_{800} elements in Figure 10. As shown in Figure 10, the Ti, C, and Si maps show separate rich and scarce areas. Moreover, the C and Si atoms have a similar distribution in most regions of the element map. The red color on the Ti map corresponds to the dark zones of C deficiency and Si deficiency on the C and Si maps, respectively, identified as the Ti phase (C, Si). After annealing at 800 °C, the three elements showed a more homogeneous distribution (Figure 11). This means that the high temperature provided a more intense diffusion of C and Si atoms.

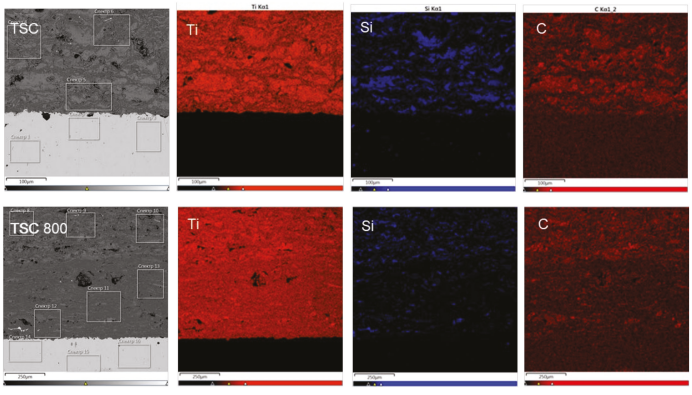

Figure 10. The microstructure of the cross section of coatings with a color images of energy-dispersive spectrometer (EDS) mapping and the result of analysis after annealing at 800 °C.

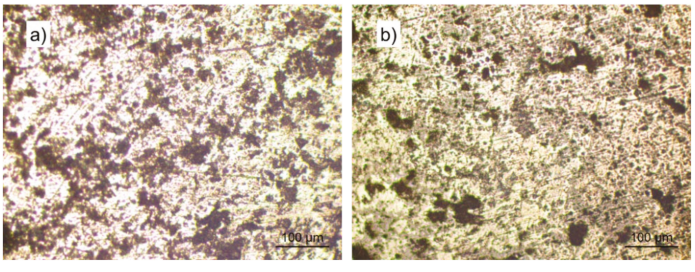

Figure 11. The coatings' surface morphology before (**a**) and after (**b**) annealing at 800 °C.

The results of tribological testing of coatings showed that the temperature of thermal annealing and the structure of the coatings themselves had a significant impact on the coefficient of friction of the coating surface and wear resistance. So, in the case of composite Ti–Si–C coatings, the friction coefficient was 0.65–0.70 before annealing. After thermal exposure at temperatures up to 800 °C, the friction coefficient at the initial stage of testing (up to 12.40 m) was 0.30–0.35 and a slight increase occurred, at which the friction coefficient increased monotonically from 0.35 to 0.70 as in the case before annealing (Figure 12). According to the results of the X-ray phase analysis, an increase in the wear resistance of the surface layers of the Ti–Si–C composite material after 800 °C was associated with the formation of TiO_2 and the presence of a larger fraction of the TiC carbide hardening phase (Figure 9). In [38,39], it was shown that an oxide compound based on TiO_2 increases

the wear resistance and strength of materials. Detonation coatings based on titanium carbosilicide are characterized by high wear resistance.

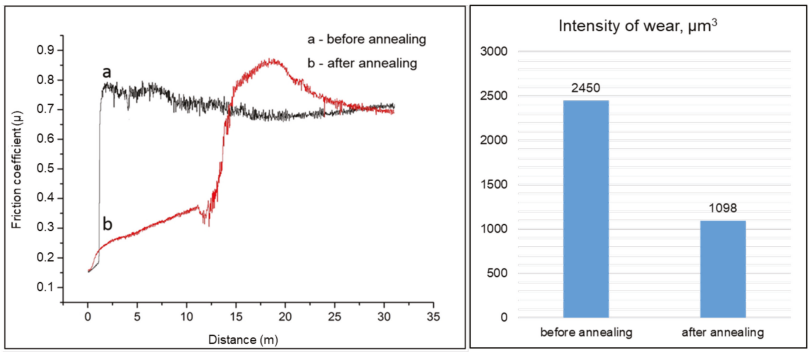

Figure 12. Results of tribological experiments of Ti–Si–C coatings before and after annealing at 800 °C.

4. Conclusions

The paper described an experimental study of the effect of the detonation gas filling mode on the phase composition and strength characteristics of the Ti–Si–C coatings system. It was shown that the phase composition of detonation coatings can be significantly changed relative to the phase composition of the initial powders, depending on the filling volume of the detonation barrel with an explosive acetylene–oxygen mixture. When the filling volume of the detonation barrel with an explosive mixture increases to 70%, the coatings consist mainly of TiC phases. The Ti_3SiC_2 powder partially decomposes into TiC due to the high-speed shock interaction of high temperatures in the detonation wave flow. The X-ray phase analysis results showed that when filling the barrel with explosive mixture to 50% and 60%, a low degree of Ti_3SiC_2 decomposition can be achieved, the coatings consist mainly of Ti_3SiC_2 phases with small TiC content. With an increase in the detonation barrel's filling volume of the explosive acetylene–oxygen mixture, the heating temperature of the sprayed powder increases. High temperature contributes to the decomposition of Ti_3SiC_2 powder into TiC. Thus, the XRD results confirmed that when the explosive gas mixture filling volume is 70%, partial decomposition and disintegration of the powders occur after detonation spraying. It is established that detonation coatings based on titanium carbosilicide obtained at the explosive gas mixture filling volume of 60% are characterized by high wear resistance and adhesive strength.

Thermal annealing was performed after spraying in the temperature range of 700–900 °C for 1 h to reduce microstructural defects and improve the Ti–Si–C coating characteristics. As a result of heat treatment in the Ti–Si–C system at 800 °C, an increase in the volume fraction of the Ti_3SiC_2 and TiO_2 phases leading to a 2-fold increase in microhardness was observed. This means that the after-heat-treatment can provide a sufficient reaction time for the incomplete reaction of the Ti–Si–C (TSC) coating during the detonation gun spraying. Thus, annealing can provide an equal distribution of elements in the coatings.

Author Contributions: B.R., Z.S., M.A. and D.B. designed the experiments; B.S. and D.B. performed the experiments; B.R., Z.S. and S.K. analyzed the data; B.R., Z.S. and D.B. wrote, reviewed and edited the paper. All authors have read and agreed to the published version of the manuscript.

Funding: The article uses the results obtained with the support of grant funding of the Ministry of Education and Science of the Republic of Kazakhstan, grant AR08957719.

Institutional Review Board Statement: Not applicable.

Informed Consent Statement: Not applicable.

Data Availability Statement: The data presented in this study are available in the article.

Conflicts of Interest: The authors declare that there is no conflict of interest regarding the publication of this manuscript.

References

1. Benamor, A.; Hadji, Y.; Chiker, N.; Haddad, A.; Guedouar, B.; Labaiz, M.; Hakem, M.; Tricoteaux, A.; Nivot, C.; Erauw, J.P.; et al. Spark Plasma Sintering and tribological behavior of Ti_3SiC_2-Ti_5Si_3-TiC composites. *Ceram. Int.* **2019**, *45*, 21781–21792. [CrossRef]
2. Shi, Q.; Zhu, H.; Li, C. The Effects of the Addition of Ti_3SiC_2 on the Microstructure and Properties of Laser Cladding Composite Coatings. *Coatings* **2020**, *10*, 498. [CrossRef]
3. Wang, J.; Luo, X.; Sun, Y. Torsional Fretting Wear Properties of Thermal Oxidation-Treated Ti_3SiC_2 Coatings. *Coatings* **2018**, *8*, 324. [CrossRef]
4. Xu, J.; Liu, L.L.; Jiang, L.; Munroe, P.; Xie, Z.H. Unraveling the mechanical and tribological properties of a novel Ti_5Si_3/TiC nanocomposite coating synthesized by a double glow discharge plasma technique. *Ceram. Int.* **2013**, *39*, 9471–9481. [CrossRef]
5. Barsoum, W. The Mn+1AXn: A new Class of Solids: Thermodynamically Stable Nanolaminates. *Prog. Solid State Chem.* **2000**, *28*, 201–281. [CrossRef]
6. Kisi, E.H.; Crossley, A.A. Structure and crystal chemistry of Ti_3SiC_2. *J. Phys. Chem. Solids* **1998**, *59*, 1437–1443. [CrossRef]
7. Islak, B.Y.; Ayas, E. Evaluation of properties of spark plasma sintered Ti_3SiC_2 and Ti_3SiC_2/SiC composites. *Ceram. Int.* **2019**, *45*, 12297–12306. [CrossRef]
8. Ulianitsky, V.; Shtertser, A.; Zlobin, S.; Smurov, I. Computer-controlled detonation spraying: From process fundamentals toward advanced applications. *J. Therm. Spray Technol.* **2011**, *20*, 791–801. [CrossRef]
9. Ulianitsky, V.; Batraev, I.; Dudina, D.; Smurov, I. Enhancing the properties of WC/Co detonation coatings using two-component fuels. *Surf. Coat. Technol.* **2017**, *318*, 244–249. [CrossRef]
10. Jonda, E.; Łatka, L.; Pakieła, W. Microstructure and Selected Properties of Cr_3C_2–NiCr Coatings Obtained by HVOF on Magnesium Alloy Substrates. *Materials* **2020**, *13*, 2775. [CrossRef]
11. Giovanni, B.; Alberto, C.; Luca, L.; Pietro, P.; Rinaldo, R.; Paolo, S.; Veronica, T. Properties of HVOF-sprayed TiC-FeCrAl coatings. *Wear* **2019**, *418–419*, 36–51.
12. Ulianitskiy, V.Y.; Nenashev, M.V.; Kalashnikov, V.V.; Ibatullin, I.D.; Ganigin, S.Y.; Yakunin, K.P.; Rogozhin, P.V.; Shtertser, A.A. Opyt issledovaniya i primeneniya tekhnologii naneseniya detonatsionnykh pokrytiy. *Izvestiya Samarskogo Nauchnogo Tsentra Rossiyskoy Akademii Nauk* **2010**, *12*, 569–575. (In Russian)
13. Batrayev, I.S.; Prokhorov, E.S.; Ulianitskiy, V.Y. Razgon i nagrev poroshkovykh chastits produktami gazovoy detonatsii v kanalakh s konicheskim perekhodom. *Fizika Goreniya Vzryva* **2014**, *3*, 78–86. (In Russian)
14. Dudina, D.V.; Batraev, I.S.; Ulianitsky, V.Y.; Korchagin, M.A. Possibilities of the computer-controlled detonation spraying method: A chemistry viewpoint. *Ceram. Int.* **2014**, *40*, 3253–3260. [CrossRef]
15. Ulianitsky, V.Y.; Batraev, I.S.; Shtertser, A.A.; Dudina, D.V.; Bulina, N.V.; Smurov, I. Detonation spraying behaviour of refractory metals: Case studies for Mo and Tabased powders. *Adv. Powder Technol.* **2018**, *29*, 1859–1864. [CrossRef]
16. *ASTM G133-95, Standard Test Method for Linearly Reciprocating Ball-on-Flat Sliding Wear*; ASTM International: West Conshohocken, PA, USA, 1995. Available online: http://www.astm.org/cgi-bin/resolver.cgi?G133-95 (accessed on 21 January 2021).
17. *ASTM G99-05, Standard Test Method for Wear Testing with a Pin-on-Disk Apparatus*; ASTM International: West Conshohocken, PA, USA, 2005. Available online: http://www.astm.org/cgi-bin/resolver.cgi?G99-05 (accessed on 21 January 2021).
18. Zhurerova, L.G.; Rakhadilov, B.K.; Popova, N.A.; Kylyshkanov, M.K.; Buraniche, V.V.; Pogrebnjak, A.D. Effect of the PEN/C surface layer modification on the microstructure, mechanical and tribological properties of the 30CrMnSiA mild-carbon steel. *J. Mater. Res. Technol.* **2020**, 78–85. [CrossRef]
19. GOST 23.208-79 Ensuring of Wear Resistance of Products. Wear Resistance Testing of Materials by Friction against Loosely Fixed Abrasive Particles. GOST No. 23.208-79 from 29 November 1979. Available online: http://vsegost.com/Catalog/40/4066.shtml (accessed on 21 January 2021).
20. GOST 23.207-79 Ensuring of Wear Resistance of Products. Testing of Engineering Materials for Impact Abrasive Wear. GOST No 23.207-79 from 26 November 1979. Available online: http://vsegost.com/Catalog/43/4374.shtml (accessed on 21 January 2021).
21. GOST 9450-76 Measurements Microhardness by Diamond Instruments Indentation. GOST No 9450-76 from 9 January 1976. Available online: http://vsegost.com/Catalog/34/34277.shtml (accessed on 21 January 2021).
22. Rakhadilov, B.K.; Buitkenov, D.B.; Tuyakbaev, B.T.; Sagdoldina, Z.B.; Kenesbekov, A.B. Structure and properties of detonation coatings based on titanium carbosilicide. In *Key Engineering Materials*; Trans Tech Publications Ltd.: Baech, Switzerland, 2019; pp. 301–306.
23. Buitkenov, D.; Rakhadilov, B.; Erbolatuly, D.; Sagdoldina, Z. Influence of Heat Treatment on the Phase Composition and Microhardness of Coatings Based on Ti_3SiC_2/TiC. In *Key Engineering Materials*; Trans Tech Publications Ltd.: Baech, Switzerland, 2020; Volume 839, pp. 137–143.
24. Sun, Z.M. Progress in research and development on MAX phases: A family of layered ternary compounds. *Int. Mater. Rev.* **2011**, *56*, 143–166. [CrossRef]
25. Sonested, M.; Frodelius, J.; Palmquist, J.P.; Högberg, H.; Hultman, L.; Stiller, K. Microstructure of high velocity oxy-fuel sprayed Ti_2AlC coatings. *J. Mater. Sci.* **2010**, *45*, 2760–2769. [CrossRef]

26. Trache, R.; Puschmann, R.; Leyens, C.; Berger, L.M.; Matthey, B.; Herrmann, M. Thermally sprayed Ti_3SiC_2 and Ti_2AlC MAX-phase coatings. In *Thermal Spray 2013, Proceedings of the International Thermal Spray Conference, Busan, Korea, 13–15 May 2013*; ASM International: Materials Park, OH, USA, 2013; pp. 74–78.
27. Barsoum, M.W.; El-Raghy, T.; Rawn, C.J.; Porter, W.D.; Wang, H.; Payzant, E.A.; Hubbard, C.R. Thermal properties of Ti_3SiC_2. *J. Phys. Chem. Solids* **1999**, *60*, 429–439. [CrossRef]
28. Zhou, Y.; Gu, W. Chemical reaction and stability of Ti_3SiC_2 in Cu during high-temperature processing of Cu/Ti_3SiC_2 composites. *Z. Met.* **2004**, *95*, 50–56. [CrossRef]
29. Wang, L.; Jiang, W.; Qin, C.; Chen, L. Effect of starting SiC particle size on in situ fabrication of Ti_5Si_3/TiC composites. *Mater. Sci. Eng.* **2006**, *425*, 219–224. [CrossRef]
30. Wang, L.; Jiang, W.; Chen, L.; Bai, G. Microstructure of Ti_5Si_3-TiC-Ti_3SiC_2 and Ti_5Si_3-TiC nanocomposites in situ synthesized by spark plasma sinterin. *J. Mater. Res.* **2004**, *19*, 3004–3008. [CrossRef]
31. Qi, F.; Shi, G.; Xu, K. Microstructure and mechanical properties of hot pressed Ti_3SiC_2/Al_2O_3. *Ceram. Int.* **2019**, *45*, 11099–11104. [CrossRef]
32. Shtansky, D.V.; Petrzhik, M.I.; Bashkova, I.A.; Kiryukhantsev-Korneev, F.V.; Sheveiko, A.N.; Levashov, E.A. Adhesion friction and deformation characteristics of Ti-(Ca, Zr)-(C, N, O, P) coatings for orthopedic and dental implants. *Solid State Phys.* **2006**, *48*, 1231–1238. [CrossRef]
33. Andrievskii, R.A.; Spivak, I.I. *Strength of Refractory Compounds and Materials Based on Them*; Guide; Metallurgy: Moscow, Russia, 1989; 368p.
34. Buitkenov, D.B.; Rakhadilov, B.K.; Wieleba, W.; Kylyshkanov, M.K.; Yerbolatuly, D. Impact of the detonation gas spraying mode on the phase composition and adhesional strength of Ti-Si-C coatings. *Bull. Univ. Karaganda Phys.* **2020**, *1*, 59–64.
35. Chen, H.; Du, Y.; Wang, D.; Zhang, C. TiC/Ti_3AlC_2-Co plasma-sprayed coatings with excellent high-temperature tribological properties. *Ceram. Int.* **2018**, *44*, 22520–22528. [CrossRef]
36. Barsoum, M.W.; El-Raghy, T.; Radovic, M. Ti_3SiC_2: A layered machinable ductile carbide. *Interceram* **2000**, *49*, 226–233.
37. Li, C.; Yan, S.; Zhang, F.; He, J. Fabrication and characterization of micro-laminated TiC-Ti_5Si_3-Ti_3SiC_2 composite coatings by atmosphere plasma spraying. *Vacuum* **2019**, *161*, 14–20. [CrossRef]
38. Patnaik, A.; Bhatt, A.D.; Siddhartha. Mechanical and dry sliding wear characterization of epoxy–TiO_2 particulate filled functionally graded composites materials using Taguchi design of experiment. *Mater. Des.* **2011**, *32*, 615–627.
39. Caravaca, M.A.; Kosteski, L.E.; Mino, J.C.; D'Ambra, R.B.; Uberti, B.; Casali, R.A. Model for Vickers microhardness prediction applied to SnO_2 and TiO_2 in the normal and high-pressure phases. *J. Eur. Ceram. Soc.* **2014**, *34*, 3791–3800. [CrossRef]

coatings

MDPI

Article

Tribocorrosion Performance of Cr/CrN Hybrid Layer as a Coating for Machine Components Used in a Chloride Ions Environment

Marcin Kowalski [1,*] and Arkadiusz Stachowiak [2]

[1] Faculty of Civil Engineering, Mechanics and Petrochemistry, Warsaw University of Technology, 09-400 Plock, Poland
[2] Institute of Mechanics and Motor Vehicles, Poznan University of Technology, 60-965 Poznan, Poland; arkadiusz.stachowiak@put.poznan.pl
* Correspondence: kofski@wp.pl

Abstract: The aim of the article was to identify the effect of material hardness on the tribocorrosion process by comparing two material solutions. The analysis concerned the assessment of the process intensity and the identification of the mechanisms responsible for material loss. Possible mechanisms of tribocorrosion common for materials of high hardness were determined. Two classic material solutions (based on AISI 1045 steel) ensuring high hardness of the subsurface layers were tested: nitriding with an additional oxidation and impregnation process, and Physical Vapour Deposition (PVD) coating. In order to better identify the impact of hardness on the tribocorrosion process in each individual test, the pressures in the contact zone were increased. The tribocorrosion tests were carried out in 3.5% NaCl with free corrosion potential (OCP) for the ball-on-plate system. The results of the tribocorrosion tests presented in the article indicate that the synergy effect of friction and corrosion can be generated by the same mechanisms of material removal in both the material solutions tested. The intensity of these mechanisms is determined by material hardness. The likely mechanism of generating the synergy effect may be related to the formation of local pits along the friction path. The corrosion processes that are initiated by the cracking of the hard surface layer create local cavities, which most probably intensify frictional wear in successive time intervals. The area around the cavities facilitates plastic deformation, the initiation of cracking of the cyclically deformed layer and the tearing of larger pieces of material (especially at higher unit pressures in the frictional contact zone).

Keywords: tribocorrosion; PVD; Cr/CrN; wear mechanics

Citation: Kowalski, M.; Stachowiak, A. Tribocorrosion Performance of Cr/CrN Hybrid Layer as a Coating for Machine Components Used in a Chloride Ions Environment. *Coatings* **2021**, *11* , 242 . https://doi.org/10.3390/coatings11020242

Academic Editor: Philipp Vladimirovich Kiryukhantsev-Korneev
Received: 21 December 2020
Accepted: 1 February 2021
Published: 18 February 2021

1. Introduction

Many sliding nodes in devices operating in a seawater environment (e.g., on oil rigs) are exposed to damage caused by tribocorrosion. The loss of material caused by the combined impact of friction and corrosion can be a significant operational problem. One way to eliminate this problem and to extend the durability of the equipment is the use of high hardness materials. High hardness of the surface layer ensures adequate resistance to mechanical stress as well as friction damage. The higher durability of the surface layer should also reduce the material loss caused by the corrosive nature of seawater. The most intense corrosive interactions resulting from mechanical forces are initiated on the freshly exposed surface of the material.

In the article, two classic material solutions (based on AISI 1045 steel) ensuring high hardness of the subsurface layers were selected for an analysis of the tribocorrosion process: nitriding with an additional oxidation and impregnation process, and the application of a physical vapour deposition (PVD) coating. The selected materials are the result of a search for solutions to be used for elements operating at high pressures in the seawater

environment (e.g., actuator pistons on drilling platforms). Classical material solutions were selected because the purpose of the research analyses was an attempt to identify some common features of the tribocorrosion process in the group of materials with high hardness.

Material hardness may be a major factor in tribocorrosion. Many analytical models used to predict tribocorrosion use material hardness as a determinant of the intensity of material loss [1,2]. Material hardness has both mechanical and corrosion-related effects. Material loss caused by friction occurs at the points of actual contact and to a smaller material loss caused by friction. The corrosive processes are initiated on a surface previously exposed by mechanical separation of the material [3,4]. The material hardness therefore affects the intensity of the electromechanical impact as well. The higher the hardness, the higher the resistance of the material to wear caused by friction. However, this does not always mean higher resistance to tribocorrosion [5]. It is often the case that a technological process used to make a material harder will reduce the resistance of the material to corrosion.

Physical vapour deposition (PVD) coatings are widely used on many machine parts and tools to produce surface with anticorrosion and antiwear properties [6–12]. The coating lifetime depends not only on the properties of the base material from which they are produced, but also on the substrate surface properties. Therefore, the benefits of using modern PVD coatings are undisputed. By increasing the hardness of their surfaces and their resistance to corrosion, the parts of machines and tools covered with PVD coatings show lower wear, good adhesion and high hardness [13].

The CrN layer produced by using the PVD method has a better corrosion resistance than the TiN/TiAlN layers. Researchers [14] have found that the corrosion resistance in a 3% NaCl solution of AISI 304 steel coated with TiN, TiAlN and CrN is the highest for CrN coating, and the lowest for TiN. Su et al. [15] compared CrN and TiN layers fabricated by using the PVD method on tools and parts of machines and found a significantly higher resistance to wear due to friction on CrN coatings in comparison to TiN coatings.

The CrN coating is quite frequently used as protection against mechanical and corrosive wear in the manufacture of machine parts (especially sliding nodes) and tools. One of the more commonly used methods of applying CrN coatings is the PVD method. Recently, tribocorrosion tests of CrN coatings created by using the PVD method in the chloride ion environment have been carried out. The tribocorrosion performance shows significant resistance to wear and corrosion [16–19].

The production of duplex and hybrid layers in combined heat and chemical treatments with PVD methods is currently widely used. As has been mentioned above, the synergy effect of the hybrid layer, resulting from the combination of two individual processes makes it possible to obtain excellent performance that would otherwise be impossible to achieve in separate processes [20]. Individual component layers of the tested hybrid Cr/CrN coating were fabricated using the PVD method. Bayon et al. [21] investigated this type of hybrid coating. The research examined the tribocorrosion behavior of multilayer coatings with different structures by instantaneous deviations measurements of standard potential under friction conditions. Tribocorrosion tests were performed in a chloride ions environment. The studies found that the wear rate has a significant effect on the tribocorrosion performance and that the tribocorrosion wear occurs as a result of the damage and removal of the surface layer and the substrate material exposure to the corrosive medium.

The excellent resistance to mechanical wear and very good corrosion resistance of hybrid Cr/CrN coatings were confirmed in subsequent studies [6,22]. The hybrid layers, manufactured by using the PVD process, widely used to increase the anticorrosive and mechanical properties of the surfaces of machines and tools, present a synergy effect [13,20]. The tests confirm the excellent resistance to mechanical wear and corrosion of a hybrid coating Cr/CrN in a chlorine environment [6,21,23].

In addition, a controlled gas nitriding process with subsequent oxidation and an impregnation process increases the tribocorrosion performance of material in a 3.5% NaCl

environment [24]. This might be used for many parts of machines and equipment exposed to tribocorrosion wear [25].

The article presents an assessment of resistance to tribocorrosion for selected materials of high hardness in a seawater environment. The tribocorrosion process was comparatively analyzed for two material solutions of different hardness rates at increasing pressures. In individual tests, the mechanical forces were differentiated in order to better identify the impact of hardness on the process of material removal.

The main goals of the research are as follows:

- A comparative assessment of resistance to tribocorrosion in 3.5% NaCl of the analyzed material solutions;
- The identification and quantitative evaluation of the synergy of friction and corrosion in the total material loss;
- The identification of the probable mechanism of the friction–corrosion synergy effect under tribocorrosion conditions.

The authors of this article assume that it is possible to identify a likely shared mechanism creating a synergy of friction and corrosion for high-hardness materials. However, the analysis is based on two different material solutions only.

2. Materials and Methods

2.1. Coatings and Identification Methods

The gas nitrided with subsequent oxidation and impregnation and the Cr/CrN hybrid coatings were formed on samples made from medium carbon steel AISI 1045 containing 0.45% C, 0.65% Mn and 0.25% Si. The formation process of the Cr/CrN coating was carried out by means of the arc-evaporation method (Arc-PVD). The device (Metaplas Ionon, Radom, Poland) was equipped with three arc sources, a substrate polarization system, the substrate temperature and operating gases monitoring systems. Pure chromium cathodes were used as the source of arc for the formation of Cr/CrN hybrid coatings. Disk-shaped samples of substrate sheets 10 mm in diameter and 6 mm thick were selected for the tests. The samples were mechanically polished to obtain a roughness parameter *R*a = 0.03 μm before the coating deposition process was initiated. Before the samples were placed in the device chamber and the hybrid surface treatment was carried out, a chemical washing process in an ultrasonic cleaner had been applied. They were skimmed at UMO-50-100 station (Radom, Poland) by using TRI and ethyl alcohol and dried thoroughly, according to the parameters given in Table 1.

Table 1. The cleaning process parameters of AISI 1045 samples made in ultrasonic cleaner.

Stage Number	Stage Name	Stage Parameters
1	submerged cleaning	time: 8 min, temperature 85 °C
2	submerged cleaning	time: 8 min, temperature 50 °C, ultrasounds
3	submerged cleaning	time: 8 min, temperature 85 °C
4	vapor cleaning	time: 8 min

Prior to the start of each process, the samples had been preheated in a vacuum chamber using resistance heaters. The preheating temperature was approx. 300 °C with a pressure of 5.0×10^{-5} mbar. The process of deposition of the Cr/CrN hybrid coating was launched by the deposition of a thin coating of chromium with a thickness below 1 μm. Then, a chromium nitride coating was produced. Table 2 summarizes the technological parameters of the Cr/CrN coating build-up process.

Table 2. Parameters of Cr/CrN metallic coating deposition process.

Type of Process	Pressure (mbar)	Temperature (°C)	Polarization Voltage U_{bias} (V)	Process Time (min)	Atmosphere
heating	$<1 \times 10^{-5}$	300	–	30	–
etching by Ar ions	5×10^{-3}	300	−300	25	100% Ar
etching by Cr ions	5×10^{-3}	400	−300	15	100% Ar
Cr deposition	5×10^{-3}	400	−50	5	100% Ar
CrN deposition	3.5×10^{-3}	380	−150	120	100% N_2

Samples made of AISI 1045 steel were subjected to a preliminary heat treatment before gas nitriding process to improve the properties. Firstly, the samples were hardened at 860 °C for 0.5 h. Secondly, the samples were tempered at 480 °C for 2 h. Then the samples were subjected to controlled gas nitriding at 570 °C, for 5 h in a 100% dissociated ammonia atmosphere with a 2.5 nitrogen potential. After the gas nitriding process, the compound layer was subjected to oxidation. This process was carried out in a steam atmosphere at the temperature of 550 °C. The resulting oxide layer was impregnated with BS 45 as a corrosion inhibitor. The surface zone of the gas nitrided coating is porous. In order to ensure better corrosion resistance, this coating is impregnated with corrosion inhibitor. The thin protective oxide layer formed on the surface of gas nitrided coating ensures the tightness of porous.

The structure and surface morphology of the coatings were analyzed through microscopic observations performed using a Hitachi TM-3000 scanning electron microscope (Radom, Poland) with a BSE detector and Tescan Mira3 (Poznan, Poland). The structure was investigated using polished metallographic cross-sections of steel samples with coatings. The X-ray phase analysis used a Bruker D8 diffractometer (Plock, Poland) with CuKα X-rays (λ = 0.1541837 mÅ).

Surface engineering is the process where the design of surface and substrate systems is defined so as to enhance their properties and achieve performance that could not be achieved either by the surface composition or by the substrate itself. According to the rules for taking hardness measurements with the use of penetration methods, plastic deformation caused by the penetrator should occur only in the tested material area. Based on this assumption, both hardness and Young modulus measurement of PVD coating was determined by using NanoHardness Tester (Radom, Poland) equipped with the Berkovich indenter and an optical microscope (Radom, Poland). The device allows for load setting within the 0.05 and 500 mN and enables precise selection of the indenter penetration depth in the tested material in the range up to 1000 μm. The following parameters were used in the measurements: F = 10 mN, dF/dt = 60 mN/min. The gas nitrided coating hardness measurement was carried out on metallographic sections perpendicular to the surface of the samples. The Neophot 2 light microscope (Plock, Poland) with the Hanemann attachment under the load of 20 g (HV0.02) was used to prepare tests in accordance with the Vickers method based on the EN ISO 6507-1 code [26]. The metallographic sections were also used for the thickness measurements of the tested coatings.

The indentation method is a destructive penetration method. The adhesion test based on this method consists of the Rockwell indenter pressing perpendicularly into the tested coating with a constant acting force on the indenter. Microscopic observations were used to assess the form and intensity of the coating damage in the penetration area. The indentation method was a comparative evaluation. The adhesion assessment was carried out by classifying forms of destruction into six categories [27]. The adhesion test was carried out using a Revetest tester (Radom, Poland) equipped with a Rockwell indenter and an optical microscope (Radom, Poland).

2.2. Tribocorrosion Tests and Wear

The tests of the tribocorrosion process were carried out for a model ball-on-plate sliding matching in an electrolytic environment. The test samples were mounted in a special PVC chamber holding a corrosive environment of 3.5% NaCl. The counter-face was an undeformed pin equipped with an Al_2O_3 alumina ball, which slides in a rotary way back and forth on the sample.

The potentiostat ATLAS 9833 (Atlas-Sollich, Poznan, Poland) with three electrode configuration was used to monitor the potential in the friction pair. A standard calomel electrode (SCE) was used as a reference electrode. Its potential versus standard hydrogen electrode was 244 mV. A platinum wire was used as the counter electrode (CE). The specimen operated as the working electrode (WE). Once each test was finished, profilometric measurements of the depth trace of wear were taken in the mid-distance of the friction path. A detailed description of the presented tribocorrosion test methodology was published in previous articles [28,29] and this methodology was designed and executed according to the concept presented by Mischler and Jemmely in their work [30,31].

During each test the ball slid over a track length of 6 mm with the frequency of 2 Hz for the period of about 60 min. All the experiments involved the use of Al_2O_3 alumina balls with the diameter of 7.0 mm. The tests were carried out at the following loads: 9, 13, and 19 N. The smallest load corresponds to the maximum initial Hertz contact stress of about 1.4 GPa. The main tribocorrosion tests were performed at the open circuit potential (OCP). In order to identify the tribocorrosion components, tests were also performed under the conditions of cathodic polarization (−900 mV vs. SCE) at the load of 13 N.

3. Results

3.1. Characterisation of the Coatings

It can be concluded from Figure 1 that in the hybrid layer composed of Cr and CrN there occur CrN phases with a regularly centered grid and Cr_2N with a hexagonal grid. The examination also shows the presence of chromium and iron phases.

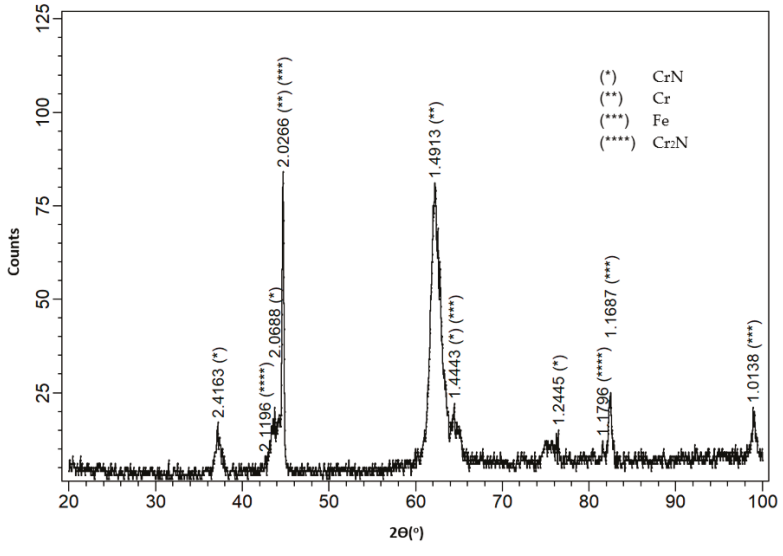

Figure 1. XRD pattern of Cr/CrN coating produced by means of the physical vapor deposition (PVD) method on AISI 1045 steel.

The surface of the Cr/CrN PVD coating at 500× magnification is shown in Figure 2. An analysis of the surface morphology of the obtained hybrid coating has shown a homogeneous structure with a small number of droplets. The tested thickness of hybrid coating was 4.7 μm. However, a thin coating of Cr was approximately 1 μm and thickness of CrN was about 3.7 μm.

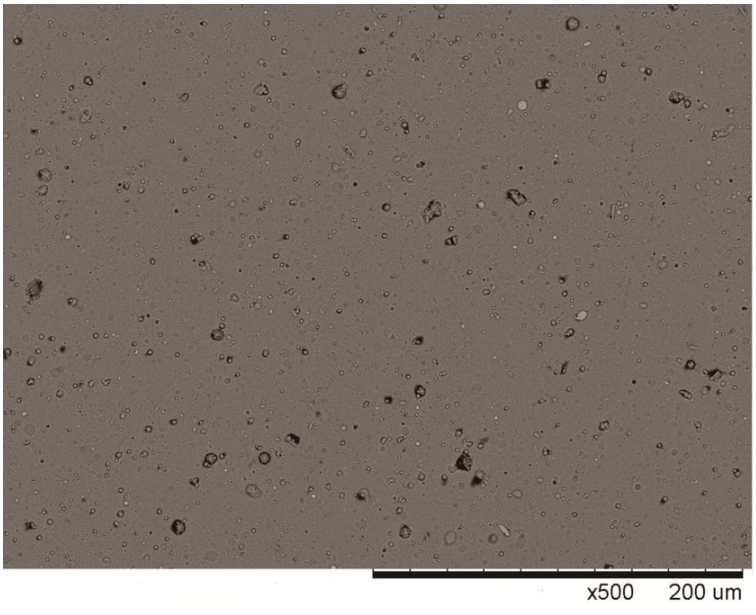

Figure 2. An image of the hybrid layer produced using a scanning electron microscope, consisting of Cr layer and CrN, produced on AISI 1045 medium carbon steel.

A microstructure investigation of the coatings produced on the surface of AISI 1045 steel was also carried out, and it is shown in Figure 3. The gas nitride coating with subsequent oxidation was disclosed by means of nital etching of metallographic cuts. The total thickness of the coating was about 27 μm. However, the thickness of the oxide layer was about 6 μm and the thickness of the nitrided gas only was about 21 μm. The microstructure of the Cr/CrN coating was obtained on polished metallographic cro

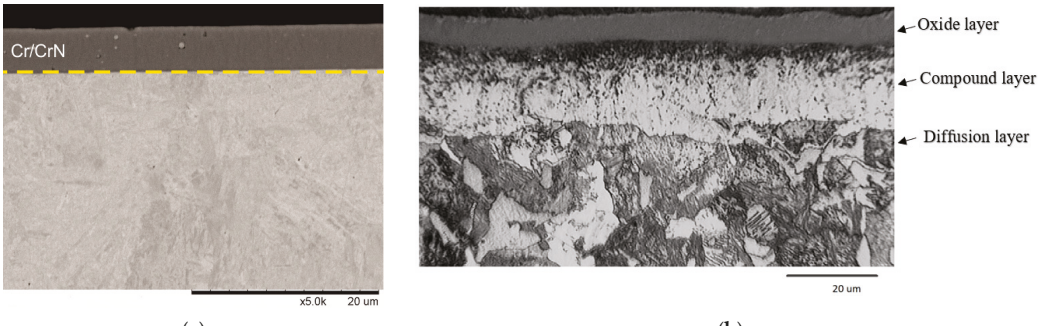

(**a**) (**b**)

Figure 3. The microstructure of the tested coatings produced on AISI 1045 steel (**a**) Cr/CrN PVD, (**b**) gas nitrided with subsequent oxidation and impregnation.

The measurements of hardness and Young's modulus of the Cr/CrN hybrid coating were carried out while maintaining the maximum indenter penetration lower than 10% of the coating thickness. The measurement results are shown in Table 3.

Table 3. The measurement results of hardness.

Coating	Hardness HV
gas nitrided	778 ± 72
Cr/CrN	2627 ± 260

The analysis of the results of hardness measurements showed that the tested Cr/CrN PVD coating is characterized by a higher hardness than the gas nitrided coating. The Young's modulus of the Cr/CrN hybrid coating is 337 GPa. The hardness and the Young's modulus of the samples made from AISI 1045 steel are 235 HV and 202 GPa, respectively [22]. The images shown in Figure 4 make it possible to estimate the coating adhesion with the use of the indentation method.

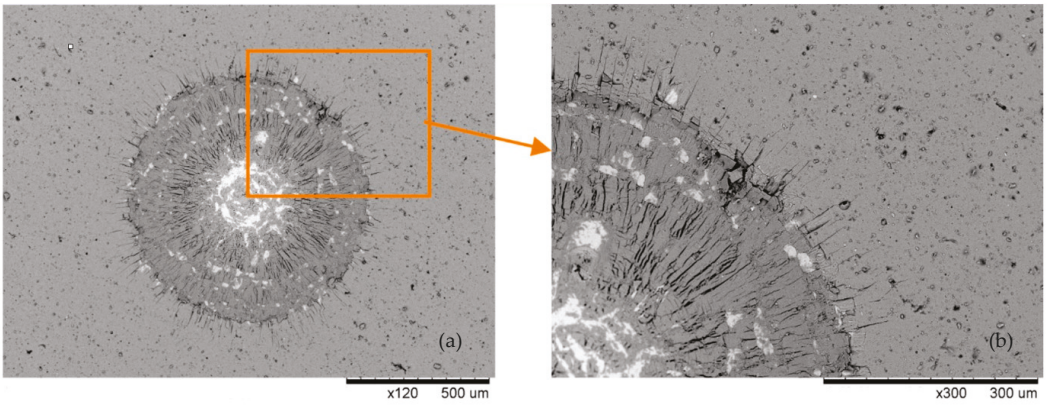

Figure 4. The adhesion results by using the indentation method of Cr/CrN coating. (**a**) contact zone; (**b**) edge of contact zone.

According to the destruction classification forms presented in [24], the adhesion assessment may be assigned to grade HF2. It indicates good Cr/CrN coating adhesion to the AISI 1045 carbon steel substrate.

3.2. Corrosion Resistance

Figure 5 shows the polarization curves of the tested coatings—Cr/CrN PVD and gas nitrided with subsequent oxidation and impregnation. The polarization curves were utilized to indicate the corrosion potential and the corrosion current density. The corrosion potential of the gas nitrided coating with subsequent oxidation and impregnation is *E*corr = −468 mV and *E*corr = −553 mV for the Cr/CrN PVD coating, while the corrosion current density, i_{corr}, is 4 and 0.5 μA/cm^2, respectively.

The factor which largely determines the coating's resistance to the impact of the corrosive environment is its thickness. In this case, after oxidation and impregnation the thickness of the nitrided coating is about 27 μm and is four times greater than the thickness of the Cr/CrN PVD coating, which is about 5 μm.

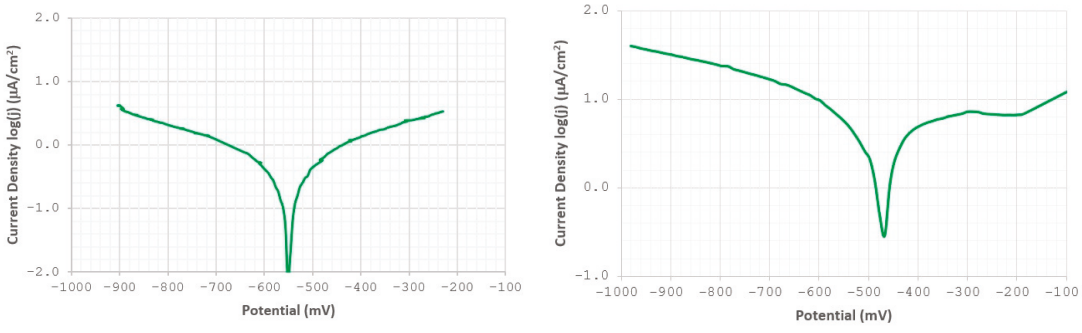

Figure 5. Polarization curves of the tested coatings: (**a**) Cr/CrN PVD, (**b**) gas nitrided with subsequent oxidation and impregnation.

3.3. Tribocorrosion Performance

The main results of the tribocorrosion tests—performed at an open circuit potential (OCP)—are shown in Tables 4 and 5. Table 4 shows the depth of the wear trace as an evaluation of material loss during the tribocorrosion test. On the other hand, Table 5 presents material loss expressed as the volume of the wear trace, which will allow for the selection of tribocorrosion components in the next part of this article. The tables show the mean values for the test series and the standard deviation. At least three tribocorrosion tests were performed for each load value. Figure 6 shows the tribocorrosion wear trace of the tested coatings. The results show that tribocorrosion wear occurred only in the tested zone.

Table 4. Tribocorrosion wear of investigated materials related to different acting forces on the basis of the wear trace.

Material Type	Acting Force (N)		
	9	13	19
	Depth of the Tribocorrosion Wear Trace (μm)		
gas nitrided coating	6.44 ± 0.18	8.46 ± 0.46	11.72 ± 0.19
Cr/CrN PVD	0.975 ± 0.035	1.307 ± 0.095	2.09 ± 0.12

Table 5. Tribocorrosion wear of investigated materials related to different acting forces on the basis of the volume wear.

Material Type	Acting Force (N)		
	9	13	19
	Volume Tribocorrosion Wear (mm^3)		
gas nitrided coating	0.01098 ± 0.00054	0.01635 ± 0.00098	0.02679 ± 0.00056
Cr/CrN PVD	0.000642 ± 0.000035	0.000996 ± 0.00011	0.00203 ± 0.00017

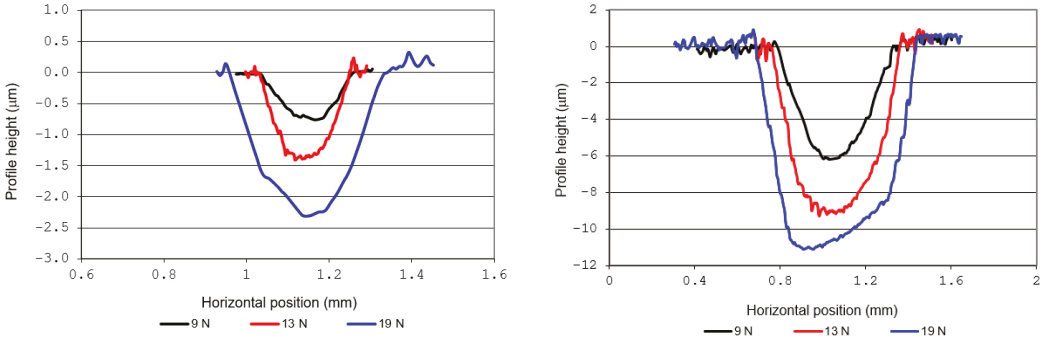

Figure 6. Profile shapes of the wear trace of the investigated coatings after tribocorrosion tests at an open circuit potential, E_{OCP}: (**a**) Cr/CrN PVD, (**b**) gas nitrided with subsequent oxidation and impregnation.

The tribocorrosion test results of the Cr/CrN PVD coating provided under the load of 9 N show the depth of the wear trace of about 1 µm. However, under the load of 19 N, it was approximately 2 µm. These values for the gas nitrided coating are approx. 6 and 12 µm, respectively. The smallest tribocorrosion wear volume in the case of AISI 1045 steel with the gas nitrided coating is 0.011 mm^3, and it corresponds to the 9 N load, whereas the largest wear volume—0.027 mm^3—corresponds to the force of 19 N. In the case of Cr/CrN PVD coating, the material loss increases when the loads in the contact zone are enhanced. The tribocorrosion wear volume varies from 0.00064 to 0.00203 mm^3 related to the changes of the acting force. All the presented results clearly show that the material loss in the case of Cr/CrN PVD coating is lower than in the case of the gas nitrided one with subsequent oxidation and impregnation coating in the chloride ions environment.

Apart from assessing the tribocorrosion resistance of the tested materials, the synergy effect between friction and corrosion in the tested process was also identified quantitatively. The research tests and computational analyses were carried out for the loading force of 13 N. The total material loss during tribocorrosion (T) is the sum of only mechanical wear (W_0), only corrosion wear (C_0), and the synergy effect of wear and corrosion (S) [32]:

$$T = W_0 + C_0 + S \quad (1)$$

The pure mechanical wear was estimated on the basis of the test with cathodic potential polarization in 3.5% NaCl environment (approx. 900 mV vs. SCE). Exemplary wear profiles obtained for the cathodic polarization are shown in Figure 7. The mere corrosive wear (C_0) was calculated on the basis of the corrosion current density by using the Faraday equation (Table 6). In the total tribocorrosion wear of both tested materials, the mechanical wear and the corrosion synergy effect can be observed. It is above 30%.

Table 6. An analysis of tribocorrosion wear components under the load of 13 N.

Material Type	Total Material Loss T (mm^3)	Pure Wear W_0 (mm^3)	Pure Corrosion C_0 (mm^3)	Synergistic Effect $S = T - (W_0 - C_0)$ (mm^3)	S/T (%)
gas nitrided	16.35×10^{-3}	11.06×10^{-3}	1.55×10^{-5}	5.28×10^{-3}	32
Cr/CrN PVD	0.99×10^{-3}	0.65×10^{-3}	7.59×10^{-7}	0.34×10^{-3}	34

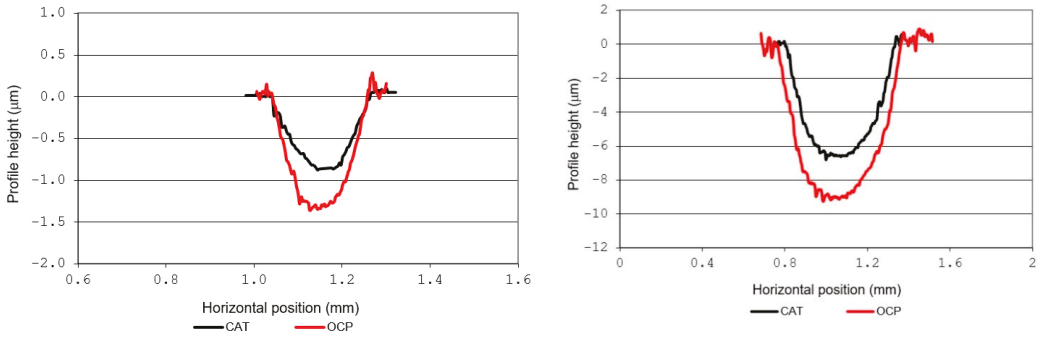

Figure 7. Profiles shape comparison of the wear traces of the investigated coatings after tribocorrosion tests at an open circuit potential and cathodic potential: (**a**) Cr/CrN PVD, (**b**) gas nitrided with subsequent oxidation and impregnation.

Figure 8 presents the potential changes during the tribocorrosion tests under the load of 19 N. Both tested coatings present similar potential characteristics, showing passivation capability. This is demonstrated by the decrease in the potential when the test was initiated with a ball movement. The ball displacement removes the passive layers on the sample surface. When the ball stops and the wear process is completed, the potential increases. A passive oxide layer occurs again on the wear trace surface.

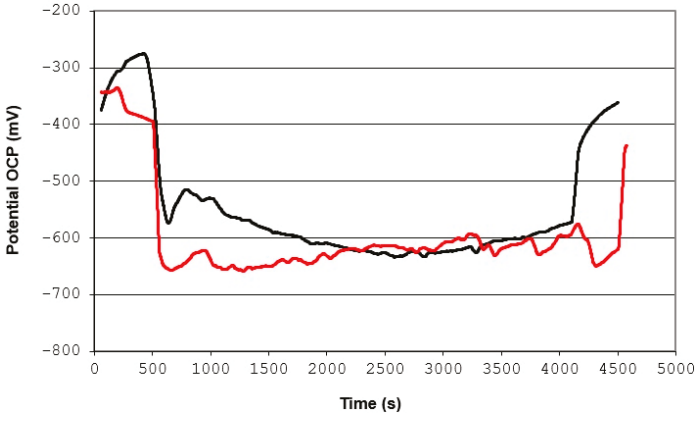

Figure 8. Time evolution of the potential during the tribocorrosion test for the tested coatings at an open circuit potential, E_{OCP}: Cr/CrN PVD (the red line) and gas nitrided with subsequent oxidation and impregnation (the black line).

4. Discussion

The first of the highlighted goals of the presented study was a comparative analysis of tribocorrosion of the Cr/CrN PVD and gas nitrided coatings produced on AISI 1045 medium carbon steel in 3.5% NaCl. The full range of all applied loads shows that the PVD coating presents lower tribocorrosion wear than the gas nitrided one. The better resistance to corrosion activity of 3.5% NaCl and a higher hardness of the PVD coating can be considered as the main causes of this state.

The actual contact zone in the friction node is smaller for the Cr/CrN PVD coating. Consequently, the separated material comes from a smaller area due to frictional interactions. It correlates directly to the intensity of tribocorrosion wear. The tribocorrosion processes are generally initiated on the surface that is exposed by mechanical removal of

the material. In the case of the harder PVD coating, tribocorrosion processes occur on a smaller area and are not as intense as in the case of the gas nitrided coating (Figure 5).

For both analyzed material solutions, in the quantitative assessment (Table 6), a clear synergy effect of friction and corrosion was found. Despite the clear difference in the total tribocorrosion wear (Tables 4 and 5), the synergy effect for both materials is very similar (ca. 30%). It can be concluded that (perhaps) in both cases the tribocorrosion process occurs due to the same elementary wear mechanisms intensified by the unit pressure in the frictional contact zone.

In order to verify this assumption, the elementary mechanisms of tribocorrosion were identified by observing the wear to the surface. Figures 9 and 10 show traces of wear on the tested coatings under various loads in the friction contact zone. The images depict the diversity of the wear mechanisms (their type and intensity). It can also be seen that the pressure in the contact zone affects the tribocorrosion process.

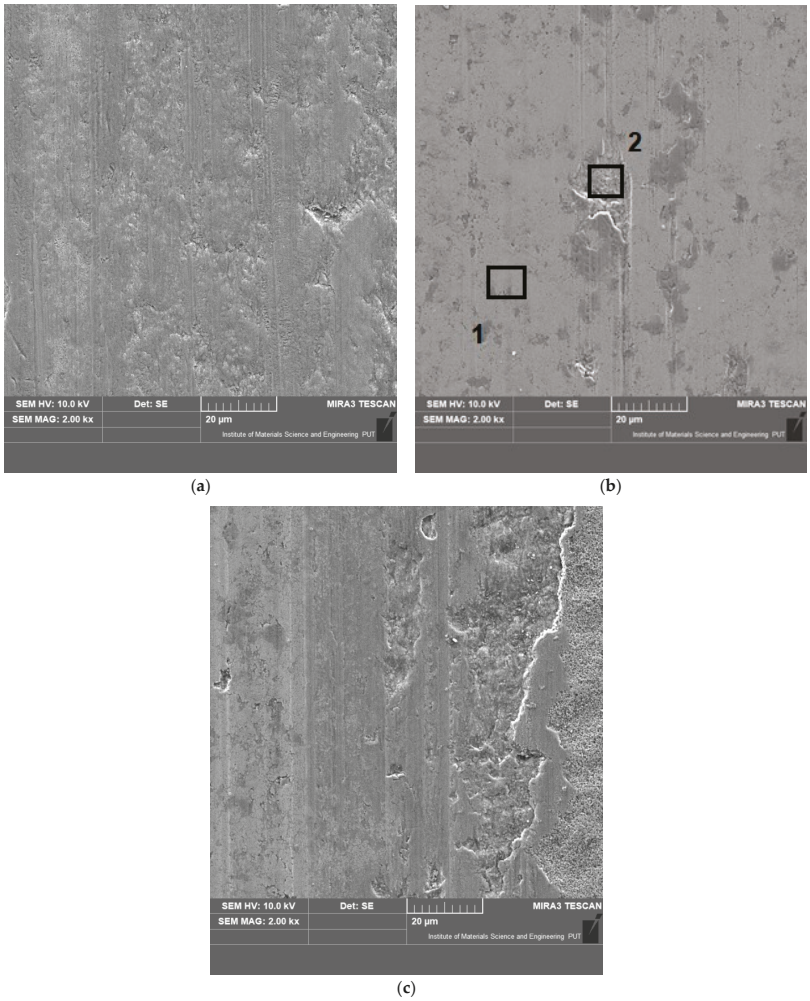

(**a**) (**b**)

(**c**)

Figure 9. Pictures of the wear trace surface for the gas nitrided coating at an open circuit potential, E_{OCP}, under specific loads: (**a**) 9 N, (**b**) 13 N, (**c**) 19 N.

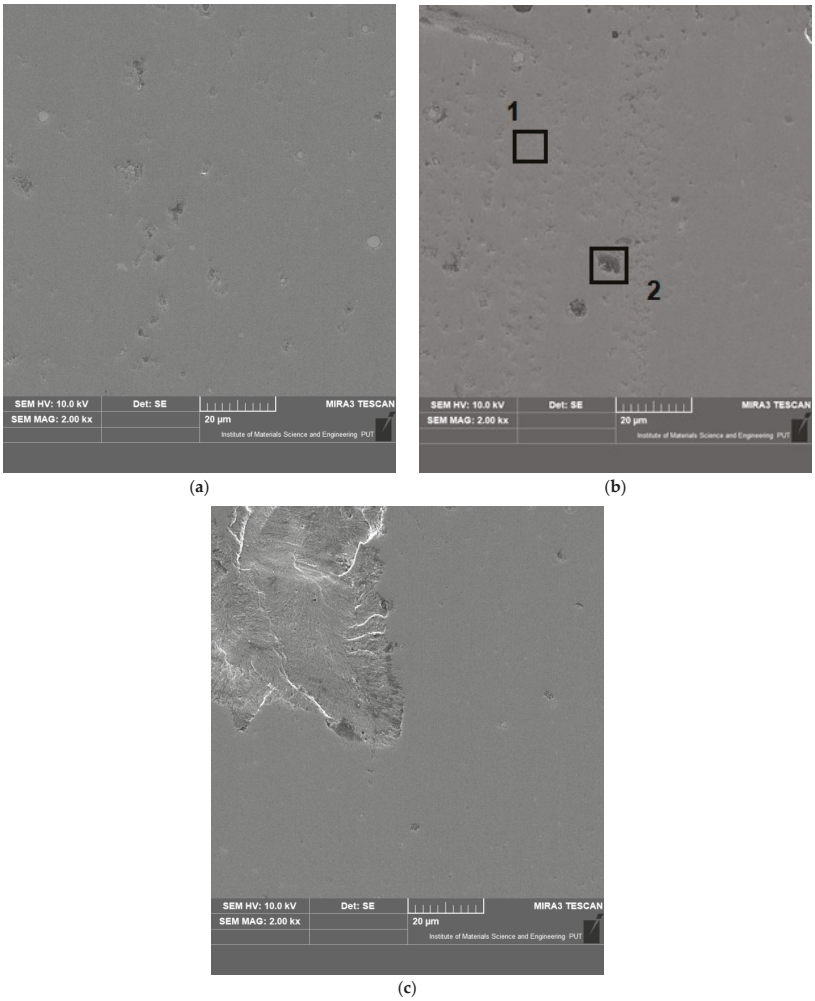

Figure 10. Pictures of the wear trace surface for Cr/CrN PVD coating at an open circuit potential, E_{OCP}, under specific loads: (**a**) 9 N, (**b**) 13 N, (**c**) 19 N.

For the lowest load value in the contact zone the abrasive wear prevails in the case of the gas nitrided coating. (Figure 9a). The parallel grooves are noticeable on the surface of the wear trace that correspond to the movement direction of the counter-sample. When the tests were completed under the load of 13 N, local cavities along the friction path occurred (Figure 9b—area 2). These are most likely due to the corrosive nature of the environment in places where the material separation (a phenomenon of local nature) had previously occurred as a result of friction. Such a mechanical separation of the material can also result from cracking of the hard surface layer. The area of the local cavity was analyzed in terms of its chemical composition. The obtained result differs from the chemical composition of the tested material in the area of a uniform material loss. The sites where the chemical composition was analyzed are marked in Figure 9b. The results of the analysis are presented in Figure 11. The difference (a lower nitrogen content) may indicate a large depth of the defect. A local cavity can create a synergy of friction and corrosion in the total tribocorrosion wear. Under the cyclic conditions, crack initiation may occur as a

result of fatigue processes leading to the separation of larger material part around cavities (pits). These forms of wear are indicated following the test under the highest load value (Figure 9c). The numerous material detachments along the friction path may also be a result of plastic deformation. The implemented force of 19 N during the test facilitates the described material damage, especially around local pits. The authors of [33–35] have also found that the tribocorrosion of nitride steel causes local indentation that initiates material loss caused by fatigue.

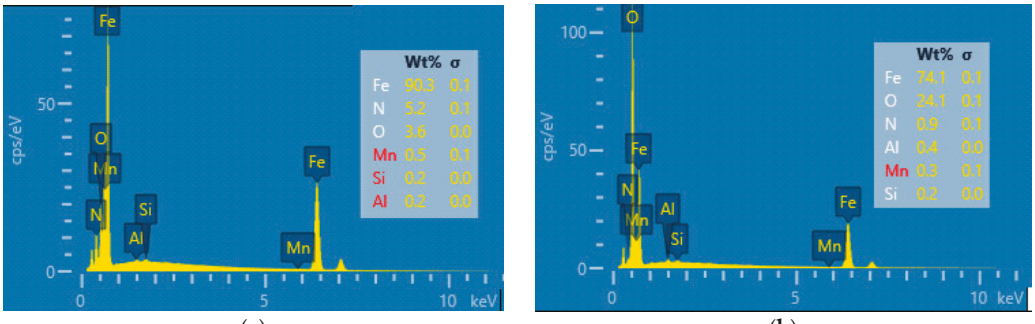

(**a**) (**b**)

Figure 11. An analysis of the chemical composition of the wear trace for the gas nitrided coating (13 N): (**a**) the area of a uniform material loss (Figure 9b—area 1), (**b**) local cavity (Figure 9b—area 2).

The Cr/CrN PVD coating is characterized by a higher hardness and better corrosion resistance in a 3.5% NaCl environment. The above-mentioned properties of the coating determine the course of elementary wear mechanisms in the tribocorrosion process. At the lowest tested load value, the PVD coating (Figure 10a) has a milder abrasive wear (shallow grooves) compared to the gas nitrided one. In the case of an average tested load value (13 N), the grooves appear less frequently, and the wear is of a milder form (Figure 10b). Figure 12 compares the chemical composition of the sample inside the local cavity (Figure 10b—area 2) and within its vicinity in the area of a uniform material defect (Figure 10b—area 1). The significantly lower content of chromium and nitrogen may indicate a large pit depth. The higher hardness of the Cr/CrN PVD coating ensures greater resistance to plastic deformation and adhesion. Therefore, the detachment of larger fragments of the material occurs only locally at the highest loads (Figure 10c). Similar tribocorrosion mechanisms were observed in other studies [17,35–37].

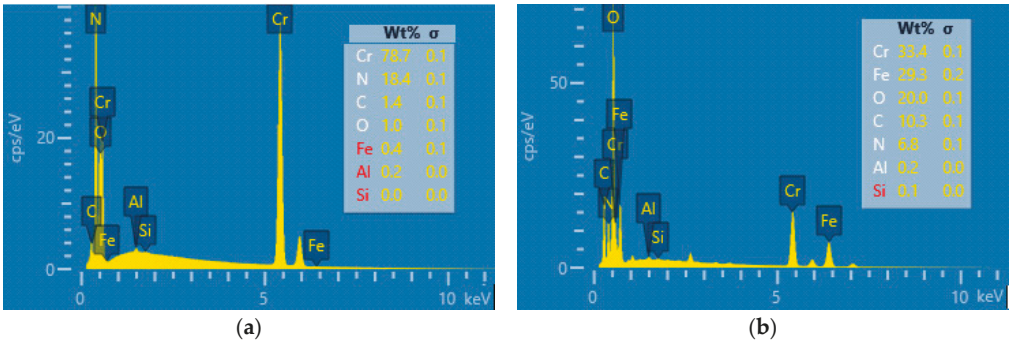

(**a**) (**b**)

Figure 12. An analysis of the chemical composition of the wear trace for Cr/CrN PVD (13 N): (**a**) the area of a uniform material loss (Figure 10b—area 1), (**b**) local cavity (Figure 10b—area 2).

Local cavities in the wear trace, which are important for the formation of the synergy of friction and corrosion, are the result of local corrosion processes. It may be proved by the fact that such forms of damage do not occur under conditions of cathodic polarization. The surface of the wear trace following the tribocorrosion tests under cathodic polarization is shown in Figure 13. In comparison with the traces obtained at the OCP potential, there are no visible local pits (for both materials). Such pits do not form under cathodic polarization conditions. Generally, material loss occurs as a result of abrasive wear.

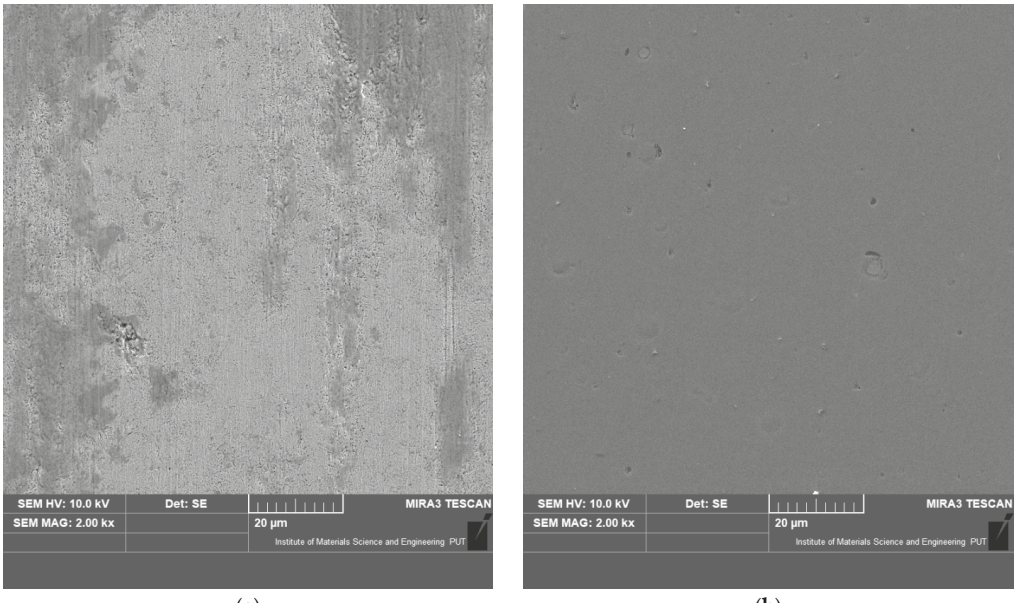

(**a**) (**b**)

Figure 13. Pictures of the wear trace surface at an open circuit potential, E_{OCP}, under the load of 13 N: (**a**) gas nitrided with subsequent oxidation and impregnation, (**b**) Cr/CrN PVD.

In the case of both tested material solutions (despite the significant difference in hardness and resistance to tribocorrosion), it was found that a common mechanism for generating the synergy of friction and corrosion is likely. This mechanism is related to the formation of local cavities along the friction path. The formation of local cavities (pits) is favored by corrosive interactions in the frictional matching and susceptibility to cracking of the hard surface layer. No pitting was observed under cathodic polarization conditions. The concentration of stress around a local cavity promotes plastic deformation of the surface layer. The cyclical nature of these interactions related to the displacement of the contact zone in the tested sliding node may lead to fatigue cracking of the deformed layer—tearing off larger pieces of material. Such forms of wear were observed at the highest pressures in the contact zone. Under the analyzed conditions (the test conditions), the described tribocorrosion mechanism seems to be common for materials of high hardness. It needs to be noted, however, that the above conclusion is based on a comparative analysis that included only two material solutions.

5. Conclusions

Attempts were made in the article to find possible mechanisms of tribocorrosion that would be common to materials of high hardness. It was found that synergy of friction and corrosion can be generated by the same mechanisms associated with the formation of local cavities (pits) on the hard surface layer for both materials. It was also observed

that the intensity of these mechanisms is determined by material hardness. A comparative analysis of tribocorrosion process was carried out only for two material solutions of high and different hardness. Under the analyzed conditions (the test conditions), the described tribocorrosion mechanism can be considered as characteristic of high hardness materials.

1. The Cr/CrN PVD coating produced on AISI 1045 medium carbon steel provides better tribocorrosion resistance than the gas nitrided with subsequent oxidation and impregnation coating in a 3.5% NaCl environment. This relation applies to the entire range of loads in the contact zone which were applied during the tribocorrosion tests.
2. In tribocorrosion tests, a clear synergy effect of friction and corrosion was identified for both tested material solutions. It was over 30% in both cases. A similar percentage of the synergy effect, despite the clear difference in the total tribocorrosive loss, may indicate that similar elementary destruction mechanisms occur in the case of both analyzed material solutions.
3. According to the diagnosed fundamental tribocorrosion mechanisms, the synergy effect is caused by the fact that corrosion processes create local cavities which at successive time intervals are most likely to intensify mechanical wear. The area around the cavities facilitates plastic deformation, the initiation of cracking of cyclically deformed layers and the tearing off larger fragments of material (especially at higher unit pressures in the frictional contact zones).

Author Contributions: Conceptualization, A.S. and M.K.; methodology, A.S. and M.K.; investigation, A.S. and M.K.; writing—original draft preparation A.S. and M.K.; writing—review and editing, M.K.; supervision, A.S. All authors have read and agreed to the published version of the manuscript.

Funding: This research received no external funding.

Institutional Review Board Statement: Not applicable.

Informed Consent Statement: Not applicable.

Data Availability Statement: Data is contained within the article.

Conflicts of Interest: The authors declare no conflict of interest.

References

1. Cao, S.; Mischler, S. Modeling tribocorrosion of passive metals—A review. *Curr. Opin. Solid State Mater. Sci.* **2018**, *22*, 127–141. [CrossRef]
2. Ghanbarzadeh, A.; Salehi, F.M.; Bryant, M.; Neville, A. A new asperity-scale mechanistic model of tribocorossive wear: Synergistic effect pf mechanical wear and corrosion. *J. Tribol.* **2019**, *141*, 1–12. [CrossRef]
3. Jemmely, P.; Mischler, S.; Landolt, D. Electrochemical modeling of passivation phenomena in tribocorrosion. *Wear* **2000**, *237*, 63–76. [CrossRef]
4. Ghanbarzadeh, A.; Salehi, F.M.; Bryant, M.; Neville, A. Modelling the evolution of electrochemical current in potentiostatic condition using and asperity-scale model of tribocorrosion. *Biotribology* **2019**, *17*, 19–29. [CrossRef]
5. Landolt, D.; Mischler, S.; Stemp, M. Electrochemical methods in tribocorrosion: A critical appraisal. *Electrochim. Acta* **2001**, *46* 3913–3929. [CrossRef]
6. Bayon, R.; Igartua, A.; Fernandez, X.; Martinez, R.; Rodriguez, R.J.; Garcia, J.A.; de Frutos, A.; Arenas, M.A.; de Damborenea, J. Corrosion-wear behaviour of PVD Cr/CrN multilayer coatings for gear applications. *Tribol. Int.* **2009**, *42*, 591–599. [CrossRef]
7. Ould, C.; Badiche, X.; Montmitonnet, P.; Gacho, Y. PVD coated mill rolls for cold rolling of stainless-steel strips—Tribological and mechanical laboratory tests. *J. Manuf. Process.* **2013**, *15*, 77–86. [CrossRef]
8. Ginting, A.; Skein, R.; Cuaca, D.; Herdianto; Pieter, Z.; Masyithah, Z. The characteristics of CVD- and PVD-coated carbide tools in hard turning of AISI 4340. *Measurement* **2018**, *129*, 548–557. [CrossRef]
9. Malvajerdi, S.S.; Malvajerdi, A.S.; Ghanaatshoar, M. Protection of CK45 carbon steel tillage tools using TiN coating deposited by an arc-PVD method. *Ceram. Int.* **2019**, *45*, 3816–3822. [CrossRef]
10. Gupta, K.M.; Ramdev, K.; Dharmateja, S.; Sivarajan, S. Cutting characteristics of PVD coated cutting tools. *Mater. Today Proc.* **2018**, *5*, 11260–11267. [CrossRef]
11. Baptista, A.; Silva, F.; Porteiro, J.; Miguez, J.; Pinto, G. Sputtering physical vapour deposition (PVD) coatings: A critical review on process improvement and market trend demands. *Coatings* **2018**, *8*, 402. [CrossRef]
12. Sousa, V.F.C.; Silva, F.J.G. Recent advances on coated milling tool technology—A comprehensive review. *Coatings* **2020**, *10*, 235. [CrossRef]

13. Liu, C.; Leyland, A.; Bi, Q.; Matthews, A. Corrosion resistance of multi-layered plasma-assisted physical vapor deposition TiN and CrN coatings. *Surf. Coat. Technol.* **2001**, *141*, 164–173. [CrossRef]
14. Ibrahim, M.A.M.; Korablov, S.F.; Yoshimura, M. Corrosion of stainless steel coated with TiN, (TiAl)N and CrN in aqueous environments. *Corros. Sci.* **2002**, *44*, 815–828. [CrossRef]
15. Su, Y.L.; Yao, S.H.; Wu, C.T. Comparison of characterizations and tribological performance of TiN and CrN deposited by cathodic arc plasma deposition process. *Wear* **1996**, *199*, 132–141. [CrossRef]
16. Chen, Q.; Cao, Y.; Xie, Z.; Chen, T.; Wan, Y.; Wang, H.; Gao, X.; Chen, Y.; Zhou, Y.; Guo, Y. Tribocorrosion behaviors of CrN coating in 3,5 wt% NaCl solution. *Thin Solid Films* **2017**, *622*, 41–47. [CrossRef]
17. Shan, L.; Wang, Y.; Zhang, Y.; Zhang, Q.; Xue, Q. *Tribocorrosion* behaviors of PVD *CrN* coated stainless steel in seawater. *Wear* **2016**, *362–363*, 97–104. [CrossRef]
18. Shan, L.; Zhang, Y.-R.; Wang, Y.-X.; Li, J.-L.; Jiang, X.; Chen, J.-M. Corrosion and wear behaviors of PVD CrN and CrSiN coatings in seawater. *Trans. Nonferr. Met. Soc. China* **2016**, *26*, 175–184. [CrossRef]
19. Shan, L.; Wang, Y.; Li, J.; Jiang, X.; Chen, J. Improving tribological performance of CrN coatings in seawater by structure design. *Tribol. Int.* **2015**, *82*, 78–88. [CrossRef]
20. Marin, E.; Offoiach, R.; Regis, M.; Fusi, S.; Lanzutti, A.; Fedrizzi, L. Diffusive thermal treatments combined with PVD coatings for tribological protection of titanium alloys. *Mater. Des.* **2016**, *89*, 314–322. [CrossRef]
21. Bayon, R.; Nevshupa, R.; Zubizarreta, C.; Ruiz de Gopegui, U.; Barriga, J.; Igartua, A. Characterisation of tribocorrosion behaviour of multilayer PVD coatings. *Anal. Bioanal. Chem.* **2010**, *396*, 2855–2862. [CrossRef]
22. Ye, Y.; Wang, Y.; Chen, H.; Li, J.; Yao, Y.; Wang, C. Doping carbon to improve the tribological performance of CrN coatings in *seawater*. *Tribol. Int.* **2015**, *90*, 362–371. [CrossRef]
23. Song, G.-H.; Yang, X.-P.; Xiong, G.-L.; Lou, Z.; Chen, L.-J. The corrosive behawior of Cr/CrN multilayer coatings with different modulation periods. *Vacuum* **2013**, *89*, 136–141. [CrossRef]
24. Kowalski, M. The Improvement of Tribocorrosion Performance of Structural Steel Components in Marine Environment. Ph.D. Thesis, Warsaw University of Technology, Warsaw, Poland, 2018.
25. Michalski, J.; Iwanow, J.; Tacikowski, J.; Tarfa, T.N.; Tymowski, J.; Sułkowski, I.; Wach, P. Anticorrosion nitriding with post-oxidation and inhibitor impregnation, and its industrial applications. *Heat Treat. Met.* **2004**, *2*, 31–35.
26. *EN ISO 6507-1 Metallic Materials—Vickers Hardness Test—Part 1: Test Method*; European Committee for Standarization: Brussels, Belgium, 2005.
27. Vidakis, N.; Antoniadis, A.; Bilalis, N. The VDI 3198 indentation test evaluation of a reliable qualitative control for layered compounds. *J. Mater. Process. Technol.* **2003**, *143–144*, 481–485. [CrossRef]
28. Stachowiak, A.; Zwierzycki, W. Tribocorrosion modeling of stainless steel in a sliding pair of pin-on-plate type. *Tribol. Int.* **2011**, *44*, 1216–1224. [CrossRef]
29. Kowalski, M.; Stachowiak, A. Tribocorrosion performance of Zn, Zn–Ni with magnesium electrodeposited on medium carbon steel in a chloride environment. *Surf. Coat. Technol.* **2019**, *366*, 75–85. [CrossRef]
30. Mischler, S.; Debaud, S.; Landolt, D. Wear accelerated corrosion of passive metal in tribocorrosion systems. *J. Electrochem. Soc.* **1998**, *145*, 750–758. [CrossRef]
31. Jemmely, P.; Mischler, S.; Landolt, D. Tribocorrosion behavior of Fe-17Cr stainless steel in acid and alkaline solutions. *Tribol. Int.* **1999**, *32*, 295–303. [CrossRef]
32. ASTM G119-09. *Standard Guide for Determining Synergism between Wear and Corrosion*; ASTM International: West Conshohocken, PA, USA, 2016.
33. Sun, Y. Tribocorrosive behavior of low temperature plasma-nitrided PH stainless steel sliding against under linear reciprocation with and without trensvere oscillations. *Wear* **2016**, *362–363*, 105–113. [CrossRef]
34. Baranowska, J.; Franklin, S.E.; Kochmanska, A. Wear behaviour of low-temperature gas nitrided austenitic stainless steel in a corrosive liquid environment. *Wear* **2007**, *263*, 669–673. [CrossRef]
35. Hacisalihogu, I.; Yildiz, F.; Celik, A. Tribocorrosion behavior of plasma nitrided Hardox steels in NaCl solution. *Tribol. Int.* **2018**, *120*, 434–445. [CrossRef]
36. Naghibi, S.A.; Ksolution, R.; Fathi, M.H. Corrosion and tribocorrosion behawior of T/TiN PVD coating on 316L stainless steel substrate in Ringer's. *Mater. Chem. Phys.* **2014**, *148*, 614–623. [CrossRef]
37. Kok, Y.N.; Akid, R.; Hovsepian, P.E. Tribocorrosion testing of stainless steel (SS) and PVD coated SS using a modified scanning reference electrode technique. *Wear* **2005**, *295*, 1472–1481. [CrossRef]

MDPI
St. Alban-Anlage 66
4052 Basel
Switzerland
Tel. +41 61 683 77 34
Fax +41 61 302 89 18
www.mdpi.com

Coatings Editorial Office
E-mail: coatings@mdpi.com
www.mdpi.com/journal/coatings

MDPI
St. Alban-Anlage 66
4052 Basel
Switzerland

Tel: +41 61 683 77 34
Fax: +41 61 302 89 18

www.mdpi.com

ISBN 978-3-0365-1037-8